

AD-A114 497

PENNSYLVANIA STATE UNIV UNIVERSITY PARK MATERIALS RE--ETC F/G 20/3
TARGETED BASIC STUDIES OF FERROELECTRIC AND FERROELASTIC MATERI--ETC(U)
NOV 81 L E CROSS, R E NEWNHAM, G R BARSCH

NO0014-78-C-0291

NL

UNCLASSIFIED

1 of 2

40
31 4437

40
31 4437

40
31 4437

(10)

TARGETED BASIC STUDIES OF FERROELECTRIC AND FERROELASTIC
MATERIALS FOR PIEZOELECTRIC TRANSDUCER APPLICATIONS

Contract No. N00014-78-C-0291

Sponsored by
The Office of Naval Research

L.E. Cross
R.E. Newnham
G.R. Barsch
J.V. Biggers

November 1981

DTIC
SELECTED
MAY 17 1982
H

DTIC FILE COPY



DISTRIBUTION STATEMENT A

Approved for public release;
Distribution Unlimited

THE MATERIALS RESEARCH LABORATORY

THE PENNSYLVANIA STATE UNIVERSITY

UNIVERSITY PARK, PENNSYLVANIA

8 2 0 5 1 7 0 8 9

11

TARGETED BASIC STUDIES OF FERROELECTRIC AND FERROELASTIC
MATERIALS FOR PIEZOELECTRIC TRANSDUCER APPLICATIONS

Period December 1, 1980 to November 30, 1981

Annual Report

OFFICE OF NAVAL RESEARCH

Contract No. N00014-78-C-0291

APPROVED FOR PUBLIC RELEASE — DISTRIBUTION UNLIMITED

Reproduction in whole or in part is permitted for
any purpose of the United States Government

L.E. Cross
R.E. Newnham
G.R. Barsch
J.V. Biggers

November 1981

DTIC
SELECTED
MAY 17 1982
S H

Contents

	<u>Page</u>
INTRODUCTION.	1
1. ELECTROSTRICTION.	10
A. Theory of Electrostriction.	10
1. Purpose and Scope	10
2. Phenomenological Theory	10
2.1 Landau-Devonshire Theory with Rotationally Invariant Expansion Coefficients	10
2.2 Phenomenological Theory of the Temperature Variation of Electrostriction of Ferroelectrics in the Paraelectric Phase	11
3. Microscopic Theory.	11
3.1 First Order Anharmonic Properties of Perovskite Oxides: Static Crystal Lattice.	11
3.2 Temperature Dependence of Electrostriction	11
4. Publications.	12
B. Experiments on Electrostriction	12
1. Purpose and Scope	12
2. Publications.	13
2. PIEZOELECTRIC COMPOSITES.	14
C. PZT:Polymer Composites.	14
1. Purpose and Scope	14
2. Publications.	15
D. Piezoelectric Composites Other than PZT	15
1. Scope and Objectives.	15
2. Publications.	16
3. PREPARATIVE STUDIES	16
3.1 Densification of PZT Ceramics.	16
3.2 Fabrication of Grain Oriented $\text{Bi}_4\text{Ti}_3\text{O}_{12}$	17
3.3 Preparations of Lead Magnesium Niobate	17
3.4 Crystal Growth Studies	17
3.4.1 Halide Perovskites.	18
3.4.2 Tungsten Bronze Oxides.	18
3.5 Publications	19

	<u>Page</u>
4. CHARACTERIZATION STUDIES.	20
4.1 Ordering in $\text{Pb}(\text{Mg}_{1/3}\text{Nb}_{2/3})\text{O}_3\text{-Pb}(\text{Mg}_{1/2}\text{W}_{1/2})\text{O}_3$	20
4.2 Studies of the $\text{PbZrO}_3\text{:PbTiO}_3$ System	20
4.3 Studies of Ferroelectric Surfaces.	20
4.4 Luminescence in Tb^{3+} and Eu^{3+} Activated Gadolinium Molybdate.	21
4.5 Domain Walls in $\text{Gd}_2(\text{MoO}_4)_3$	21
4.6 Publications	21
5. FERROFLASTICS	22
5.1 Lead Bismuth Niobate	22
5.2 Shape Memory Effects in PLZT Ceramics.	22
5.3 Publications	23
6. FERROELECTRIC BICRYSTALS.	23
6.1 Scope and Purpose.	23
6.2 Publications	24
7. PYROELECTRIC STUDIES.	24
7.1 Theoretical Studies.	24
7.2 Experimental	24
7.3 Publications	25
8. GENERAL	26
8.1 Introduction	26
8.2 Publications	26
APPENDICES.	27

Accession For	
NTIS GRA&I	<input checked="" type="checkbox"/>
DTIC TAB	<input type="checkbox"/>
Unannounced	<input type="checkbox"/>
Justification	
By	
Distribution/	
Availability Codes	
Dist	Avail and/or Special

DTIC
COPY
INSPECTED
2

A

UNCLASSIFIED

SECURITY CLASSIFICATION OF THIS PAGE (When Data Entered)

REPORT DOCUMENTATION PAGE		READ INSTRUCTIONS BEFORE COMPLETING FORM
1. REPORT NUMBER	2. GOVT ACCESSION NO. AD-A114 497	3. RECIPIENT'S CATALOG NUMBER
4. TITLE (and Subtitle) TARGETED BASIC STUDIES OF FERROELECTRIC AND FERROELASTIC MATERIALS FOR PIEZOELECTRIC TRANSDUCER APPLICATIONS		5. TYPE OF REPORT & PERIOD COVERED Annual Dec. 1, 1980 to Nov. 30, 1981
7. AUTHOR(s) L.E. Cross, R.E. Newnham, G.R. Barsch J.V. Biggers		6. PERFORMING ORG. REPORT NUMBER
9. PERFORMING ORGANIZATION NAME AND ADDRESS Materials Research Laboratory The Pennsylvania State University University Park, PA 16802		8. CONTRACT OR GRANT NUMBER(s) N00014-78-C-0291
11. CONTROLLING OFFICE NAME AND ADDRESS Office of Naval Research, Room 619 Ballston Tower, 800 N. Quincy Street Arlington, VA 22217		10. PROGRAM ELEMENT, PROJECT, TASK AREA & WORK UNIT NUMBERS
14. MONITORING AGENCY NAME & ADDRESS (if different from Controlling Office)		12. REPORT DATE November 1981
		13. NUMBER OF PAGES
		15. SECURITY CLASS. (of this report) UNCLASSIFIED
		15a. DECLASSIFICATION/DOWNGRADING SCHEDULE
16. DISTRIBUTION STATEMENT (of this Report) Reproduction in whole or in part is permitted for any purpose of the United States Government		
<div style="border: 1px solid black; padding: 5px; text-align: center;"> DISTRIBUTION STATEMENT A Approved for public release; Distribution Unlimited </div>		
17. DISTRIBUTION STATEMENT (of the abstract entered in Block 20, if different from Report)		
18. SUPPLEMENTARY NOTES		
19. KEY WORDS (Continue on reverse side if necessary and identify by block number)		
20. ABSTRACT (Continue on reverse side if necessary and identify by block number) This program on "Targeted Basic Studies of Ferroelectric and Ferroelastic Crystals for Piezoelectric Transducer Applications" is now in the fourth year of operation. Achievement over the past year have included: (1) The development of a correct phenomenology for electrostriction which leads to a Gibbs function which is invariant under simple body rotation. (2) Refinement of the full microscopic theory including temperature dependence of electrostriction in the important perovskite structure oxides.		

DD FORM 1 JAN 73 1473 EDITION OF 1 NOV 65 IS OBSOLETE

SECURITY CLASSIFICATION OF THIS PAGE (When Data Entered)

(3) Development of new processing methods for $\text{PbMg}_{1/3}\text{Nb}_{2/3}\text{O}_3$ based relaxor ferroelectric compositions which eliminate the troublesome unwanted pyrochlore phase.

(4) The design of new 1:3 and 2:3 connected PZT:polymer composites which have very high d_{hgh} product and freedom from pressure dependence up to 1,000 psi pressure.

(5) Crystal pulling of $(\text{Pb}_{1-x}\text{Ba}_x)\text{Nb}_2\text{O}_6$ crystals at compositions close to the important morphotropic boundary.

(6) A clear demonstration of the importance of piezoelectric grain resonance as the source of dielectric dispersion in LiNbO_3 ceramics.

(7) The development of an important new family of polar glass ceramics which are polar but non-ferroelectric and are poled by growth in a strong temperature gradient. Materials which combine high transverse coupling and low temperature coefficient of resonant frequency have been fabricated by this method.

The group was heavily involved over the summer in the local organization of the Fifth International Meeting on Ferroelectricity IMF 5 which was held at Penn State in August.

Work on the program is documented in more than 40 papers published in refereed journals during 1981. Seven invited and 25 contributed papers were presented at National and International meetings during the year.

INTRODUCTION

The program on targeted basic studies of ferroelectric and ferroelastic crystals for piezoelectric transducer applications is now in its fourth year of operation. It is pleasing to note that several of the original topics have now matured to the level where major companies are beginning to take up development. In the electrostriction area, the lead magnesium niobate-lead titanate relaxor is now under active development at ITEK optics division for applications in multi-position-mirrors (MPMs). A new joint program is starting with Honeywell Corporation to explore multilayer implanted electrodes for power transducers. For the composite hydrophone materials, Materials International in Maine, and Honeywell are interested in developing capability for large area sensors.

In the program of work, major achievements during the last year have been

- (1) The development of an adequate phenomenology which does yield a rotationally invariant correct description of stored energy in an electrostrictive solid.
- (2) Further evolution of a full microscopic theory for the temperature dependence of electrostriction in the important perovskite structure.
- (3) Development of a new processing method for lead magnesium niobate which eliminates the problem of unwanted pyrochlore phases.
- (4) The design of a new much more robust piezoelectric hydrophone composite which combines very high sensitivity with freedom from pressure dependence to beyond 1,000 psi pressure.
- (5) Crystal pulling of $(\text{Pb}_{1-x}\text{Ba}_x)\text{Nb}_2\text{O}_6$ tungsten bronze crystal at compositions close to the important morphotropic boundary.
- (6) A new breakthrough in understanding the piezoelectric origin of high frequency dielectric loss in LiNbO_3 ceramics.

(7) The development of a new family of polar glass ceramics which are non-ferroelectric and combine high transverse coupling with low temperature coefficient of resonant frequency.

Work on the program was significantly aided by a new apprentice training scheme which made 4 high school seniors and college freshman available over the Summer. These eager youngsters gave the graduate students excellent experience in organizing their work to exploit the 'extra hands.'

The group was heavily involved over the summer in the organization of IMF-5 the Fifth International Meeting on Ferroelectricity which was held at Penn State in August. That the additional work on this project did not detract from our ONR contract studies is attested by the fact that based on contract work the group published more than 40 papers in 1980-81, and participated with 7 invited papers and 25 contributed talks at National and International meetings.

In view of the very large published output in this year of the program, the annual report departs from previous practice of providing all publications in technical appendices. To avoid overloading the reader, the 20 most important papers are selected and presented in full, the write up in the text of the report is expanded a little to provide the rationale for each approach and only the references and abstracts of the remaining papers included.

It may be noted that the topic of pyroelectricity has been added to the report. This work was carried out under DARPA order no. 4195 and coupled to the Navy program for monitoring purposes so as to consolidate all work on the composite systems. We also note that some of the piezoelectric work on polar glass ceramics was partially supported by the Army Research Office under contract DAAG 29-80-C-0008.

Publications

The following papers have been published.

PUBLICATIONS

51. B.N.N. Achar, G.R. Barsch and L.E. Cross. Static Shell Model Calculation of Electrostriction and Third Order Elastic Coefficients of Perovskite Oxides. Ferroelectrics 37, 495-498 (1981).
52. B.N.N. Achar and G.R. Barsch. Anharmonic Perturbation Calculation of Electrostriction for SrTiO_3 . Ferroelectrics 37, 491-493 (1981).
53. G.R. Barsch, B.N.N. Achar and L.E. Cross. Phenomenological Theory of the Temperature Variation of Electrostriction of Ferroelectrics in the Paraelectric Phase. Ferroelectrics 35, 191-194 (1981).
54. G.R. Barsch, B.N.N. Achar and L.E. Cross. Landau-Devonshire Theory with Rotationally Invariant Expansion Coefficients. Ferroelectrics 35, 187-190 (1981).
55. K. Uchino, S. Nomura, L.E. Cross, S.J. Jang and R.E. Newnham. Pressure Gauge Using Relaxor Ferroelectrics. Jpn. Journ. Appl. Phys. 20, L367-L370 (1981).
56. Z. Chen, N. Setter and L.E. Cross. Diffuse Ferroelectric Phase Transition and Cation Order in the Solid Solution System $\text{Pb}(\text{Sc}_{1/2}\text{Nb}_{1/2})\text{O}_3$: $\text{Pb}(\text{Sc}_{1/2}\text{Ta}_{1/2})\text{O}_3$. Ferroelectrics 37, 619-622 (1981).
57. N. Setter and L.E. Cross. An Optical Study of the Ferroelectric Relaxors $\text{Pb}(\text{Mg}_{1/3}\text{Nb}_{2/3})\text{O}_3$, $\text{Pb}(\text{Sc}_{1/2}\text{Ta}_{1/2})\text{O}_3$, and $\text{Pb}(\text{Sc}_{1/2}\text{Nb}_{1/2})\text{O}_3$. Ferroelectrics 37, 551-554 (1981).
58. K. Uchino, S. Nomura, L.E. Cross and R.E. Newnham. Electrostrictive Effects in Potassium Tantalate Niobate. Ferroelectrics 38, 825-828 (1981).
59. A. Safari, R.E. Newnham, L.E. Cross and W.A. Schulze. Perforated PZT-Polymer Composites for Piezoelectric Transducer Applications.
60. A. Safari, A. Halliyal, R.E. Newnham and I.M. Lachman. Transverse Honeycomb Composite Transducers. Mat. Res. Bull. 17, 301-308 (1982).

61. K. Rittenmyer, T. Shrout, W.A. Schulze and R.E. Newnham. Piezoelectric 3-3 Composites. Ferroelectrics
62. A. Safari, A. Halliyal, L.J. Bowen and R.E. Newnham. Flexible Composite Transducers. Ceramic Journal, 12-29 (1981).
63. T.R. Gururaja, W.A. Schulze, T.R. Shrout, A. Safari, L. Webster and L.E. Cross. High Frequency Applications of PZT/Polymer Composite Materials. Ferroelectrics 39, 1245-1248 (1981).
64. S.Y. Lynn, R.E. Newnham, K.A. Klicker, K. Rittenmyer, A. Safari and W.A. Schulze. Ferroelectric Composites for Hydrophones. Ferroelectrics 38, 955-958 (1981).
65. A. Halliyal, A.S. Bhalla, R.E. Newnham, L.E. Cross and T.R. Gururaja. Study of the Piezoelectric Properties of $\text{Ba}_2\text{Ge}_2\text{TiO}_8$ Glass-Ceramic and Single Crystals. Journal of Materials Science 17, 295-300 (1982).
66. A. Halliyal, A.S. Bhalla, R.E. Newnham and L.E. Cross. Piezoelectric Properties of Lithium Borosilicate Glass Ceramics. Journal of Applied Physics (accepted).
67. A. Halliyal, A.S. Bhalla, R.E. Newnham and L.E. Cross. Piezoelectric and Elastic Properties of Barium Germanium Titanate and Lithium Borosilicate Glass Ceramics. IEEE Ultrasonics Symposium Proceedings 315-318 (1981).
68. S. Venkataramani and J.V. Biggers. Densification in PZT. Ferroelectrics 37, 607-610 (1981).
69. S. Swartz, W.A. Schulze and J.V. Biggers. Fabrication and Electrical Properties of Grain Oriented $\text{Bi}_4\text{Ti}_3\text{O}_{12}$ Ceramics. Ferroelectrics 38, 765-768 (1981).
70. A. Amin, R.E. Newnham, L.E. Cross and S. Nomura. Ordering in $\text{Pb}(\text{Mg}_{1/3}\text{Nb}_{2/3})\text{O}_3$ - $\text{Pb}(\text{Mg}_{1/2}\text{W}_{1/2})\text{O}$ Solid Solutions. Journal of Solid State Chemistry 35(2), 267-271 (1980).

71. A. Amin, L.E. Cross and R.E. Newnham. Calorimetric and Phenomenological Studies of the $\text{PbZrO}_3\text{:PbTiO}_3$ System. Ferroelectrics **37**, 647-650 (1981).
72. A. Amin, R.E. Newnham and L.E. Cross. Phenomenological and Structural Study of a Low-Temperature Phase Transition in the $\text{PbZrO}_3\text{-PbTiO}_3$ System. Journal of Solid State Chemistry **37**, 248-255 (1981).
73. L.L. Tongson, A.S. Bhalla and L.E. Cross. Studies of Ferroelectric Surfaces Using Ion Beam and Chemical Etching Techniques. Ferroelectrics **36**, 471-474 (1981).
74. L.L. Tongson, A.S. Bhalla and B.E. Knox. Low Energy Inert Gas Ion Scattering from GdF_3 , Gd_2O_3 and $\text{Gd}_2(\text{MoO}_4)_3$ Surfaces: 1. Inelastic Effects. Mat. Res. Bull. **16**, 775-783 (1981).
75. L.L. Tongson, A.S. Bhalla, L.E. Cross and B.E. Knox. Investigation of BaTiO_3 and $\text{Gd}_2(\text{MoO}_4)_3$ Crystal Surfaces by Complementary AES and ISS Techniques. Applications of Surface Science **4**, 263-270 (1980).
76. A.S. Bhalla and L. Tongson. Direct Method of Measuring Ion Beam Irradiated Areas. Journal of Vacuum Science (accepted).
77. B.K. Chandrasekhar, A.S. Bhalla and W.B. White. Luminescence of Tb^{3+} and Eu^{3+} Activated Ferroelectric-Ferroelastic Gadolinium Molybdate. Ferroelectrics **36**, 415-418 (1981).
78. A.S. Bhalla and L.E. Cross. Interactions Between Orthogonal Domain Walls In Gadolinium Molybdate. Ferroelectrics **36**, 403-406 (1981).
79. O. Delaporte, G.R. Barsch, L.E. Cross and E. Ryba. Unusual Ferroelastic Behavior in Ferroelectric Lead Bismuth Niobate ($\text{PbBi}_2\text{Nb}_2\text{O}_9$).
80. T. Kimura, R.E. Newnham and L.E. Cross. Shape-Memory Effect in PLZT Ferroelectric Ceramics. Phase Transitions **2**, 113-130 (1981).
81. Yao Xi and L.E. Cross. Lithium Niobate Bicrystal. Ferroelectrics **38**, 829-832 (1981).

82. A.S. Bhalla and L.E. Cross. Primary and Secondary Pyroelectricity in Proper and Improper Ferroelectrics. Ferroelectrics **38**, 935-938 (1981).
83. A.S. Bhalla and R.E. Newnham. Primary and Secondary Pyroelectricity. Phys. Stat. Sol (a) **58**, K19 (1980).
84. A.S. Bhalla, R.E. Newnham, L.E. Cross and W.A. Schulze. Pyroelectric PZT-Polymer Composites. Ferroelectrics **33**, 139-146 (1981).
85. A.S. Bhalla, R.E. Newnham and L.E. Cross. Pyroelectricity in SbSI. Ferroelectrics **33**, 3-7 (1981).
86. A. Halliyal, A.S. Bhalla, R.E. Newnham and L.E. Cross. Polar Glass Ceramics. Ferroelectrics **38**, 781-784 (1981).
87. G.J. Gardopee, R.E. Newnham and A.S. Bhalla. Pyroelectric $\text{Li}_2\text{Si}_2\text{O}_5$ Glass-Ceramics. Ferroelectrics **33**(1-4), 155-166 (1981).
88. G.J. Gardopee, R.E. Newnham, A.G. Halliyal and A.S. Bhalla. Pyroelectric Glass-Ceramics. Appl. Phys. Lett. **36**(10), 817-818 (1980).
89. A. Halliyal, A.S. Bhalla, R.E. Newnham and L.E. Cross. $\text{Ba}_2\text{TiGe}_2\text{O}_8$ and $\text{Ba}_2\text{TiSi}_2\text{O}_8$ Pyroelectric Glass-Ceramics. Journal of Materials Science **16**, 1023-1028 (1981).
90. R.E. Newnham and L.E. Cross. Ferroic Crystals, Ceramics, and Composites. Chapter in Preparation and Characterization of Materials, J.M. Honig and C.N.R. Rao, Editors, pp. 249-266 (1981).
91. R.E. Newnham. Ferroic Crystals. Chapter in History of American Crystallographic Association.
92. R.E. Newnham. Crystallography at Penn State. Chapter in History of American Crystallographic Association.

The papers presented at National and International meetings are listed in Table 1.

Table 1. Papers Presented at National and International Meetings

MEETING	LOCATION	TIME	INVITED	CONTRIBUTED
Joint Japan:USSR Meeting on Ferroelectrics	Kyoto, Japan	Sept. 80	1	0
Joint US:India Symp. on Materials Science	Bangalore	Feb. 81	1	0
American Cryst Assn.	Texas, USA	March 81	0	1
American Phys. Soc. Spring Meeting	Arizona USA	March 81	0	3
Int. Mtg. Ferroelectrics IMF 5	Penn State USA	Aug. 81	1	18
Am. Ceram. Soc.	Washington USA	May 81	4	2
I.E.E.E. Ultrasonics	Chicago, USA	Oct. 81	0	1
TOTAL			Inv = 7	Cont = 25

During the year the Navy Patent Office in Boston provided the following summary of the disposition of patents established as a consequence of work on this program.

Table 2. Navy Patent Position

Navy Case No.	Inventor	Subject	Disposition
63,430	Cross, L.E. Newnham, R.E. Skinner, P.	Flexible Piezoelectric Composite Transducer	U.S. Patent NJ 4,227,111
64,667	Schulze, W.A. Biggers, J.V.	Lead Germanate Bonded PZT Composite Piezoelectrics	Filed 6/2/80 Amendment "A" 6/19/81
64,470	Bowen Schulze Biggers	A Hot Isostatic Pressure Process for Powder	1/31/80

Table 2 (Continued)

Navy Case No.	Inventor	Subject	Disposition
64,996	Schulze, W.A. Biggers, J.V. Bowen, L.J.	Internally Electroded Ceramic Piezoelectric Transformer	Filed - 4/16/81
64,407	Cross, L.E. Uchino, K.	A New Type of Ultra- Sensitive AC Capacitance Dilatometer	Placed in pend. status 1/18/80 Published in Nov.
65,051	Shrout, T.R. Schulze, W.A. Biggers, J.V.	Simplified Fabrication of PZT/Polymer Composites	Authorized w/o search 8/7/80 - Filed 11/12/80 Amendment "A" 8/28/81
65,121	Klicker, K.A. Newnham, R.E. Cross, L.E. Biggers, J.V.	3-1 Phase Connected PZT- Polymer Composites for Transducer Application	Filed 4/26/81
65,463	Gururaja, T.R. Cross, L.E. Newnham, R.E. Bowen, L.J.	Continuous Poling Tech- nique for Piezoelectric Fibers	Authorized -
65,464	Uchino, K. Jang, S.J. Cross, L.E. Newnham, R.E.	Pressure Gauge Using Relaxor Ferroelectrics	Placed in Pend. status - 8/11/81
65,465	Klicker, K.A. Newnham, R.E. Cross, L.E. Bowen, L.J.	Broadband Bandwidth Composite Transducer For Resonance Applications	Evaluated 8/81 (In

We are pleased to report that S. Venkataramani was awarded the degree of Ph.D. in Solid State Science for his work on

"Calcining and Its Effects on Sintering and Properties of Lead Zirconate Titanate Ceramics"

which was supported on contract funds. V.E. McCallen presented a BSc thesis on "Fabrication of SbSI composites for Transducers" and M. Granahan a BSc thesis on the topic "Grain Oriented PbNb_2O_6 Piezoceramics." This latter was chosen for the

Xerox Award as one of the best BS thesis in Materials at Penn State in 1981.

It is also gratifying to note that Tom Shrout much of whose earlier work was on topics in the ONR contract was also a Xerox Award winner for 1981.

ONR apprentices who contributed to work in 1981 were, F. Andrew Dix, Colleen Ottoson and Tim Bachman. We shall be most interested to follow the developing education of these bright young people, all of whom responded in a most positive manner to their time in MRL.

1. ELECTROSTRICTION

A. Theory of Electrostriction

1. Purpose and Scope

The objective of this work is to investigate theoretically the magnitude and temperature variation of the electrostriction coefficients of ionic crystals in order to account for, and ultimately predict, tendencies in the effect of crystal structure and of the properties of the constituent ions.

Work during the previous year included (a) a study on the continuum theoretical framework necessary for a consistent definition and description of electrostriction coefficients, and (b) the derivation and verification of phenomenological expressions for the temperature variation of electrostriction coefficients of ferroelectric crystals in their centrosymmetric paraelectric prototype. A major effort was devoted to the microscopic theory of electrostriction in perovskite oxides and dealt both with the effect of the cohesive forces on the properties of the static crystal and with the effect of anharmonic phonon-phonon interactions on the temperature variation of the electrostriction coefficients. The results are summarized below under their respective subject headings.

2. Phenomenological Theory

2.1 Landau-Devonshire Theory with Rotationally Invariant Expansion Coefficients. General expressions pertaining to a centrosymmetric prototype phase are given for the correction terms to the third and fourth order expansion coefficients of the Landau-Devonshire free energy with respect to the displacement gradient and the polarization, that arise as a consequence of the rotational invariance condition. Application to crystals of O_h symmetry shows that the correction terms may be numerically significant for the first and higher order electrostriction coefficients and for the third and higher order elastic constants.

2.2 Phenomenological Theory of the Temperature Variation of Electrostriction of Ferroelectrics in the Paraelectric Phase. A properly constructed static Landau-Devonshire free energy function implies the validity of the Curie-Weiss law for a homogeneously strained crystal up to first order in the strain and has been used to deduce phenomenological expressions for the temperature dependence of the first order electrostriction coefficients of ferroelectric crystals in the paraelectric phase. If the prototype phase has cubic symmetry, the coefficients $Q_{rs,ij}$ depend linearly on temperature. Moreover, if the ferroelectric transition is of second order the electrostriction coefficients pertaining to shear deformations vanish at the Curie temperature T_c . These theoretical results are in agreement with the experimental data available for perovskite oxides.

3. Microscopic Theory

3.1 First Order Anharmonic Properties of Perovskite Oxides: Static Crystal Lattice. Lattice dynamical calculations of electrostriction and third order elastic coefficients have been performed on the basis of a shell model for BaTiO_3 , SrTiO_3 (both in the cubic phase) and for KTaO_3 . Harmonic and anharmonic interactions arising from the Coulomb forces and from n.n. short-range central forces are included. The calculations refer to a static crystal and are based on empirical model parameters determined by fitting to experimental input data obtained by linear extrapolation to absolute zero. The model gives a consistent description of third order elastic and of electrostriction constants.

3.2 Temperature Dependence of Electrostriction. The hydrostatic electrostriction coefficient of SrTiO_3 has been calculated as a function of temperature on the basis of anharmonic perturbation theory. The same anharmonic shell model as used before for the calculation of the electrostriction coefficients of the static crystal is employed. The anharmonic contributions from the Coulomb

interactions are found to be comparable to those from the short-range interactions, and their inclusion leads to better agreement with experimental data than earlier calculations based on the simpler model of Bruce and Cowley.

4. Publications

51. B.N.N. Achar, G.R. Barsch and L.E. Cross. Static Shell Model Calculation of Electrostriction and Third Order Elastic Coefficients of Perovskite Oxides. Ferroelectrics 37, 495-498 (1981). APPENDIX 1.
52. B.N.N. Achar and G.R. Barsch. Anharmonic Perturbation Calculation of Electrostriction for SrTiO_3 . Ferroelectrics 37, 491-493 (1981).
53. G.R. Barsch, B.N.N. Achar and L.E. Cross. Phenomenological Theory of the Temperature Variation of Electrostriction of Ferroelectrics in the Paraelectric Phase. Ferroelectrics 35, 191-194 (1981).
54. G.R. Barsch, B.N.N. Achar and L.E. Cross. Landau-Devonshire Theory with Rotationally Invariant Expansion Coefficients. Ferroelectrics 35, 187-190 (1981). APPENDIX 2.

B. Experiments on Electrostriction

1. Purpose and Scope

Development of the practical application of the $\text{PbMg}_{1/3}\text{Nb}_{2/3}\text{O}_3:\text{PbTiO}_3$ ceramics for position control in multiposition mirrors has now been taken up by Aldrich, Daignault and Wheeler of ITEK Optic Division in Boston, with Penn State in a consultant role.

A new type of application which is being explored concerns the inverse electrostrictive effect (stress dependence of the weak field dielectric permittivity) in the relaxor ferroelectric system $\text{Pb}(\text{Mg}_{1/3}\text{Nb}_{2/3})\text{O}_3:\text{PbTiO}_3:\text{Ba}(\text{Zn}_{1/3}\text{Nb}_{2/3})\text{O}_3$ ternary solid solutions. In this system, the temperature dependence of permittivity can be largely tuned out for a fixed frequency by balancing the two

relaxation regions. Thus the sensitive pressure dependence of K can now be used as an inexpensive compact pressure or stress gauge (Appendix 3).

Major work in the Laboratory has concentrated upon the relaxation behavior and the modification to this response by order:disorder of the B site cations in $\text{PbSc}_{1/2}\text{Nb}_{1/3}\text{O}_3$, $\text{PbSc}_{1/2}\text{Ta}_{1/2}\text{O}_3$ and solid solutions between these end member components. Current work has shown that both the centroid and the span of the diffuse Curie range can be controlled in this family by composition manipulation and thermal treatment. Since the depolarization curves can be modified and controlled, there is the possibility of developing a strong extrinsic domain contribution to the reversible pyroelectric response in this system.

Optical microscope studies of single crystals in the $\text{PbSc}_{1/2}\text{Ta}_{1/2}\text{O}_3$, $\text{PbSc}_{1/2}\text{Nb}_{1/2}\text{O}_3$ and $\text{PbMg}_{1/3}\text{Nb}_{2/3}\text{O}_3$ compositions have been used to further explore the influence of ordering on the optical consequences of the phase change in the Curie Range. Disordered tantalate crystals show no optical birefringence at temperature below the T_c range, whilst ordering brings up conventional ferroelectric behavior with domain structure corresponding to a rhombohedral symmetry (Appendix 4).

To explore the effects of cation disorder in a non relaxor system, a strain gauge technique was used to measure Q_{11} , Q_{12} and Q_h in $\text{K}(\text{Ta}_{0.55}\text{Nb}_{0.45})\text{O}_3$ crystals. Both Curie content and Q values are almost the same as for the end member compositions with no anomalous lowering of Q or rise in C in the solid solutions.

2. Publications

55. K. Uchino, S. Nomura, L.E. Cross, S.J. Jang and R.E. Newnham. Pressure Gauge Using Relaxor Ferroelectrics. Jpn. Journ. Appl. Phys. 20, L367-L370 (1981). APPENDIX 3

56. Z. Chen, N. Setter and L.E. Cross. Diffuse Ferroelectric Phase Transition and Cation Order in the Solid Solution System $\text{Pb}(\text{Sc}_{1/2}\text{Nb}_{1/2})\text{O}_3$: $\text{Pb}(\text{Sc}_{1/2}\text{Ta}_{1/2})\text{O}_3$. Ferroelectrics 37, 619-622 (1981).
57. N. Setter and L.E. Cross. An Optical Study of the Ferroelectric Relaxors $\text{Pb}(\text{Mg}_{1/3}\text{Nb}_{2/3})\text{O}_3$, $\text{Pb}(\text{Sc}_{1/2}\text{Ta}_{1/2})\text{O}_3$, and $\text{Pb}(\text{Sc}_{1/2}\text{Nb}_{1/2})\text{O}_3$. Ferroelectrics 37, 551-554 (1981). APPENDIX 4
58. K. Uchino, S. Nomura, L.E. Cross and R.E. Newnham. Electrostrictive Effects in Potassium Tantalate Niobate. Ferroelectrics 38, 825-828 (1981).

2. PIEZOELECTRIC COMPOSITES

C. PZT:Polymer Composites

1. Purpose and Scope

The major emphasis of work upon the composite transducers in this family has been focused upon the development of systems with very high stable d_{hg_h} product which would be suitable for use in large area low frequency hydrophone systems. Two new methods of construction have been explored in which the PZT phase itself provides bridging to develop stress amplification. These 3:1 and 3:2 patterns produced by drilling and by extrusion have exhibited sensitivities up to $d_{hg_h} \approx 45,000 \cdot 10^{-5} \text{ m}^2\text{N}^{-1}$ with no significant pressure dependence to pressures beyond 1,000 psi (Appendix 5).

Earlier studies of 3-3 connected composite structures generated using a Burn out of plastic microspheres (BURPS) process have now been written up for publication (Appendix 6).

Higher frequency applications for the composite structures are now also being explored PZT spheres, and 3:1 connected rods have been compared with 3:3 connected composites, and it is clear that only the longitudinal rod structures offer satisfactory coupling in simple send receive geometries.

A general summary of the status for the polymer:PZT systems is given in Appendix 7.

2. Publications

59. A. Safari, R.E. Newnham, L.E. Cross and W.A. Schulze. Perforated PZT-Polymer Composites for Piezoelectric Transducer Applications. (APPENDIX 5).
60. A. Safari, A. Halliyal, R.E. Newnham and I.M. Lachman. Transverse Honeycomb Composite Transducers. Mat. Res. Bull. 17, 301-308 (1982).
61. K. Rittenmyer, T. Shrout, W.A. Schulze and R.E. Newnham. Piezoelectric 3-3 Composites. Ferroelectrics. (APPENDIX 6)
62. A. Safari, A. Halliyal, L.J. Bowen and R.E. Newnham. Flexible Composite Transducers. Ceramic Journal, 12-29 (1981).
63. T.R. Gururaja, W.A. Schulze, T.R. Shrout, A. Safari, L. Webster and L.E. Cross. High Frequency Applications of PZT/Polymer Composite Materials. Ferroelectrics 39, 1245-1248 (1981).
64. S.Y. Lynn, R.E. Newnham, K.A. Klicker, K. Rittenmyer, A. Safari and W.A. Schulze. Ferroelectric Composites for Hydrophones. Ferroelectrics 38, 955-958 (1981). (APPENDIX 7).

D. Piezoelectric Composites Other Than PZT

1. Scope and Objectives

A number of studies have been focused upon the possibility of using the principles developed in the PZT:polymer composites to explore other interesting piezoelectric composite systems.

The piezoelectric SbSI:polymer system is a direct extension of earlier work in which single crystal needles of SbSI replaced the PZT extruded rods. Again a poling operation is necessary, but an unexpected bonus from the composite structure is a shifting of the dielectric permittivity peak to higher temperature without a shifting of the piezoelectric d_{33} and d_h peaks, leading to a significant improvement in $d_h g_h$ product over the single phase SbSI. (APPENDIX 8)

A second important sequence of studies has been concerned with the recrystallization of polar glass ceramics. It has been found that for $\text{Ba}_2\text{Ge}_2\text{TiO}_8$, $\text{Ba}_2\text{Si}_2\text{TiO}_8$, Li_2SiO_3 and $\text{Li}_2\text{O}:\text{SiO}_2:\text{B}_2\text{O}_3$ glasses that by recrystallizing the quenched glass in a strong temperature gradient, the polar crystallites can be oriented and preserve a dominant polar axis. In this manner, a completely new type of piezoceramics can be fabricated from a polar but non ferroelectric crystal phase. (APPENDIX 9)

2. Publications

65. A. Halliyal, A.S. Bhalla, R.E. Newnham, L.E. Cross and T.R. Gururaja. Study of the Piezoelectric Properties of $\text{Ba}_2\text{Ge}_2\text{TiO}_8$ Glass-Ceramic and Single Crystals. Journal of Materials Science **17**, 295-300 (1982).
66. A. Halliyal, A.S. Bhalla, R.E. Newnham and L.E. Cross. Piezoelectric Properties of Lithium Borosilicate Glass Ceramics. Journal of Applied Physics (accepted).
67. A. Halliyal, A.S. Bhalla, R.E. Newnham, and L.E. Cross. Piezoelectric and Elastic Properties of Barium Germanium Titanate and Lithium Borosilicate Glass Ceramics. IEEE Ultrasonics Symposium Proceedings, 315-318 (1981). (APPENDIX 9)

3. PREPARATIVE STUDIES

3.1 Densification of PZT Ceramics

Much of the extensive preparative work on this contract has been concerned with fabricating PZT ceramics in unusual geometries for the composites program, and with lead magnesium niobate and other relaxor ferroelectric compositions.

In parallel with these very necessary practical measures, more detailed work has been carried forward upon the calcining process for PZTs fabricated by mixed oxide process, and the detailed effects of different calcining phase

assemblages upon the final densification, poling and resultant properties in model compositions. (APPENDIX 10)

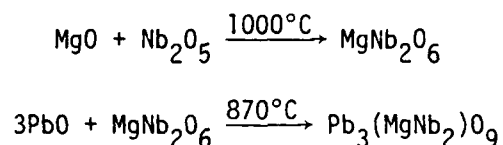
3.2 Fabrication of Grain Oriented $\text{Bi}_4\text{Ti}_3\text{O}_{12}$ Ceramics

Molten salt synthesis from eutectic KCl:NaCl mixtures has been used to fabricate platelet starting powders of $\text{Bi}_4\text{Ti}_3\text{O}_{12}$. By tape casting and conventional sintering grain correlations of > 95% and density of 92% theoretical can be achieved yielding ceramics which can be pulse poled to a $d_{33} \approx 10 \times 10^{-12}$ C/N.

3.3 Preparations of Lead Magnesium Niobate

A problem which has caused repeated difficulty in the preparation of batches of lead magnesium niobate $\text{PbMg}_{1/3}\text{Nb}_{2/3}\text{O}_3$ and its solid solutions with lead titanates PbTiO_3 is the appearance early in calcining of a stable pyrochlore structure phase which is difficult to eradicate from the final sintered compact.

We believe that a source of the problem is the reaction of PbO and Nb_2O_5 to form a fairly stable pyrochlore structure phase before the MgO begins to participate in the reaction sequence. A good initial solution to the problem has been to preform a MgNb_2O_6 precursor which can then be reacted with the lead oxide in the sequence



For the pure $\text{PbMg}_{1/3}\text{Nb}_{2/3}\text{O}_3$ mixed oxides calcined at 850°C for 8 hours yield only 30-60% perovskite phase, whilst the above reaction sequence yields better than 90% perovskite. In 10% PbTiO_3 solutions, this yield increases to better than 98%.

3.4 Crystal Growth Studies

The Crystalox model MCG3 material preparation system which was acquired last year on contract and University funds is now being used to study the growth of two families of ferroic crystals which are of interest for the group.

3.4.1 Halide Perovskites. Perovskite structure mixed halides in the general formula



where A is a larger monovalent cation

B is small divalent cation

X the halide ion

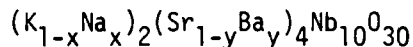
are needed for extending the theoretical studies of the origins of electrostriction in perovskite structure crystals.

Initial Czochralski pulling has been applied to crystals in the compositions $KMgF_3$, $KMnF_3$, $KZnF_3$ and $KCaF_3$. For the first three water clear crystals up to 2 cm in diameter have been pulled, oriented and cut for electrostriction measurements.

In $KCaF_3$, all the crystals grown contain small opaque solid inclusions, probably CaO and attempts are now under way to purify and remove all oxygen from the starting charge.

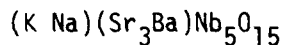
3.4.2 Tungsten Bronze Oxides. Two projects are underway with the bronze family oxides.

- 1) The structural formula for the bronze is $A_1(2)A_2(4)C(4)B_{10}O_{30}$. In many bronzes, the chemical formula is such that not all A_1 or A_2 sites are filled, and in many compositions all the very small C_4 sites are often vacant. It is our objective to grow compositions in the system



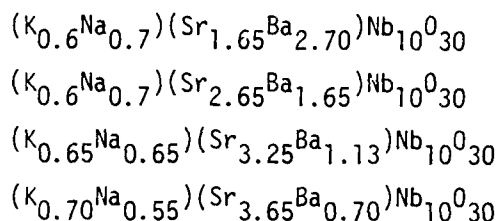
in which all larger A_1 and A_2 sites are occupied.

So far the best success has been achieved with the composition



where the composition was determined directly from analysis of the boule material.

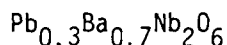
Other crystals grown in this family had compositions



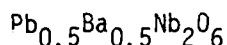
Samples adequate for initial electrical characterization and for ferroelectric domain and polarization studies were obtained.

2) $\text{Pb}_x\text{Ba}_{1-x}\text{Nb}_2\text{O}_6$ Bronzes.

The lead barium bronze compositions are of particular interest in piezoelectricity since there is a morphotropic boundary between tetragonal and orthorhombic ferroelectric forms for compositions with $x \approx 0.6$. To approach the morphotropic composition from the tetragonal side, crystals have been grown in the compositions



and



Both crystals are in the tetragonal structure field, with Curie points at 340°C and 260°C as expected from earlier studies on ceramics. Additional growth runs are now being carried forward for compositions which will bracket the morphotropic phase boundary.

3.5 Publications

68. S. Venkataramani and J.V. Biggers. Densification in PZT. Ferroelectrics 37, 607-610 (1981). (APPENDIX 10)
69. S. Swartz, W.A. Schulze, and J.V. Biggers. Fabrication and Electrical Properties of Grain Oriented $\text{Bi}_4\text{Ti}_3\text{O}_{12}$ Ceramics. Ferroelectrics 38, 765-768 (1981).

4. CHARACTERIZATION STUDIES

4.1 Ordering in $\text{Pb}(\text{Mg}_{1/3}\text{Nb}_{2/3})\text{O}_3$ - $\text{Pb}(\text{Mg}_{1/2}\text{W}_{1/2})\text{O}_3$

Compositional ordering was explored in the system $(1-x)\text{Pb}(\text{Mg}_{1/3}\text{Nb}_{2/3})\text{O}_3$ - $x\text{Pb}(\text{Mg}_{1/2}\text{W}_{1/2})\text{O}_3$ solid solutions using x-ray diffraction and neutron profile fitting. Structures with $x < 0.2$ exhibit ordering of B site cations and symmetry in space group Fm3m. Oxygen octahedra are not tilted in the ordered phases, but are no longer equivalent.

4.2 Studies of the PbZrO_3 : PbTiO_3 System

Careful calorimetric measurements of the heat of transition at the Curie point T_c have been made for a range of chemically prepared $\text{PbZr}_x\text{Ti}_{1-x}\text{O}_3$ compositions in the range $0.0 < x < 0.6$, using a Perkin-Elmer DSC2 thermal analyser. Transition entropy and Curie Weiss constant were determined to show anomalous values near the morphotropic boundary compositions. (APPENDIX 11)

Neutron diffraction analysis and fitting using the Rietveld profile technique have been used to explore the rhombohedral:rhombohedral (R3m - R3c) phase change at low temperature in the composition $\text{PbZr}_{0.6}\text{Ti}_{0.4}\text{O}_3$. (APPENDIX 12)

Results are indicative of a diffuse change in the region 250-300°K. Values of P_s obtained from Zr/Ti ion shifts are in good agreement with phenomenological theory.

4.3 Studies of Ferroelectric Surfaces

Low energy inert gas ion scattering (ISS) techniques have been used to explore the surfaces of gadolinium molybdate and barium titanate single crystals. The chemical nature of the surface layer on Remeika type BaTiO_3 has been explored and potassium and fluorine impurities detected. In GMO positive and negative domain surfaces are chemically identical however the orientation of P_s does have a strong effect on the scattering of He-4 ions. (APPENDIX 13)

Inelastic effects in ion scattering from GdF_3 , Gd_2O_3 and $\text{Gd}_2(\text{MoO}_4)_3$ surfaces have also been explored to explain the low energy tail which appears on the elastic scattering.

In addition Auger Electron Scattering (AES), sputter-induced photo-emission spectroscopy (SIPS), and secondary ion mass spectrometry (SIMS) have been used to explore GMO surfaces, and HF substituted surfaces.

4.4 Luminescence in Tb^{3+} and Eu^{3+} Activated Gadolinium Molybdate

In a cooperative study with Dr. W.B. White's optics group, luminescence spectra were observed for terbium and europium activated ferroelectric:ferro-elastic GMO. Surprisingly the spectra change hardly at all at temperatures below and above the Curie point, T_c , indicating that the improper ferroelectric transition has very little effect on the local crystal field.

4.5 Domain Walls in $\text{Gd}_2(\text{MoO}_4)_3$

Following an excellent theoretical analysis by Indenbom and Chamrov, high resolution decoration techniques were used to explore and confirm features predicted for structures involving encountering orthogonal walls. Both the cusp-like features, and the bowing of the planar walls predicted from the long range strain fields were observed, and the thickness of the wall confirmed to be much less than 1 μ meter. (APPENDIX 14)

4.6 Publications

70. A. Amin, R.E. Newnham, L.E. Cross and S. Nomura. Ordering in $\text{Pb}(\text{Mg}_{1/3}\text{Nb}_{2/3})\text{O}_3 - \text{Pb}(\text{Mg}_{1/2}\text{W}_{1/2})\text{O}$ Solid Solutions, Journal of Solid State Chemistry **35**(2), 267-271 (1980).
71. A. Amin, L.E. Cross and R.E. Newnham. Calorimetric and Phenomenological Studies of the $\text{PbZrO}_3\text{:PbTiO}_3$ System, Ferroelectrics **37**, 647-650 (1981). (APPENDIX 11)
72. A. Amin, R.E. Newnham and L.E. Cross. Phenomenological and Structural Study of a Low-Temperature Phase Transition in the $\text{PbZrO}_3\text{-PbTiO}_3$ System, Journal of Solid State Chemistry **37**, 248-255 (1981). (APPENDIX 12)

73. L.L. Tongson, A.S. Bhalla and L.E. Cross. Studies of Ferroelectric Surfaces Using Ion Beam and Chemical Etching Techniques, Ferroelectrics **36**, 471-474 (1981). (APPENDIX 13)
74. L.L. Tongson, A.S. Bhalla and B.E. Knox. Low Energy Inert Gas Ion Scattering From GdF_3 , Gd_2O_3 and $\text{Gd}_2(\text{MoO}_4)_3$ Surfaces: 1. Inelastic Effects, Mat. Res. Bull. **16**, 775-783 (1981).
75. L.L. Tongson, A.S. Bhalla, L.E. Cross and B.E. Knox. Investigation of BaTiO_3 and $\text{Gd}_2(\text{MoO}_4)_3$ Crystal Surfaces by Complementary AES and ISS Techniques, Applications of Surface Science **4**, 263-270 (1980).
76. A.S. Bhalla and L. Tongson. Direct Method of Measuring Ion Beam Irradiated Areas, Journal of Vacuum Science (accepted).
77. B.K. Chandrasekhar, A.S. Bhalla and W.B. White. Luminescence of Tb^{3+} and Eu^{3+} Activated Ferroelectric-Ferroelastic Gadolinium Molybdate, Ferro-Electrics **36**, 415-418 (1981).
78. A.S. Bhalla and L.E. Cross. Interactions Between Orthogonal Domain Walls In Gadolinium Molybdate, Ferroelectrics **36**, 403-406 (1981). (APPENDIX 14)

5. FERROELASTICS

5.1 Lead Bismuth Niobate

X-ray and optical measurements have been used to show that the spontaneous strain ($b/a - 1$) and optical birefringence Δn_{ab} in single crystals of $\text{PbBi}_2\text{Nb}_2\text{O}_9$ are a function of the state of electrical poling, going to zero in the unpoled state. The behavior is reminiscent of the relaxor-ferroelectric perovskites in that the poled strain (birefringence) goes to zero some 200°C below the dielectric Curie peak. (APPENDIX 15)

5.2 Shape Memory Effects in PLZT Ceramics

A shape memory effect qualitatively similar to that observed in martensitic metal systems such as the nickel:titanium alloys (Nitinol) has been

extensively investigated in the PLZT family for compositions in the $x/65/35$ system in the range $4.0 \leq x \leq 8.0$.

Ferroelastic domain reorientation, and temperature dependent changes in the magnitude of the spontaneous strain are important factors in governing the shape memory. Ferroelastic domain reorientation was confirmed by x-ray diffraction methods. (APPENDIX 16)

5.3 Publications

79. O. Delaporte, G.R. Barsch, L.E. Cross and E. Ryba. Unusual Ferroelastic Behavior in Ferroelectric Lead Bismuth Niobate ($\text{PbBi}_2\text{Nb}_2\text{O}_9$), (APPENDIX 15).
80. T. Kimura, R.E. Newnham and L.E. Cross. Shape-Memory Effect in PLZT Ferroelectric Ceramics. Phase Transitions 2, 113-130 (1981). (APPENDIX 16)

6. FERROELECTRIC BICRYSTALS

6.1 Scope and Purpose

Studies have continued on artificial planar boundaries produced by diffusion bonding single domain single crystals of lithium niobate at temperatures below the Curie point, T_c . Dielectric, piezoelectric and pyroelectric studies have been used to compare bicrystal and single crystal properties and to explore the charge trapping at the interface.

Piezoelectric resonance measurements indicate that encountering (head-to-head or tail-to-tail) crystals resonate separately, and based on these studies calculations have been made for the grain resonance effects in ceramic LiNbO_3 fabricated with a narrow range of grain sizes. It is found that by using an IBM ecap program, modified so as to calculate the impedance for families of grains in series and parallel connections both real and imaginary parts of the complex impedance over the frequency range from 100 Hz to 100 MHz can be modeled from single crystal parameters to a precision of better than $\pm 5\%$.

6.2 Publications

81. Yao Xi and L.E. Cross. Lithium Niobate Bicrystal, Ferroelectrics 38, 829-832 (1981). (APPENDIX 17)

7. PYROELECTRIC STUDIES

7.1 Theoretical Studies

A feature of the pyroelectrics which we believe to be of major importance but which has been most inadequately dealt with in the past is the separation of primary and secondary effects. Clearly the total pyroelectric coefficient p_i^σ which is usually measured at constant stress and temperature T is made up of two parts

$$p_i^\sigma = p_i^\epsilon + d_{ijk}^T c_{jklm}^E \alpha_{lm}$$

where p_i^ϵ is the primary coefficient measured at constant strain ϵ and the second term is the secondary effect which depends upon the piezoelectric constants, d , the elastic constants, c , and the thermal expansion, α .

All coefficients in the equation are functions of temperature, and much of the complexity in the temperature dependence of the total effect stems from the fact that in many ferroelectrics primary and secondary terms are of opposite sign but of similar magnitude.

Using both literature values and new measurements, primary and secondary components have been separated and systematized for a number of simple proper ferroelectrics, improper ferroelectrics, polar nonferroelectric crystals and polar semiconductors. (APPENDIX 18)

7.2 Experimental

A number of dominantly 3:1 and 3:3 connected composite systems have been explored for their pyroelectric response. In the first studies, PZT:polymer

composites in the form used earlier for hydrophones were explored. For the 3:3 connected material the figure of merit p/ϵ can be enhanced by a factor of ~ 7 in epoxy PZT composites, clearly a secondary effect as no change occurs in similar composites with soft elastomers.

SbSI is a most interesting component for composite systems. Single crystal data are presented for which p reaches the unusually large value $1.2 \times 10^4 \mu\text{C}/\text{m}^2\text{C}$ at $T - T_c \simeq 2^\circ\text{C}$. (APPENDIX 19)

A range of interesting new polar glass ceramics have been fabricated by annealing a quenched glass in a strong temperature gradient so as to orient the crystallization of a polar crystal component. $\text{Li}_2\text{Si}_2\text{O}_5$, $\text{Ba}_2\text{TiGe}_2\text{O}_8$, $\text{Ba}_2\text{TiSi}_2\text{O}_8$ and compositions modified with ZnO and B_2O_3 have been tried. In several of these systems strong pyroelectric response has been observed. For compositions where more than one polar crystalline phase can be recrystallized there appears to be the interesting possibility of producing:

- (a) Pyroelectrics with negligible piezoelectricity
- (b) Piezoelectrics with negligible pyroelectricity
- (c) Material combinations with strong piezoelectric radial coupling at low RF frequency but very low temperature coefficient of resonant frequency.

We believe that in future development then glass ceramic compositions may be mated in interesting fiber optic structures to perhaps provide completely transparent electromagnetic wave antennae.

7.3 Publications

- 82. A.S. Bhalla and L.E. Cross. Primary and Secondary Pyroelectricity in Proper and Improper Ferroelectrics, Ferroelectrics **38**, 935-938 (1981).
- 83. A.S. Bhalla and R.E. Newnham. Primary and Secondary Pyroelectricity, Phys. Stat. Sol (a) **58**, K19 (1980). (APPENDIX 18)

84. A.S. Bhalla, R.E. Newnham, L.E. Cross and W.A. Schulze. Pyroelectric PZT-Polymer Composites, Ferroelectrics **33**, 139-146 (1981).
85. A.S. Bhalla, R.E. Newnham and L.E. Cross. Pyroelectricity in SbSI, Ferroelectrics **33**, 3-7 (1981). (APPENDIX 19)
86. A. Halliyal, A.S. Bhalla, R.E. Newnham and L.E. Cross. Polar Glass Ceramics, Ferroelectrics **38**, 781-784 (1981).
87. G.J. Gardopee, R.E. Newnham and A.S. Bhalla. Pyroelectric $\text{Li}_2\text{Si}_2\text{O}_5$ Glass-Ceramics,
88. G.J. Gardopee, R.E. Newnham, A.G. Halliyal and A.S. Bhalla. Pyroelectric Glass-Ceramics, Appl. Phys. Lett. **36**(10), 817-818 (1980).
89. A. Halliyal, A.S. Bhalla, R.E. Newnham and L.E. Cross. $\text{Ba}_2\text{TiGe}_2\text{O}_8$ and $\text{Ba}_2\text{TiSi}_2\text{O}_8$ Pyroelectric Glass-Ceramics, Journal of Materials Science **16**, 1023-1028 (1981). (APPENDIX 20)

8. GENERAL

8.1 Introduction

In connection with the Joint US:India seminar on Preparation and Characterization one of us presented a survey paper on Ferroic Crystals, Ceramics and Composites. Somewhat similar material was also covered in a general survey for the American Crystallographic Association in "Ferroic Crystals" which was presented together with a survey of "Crystallography at Penn State."

8.2 Publications

90. R.E. Newnham, and L.E. Cross. Ferroic Crystals, Ceramics, and Composites, Chapter in Preparation and Characterization of Materials, J.M. Honig and C.N.R. Rao, Editors, pp. 249-266 (1981).
91. R.E. Newnham. Ferroic Crystals. Chapter in History of American Crystallographic Association.
92. R.E. Newnham. Crystallography at Penn State. Chapter in History of American Crystallographic Association.

APPENDIX 1

Static Shell Model Calculation of Electrostriction and Third Order Elastic Coefficients of Perovskite Oxides

STATIC SHELL MODEL CALCULATION OF ELECTROSTRICTION AND THIRD ORDER ELASTIC COEFFICIENTS OF PEROVSKITE OXIDES*

B.N.N. ACHAR^a, G.R. BARSCH AND L.E. CROSS
The Pennsylvania State University, University Park, PA 16802, U.S.A.

Abstract--Lattice dynamical calculations of electrostriction and third order elastic coefficients have been performed on the basis of a shell model for BaTiO_3 , SrTiO_3 (both in the cubic phase) and for KTaO_3 . Harmonic and anharmonic interactions arising from the Coulomb forces and from n.n. short-range central forces are included. The calculations refer to a static crystal and are based on empirical model parameters determined by fitting to experimental input data obtained by linear extrapolation to absolute zero.

ANHARMONIC PROPERTIES OF THE STATIC CRYSTAL

First order anharmonic properties, such as electrostriction (ES) and third order elastic (TOE) coefficients in general arise from two contributions: the contribution from the cohesive forces responsible for the properties of the static crystal lattice, and the phonon self-energy contribution arising from thermal and zero point motion. Although the former depends only on the third order interatomic coupling parameters, the latter includes still higher order derivatives of the potential energy, that are usually not well known. In addition, an adequate theoretical description of first order anharmonic properties at finite temperature, e.g. via the self-consistent phonon approximation or anharmonic perturbation theory is a complex and, especially for soft-mode materials, an ambiguous procedure. In a previous theoretical study of SrTiO_3 these difficulties were circumvented by eliminating the thermal and zero-point contributions through extrapolation of the experimental data to absolute zero, and by performing a lattice dynamical calculation pertaining to the static metastable crystal, resulting in a consistent description of first order anharmonic properties¹. In the present paper this procedure is extended to BaTiO_3 and KTaO_3 , the only other perovskite oxides with a sufficient amount of pertinent experimental data available.

SHELL MODEL

The calculations are based on a rigid-shell model, the harmonic part of which is identical with that of Cowley² for the cubic perovskite structure of ABO_3 and includes the following interactions described by the parameters given in parenthesis in standard notation^{1,2}. Coulomb interactions, (ionic charges Z_β ; $\beta = \text{A, B, O}$), short range two-body central forces between nearest neighbors (A_i, B_i ; $i = \text{A-O, B-O, O-O}$), and the polarizability parameters of the three ions (α_β, d_β ; $\beta = \text{A, B, O}$). Anharmonicity arising from Coulomb and repulsive interactions (C_i ; $i = \text{A-O, B-O, O-O}$) is included. Intraionic

*Work supported by ONR Contract No. N00014-78-C-0291.

^aAlso affiliated with Bucknell University, Lewisburg, PA 17837, USA.

anharmonicity recently considered by Migoni et al.³ does not affect the first order anharmonic properties of the static perovskite crystal.

The harmonic model parameters were determined (as described in detail in Ref. 1) by means of a least squares fit to the following experimental data linearly extrapolated from the high temperature region to absolute zero: the elastic constants c_{11} , c_{12} , c_{111} , the static and the high frequency dielectric constants, ϵ_0 and ϵ_∞ , respectively, and the seven zone center optic mode frequencies $\omega_{TO}^{(\alpha)}(\Gamma_{15})$, $\omega_{LO}^{(\alpha)}(\Gamma_{15})$ ($\alpha = 1, 2, 3$) and $\omega(\Gamma_{25})$. In addition, the charge neutrality and equilibrium conditions were used. The anharmonic parameter C_2 for the B-O interaction was determined from the pressure derivative ($d \ln \epsilon_0 / dp$), extrapolated from the experimental high temperature data to absolute zero, as described in Ref. 1. The remaining anharmonic parameters C_1 and C_3 were calculated from the corresponding harmonic parameters A_1 , B_1 and A_3 , B_3 by assuming the Born-Mayer form for the interatomic potential (found adequate for SrTiO₃ (Ref. 1)).

Table I. Shell model parameters for perovskite oxides AB₃O₃.

Interaction	Parameter	SrTiO ₃	BaTiO ₃	KTaO ₃
A-O	A ₁	11.44	25.10	36.60
	B ₁	-2.18	-12.67	-11.95
B-O	A ₂	111.07	125.57	140.94
	B ₂	-47.40	12.88	67.37
O-O	A ₃	27.36	-1.56	1.19
	B ₃	7.92	4.58	-6.50
	Z _A	1.24	1.18	0.70
	Z _B	2.42	2.12	1.18
	Z _O	-1.22	-1.10	-0.63
	α_A	0.179	0.20	0.082
	α_B	0.068	0.043	0.006
	α_O	0.026	0.026	0.023
	d _A	-1.040	0.029	-0.948
	d _B	-0.162	-1.054	-0.434
	d _O	0.937	0.86	0.951
A-O	C ₁	-60.1	-49.7	-112.0
B-O	C ₂	-1782.5	-1034.1	-2038.7
-	C ₃	-94.5	-0.53	-0.22

cient ($d \ln \epsilon_0 / dp$), of the electrostriction constants $Q_h = Q_{1111} + 2Q_{2211}$, $Q_s = Q_{1111} - Q_{2211}$ and Q_{1212} , and of the soft optic mode frequency ω_{T1} and the associated microscopic Grüneisen parameter γ_{T1} (calculated from an approximate formula of Samara¹²) are compared with the available experimental data, extrapolated to absolute zero. Also included are the χ^2 values for the least squares fit of all 12 harmonic quantities calculated from the assumption that all experimental data are subject to an error of 10% arising mostly from the extrapolation to absolute zero. In general for the harmonic quantities fair to good agreement is obtained, with the largest discrepancy occurring for ϵ_0 and amounting to about 20% for SrTiO₃ and BaTiO₃. Furthermore, the present central force model does not account for the deviation of the elastic constants from the Cauchy relation $c_{12} = c_{44}$.

The calculated TOE constants c_{111} and c_{112} are for BaTiO₃ about half as large as for SrTiO₃, whereas for KTaO₃ they are approximately the same. For SrTiO₃ the calculated value of c_{111} agrees very well with the experimental value, and c_{123} agrees with

The parameters so obtained are listed in Table I, where the values for SrTiO₃ have been included for comparison. It is apparent that for all three compounds the B-O interaction is dominant. Surprisingly, in BaTiO₃ and KTaO₃ the second and especially the third derivatives of the O-O interaction potential are smaller than for SrTiO₃, although the lattice constants differ by no more than 2 percent. For all three compounds the anharmonicity of the short range interactions characterized by the ratio C_1/A_1 is largest for the B-O interaction and quite small for the O-O interaction.

RESULTS AND DISCUSSION

In Table II the calculated values of the second and third order elastic constants, of the static and high frequency dielectric constant, of the pressure coefficient

STATIC SHELL MODEL CALCULATION OF ELECTROSTRICTION AND THIRD ORDER...

Table II. Second and third order elastic constants (10^{11} N/m²), high frequency and static relative dielectric constants, logarithmic pressure derivative of the static dielectric constant (10^{-9} m²/N), electrostriction constants (m⁴/C²), soft-mode frequency (10^{13} rad/sec) and soft-mode γ , and χ^2 value for least squares fit of all 12 harmonic quantities.

	SrTiO ₃		BaTiO ₃		KTaO ₃	
	Experimental Extrapolated	Calculated	Experimental Extrapolated	Calculated	Experimental Extrapolated	Calculated
c_{11} (*)	3.337 ^a	3.15	2.55 ^j	2.29	4.31 ⁿ	3.70
c_{12} (*)	1.050 ^a	1.12	0.83 ^j	0.95	1.30 ⁿ	1.36
c_{13} (*)	1.265 ^a	1.12	1.09 ^j	0.95	1.09 ⁿ	1.36
c_{44}	-49.6 ^b	-47.1	---	-24.1	---	-54.9
c_{66}	-7.7 ^b	-4.7	---	-2.8	---	-3.6
c_{123}	0.2 ^b	-1.2	---	-0.9	---	-0.3
c_{11} (*)	5.5 ^c	5.36	5.31 ^k	6.23	4.62 ⁿ	4.57
c_{12} (*)	-2297. ^d	-1852.	-418. ^e	-330.0	-766.4	-707.
$\partial \ln \epsilon_0 / \partial p$	4.08 ^e	4.08	0.42 ^e	0.42	0.68 ^r	0.68
Q_h	0.103 ^f	0.125	0.006 ^f	0.0076	0.051 ^s	0.054
Q_s	0.136 ^g	-0.076	-0.32 ^l	-1.02	0.136 ^t	0.718
Q_{1212}	---	0.011	---	---	0.037 ^t	0.027
γ_{11} (*)	$i \times 0.605^h$	$i \times 0.542$	$i \times 2.047^m$	$i \times 1.899$	$i \times 0.290^u$	$i \times 0.278$
χ^2	-368.0 ⁱ	-306.2	-29.5 ⁱ	-25.7	-77.8 ⁱ	-67.2
	26		24		110	

^aRef. 4; ^bRef. 5; ^cRef. 6; ^dRef. 7; ^eRef. 8; ^fRef. 9 (based on Ref. 8); ^gRef. 9 (based on Ref. 10); ^hRef. 11; ⁱcalculated from the approximate formula $\gamma_{T1} = -(B/2) (\partial \ln \epsilon_0 / \partial p)$ (Ref. 12); ^jRef. 13; ^kRef. 14; ^lRef. 9 (based on Ref. 15); ^mRef. 16; ⁿRef. 17; ^pRef. 18; ^qRef. 19; ^rRef. 12,20; ^sbased on Ref. 20; ^tExperimental data at 4K from Ref. 21; ^uRef. 22; (*) Denotes quantities included in least squares fit.

the large experimental error of $\pm 4.3 \times 10^{11}$ N/m². No experimental TOE constant data are available for BaTiO₃ and KTaO₃. However, experimental data for the TOE compliance ϵ_{111} obtained by a resonance method have been reported for SrTiO₃ and BaTiO₃, amounting to 1.0×10^{-20} m⁴/N² (at 190K) and 4×10^{-19} m⁴/N² (at 195°C), respectively, and have been found to increase considerably with decreasing temperature (Refs. 10b and 23; the values quoted have been converted²⁴ to Brugger's notation²⁵). These values are two to three orders of magnitude larger than those calculated²⁴ from the ultrasonically measured TOE constants (1.8×10^{-22} m⁴/N for SrTiO₃) or from the lattice theoretically calculated TOE constants (3.735×10^{-22} m⁴/N for BaTiO₃). It is conceivable that for BaTiO₃ this discrepancy could arise from "polar" defect regions present above the Curie temperature¹⁵.

Although $(\partial \ln \epsilon_0 / \partial p)$ is fitted exactly, for SrTiO₃ and BaTiO₃ a discrepancy of about 25% occurs in Q_h , which arises from the discrepancy in ϵ_0 . The calculated values of Q_s are of the correct order of magnitude, and for BaTiO₃ and KTaO₃ they have the correct sign. For KTaO₃ the discrepancy in Q_s could arise from quantum effects, although for Q_{1212} the agreement is better than for Q_s .

It may further be noted that for BaTiO₃ and KTaO₃ the magnitude of the calculated soft mode gamma is considerably smaller than for SrTiO₃.

In summary, it has been shown for the three perovskite oxides considered that the first order anharmonic quantities pertaining to a static crystal can be accounted for by a simple shell model, in which the anharmonicity of the Coulomb and of the short range repulsive interactions is included. The discrepancies found may arise from limitations of the model, such as neglect of non-central forces, and from the uncertainties in the extrapolation to absolute zero of the experimental input data, especially⁹ the ES constant Q_s .

REFERENCES

1. B.N.N. Achar, G.R. Barsch and L.E. Cross, Phys. Rev. B24, 1209 (1981).
2. R.A. Cowley, Phys. Rev. 134, A981 (1964).
3. R. Migoni, H. Bilz and D. Bäuerle, Phys. Rev. Lett. 37, 1155 (1976); Lattice Dynamics, edited by M. Balkanski (Flammarion, Paris, 1978), p. 650.
4. R.O. Bell and G. Rupprecht, Phys. Rev. 129, 90 (1963).
5. A.G. Beattie and G.A. Samara, J. Appl. Phys. 42, 2376 (1971).
6. S.B. Levin, N.J. Field, F.M. Plock, and L. Merker, J. Opt. Soc. Am. 45, 737 (1955).
7. T. Mitsui and W.B. Westphal, Phys. Rev. 124, 1354 (1961).
8. G.A. Samara, Phys. Rev. 151, 378 (1966).
9. G.R. Barsch, B.N.N. Achar, and L.E. Cross, Proceedings of the Fifth International Meeting on Ferroelectricity, The Pennsylvania State University, August 17-21, 1981 (these Proceedings, p. 191).
10. (a) G. Schmidt and E. Hegenbarth, Phys. Status Solidi 3, 329 (1971); (b) G. Sorge, H. Beige and G. Schmidt, Phys. Status Solidi (a)26, K153 (1974).
11. Y. Yamada and G. Shirane, J. Phys. Soc. Japan 26, 396 (1969).
12. G.A. Samara, Ferroelectrics 2, 177 (1971).
13. D. Berlincourt and H. Jaffe, Phys. Rev. 111, 143 (1958).
14. W.N. Lawless and R.C. DeVries, J. Appl. Phys. 34, 2638 (1964).
15. H. Beige and G. Schmidt, Exp. Technik d. Physik 22, 393 (1974).
16. Y. Luspain, J.L. Servoin and F. Gervais, Ferroelectrics 25, 527 (1980).
17. H.H. Barrett, Physics Lett. 26A, 217 (1968).
18. R.C. Miller and W.G. Spitzer, Phys. Rev. 129, 94 (1963).
19. W.R. Abel, Phys. Rev. B4, 2696 (1971).
20. G.A. Samara and B. Morosin, Phys. Rev. B8, 1256 (1973).
21. H. Uwe and T. Sakudo, J. Phys. Soc. Japan 38, 183 (1975).
22. G. Shirane, R. Nathans and V.J. Minkiewicz, Phys. Rev. 157, 396 (1967).
23. (a) H. Beige and G. Schmidt, Exp. Technik d. Physik 12, 393 (1974); (b) H. Beige, Acta Phys. Slov. 30, 71 (1980).
24. G.R. Barsch, J. Appl. Phys. 39, 3780 (1968).
25. K. Brugger, Phys. Rev. 133, A1611 (1964).

APPENDIX 2

Landau-Devonshire Theory with Rotationally Invariant Expansion Coefficients

LANDAU-DEVONSHIRE THEORY WITH ROTATIONALLY INVARIANT EXPANSION COEFFICIENTS*

G.R. BARSCH, B.N.N. ACHAR^a AND L.E. CROSS

The Pennsylvania State University, University Park, PA 16802, U.S.A.

Abstract--General expressions pertaining to a centrosymmetric prototype phase are given for the correction terms to the third and fourth order expansion coefficients of the Landau-Devonshire free energy with respect to the displacement gradient and the polarization, that arise as a consequence of the rotational invariance condition. Application to crystals of O_h symmetry shows that the correction terms may be numerically significant.

TOUPIN'S THEOREM

In the electrostatic approximation (i.e. without retardation of the electromagnetic field and in the absence of a magnetic field) the internal energy U (per unit mass) of a homogeneous infinite elastic dielectric medium isentropically subjected to a finite elastic deformation and a finite electric field (for isothermal conditions: the Helmholtz free energy F) is a function of the deformation gradient $(\partial \bar{x}_i / \partial a_j) = (\partial x_i / \partial a_j)$ and the polarization vector $\bar{P} = \{P_r\}$ (electric dipole moment per unit volume in the deformed state), $U = \bar{U}(\partial \bar{x} / \partial \bar{a}, \bar{P})$. Here x_i and a_j ($i, j = 1, 2, 3$) denote the coordinates of a material point in the deformed state and in the undeformed and unpolarized reference state, respectively, referred to a common stationary cartesian frame. The rotational invariance condition requires that¹ $\bar{U}(\bar{R}(\partial \bar{x} / \partial \bar{a}), \bar{R}\bar{P}) = \bar{U}(\partial \bar{x} / \partial \bar{a}, \bar{P})$ for all rotation matrices $\bar{R} = \{R_{ij}\}$. As a consequence, the internal energy may be expressed in terms of the symmetric Lagrangian strain tensor (LST) $\eta = \{\eta_{ij}\}$ defined by (tensor notation; summation convention!)

$$\eta_{ij} = \frac{1}{2}[(\partial x_k / \partial a_i)(\partial x_k / \partial a_j) - \delta_{ij}] \quad (1)$$

and in terms of Toupin's material measure of polarization (MMP) $\bar{\pi} = \{\pi_i\}$ defined by

$$\pi_i = J(\partial a_i / \partial x_r) P_r \quad (2)$$

where

$$J = (\partial / \partial a) = \det(\partial x_i / \partial a_j) \quad (3)$$

denotes the Jacobian of the deformation, and ρ (ρ_0) the density in the deformed (undeformed) state, respectively¹. The resulting internal energy function $U(\eta, \bar{\pi})$ is then automatically invariant under rigid rotations¹ (Toupin's Theorem).

An alternative formulation of the theory of the nonlinear elastic dielectric was given by Grindlay² in terms of the dielectric displacement instead of the polarization and has been shown to be equivalent to Toupin's theory³. Following Toupin, we prefer

*Work supported by ONR Contract No. N00014-78-C-0291.

^aAlso affiliated with Bucknell University, Lewisburg, PA 17832, USA.

to use the polarization, because in the Landau-Devonshire theory it contains the order parameter.

LANDAU-DEVONSHIRE FREE ENERGY

As a consequence of Toupin's Theorem the Taylor expansion of the Landau-Devonshire (LD) energy function with respect to elastic and electric variables must be expressed in terms of the LST and the MMP, or their proper thermodynamic conjugate variables, if the expansion coefficients are to have the symmetry of indices familiar from the linear theory of elasticity and piezoelectricity. The Taylor expansion of the LD free energy density per unit initial volume $\rho_0 F(\tilde{\eta}, \tilde{\Pi})$ pertaining to a centrosymmetric prototype phase has the form

$$\begin{aligned} \rho_0 F(\tilde{\eta}, \tilde{\Pi}) = & \frac{1}{2} c_{ijkl} \eta_{ij} \eta_{kl} + \frac{1}{2} b_{rs} \Pi_r \Pi_s + \frac{1}{6} c_{ijklmn} \eta_{ij} \eta_{kl} \eta_{mn} - \frac{1}{2} h_{rs,mn} \Pi_r \Pi_s \eta_{mn} \\ & + \frac{1}{24} c_{ijklmnpq} \eta_{ij} \eta_{kl} \eta_{mn} \eta_{pq} - \frac{1}{4} h_{rs,mnpq} \Pi_r \Pi_s \eta_{mn} \eta_{pq} + \frac{1}{24} b_{rstu} \Pi_r \Pi_s \Pi_t \Pi_u + \dots \end{aligned} \quad (4)$$

The coefficients $c_{ijkl} \dots$ are the isothermal second, third and fourth order elastic constants according to the definition of Brugger⁴, the $h_{rs,mn} \dots$ are the first and second order electrostriction coefficients, and the $b_{rs} \dots$ are the second and fourth order reciprocal dielectric susceptibilities. All coefficients pertain to the reference state of the medium, assumed to be stress free. The choice of the kernel letters and of the signs for the expansion coefficients follows the IEEE convention⁵ for the linear theory of piezoelectricity and extends it to the nonlinear elastic dielectric, except that the coefficients are referred to the MMP.

The coefficients are invariant under exchange of indices of the following kind:

- I. $c_{ijkl} \dots$ (a) Index pairs, e.g. $c_{ijklmn} = c_{klijmn}$; (b) Indices within a given pair, e.g. $c_{ijklmn} = c_{jiklmn}$.
- II. $h_{rs,mn} \dots$ (a) Indices preceding the comma (pertaining to the MMP), e.g. $h_{rs,mn} = h_{sr,mn}$; (b) Index pairs following the comma (pertaining to the LST), e.g. $h_{rs,mnpq} = h_{rs,pqmn}$; (c) Indices within a given pair following the comma (pertaining to the LST), e.g. $h_{rs,mnpq} = h_{rs,nmpq}$.
- III. $b_{rs} \dots$ Any two indices, e.g. $b_{rstu} = b_{srtu} = b_{tsru}$.

Alternatively, the LD free energy density may be expressed as a function of the displacement gradient (DG) $v_{ij} = [(\partial x_i / \partial a_j) - \delta_{ij}]$ and the polarization \bar{P} with the Taylor expansion:

$$\begin{aligned} \rho_0 \bar{F}(\tilde{v}, \bar{P}) = & \frac{1}{2} \hat{c}_{ijkl} v_{ij} v_{kl} + \frac{1}{2} \hat{b}_{rs} \bar{P}_r \bar{P}_s + \frac{1}{6} \hat{c}_{ijklmn} v_{ij} v_{kl} v_{mn} - \frac{1}{2} \hat{h}_{rs,mn} \bar{P}_r \bar{P}_s v_{mn} \\ & + \frac{1}{24} \hat{c}_{ijklmnpq} v_{ij} v_{kl} v_{mn} v_{pq} - \frac{1}{4} \hat{h}_{rs,mnpq} \bar{P}_r \bar{P}_s v_{mn} v_{pq} + \frac{1}{24} \hat{b}_{rstu} \bar{P}_r \bar{P}_s \bar{P}_t \bar{P}_u + \dots \end{aligned} \quad (5)$$

The coefficients $\hat{c}_{ijkl} \dots$, $\hat{h}_{rs,mn} \dots$ and $\hat{b}_{rs} \dots$ represent an alternative set of second through fourth order elastic constants, first and second order electrostriction constants, and second and fourth order reciprocal dielectric susceptibilities, respectively. Since the DG is not symmetric ($v_{ij} \neq v_{ji}$) the coefficients $\hat{c}_{ijkl} \dots$ and $\hat{h}_{rs,mn} \dots$ are not invariant under exchange of indices within a given pair pertaining to the DG. That is, the $\hat{c}_{ijkl} \dots$ only have the symmetry property I(a) but not I(b), and the $\hat{h}_{rs,mn}$ only have the symmetry properties II(a) and II(b), but not II(c). However, the $\hat{b}_{rs} \dots$ and the $b_{rs} \dots$ have the same symmetry III, so one expects $\hat{b}_{rs} \dots = b_{rs} \dots$. The free energy function $\rho_0 \bar{F}(\tilde{v}, \bar{P})$ is constrained by the rotational invariance condition, from which, following Leibfried and Ludwig⁶, it may be deduced that certain linear combinations of the coefficients $\hat{c}_{ijkl} \dots$, $\hat{h}_{rs,mn} \dots$, etc. obtained by index permutation must have the additional symmetries I(b) and II(c), and that these conditions are

LANDAU-DEVONSHIRE THEORY WITH ROTATIONALLY INVARIANT...

equivalent to Eqs. (6a,b,c) to (8a,b) given below.

RELATION BETWEEN EXPANSION COEFFICIENTS OF $\rho_0 F(\tilde{\eta}, \tilde{\pi})$ AND $\rho_0 F(\tilde{v}, \tilde{p})$

The relations between the coefficients $\hat{c}_{ijkl}...$, etc. and the $c_{ijkl}...$, etc. are obtained by expanding $\tilde{\eta}$ and $\tilde{\pi}$ in Equ. (4) with respect to \tilde{v} and \tilde{p} , and equating equal powers of P_r and v_{kl} in Eqs. (4) and (5). The result is:

$$\hat{c}_{ijkl} = c_{ijkl} \quad (6a) \quad \hat{c}_{ijklmn} = c_{ijklmn} + c_{ijln} \delta_{km} + c_{kljn} \delta_{im} + c_{mnlj} \delta_{ik} \quad (6b)$$

$$\hat{c}_{ijklmnpq} = c_{ijklmnpq} + c_{ijklnq} \delta_{mp} + c_{ijmnlq} \delta_{kp} + c_{ijpqln} \delta_{km} + c_{klmnpj} \delta_{ip} + c_{klpqjn} \delta_{im} + c_{mnpqjl} \delta_{ik} + c_{jlnq} \delta_{ik} \delta_{mp} + c_{jnql} \delta_{im} \delta_{kp} + c_{jqln} \delta_{ip} \delta_{km} \quad (6c)$$

$$\hat{h}_{rs,mn} = h_{rs,mn} + b_{rm} \delta_{sn} + b_{sm} \delta_{rn} - 2b_{rs} \delta_{mn} \quad (7a)$$

$$\begin{aligned} \hat{h}_{rs,mnpq} = & h_{rs,mnpq} + 2(h_{rs,mn} \delta_{pq} + h_{rs,pq} \delta_{mn}) + h_{rs,nq} \delta_{mp} - (h_{rm,pq} \delta_{sn} + h_{sm,pq} \delta_{rn}) \\ & - (h_{rp,mn} \delta_{sq} + h_{sp,mn} \delta_{rq}) + 2b_{rs} (\delta_{mq} \delta_{np} - 2\delta_{mn} \delta_{pq}) + 2(b_{rp} \delta_{sq} + b_{sp} \delta_{rq}) \delta_{mn} \\ & + 2(b_{rm} \delta_{sn} + b_{sm} \delta_{rn}) \delta_{pq} - b_{mp} (\delta_{rn} \delta_{sq} + \delta_{rq} \delta_{sn}) - (b_{rm} \delta_{sq} + b_{sm} \delta_{rq}) \delta_{np} \\ & - (b_{rp} \delta_{sn} + b_{sp} \delta_{rn}) \delta_{mq} \end{aligned} \quad (7b)$$

$$\hat{b}_{rs} = b_{rs} \quad (8a) \quad \hat{b}_{rstu} = b_{rstu} \quad (8b)$$

Table I: Correction terms to third order elastic^a and first order electrostriction constants for O_h symmetry and their relative magnitude for $SrTiO_3$ and NaCl at 300K, calculated from experimental data of Refs. 7 to 10.

ijklmn	ΔC_{ijklmn}	$\Delta C_{ijklmn}/C_{ijklmn}$	
		$SrTiO_3$	NaCl
11 11 11	$3C_{1111}$	-2.00	-0.18
11 11 22	C_{1122}	-0.13	-0.25
11 22 33	0	0	0
11 12 12	$C_{1122} + 2C_{1212}$	-1.16	-0.64
11 21 12	C_{1212}	-0.41	-0.21
11 21 21	C_{1111}	-1.10	-0.82
11 23 23; 11 32 32	C_{1122}	-0.12	0.44
11 32 23	0	0	0
12 23 31; 21 32 13	0	0	0
12 23 13; 12 32 13	C_{1212}	1.38	0.49
rs, mn	$\Delta h_{rs,mn}$	$\Delta h_{rs,mn}/h_{rs,mn}$	
		$SrTiO_3$	NaCl
11, 11	0	0	0
11, 22	-2b	0.27	-0.31
12, 12; 12, 21	b		-0.26

^a Second order elastic constants are given in tensor notation.

DISCUSSION AND CONCLUSIONS

As shown elsewhere¹¹ it is possible to construct the usual thermodynamic potentials and the corresponding LD energy functions either with $\tilde{\eta}$ and $\tilde{\pi}$, and their conjugate

Equ. (6b) has been given before by Leibfried and Ludwig⁶. For the higher order elastic and electrostriction constants $\hat{c}_{ijklmn}...$ and $h_{rs,mn}...$ the loss of symmetries Ib and IIc arises from correction terms of lower order and in general leads to an increase in the number of independent coefficients.

In Table I the correction terms for the third order elastic constants and for the first order electrostriction constants are listed for the cubic point group O_h , together with their numerical values for $SrTiO_3$ and NaCl. The correction terms increase the number of third order elastic constants, but not the number of electrostriction constants. The magnitude of the correction is in general quite substantial. However, because of the Curie-Weiss Law for ferroelectric materials the correction to the electrostriction coefficients should according to Eqs. (7a,b) vanish at the Curie temperature.

intensive variables $t_{ij} = \rho_0(\partial F/\partial n_{ij})_{T,\bar{n}}$ and $f_r = \rho_0(\partial F/\partial \Pi_r)_{T,\bar{\eta}}$, or with \bar{v} and \bar{P} , and their conjugate intensive variables $\tau_{ij} = \rho_0(\partial \bar{F}/\partial v_{ij})_{T,\bar{P}}$ and $\bar{E}_r = \rho_0(\partial \bar{F}/\partial P_r)_{T,\bar{v}}$. It should be noted, however, that the Cauchy stress tensor $\sigma = \{\sigma_{ij}\}$ (force per unit area in the deformed state) is not the conjugate variable for any of the thermodynamic potentials so introduced, but is related to the Piola-Kirchhoff stress tensor $\gamma = \{\tau_{ij}\}$ (force per unit area in the reference state) by $\sigma_{ij} = (1/J)(\partial x_i/\partial a_k)\tau_{jk}$ where the Piola-Kirchhoff stress tensor is related to the thermodynamic tensions t_{kl} by $\tau_{jk} = (\partial x_j/\partial a_n)t_{kn}$. The electric field E_r is related to the conjugate variable f_s according to $\bar{E}_r = (\partial \bar{a}_r/\partial x_s)f_s$. Whereas the expansion coefficients of the thermodynamic potentials with respect to the thermodynamic tensions t_{ij} have the full symmetry I(a,b), II(a,b,c) and III as listed above, the higher than second order expansion coefficients with respect to the asymmetric Piola-Kirchhoff stress tensor have the same reduced symmetry as the $\hat{c}_{ijkl} \dots$, etc.

The choice of variables is a matter of convenience as suggested by the experimental situation. However, whenever the "physical" variables $\bar{\gamma}, \bar{E}$ (or \bar{v}, \bar{P}) rather than the "thermodynamic" variables $\bar{\gamma}, \bar{f}$ (or $\bar{\eta}, \bar{\Pi}$) are used, the number of independent higher order elastic and electrostriction coefficients is increased, and the experimental data cannot be fitted to the coefficients pertaining to the thermodynamic variables, which possess the full symmetry I(a,b,c) to III listed above.

Furthermore, in spite of its widespread use, the linearized strain tensor $\epsilon_{ij} = (1/2)(v_{ij} + v_{ji})$ in general is not an appropriate strain variable in a LD free energy function, and its use amounts to replacing the correction terms in Eqs. (6b,c) and (7b,c) and in Table I by their average values.

The symmetry-reducing correction terms may be expected to be especially significant where the dependence of the ferroelectric or ferroelastic transition on stress or strain is involved. However, for zero stress or strain according to Equ. (2) the MMP $\bar{\Pi}$ reduces to the polarization \bar{P} , and the familiar results of the LD theory are recovered.

REFERENCES

1. R.A. Toupin, (a) J. Rat. Mech. Anal. **5**, 849 (1956); (b) Int. J. Engng. Sci. **1**, 101 (1963).
2. J. Grindlay, (a) Phys. Rev. **149**, 637 (1966); (b) Phys. Rev. **160**, 698 (1967); (c) An Introduction to the Phenomenological Theory of Ferroelectricity (Pergamon, Oxford, 1970), Chapter 4.
3. P. Hájíček, Phys. Lett. **25A**, 36 (1967).
4. K. Brugger, Phys. Rev. **133**, A1611 (1964).
5. IEEE Standard on Piezoelectricity, IEEE Std. 176-1978 (The Institute of Electrical and Electronics Engineers, Inc., New York, 1978).
6. G. Leibfried and W. Ludwig, Z. Phys. **169**, 80 (1960).
7. A.G. Beattie and G.A. Samara, J. Appl. Phys. **42**, 2376 (1971).
8. J.R. Drabble and R.E.B. Strathern, Proc. Phys. Soc. **92**, 1090 (1967).
9. G. Schmidt and E. Hegenbarth, Phys. Status Solidi **3**, 329 (1963).
10. L. Bohatý and S. Haussühl, Acta Cryst. **A33**, 114 (1977).
11. G.R. Barsch, B.N.N. Achar, and L.E. Cross, Phys. Rev. **B25** (to be published, 1982).

APPENDIX 3

Pressure Gauge Using Relaxor Ferroelectrics

Pressure Gauge Using Relaxor Ferroelectrics

Kenji UCHINO, Shoichiro NOMURA, Leslie E. CROSS,[†]
Sei J. JANG[†] and Robert E. NEWNHAM[†]

*Department of Physical Electronics, Tokyo Institute of Technology,
Ookayama, Meguro-ku, Tokyo 152*

*[†]Materials Research Laboratory, The Pennsylvania State University,
University Park, Pennsylvania 16802, U.S.A.*

(Received March 26, 1981; accepted for publication April 7, 1981)

A new type of pressure gauge using relaxor ferroelectrics such as the $\text{Pb}(\text{Mg}_{1/3}\text{Nb}_{2/3})\text{O}_3$ - PbTiO_3 - $\text{Ba}(\text{Zn}_{1/3}\text{Nb}_{2/3})\text{O}_3$ ternary solid solution is described, which reveals a sensitive pressure characteristic of permittivity. This device is much less expensive than conventional gauges and is very compact.

§1. Introduction

There are a number of methods for measuring stress or pressure, based on various physical phenomena such as piezoresistivity, piezomagnetism and piezoelectricity. The inverse electrostrictive effect, that is, the pressure dependence of the dielectric constant, offers another possible method.

In earlier papers concerned with the electrostrictive effects in $\text{Pb}(\text{Mg}_{1/3}\text{Nb}_{2/3})\text{O}_3$,^{1,2)} and $\text{Pb}(\text{Zn}_{1/3}\text{Nb}_{2/3})\text{O}_3$,³⁾ it has been shown that relaxor ferroelectrics have the capability of producing enormous electrostriction. Strains an order of magnitude larger than those of piezoelectric $\text{Pb}(\text{Zr}, \text{Ti})\text{O}_3$ ceramics have been demonstrated in the solid solution $\text{Pb}(\text{Mg}_{1/3}\text{Nb}_{2/3})\text{O}_3$ - PbTiO_3 .^{4,5)} In the inverse electrostrictive effect, a sensitive pressure characteristic has also been observed in the same material.¹⁾

This paper is concerned with a new type of pressure gauge using relaxor ferroelectrics such as the $\text{Pb}(\text{Mg}_{1/3}\text{Nb}_{2/3})\text{O}_3$ - PbTiO_3 - $\text{Ba}(\text{Zn}_{1/3}\text{Nb}_{2/3})\text{O}_3$ ternary system.⁶⁾ The addition of $\text{Ba}(\text{Zn}_{1/3}\text{Nb}_{2/3})\text{O}_3$ to the $\text{Pb}(\text{Mg}_{1/3}\text{Nb}_{2/3})\text{O}_3$ - PbTiO_3 solid solution results in astonishingly stable temperature-characteristics which enable these ceramics to be used in high-sensitivity pressure gauges.

§2. Theoretical Background of A New Pressure Gauge

For a parallel plate capacitor with an area A and a thickness t , the capacitance C and its

variation with uniaxial stress X perpendicular to the plate, and with temperature T , are given as follows:

$$C = \epsilon_0 \epsilon A / t, \quad (1)$$

$$(\partial \ln C / \partial X) = (\partial \ln \epsilon / \partial X) + (\partial \ln A / \partial X) - (\partial \ln t / \partial X), \quad (2)$$

$$(\partial \ln C / \partial T) = (\partial \ln \epsilon / \partial T) + (\partial \ln A / \partial T) - (\partial \ln t / \partial T), \quad (3)$$

where ϵ is the relative dielectric constant of the material and $\epsilon_0 = 8.854 \times 10^{-12} \text{ Fm}^{-1}$. In the paraelectric state, the stress dependence of the permittivity is related to the electrostrictive coefficient Q_{11} by

$$(\partial(1/\epsilon_0 \epsilon) / \partial X) = -2Q_{11}. \quad (4)$$

By use of the defining relations for thermal expansivity

$$\Delta L / L = \alpha T, \quad (5)$$

and for elastic compliances

$$s_{11} = (1/t)(\partial t / \partial X), \quad (6)$$

$$s_{12} = (1/2A)(\partial A / \partial X), \quad (7)$$

eqs. (2) and (3) can be written as

$$(1/C)(\partial C / \partial X) = 2Q_{11}\epsilon_0 \epsilon + (2s_{12} - s_{11}), \quad (8)$$

$$(1/C)(\partial C / \partial T) = (1/\epsilon)(\partial \epsilon / \partial T) + \alpha. \quad (9)$$

When hydrostatic pressure, instead of uniaxial one, is applied to the plate, eq. (8) should be replaced by the following:

$$(1/C)(\partial C / \partial p) = -2Q_{11}\epsilon_0 \epsilon - \chi_T/3, \quad (10)$$

where the sign of pressure is taken as positive

for compression, χ_T is the isothermal compressibility given by $s_{11} + 2s_{12}$, and $Q_b = Q_{11} + 2Q_{12}$.

If the condition $|(1/C)(\partial C/\partial X)|$ or $|(1/C)(\partial C/\partial p)| \gg |(1/C)(\partial C/\partial T)|$ is well satisfied, a thermally stable pressure detector based on the capacitance measurement can be constructed. Relaxor ferroelectrics which have small thermal expansion,^{7,8)} small electrostrictive coefficients, but very large permittivity,⁹⁾ excel the usual perovskite ferroelectrics (e.g. $\text{Pb}(\text{Zr}, \text{Ti})\text{O}_3$ and BaTiO_3 -based ceramics) in this application.

§3. Sample Preparation

The solid solution $0.45\text{Pb}(\text{Mg}_{1/3}\text{Nb}_{2/3})\text{O}_3$ - 0.36PbTiO_3 - $0.19\text{Ba}(\text{Zn}_{1/3}\text{Nb}_{2/3})\text{O}_3$ was chosen because of its stable temperature characteristic of electrostriction in the temperature range -20°C to $+50^\circ\text{C}$. Ceramic samples were prepared by the usual solid reaction from mixed oxides. Reagent grade PbO , MgO , Nb_2O_5 , TiO_2 , BaCO_3 and ZnO were mixed in the appropriate proportions, ball-milled in alcohol, then dried and calcined in air in a closed alumina crucible. Calcining temperature of 920°C was maintained for 15 hours. The resulting calcine was ground and refired for two additional 15-hour periods at 950°C , to ensure complete reaction. After cold pressing into disks 25.4 mm in diameter, samples were sintered at 1300°C for 2 hours on platinum setters in air. The final densities of the ceramics were about 94% of the ideal density.

§4. Basic Experiments

Dielectric, thermal-dilatational and electrostrictive experimental data are described for the solid solution $0.45\text{Pb}(\text{Mg}_{1/3}\text{Nb}_{2/3})\text{O}_3$ - 0.36PbTiO_3 - $0.19\text{Ba}(\text{Zn}_{1/3}\text{Nb}_{2/3})\text{O}_3$.

Figure 1 shows the permittivity curves at three different frequencies plotted as a function of temperature. The addition of $\text{Ba}(\text{Zn}_{1/3}\text{Nb}_{2/3})\text{O}_3$ to the $\text{Pb}(\text{Mg}_{1/3}\text{Nb}_{2/3})\text{O}_3$ - PbTiO_3 solid solution results in an improvement in the temperature characteristic of the permittivity around room temperature ($|(1/\epsilon)(\partial\epsilon/\partial T)| < 5 \times 10^{-4} \text{ K}^{-1}$).

Figure 2 shows the temperature dependence of thermal strain $\Delta L/L$. The thermal expansion coefficient of the ceramics in the temperature range -20°C to $+50^\circ\text{C}$ is less than 2×10^{-6}

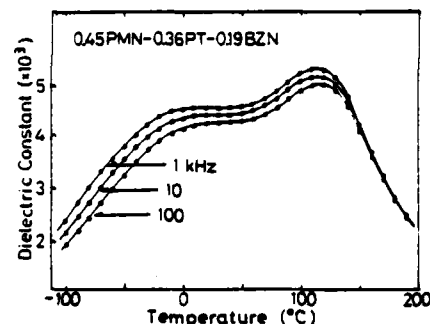


Fig. 1. Dielectric constant of $0.45\text{Pb}(\text{Mg}_{1/3}\text{Nb}_{2/3})\text{O}_3$ - 0.36PbTiO_3 - $0.19\text{Ba}(\text{Zn}_{1/3}\text{Nb}_{2/3})\text{O}_3$ at three different frequencies as a function of temperature.

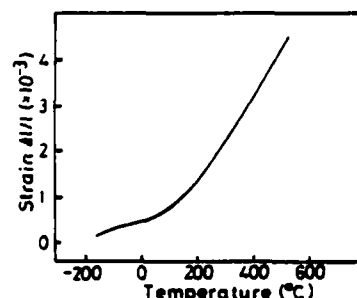


Fig. 2. Thermal strain $\Delta L/L$ in $0.45\text{Pb}(\text{Mg}_{1/3}\text{Nb}_{2/3})\text{O}_3$ - 0.36PbTiO_3 - $0.19\text{Ba}(\text{Zn}_{1/3}\text{Nb}_{2/3})\text{O}_3$.

K^{-1} , which is much smaller than those of a normal perovskite ($\sim 10 \times 10^{-6} \text{ K}^{-1}$).

Figure 3 shows the transverse electrostrictive strain (contraction) plotted as a function of bias field at several different temperatures. The induced strain at room temperature approaches 10^{-4} at a field of 15 kV/cm, with a slight hysteresis under rising and falling fields. Thermal variations of the electrostrictive effect are extremely small compared with other ferroelectrics. Electrostrictive coefficient Q_{12} defined by $S_2 = Q_{12}P_1^2$, where S_2 is the transverse elastic strain and P_1 is the polarization induced by an electric field, is calculated to be $-1.6 \times 10^{-2} \text{ m}^4\text{C}^{-2}$ for the ceramics.

§5. Pressure Gauges

The capacitance change with uniaxial stress can be estimated as follows, using the experimental data for $0.45\text{Pb}(\text{Mg}_{1/3}\text{Nb}_{2/3})\text{O}_3$ - 0.36PbTiO_3 - $0.19\text{Ba}(\text{Zn}_{1/3}\text{Nb}_{2/3})\text{O}_3$: $Q_{11} = 4.1 \times 10^{-2} [\text{m}^4\text{C}^{-2}]$, $\epsilon(p=0) = 4500$, $s_{11} = 10 \times 10^{-4} [\text{kbar}^{-1}]$, $s_{12} = -3 \times 10^{-4} [\text{kbar}^{-1}]$ (the

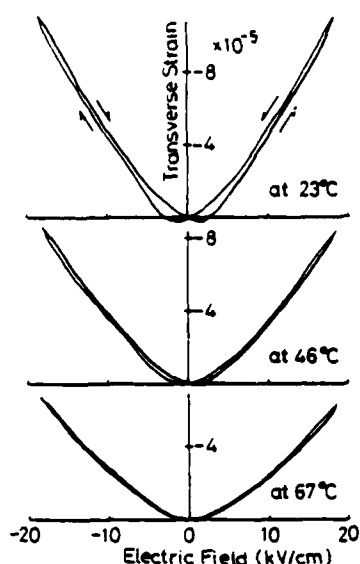


Fig. 3. Transverse electrostrictive strains of $0.45\text{Pb}(\text{Mg}_{1/3}\text{Nb}_{2/3})\text{O}_3-0.36\text{PbTiO}_3-0.19\text{Ba}(\text{Zn}_{1/3}\text{Nb}_{2/3})\text{O}_3$ as a function of bias field at several temperatures.

value estimated from Reference (2)), $|(1/\epsilon)(\partial\epsilon/\partial T)| = 5 \times 10^{-4} [\text{K}^{-1}]$, and $\alpha = 2 \times 10^{-6} [\text{K}^{-1}]$. Equations (8) and (9) become

$$(1/C)(\partial C/\partial X) = 0.33 [\text{kbar}^{-1}], \quad (11)$$

and

$$|(1/C)(\partial C/\partial T)| = 5 \times 10^{-4} [\text{K}^{-1}]. \quad (12)$$

The capacitance change with hydrostatic pressure can also be estimated as

$$(1/C)(\partial C/\partial p) = -7.1 \times 10^{-2} [\text{kbar}^{-1}]. \quad (13)$$

Since the value of $|(1/\epsilon)(\partial\epsilon/\partial T)|$ is extremely small near room temperature, the capacitance fluctuations caused by temperature changes (e.g., room temperature variations and the temperature change caused by adiabatic compression) are almost negligible.

Two plate capacitors with dimensions $9.6 \text{ mm} \times 8.1 \text{ mm} \times 1.4 \text{ mm}$ and $6.4 \text{ mm} \times 6.5 \text{ mm} \times 0.25 \text{ mm}$ were used as a uniaxial stress gauge and a hydrostatic pressure gauge, respectively. After cutting and polishing, gold electrodes were sputtered on, and the samples were annealed at 500°C for 30 minutes.

The uniaxial-stress gauge chip mounted between teflon sheets was positioned in an Instron stressing machine. The capacitance was measured with an automatic capacitance meter accurate to 0.05% of the reading, for

smaller than the capacitance fluctuations caused by temperature changes. The 3001 digital capacitance meter manufactured by Continental Specialties Corporation, CA is an inexpensive choice. Figure 4 shows a typical plot of capacitance as a function of rising and falling uniaxial stress. A slight hysteresis due mainly to slippage of the teflon buffer was observed.

The capacitance sensor for hydrostatic-pressure with two lead wires was immersed in a pressure vessel (Pressure Products, PA). Figure 5 shows a capacitance versus hydrostatic-pressure curve. The capacitance change is linear with the hydrostatic pressure in the region below 1 kbar and deviates slightly from

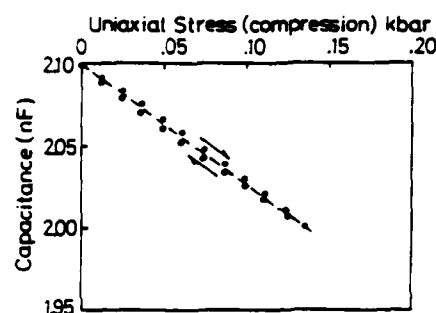


Fig. 4. Capacitance versus uniaxial-stress curve for $0.45\text{Pb}(\text{Mg}_{1/3}\text{Nb}_{2/3})\text{O}_3-0.36\text{PbTiO}_3-0.19\text{Ba}(\text{Zn}_{1/3}\text{Nb}_{2/3})\text{O}_3$.

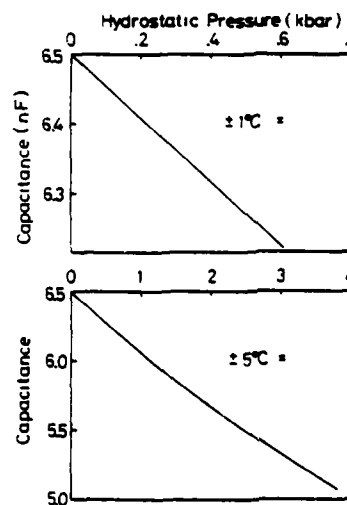


Fig. 5. Capacitance versus hydrostatic-pressure curve for $0.45\text{Pb}(\text{Mg}_{1/3}\text{Nb}_{2/3})\text{O}_3-0.36\text{PbTiO}_3-0.19\text{Ba}(\text{Zn}_{1/3}\text{Nb}_{2/3})\text{O}_3$.

a straight line at higher pressures. The accuracy of the pressure reading is governed mainly by temperature fluctuations and is about ± 10 bar for fluctuations of $\pm 1^\circ\text{C}$, which is the same order of magnitude as the accuracy of an expensive Heise gauge (Heise, CT), ± 8 bar.

Agreement between the slopes estimated in eqs. (11) and (13) and those observed, is fairly good.

§6. Summary

The new pressure gauge constructed from relaxor ferroelectrics is much less expensive than conventional gauges (less than one-tenth in price, including a capacitance meter) and is very compact.

Relaxor ferroelectrics with very large permittivity, small thermal expansion and excellent temperature-stability of the permittivity, are preferred to the usual perovskite dielectrics. Based on eqs. (8), (10), (11) and (13), the dimensions of the device have little effect on

the sensitivity. We can use much smaller gauges than those used in this study if the capacitances lie in a suitable range for the capacitance meter.

References

- 1) K. Uchino, S. Nomura, L. E. Cross, S. J. Jang and R. E. Newnham: *J. Appl. Phys.* **51** (1980) 1142.
- 2) J. Kuwata, K. Uchino and S. Nomura: *Jpn. J. Appl. Phys.* **19** (1980) 2099.
- 3) S. Nomura, J. Kuwata, S. J. Jang, L. E. Cross and R. E. Newnham: *Mater. Res. Bull.* **14** (1979) 769.
- 4) L. E. Cross, S. J. Jang, R. E. Newnham, S. Nomura and K. Uchino: *Ferroelectrics* **23** (1980) 187.
- 5) S. J. Jang, K. Uchino, S. Nomura and L. E. Cross: *Ferroelectrics* **27** (1980) 31.
- 6) S. J. Jang, L. E. Cross, K. Uchino and S. Nomura: *J. Am. Cer. Soc.* (1980) in press.
- 7) J. Kuwata, K. Uchino and S. Nomura: *Ferroelectrics* **22** (1979) 863.
- 8) K. Uchino, S. Nomura, A. Amin, Z. P. Chang, L. E. Cross and R. E. Newnham: *Jpn. J. Appl. Phys.* **19** (1980) L398.
- 9) K. Uchino, S. Nomura, L. E. Cross and R. E. Newnham: *J. Phys. Soc. Jpn.* **49** Suppl. B (1980) 45.

APPENDIX 4

An Optical Study of the Ferroelectric Relaxors

$\text{Pb}(\text{Mg}_{1/3}\text{Nb}_{2/3})\text{O}_3$, $\text{Pb}(\text{Sc}_{1/2}\text{Ta}_{1/2})\text{O}_3$, and $\text{Pb}(\text{Sc}_{1/2}\text{Nb}_{1/2})\text{O}_3$

AN OPTICAL STUDY OF THE FERROELECTRIC RELAXORS $\text{Pb}(\text{Mg}_{1/3}\text{Nb}_{2/3})\text{O}_3$,
 $\text{Pb}(\text{Sc}_{1/2}\text{Ta}_{1/2})\text{O}_3$, and $\text{Pb}(\text{Sc}_{1/2}\text{Nb}_{1/2})\text{O}_3$

N. SETTER*, L.E. CROSS†

Materials Research Laboratory, The Pennsylvania State University, University
Park, PA 16802, USA

Abstract—Complex-perovskite ferroelectric relaxors $\text{A}(\text{B}'_x\text{B}''_{1-x})\text{O}_3$ have isotropic appearance in the polar phase, as demonstrated by $\text{Pb}(\text{Mg}_{1/3}\text{Nb}_{2/3})\text{O}_3$ and B-site disordered $\text{Pb}(\text{Sc}_{1/2}\text{Ta}_{1/2})\text{O}_3$ crystals. In $\text{Pb}(\text{Sc}_{1/2}\text{Ta}_{1/2})\text{O}_3$, ordering of the B-site cations causes birefringence and ferroelectric domains to appear. $\text{Pb}(\text{Sc}_{1/2}\text{Nb}_{1/2})\text{O}_3$ shows an intermediate behavior. In the ferroelectric phase all three materials show rhombohedral symmetry. Comparison of the ordered and the disordered $\text{Pb}(\text{Sc}_{1/2}\text{Ta}_{1/2})\text{O}_3$ supports the theory that the optical anomaly in ferroelectric relaxors results from existence of microdomains due to compositional fluctuation.

INTRODUCTION

Complex-perovskite ferroelectric relaxors $\text{A}(\text{B}'_x\text{B}''_{1-x})\text{O}_3$ are optically isotropic in the polar phase. They have diffuse phase transition due to the compositional fluctuations. In the transition range, ferroelectric microdomains of $\sim 100\text{\AA}$ can be formed independently. Being smaller than the wavelength of visible light, the size of the microdomains can account for the observed optical isotropy^{1,2}

$\text{Pb}(\text{Sc}_{1/2}\text{Ta}_{1/2})\text{O}_3$ (PST) can be prepared with various degrees of B-site order³. It has been shown that disordering of B-site cations changes the material from an almost normal first-order ferroelectric to a ferroelectric relaxor⁴. In the present work anomalies in the birefringent properties of ferroelectric relaxors are studied. Measurements performed with $\text{Pb}(\text{Sc}_{0.5}\text{Nb}_{0.5})\text{O}_3$ (PSN), $\text{Pb}(\text{Mg}_{1/3}\text{Nb}_{2/3})\text{O}_3$ (PMN) and $\text{Pb}(\text{Sc}_{1/2}\text{Ta}_{1/2})\text{O}_3$ are compared.

EXPERIMENTS

The samples used were flux grown single crystals.

- ordered and disordered PST⁴
- PSN as grown and PSN fired at 1350°C for 2 hours
- PMN

The materials were studied with a polarizing microscope using hot or cold stage as needed. For birefringence measurements, a rotating analyzer apparatus with He/Ne light source⁵ was used.

— Also affiliated with Department of Electrical Engineering.

*Present address: Dept of Applied Chemistry, University of Geneva, 30 quai Ernest Ansermet, Geneva CH-1211, Switzerland.

RESULTS

Disordered $\text{Pb}(\text{Sc}_{1/2}\text{Ta}_{1/2})\text{O}_3$

Disordered PST is a ferroelectric with diffuse phase transition. It remains optically isotropic far below the transition temperature. When electric field is applied reversible birefringence is observed. Ferroelectric domains can be seen at temperatures lower than -37°C . Upon removal of the field, residual birefringence remains (Figure 1). The direction of the domain walls and the symmetrical extinction indicate rhombohedral symmetry.

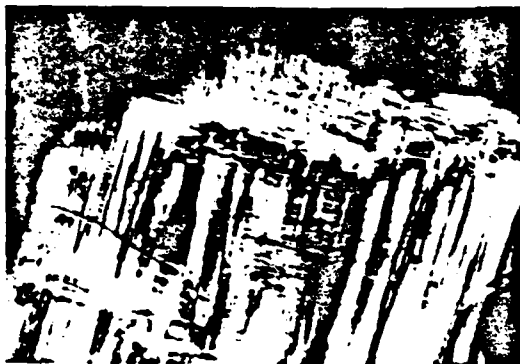


FIGURE 1. Ferroelectric domains in disordered PST. $T = -95^\circ\text{C}$, $E = 0$. Cooled with $E = 10 \text{ kV/cm}$ (001) plate (X80).

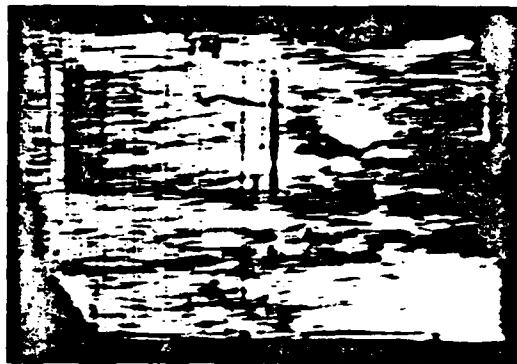


FIGURE 2. Ferroelectric domains in ordered PST. $T = -120^\circ\text{C}$ (001) plate (X70).

Ordered $\text{Pb}(\text{Sc}_{1/2}\text{Ta}_{1/2})\text{O}_3$

Ordered PST is a ferroelectric with sharp first order transition spontaneous birefringence and domain walls corresponding to rhombohedral symmetry appear when cooling below the transition (Figure 2). Applying electric field in the [001] direction results in an increase of the domain wall density. In a (112) plate, (100) domain walls disappear when an electric field is applied parallel to [111] and (110) walls appear instead. Removal of E at low temperatures leaves this picture unaltered. At temperatures near the transition the domains switch back to the original rhombohedral direction.

The apparent birefringence versus temperature of a multidomain (100) plate of ordered and disordered PST is shown in Figure 3.

$\text{Pb}(\text{Sc}_{1/2}\text{Nb}_{1/2})\text{O}_3$

As-grown PSN shows rhombohedral symmetry at room temperature. The birefringence change at the transition is sharp with a small thermal hysteresis (Figure 4). Superlattice reflections could not be detected by x-ray. Spontaneous birefringence appears also in samples quenched from high temperature for enhancing the B-site disorder. However, the transition is less sharp in this case.

AN OPTICAL STUDY OF THE FERROELECTRIC RELAXORS

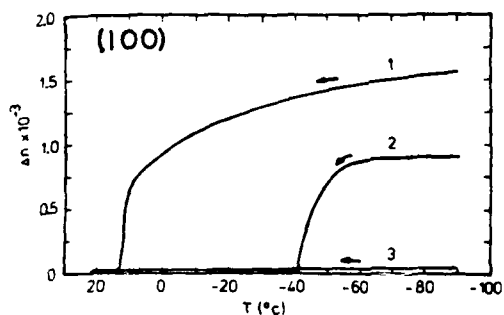


FIGURE 3. Birefringence vs temperature for PST: 1-ordered PST; 2-disordered PST cooled under 10 KV/cm; 3-disordered PST cooled without E.

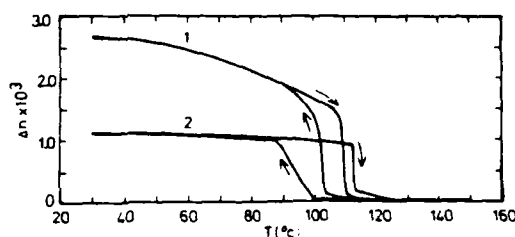
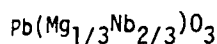


FIGURE 4. Apparent birefringence versus temperature for PSN multidomain (001) plates. 1-as grown; 2-after 2 hrs at 1350°C.



Birefringence is seen below the transition only after an electric field is applied. The (001) plate shows symmetrical extinction. Domain spikes appear only after reversing the applied field a few times. Birefringence versus temperature is consistent with previous reports². When E is applied along [111], (100) domain walls are clearly observed in (112) plate (Figure 5). Extinction direction and walls orientation correspond to rhombohedral symmetry and not to the previously reported orthorhombic² or tetragonal⁶ unit cell.



FIGURE 5. Ferroelectric domains in a PMN (112) plate. $T = -120^\circ\text{C}$. Cooled with $E = 5 \text{ KV/cm}$ at the [111] direction.

CONCLUSION

As has been previously seen for dielectric properties⁴ also the optical behavior of PST depends on the order in the B-cation site.

Ordered PST behaves like a normal ferroelectric with a sharp phase transition. Upon disordering alone the material becomes optically isotropic in the ferroelectric phase, similar to $\text{Pb}(\text{Mg}_{1/3}\text{Nb}_{2/3})\text{O}_3$. In disordered PST the spontaneous birefringence remains after the field is switched off below -40°C . This behavior is identical to that of other ferroelectric relaxors and therefore supports the view that the optical anomaly in ferroelectric relaxors results from existence of microdomains due to compositional fluctuations.

N. SETTER, L.E. CROSS

ACKNOWLEDGMENT

The authors would like to thank Dr. A.M. Glaser for his hospitality during NS. stay in Clarendon Laboratory where part of this work was performed. This work was supported by the Office of Naval Research, Contract No. N00014-78-C-0291.

REFERENCES

1. G.A. Smolenskii, J. Phys. Soc. Jpn. 285, 26 (1970).
2. N.A. Bokov, I.E. Mylnikova, Sov. Phys.-Solid State 3, 613 (1961).
3. N. Setter, L.E. Cross, J. Mat. Sci. 15, 2478 (1980).
4. N. Setter, L.E. Cross, J. Appl. Phys. 51, 4356 (1980).
5. I.G. Wood, A.M. Glaser, J. Appl. Cryst. 13, 217 (1980).
6. J. Smith, Ph.D. Thesis, The Pennsylvania State University (1967).

APPENDIX 5

Perforated PZT-Polymer Composites for
Piezoelectric Transducer Applications

PERFORATED PZT-POLYMER COMPOSITES FOR PIEZOELECTRIC TRANSDUCER APPLICATIONS

A. SAFARI, R. E. NEWNHAM, L. E. CROSS[†] and W. A. SCHULZE

Materials Research Laboratory, The Pennsylvania State University, University Park,
Pennsylvania 16802, USA

(Received April 5, 1981)

Composites of PZT and polymer with 3-1 and 3-2 connectivity patterns have been fabricated by drilling holes in sintered PZT blocks and filling the holes with epoxy. The influence of hole size and volume fraction PZT on the hydrostatic properties of the composite was evaluated. By decoupling the piezoelectric d_{31} and d_{32} coefficients in the composite, the hydrostatic coefficients are greatly enhanced. On samples optimized for hydrophone performance, the dielectric constants of 3-1 and 3-2 composites are 600 and 300 respectively. The piezoelectric coefficients d_h , \bar{g}_h , and $\bar{g}_h d_h$ for 3-1 composites are 230 (pC/N), 34 ($\times 10^{-3}$ Vm/N), and 7800 (10^{-13} m²/N) respectively, and the corresponding values for 3-2 composites are 372 (pC/N), 123 (10^{-3} Vm/N), and 45000 (10^{-13} m²/N).

1. INTRODUCTION

In recent years several types of PZT-polymer composites have been fabricated to improve the piezoelectric properties of poled PZT (lead zirconate titanate) ceramics. Different types of macro-symmetry and interphase connectivity were utilized in the design of the PZT-polymer composites listed in Table I.¹⁻⁸ Here connectivity 1-3 means that the PZT phase is self-connected in one direction, and the polymer phase is self-connected in all three directions. In all composites, the dielectric constant K_{33} of solid PZT is lowered by the introduction of a polymer phase, and in all cases the hydrostatic piezoelectric charge coefficient d_h is also enhanced. The hydrostatic piezoelectric voltage coefficient \bar{g}_h and the $d_h \bar{g}_h$ product used as a figure of merit for hydrophone application are therefore considerably enhanced in all the composite designs.

Klicker *et al.*⁸ have fabricated 1-3 composites of PZT rods embedded in an epoxy matrix. As shown in Table I, these composites have better piezoelectric properties than solid PZT. The hydrostatic coefficients d_h and \bar{g}_h are a function of the dimension of PZT rods, the spacing between the PZT rods, and the thickness of the composite. Based on the previous work with PZT-polymer

composites and on simple series and parallel models,¹ it is clear that the difference in the elastic compliances of the PZT and epoxy has a favorable influence on piezoelectric properties by altering the stress pattern inside the composites.

Rittenmyer *et al.*³ have fabricated 3-3 composites of PZT and polymer (polymethyl methacrylate) with PZT powder in an organic binder and firing the mixture to give a ceramic skeleton. After cooling, the ceramic skeletons were back-filled with polymer (Burps composites). As shown in Table I, these composites have better piezoelectric and mechanical properties compared to 1-3 composites of PZT rods with epoxy. In addition, the Burps composites are much easier to prepare.

The present study focuses on composites with 3-1 and 3-2 connectivity patterns, in which the PZT phase is self-connected in three dimensions and the polymer phase is self-connected in either one or two dimensions. Samples were prepared by drilling holes in sintered PZT blocks either in one direction (3-1 connectivity) or in two directions (3-2 connectivity) and backfilling the perforated PZT blocks with a suitable polymer. Enhancement of d_h was anticipated in these composites because of the modified stress distribution within the composite.

2. SAMPLE PREPARATION

PZT-polymer composites were prepared by drilling holes in sintered PZT blocks and filling the

[†] Also affiliated with the Department of Electrical Engineering.

TABLE I

Piezoelectric Properties of PZT-Polymer Composites

	\bar{K}_{33}	\bar{d}_h (PCN ⁻¹)	\bar{g}_h (10 ⁻³ VmN ⁻¹)	$\bar{d}_h\bar{g}_h$ (10 ⁻¹⁵ m ² N ⁻¹)	Reference
PZT	1600	50	4	200	Present work
PZT particles in silicone rubber matrix (0-3 connectivity)	100	28.3	32	900	4
PZT replamine in a silicone rubber matrix (3-3 connectivity)	50	35.8	80	2800	2
PZT rods in an epoxy matrix (1-3 connectivity)	200	77.6	40.4	3138	5
PZT rods in a polyurethane matrix (1-3 connectivity)	83	176.2	239	42100	5
Burps composite (epoxy matrix) (3-3 connectivity)	500	120	27	3200	3
Burps composite (silicone rubber matrix (3-3 connectivity)	300	260	100	26000	3

perforated block with a polymer. To prepare the ceramic, 95 wt% of PZT 501A† was mixed with 5 wt% of 15% PVA solution. After mixing and drying the powder, square pellets measuring 2 cm on edge and 4 to 8 mm thick, were pressed at 20,000 psi (140 MPa). The pellets were placed on a platinum sheet and the binder was burned out at 550°C for one hour. Sintering was carried out in a sealed alumina crucible using a silicon carbide resistance furnace at a heating rate of 200°C per hour, with a soak period of one hour at 1285°C. A PbO-rich atmosphere was maintained with sacrificial ceramic pellets of composition 97 mole% PZT and 3 mole% PbO inside the crucible.⁹ After firing, the samples were polished and cut into smaller pieces of various dimensions. Air-dried silver paste electrodes‡ were applied to the pellets. Poling was done in a stirred oil bath at 140°C at a field of 25 KV/cm for three minutes. After poling, three or four holes were drilled perpendicular to the poling direction using an ultrasonic cutter.§ Samples were prepared with different hole sizes and hole separation X (Figure 8a). The drilled samples were then placed in a small plastic tube and a commercial polymer (vinylcyclohexene dioxide-epoxy||) was poured into the tube. The epoxy was cured

at 70°C for eight hours. Finally, the composites were polished on silicon carbide paper to expose the PZT and to ensure that the faces of the disk were smooth and parallel. Electrodes of air-dried silver paste were applied and the composites were aged for at least 24 hours prior to any measurement. Some of the 3-1 and 3-2 composites are shown in Figure 1.

3. MEASUREMENTS

The dielectric constants and loss factors of all the samples were measured at a frequency of 1 KHz using an automated capacitance bridge.¶ The piezoelectric coefficient \bar{d}_{33} along the poling direction was measured using a d_{33} meter.†† The hydrostatic piezoelectric \bar{d}_h was measured by a pseudo-static method.⁵ Samples were immersed in an oil-filled cylinder, and pressure was applied at a rate of 3.5 MPa/sec. The resulting charge was collected with a Keithley electrometer‡‡ operated in a feedback charge integration mode. The piezoelectric voltage coefficients $\bar{g}_{33} = \bar{d}_{33}/\epsilon_0\bar{K}_{33}$ and $\bar{g}_h = \bar{d}_h/\epsilon_0\bar{K}_{33}$ were calculated from the measured values of \bar{d}_{33} , \bar{d}_h and \bar{K}_{33} .

† Ultrasonic Powders, Inc., South Plainfield, NJ (PZT 501A).

‡ Materials for Electronics, Inc., Jamaica, NY. Demetron 200.

§ Sheffield Ultrasonic Machine Tool, Dayton OH.

|| Spurr's low viscosity embedding media, No. 5135, Poly-science Inc., Warrington, PA, 18976.

¶ Hewlett Packard (Model 4270A) Automated Capacitance Bridge, Hewlett Packard, 1-59-1 Yoyogi, Tokyo, Japan 151.

†† Berlincourt (Model 333) d_{33} meter, Channel Product, Inc., 16722 Park Circle Drive, Chagrin Falls, OH, 44020.

‡‡ Keithley (Model 616) Digital Electrometer, Keithley Instruments, Inc., Cleveland, OH.

PERFORATED PZT POLYMER COMPOSITES

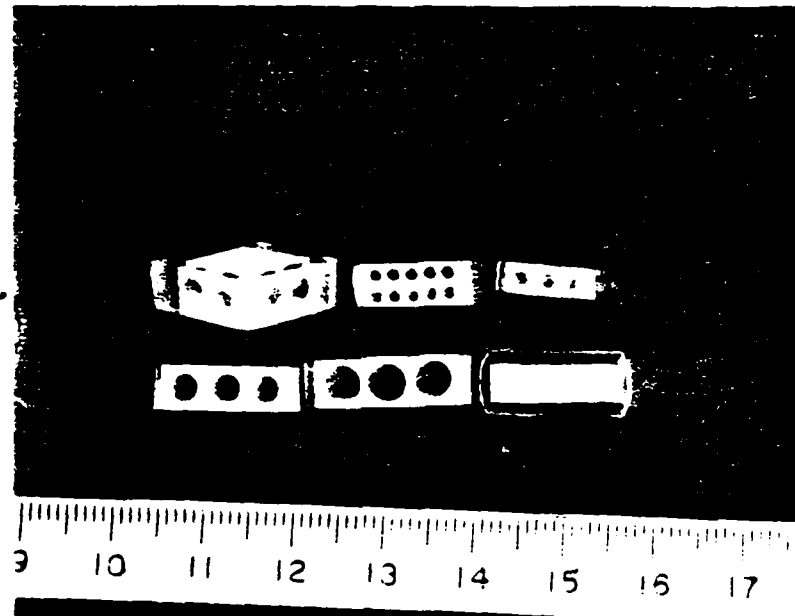


FIGURE 1.

4. RESULTS AND DISCUSSION

Unless otherwise stated, the results refer to composites with 3-1 connectivity. The dielectric constants for 3-1 composites are plotted in Figures 2 and 3 as a function of X (the center-to-center distance for adjacent holes) for two different hole sizes. The dielectric constant increases linearly with X at lower values of X , but reaches a saturation value for higher values. Composites with smaller thicknesses have lower dielectric constants. Also, it is observed that for the same D/t (diameter to thickness ratio), composites with smaller diameter holes have higher dielectric constants than composites with larger holes (see Figures 2 and 3). Dielectric constants of 3-2 composites were much lower than the 3-1 composites for samples with identical hole sizes (Table II). Calculated values of dielectric constants are also plotted in Figures 2 and 3 for comparison.

The values of d_{33} were used as a measure of the degree of poling. Measured values of d_{33} for 3-1 composites are plotted as a function of X in Figure 4. It is observed that d_{33} increases linearly with X at lower values of X , but approaches a saturation value at higher values of X . Each of the data points represents the average of at least twelve

value measurements at different places on the electroded surface of the composites. The measured values of d_{33} in the regions over the holes were about 10% lower than the d_{33} values in solid regions (Figure 8a). It is significant that the d_{33} values for most of the composites exceed 300 pC/N, which is close to the d_{33} coefficients of solid PZT (400 pC/N). It is found that in all composites d_{33} decreases slightly with thickness. Also, composites with smaller hole sizes had larger d_{33} coefficients than composites with larger hole sizes. In all 3-2 composites the measured d_{33} values were also higher than 300 pC/N (Table I).

In Figure 5 the hydrostatic piezoelectric coefficient (d_h) of 3-1 composites is plotted as a function of X for different thicknesses. A broad maximum is observed for X values between 4 and 4.5 mm for composites containing 60% to 70% PZT by volume. Figure 6 shows d_h plotted as a function of thickness for composites with different X . Again it is found that d_h increases with thickness, up to certain thickness, and then decreases. Figure 7 shows the effect of poling on the values of d_h , when poling is carried out at several different stages in the process:

1. Poling PZT block before drilling the holes.

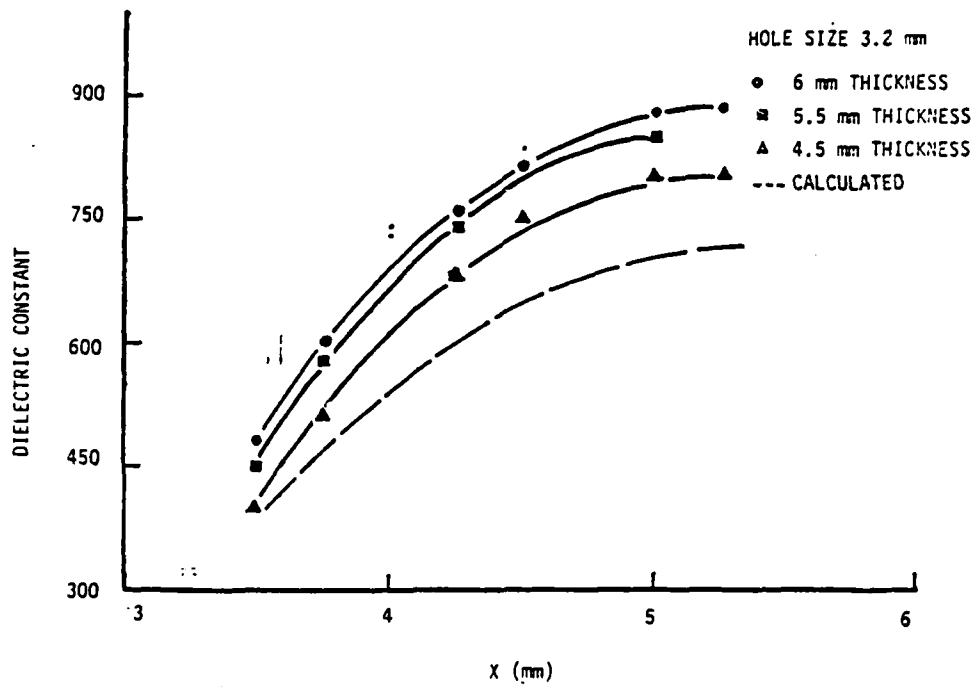


FIGURE 2.

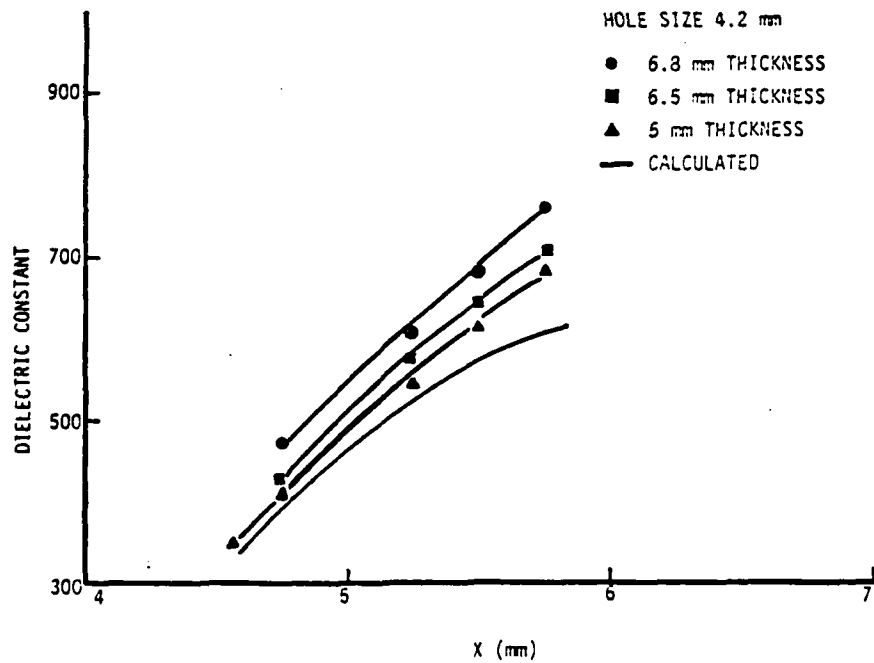


FIGURE 3.

PERFORATED PZT POLYMER COMPOSITES

TABLE II

	Hole Size (mm)	Composite Thickness (mm)	X (mm)	\bar{K}_{33}	\bar{d}_{33} (PCN ⁻¹)	\bar{g}_{33} (10 ⁻¹ VmN ⁻¹)	\bar{d}_h (PCN ⁻¹)	\bar{g}_h (10 ⁻¹ VmN ⁻¹)	$\bar{d}_h \bar{g}_h$ (10 ⁻¹⁵ M ² N ⁻¹)
Perforated PZT/epoxy (3-1 connectivity)	3.2	6.5	4.25	810	340	47	210	29	6000
Perforated PZT/epoxy (3-1 connectivity)	3.2	6	4.25	760	350	52	230	34	7800
Perforated PZT/epoxy (3-1 connectivity)	3.2	5.5	4.25	740	330	50	200	30	6000
Perforated PZT/epoxy (3-1 connectivity)	3.2	4.5	4.25	680	320	53	190	31	5900
Perforated PZT/epoxy (3-1 connectivity)	4.2	6.8	4.75	470	290	70	190	46	8600
Perforated PZT/epoxy (3-1 connectivity)	4.2	6.5	4.75	450	290	73	222	56	12300
Perforated PZT/epoxy (3-1 connectivity)	4.2	6	4.75	425	280	74	170	45	7600
Perforated PZT/epoxy (3-1 connectivity)	4.2	5.5	4.75	410	275	76	120	33	3950
Perforated PZT/epoxy (3-2 connectivity)	3.2	6.7	4.5	360	290	90	238	74	17600
Perforated PZT/epoxy (3-2 connectivity)	3.2	6.2	4.5	330	290	99	294	100	29000
Perforated PZT/epoxy (3-2 connectivity)	3.2	6	4.5	320	300	105	322	113	36300
Perforated PZT/epoxy (3-2 connectivity)	3.2	5.8	4.5	290	290	114	329	128	42000
Perforated hollow PZT sealed with polymer (3-2 connectivity)	3.2	6.2	4.5	340	340	112	372	123	45700

2. Poling the perforated PZT before filling it with epoxy.

3. Poling after embedding the perforated PZT block with epoxy.

From these experiments it was concluded that to get higher values of \bar{d}_h it is necessary to prepole the PZT blocks before drilling.

It should be emphasized that for all composites, the \bar{d}_h coefficients are at least twice that of solid PZT (50 pC/N). Hydrostatic coefficients for the 3-2 composites are much larger than those of 3-1 composites. An even higher value of \bar{d}_h was observed when measurements were made on perforated blocks of PZT in which the open sides were enclosed with a thin polymer sheet, thereby keeping the inside region completely empty. When measured in this way a \bar{d}_h value of nine times greater than that of solid PZT was observed (Table II).

Some typical values of \bar{K}_{33} , \bar{d}_{33} , and \bar{d}_h are given in Table II. It is important to note that \bar{d}_h depends markedly on the thickness of the PZT region above and below the holes (see Figure 8a). There

is a critical thickness ~~for~~ of which \bar{d}_h becomes a maximum (Table II).

Piezoelectric voltage coefficients \bar{g}_{33} and \bar{g}_h are also substantially larger than those of solid PZT. As shown in Table II, the piezoelectric voltage coefficients \bar{g}_{33} and the hydrostatic voltage coefficients \bar{g}_h are very large for 3-2 composites. The $\bar{d}_h \bar{g}_h$ product used as a figure of merit for hydrostatic applications is more than 200 times the corresponding value for solid PZT.

5. THEORETICAL MODEL

The physical properties of 3-1 composites can be approximated with the model illustrated in Figure 8. For simplicity, consider a square of length l whose area is equal to that of a circle with radius r . Then $l = r\sqrt{\pi}$.

We can visualize the 3-1 composite as made up of two parts A and B connected in parallel as shown in Figure 8b. Part B is composed of two phases connected in series, PZT and polymer. The

A. SAFARI *et al.*

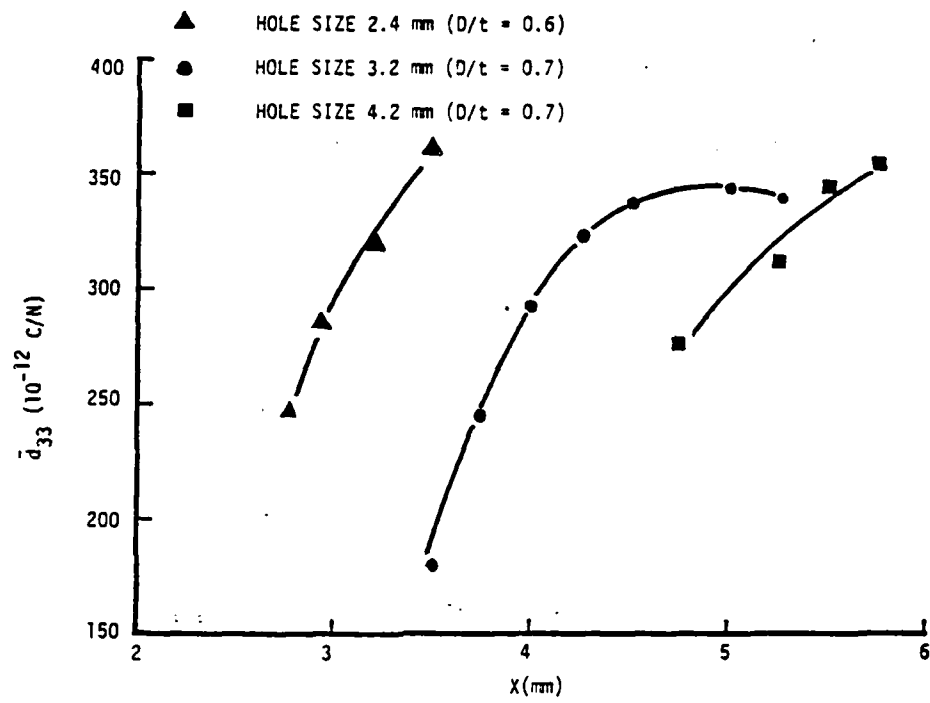


FIGURE 4.

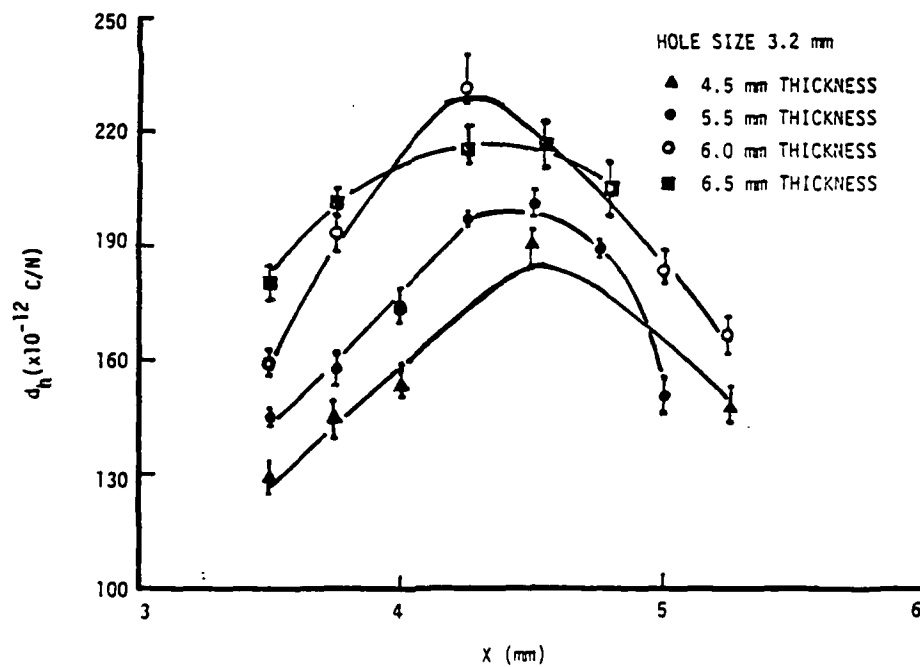


FIGURE 5.

PERFORATED PZT POLYMER COMPOSITES

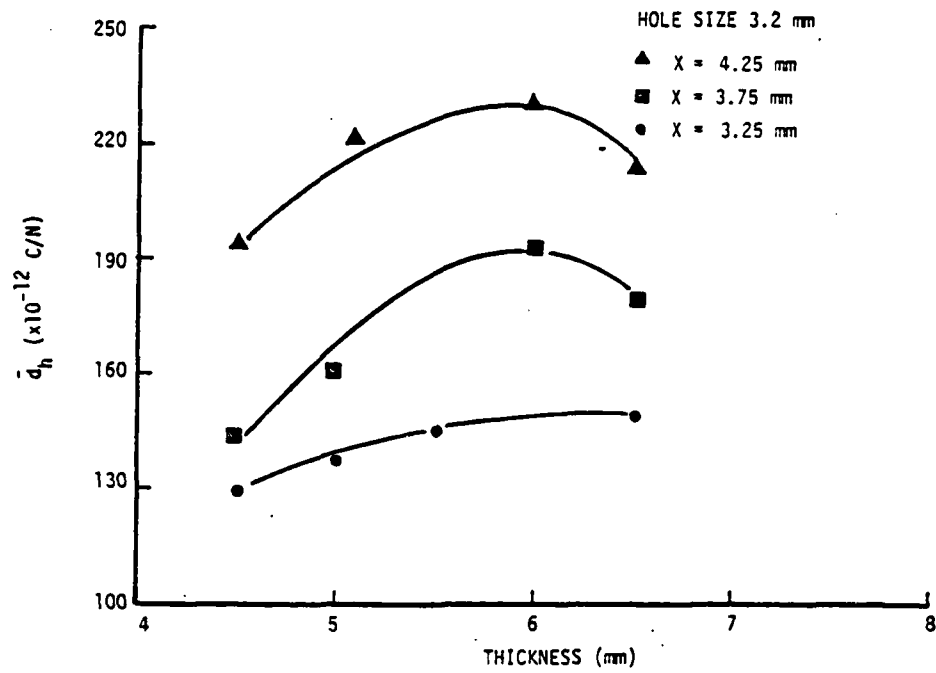


FIGURE 6.

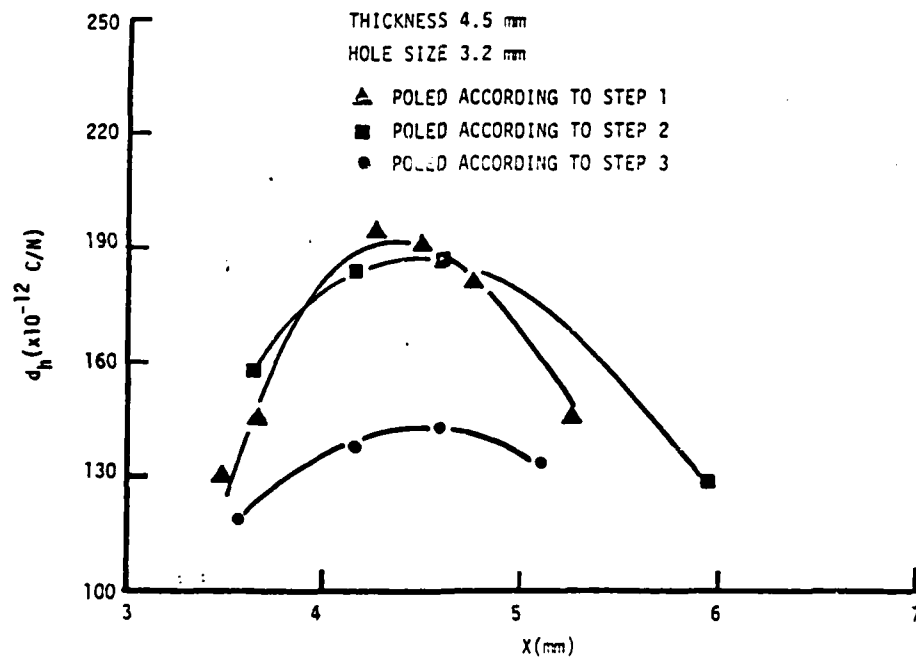


FIGURE 7.

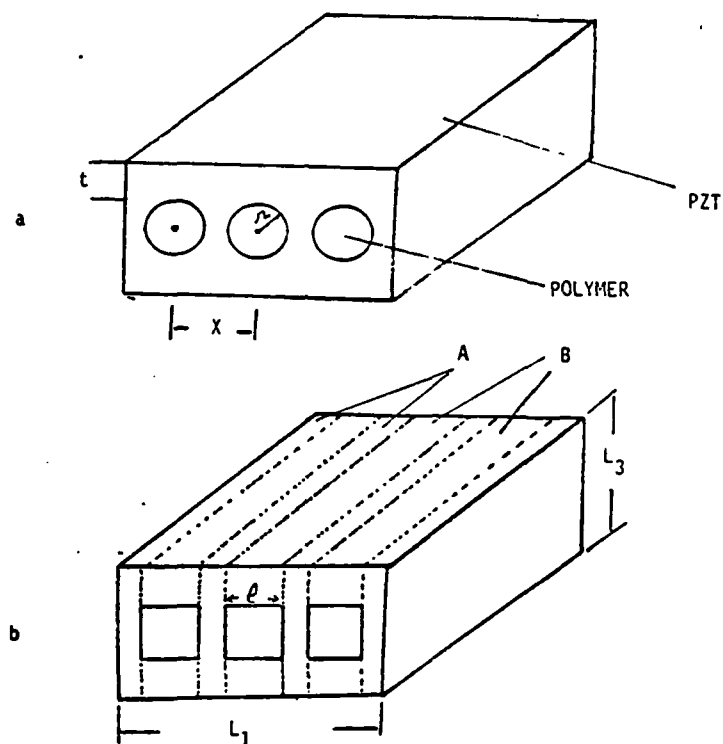


FIGURE 8.

following quantities can be defined with respect to the dimensions of the composites.

$$V_A \quad (\text{volume fraction of PZT of part A}) = (L_1 - nl)/L_1$$

$$V_B \quad (\text{volume fraction of part B}) = nl/L_1$$

$$V_{B1} \quad (\text{volume fraction of PZT in part B}) = (L_3 - l)/L_3$$

$$V_{B2} \quad (\text{volume fraction of polymer in part B}) = l/L_3$$

where L_1 and L_3 are length and thickness of composite and n is the number of holes.

5.1 Dielectric Constant

The component of the dielectric constant of interest is K_{33} , since the electrode surfaces are perpendicular to the poling direction. In the notation used here, K_{33} is the dielectric constant of the composite, ${}^A K_{33}$ the dielectric constant of PZT, ${}^B K_{33}$ that

of the polymer, and ${}^{B1} K_{33}$ is the dielectric constant of part B. Since part A and part B are in parallel connection,

$$\bar{K}_{33} = V_A {}^A K_{33} + V_B {}^B K_{33}$$

Because PZT and polymer in part B are in series connection we can apply series model:

$$\frac{1}{\bar{K}_{33}} = \frac{V_{B1}}{V_B} \frac{1}{{}^{B1} K_{33}} + \frac{V_{B2}}{V_B} \frac{1}{{}^{B2} K_{33}}$$

Using these relations we can calculate \bar{K}_{33} of composites. Since ${}^A K_{33} = 1600$ and ${}^B K_{33} = 5$, most of the contribution to \bar{K}_{33} comes from part A, which is PZT. Calculated values are plotted in Figures 2 and 3. In general, the measured dielectric constants are somewhat higher than the predicted values. This may be due to the approximations involved in the above calculations. The contribution to the dielectric constant from part B may be much higher than that assumed above because of the bending of the flux lines around the holes containing the polymer.

PERFORATED PZT POLYMER COMPOSITES

5.2 Piezoelectric Coefficients

The longitudinal coefficient \bar{d}_{33} relates the polarization component P_3 to stress component σ_3 by the following relation: $P_3 = \bar{d}_{33}\sigma_3$. As stated earlier, the \bar{d}_{33} values of 3-1 composites are slightly smaller than that of solid PZT. In a composite most of the stresses are borne by the ceramic, and if the stress transfer to the vertical columns (section A, Figure 8b) is complete, the \bar{d}_{33} of the composite should be equal to the value of d_{33} for PZT. But because of the curved shapes around the perforations, the stress distribution in the composite is not as simple as the model predicts. Horizontal components of stress are produced which lower the \bar{d}_{33} coefficient.

The hydrostatic coefficient of the composite is given by the relation $\bar{d}_h = \bar{d}_{33} + 2\bar{d}_{31}$. In a solid PZT ceramic, the value of d_h is low due to the fact that $d_{33} \approx -2d_{31}$. In the 3-1 composites the arc-like geometry of the composite results in mechanically stiffened electrodes which transfer the horizontal stress pattern, significantly lowering \bar{d}_{31} , and enhancing \bar{d}_h . The fact that in some of the 3-1 and 3-2 composites $\bar{d}_h \approx \bar{d}_{33}$ clearly indicates that \bar{d}_{31} is almost zero in some cases.

SUMMARY

A simple technique for fabricating PZT polymer composites with 3-1 and 3-2 connectivity patterns has been proposed. These composites exhibit better piezoelectric properties than the previously

studied PZT polymer composites with different types of connectivity patterns. For 3-2 composites the K_{33} , \bar{d}_h , \bar{g}_h , and $\bar{d}_h\bar{g}_h$ values are 300, 370×10^{-12} C/N, 123×10^{-3} Vm/N and $45,000 \times 10^{-15}$ m²/N respectively.

ACKNOWLEDGEMENT

This work was sponsored by the Office of Naval Research through Contract No. N00014-78-C-0291. We also wish to thank Mr. Arvind Halliyal and our other colleagues at the Materials Research Laboratory.

REFERENCES

1. R. E. Newnham, D. P. Skinner and L. E. Cross, *Mat. Res. Bull.*, **1B**, 525 (1978).
2. D. P. Skinner, R. E. Newnham and L. E. Cross, *Mat. Res. Bull.*, **13**, 599 (1978).
3. K. Rittenmyer, T. Shrout, W. A. Schulze and R. E. Newnham, *Ferroelectrics* (accepted).
4. W. B. Harrison, Proc. Workshop on Sonar Transducer Materials, Naval Research Laboratory (Feb. 1976).
5. K. A. Klicker, Ph.D. Thesis, Solid State Science, The Pennsylvania State University (1980).
6. T. R. Shrout, L. J. Bowen and W. A. Schulze, *Mat. Res. Bull.*, **15**, 1371 (1980).
7. R. E. Newnham, L. J. Bowen, K. A. Klicker and L. E. Cross, *Int. J. Mat. in Eng.*, **2**, 93 (1980).
8. K. A. Klicker, J. V. Biggers and R. E. Newnham, *J. Amer. Ceram. Soc.*, **64**, 5 (1981).
9. K. A. Klicker, Control of PbO Partial Pressure During the Sintering of PZT Ceramic, M. S. Thesis, The Pennsylvania State University (1979).
10. J. F. Nye, *Physical Properties of Crystal*, Oxford University Press, London (1957).

APPENDIX 6

Piezoelectric 3-3 Composites

PIEZOELECTRIC 3-3 COMPOSITES

K. RITTENMYER, T. SHROUT, W. A. SCHULZE and R. E. NEWNHAM

*Materials Research Laboratory, The Pennsylvania State University,
University Park, Pennsylvania 16802, U.S.A.*

(Received February 4, 1981)

Piezoelectric composites of PZT and polymers were prepared by mixing tiny plastic spheres with PZT powder in an organic binder and firing the mixture to give a ceramic skeleton. After cooling, the skeleton was back-filled with polymer and poled. Dielectric and piezoelectric properties were measured on samples ranging from 30 to 70 volume % PZT, and compared with a rectangular skeleton model for 3-3 composites. Composites containing 50% PZT-50% silicone rubber appear especially useful for hydrophone applications with d_{33} products a hundred times larger than PZT.

INTRODUCTION

In a 3-3 composite,¹ each of the constituent phases is continuously self-connected in three dimensions to give two interlocking skeletons in intimate contact with one another. This type of structure is exhibited by certain polymer foams, by some phase-separated metals and glasses, by three-dimensional weaves, and by natural substances such as wood and coral. The piezoelectric and pyroelectric properties of 3-3 composites have been investigated recently with some rather remarkable results.²⁻⁶ For certain coefficients, dramatic improvements can be made over the best single-phase piezoelectrics.

Piezoelectric ceramic-polymer composites with 3-3 connectivity were first made by Skinner² using a lost-wax method with coral as a starting material. Among the advantages of these composites are high hydrostatic sensitivity, low dielectric constant, low density for improved acoustic impedance matching with water, high compliance to provide damping, and the mechanical flexibility needed to develop conformable transducers. ShROUT³ has described a simpler method for fabricating a three-dimensionally interconnected lead zirconate-titanate (PZT) and polymer composite with properties similar to the coral-based composites. The simplified preparation method involves mixing plastic spheres and PZT powder in an organic binder. When carefully sintered, a porous PZT skeleton is formed, and later back-filled with polymer to form a 3-3 composite. This technique

is commonly referred to as the BURPS process, an acronym for burned-out plastic spheres. Since the process involves the generation and emission of gaseous hydrocarbons, the name BURPS is highly appropriate. The composites prepared by ShROUT³ contained a PZT/polymer volume ratio of 30/70. In this study, we report the electromechanical properties of 3-3 composites having a wide range of PZT/polymer ratios, and compare the results with other piezoelectric materials, including some recent Japanese work^{4,5} on similar composites. A three-dimensional skeleton model is proposed to explain the results.

EXPERIMENTAL PROCEDURE

Sample preparation

The 3-3 composites were made from commercially available PZT powder* mixed in a ball mill with tiny spheres of polymethyl methacrylate[†] (PMM) in PZT/PMM volume ratios of 30/70, 40/60, 50/50, 60/40, and 70/30. The PMM spheres ranged from 50 to 150 microns in diameter, and the PZT particles were about 1-4 microns in diameter. Four to eight weight percent of polyvinyl alcohol was added to the mixture as a bonding agent, and one inch diameter pellets were pressed

* Ultrasonic Powder PZT-501A, Ultrasonics Powders, Inc., 2383 S. Clinton Ave., South Plainfield, NJ 07080.

† Polysciences, Inc., Warrington, PA 18976.

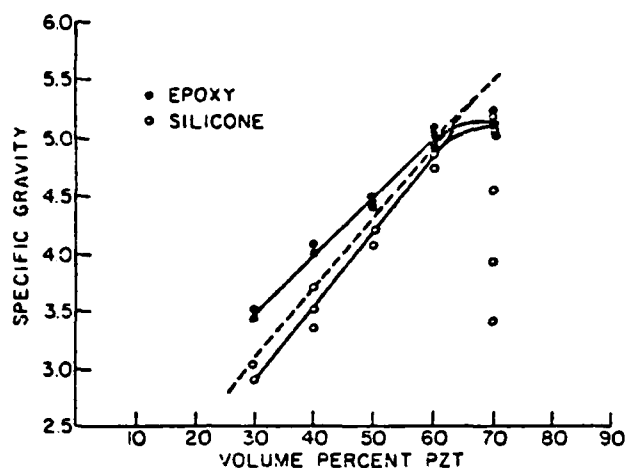


FIGURE 1. Specific gravity of 3-3 composites plotted as a function of volume fraction PZT in the starting mix. Composites filled with epoxy are denoted by solid circles, those with silicone rubber by open circles. The dashed line is the ideal density computed from the initial volume percent PZT.

at 10,000 psi. The pellets were heated over a 48-hour period to 450°C in order to volatilize the PMM spheres; a slow heating rate is necessary to prevent excessive cracking. The samples were then placed on a platinum sheet in high purity aluminum crucibles and sintered in a silicon carbide resistance furnace at a heating rate of 200°C per hour, with a soak period of 30 minutes at 1340°C. A lead-rich atmosphere was maintained during sintering by placing powdered lead zirconate near the PZT samples. After firing, the samples were impregnated with either a stiff vinylcyclohexene dioxide epoxy† or a high-purity soft silicone elastomer.‡ Finally, the samples were polished on silicon carbide paper to ensure that the faces of the disk were parallel and smooth. Electrodes of air-dry silver were applied and the samples poled for two minutes in a stirred oil bath at 80°C with fields of 20–25 kv/cm. The composites were aged for at least twenty-four hours before measurements were taken.

Characterization

The density of the composites was computed from the mass and the measured volume of each disk. This procedure was performed prior to electroding

to avoid including the silver in the measurement. In Figure 1, the measured densities are plotted as a function of the nominal volume percent PZT. The relationship is essentially linear for both types of composites. As expected, the epoxy samples are slightly denser than the silicone rubber samples because epoxy wets the surface of PZT extremely well and densifies the samples. Incomplete back-filling in high volume percent PZT samples causes a noticeable scatter in the values. These density variations affect all subsequent measurements.

Figures 2a and 2b show micrographs at two different magnifications of a polished surface of a composite made from 50/50 volume ratio. The samples are poled in the vertical direction, as indicated in Figure 2a. At lower magnification (Figure 2b, 55X) the material appears reasonably homogeneous. Figure 2c shows a 30/70 PZT/polymer composite in which the PZT is only slightly interconnected. A certain amount of interconnectedness is, of course necessary for electric poling, but to minimize the density and dielectric permittivity, the PZT content should be as low as possible.

In all the sections examined the PZT regions range from a few microns to about 100 μm . The same is true of the polymer regions. The microstructure shows visible cracks in the PZT regions perpendicular to the poling direction. This has an important effect on the dielectric permittivity of the sample, as discussed later. Since microstruc-

† Spurr's Low-Viscosity Embedding Media, No. 5135, Polysciences, Inc., Warrington, PA 15976.

‡ Dow Corning MDX-44210, Dow Corning Medical Products, Midland, MI 48640.

PIEZOELECTRIC 3-3 COMPOSITES

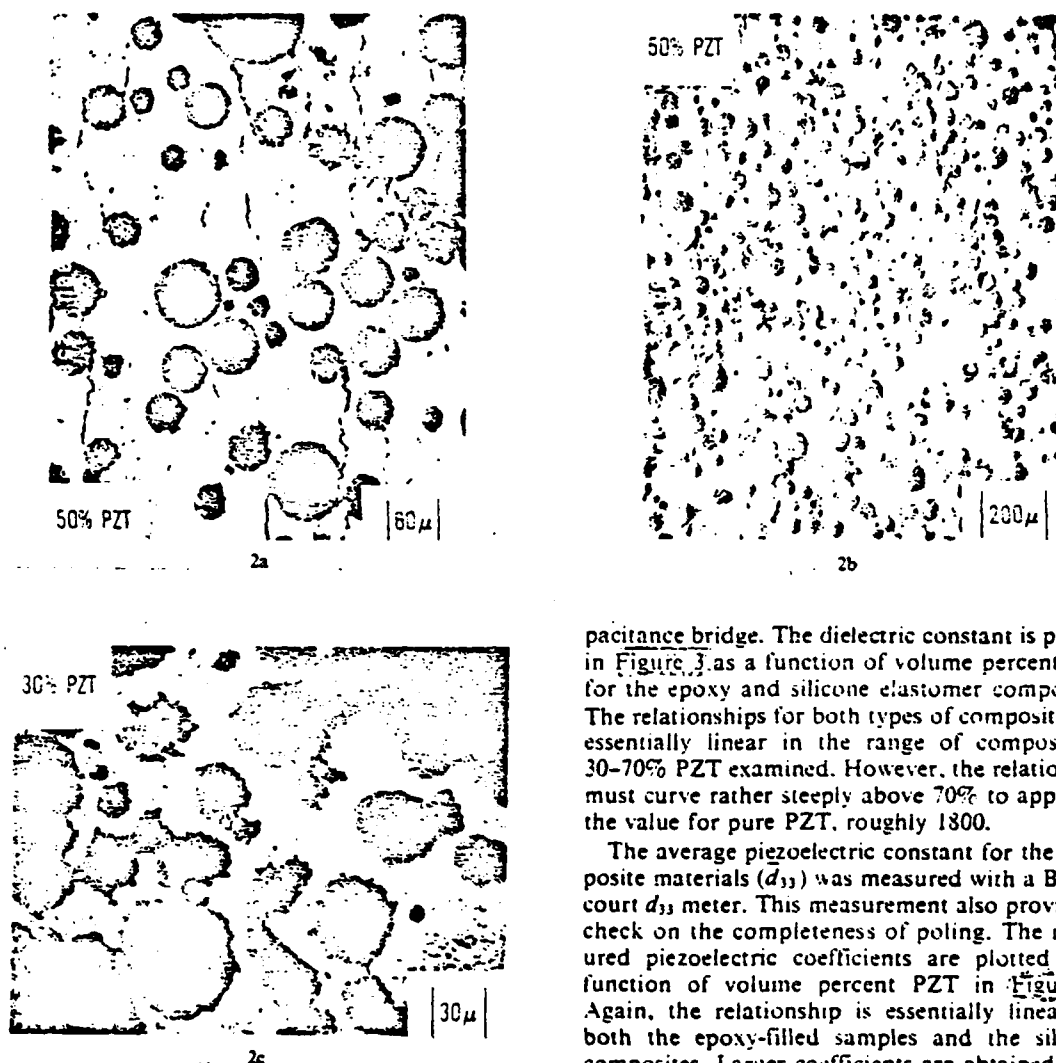


FIGURE 2 SEM micrographs of 3-3 composites (a and b) filled with 50% polymer and (c) with 30% polymer. Note the horizontal fracture lines in (a) introduced during poling.

ture of these samples is on a finer scale than many other composites, more homogeneous electromechanical properties can be expected, which is advantageous for high frequency applications.

Measurements

The dielectric permittivity and loss were measured at a frequency of 1 kHz using an automated ca-

pacitance bridge. The dielectric constant is plotted in Figure 3 as a function of volume percent PZT for the epoxy and silicone elastomer composites. The relationships for both types of composites are essentially linear in the range of compositions 30-70% PZT examined. However, the relationship must curve rather steeply above 70% to approach the value for pure PZT, roughly 1800.

The average piezoelectric constant for the composite materials (d_{33}) was measured with a Berlincourt d_{33} meter. This measurement also provides a check on the completeness of poling. The measured piezoelectric coefficients are plotted as a function of volume percent PZT in Figure 4. Again, the relationship is essentially linear for both the epoxy-filled samples and the silicone composites. Larger coefficients are obtained from the silicone specimens, perhaps because of their high elastic compliance which promotes stress transfer to the PZT. The d_{33} coefficient of solid PZT 501A is approximately 400 pC/N. Hydrostatic piezoelectric coefficients (d_h) were measured by a pseudostatic method. Pressure was applied in an oil-filled cylinder at a rate of 500 psi/sec. and the resulting charge was collected with a Keithley Electrometer operated in a feedback charge-integration mode. Figure 5 shows d_h plotted as a function of volume percent PZT. A broad maximum is observed in the 50-70% PZT composition range. Hydrostatic coefficients for the silicone

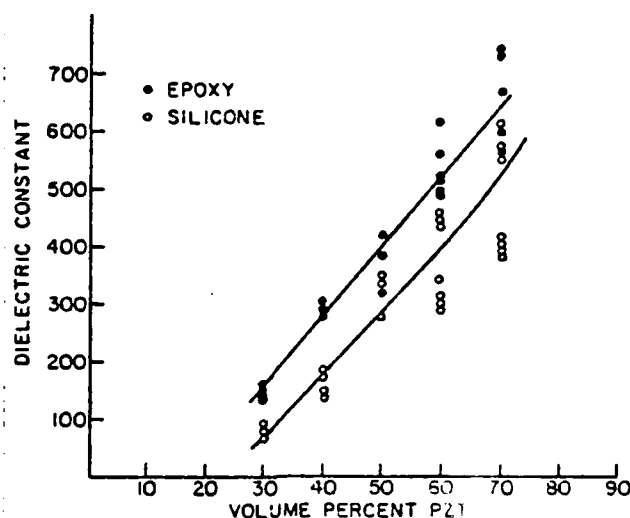
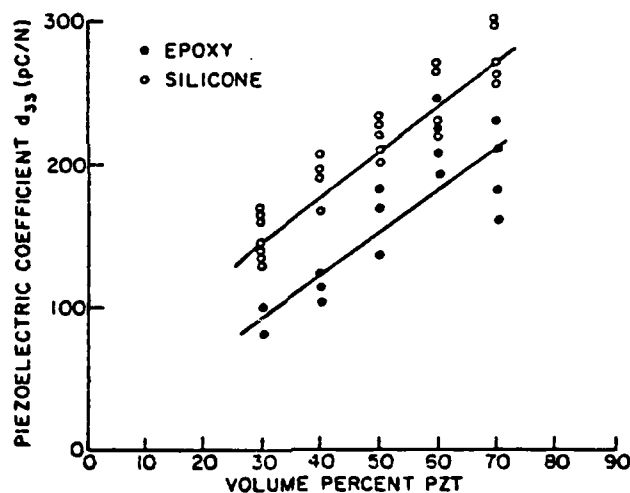


FIGURE 3 Dielectric constant of PZT-polymer composites plotted as a function of volume percent PZT.

FIGURE 4 Longitudinal piezoelectric coefficient \bar{d}_{33} for PZT-polymer composites with 3-3 connectivity.

composites are about twice as large as epoxy composites of the same volume fraction PZT and up to five times larger than the d_h value of PZT (~ 50 pC/N).

The piezoelectric voltage coefficients g_{33} and g_h are also substantially larger than those of solid PZT because the composites have much lower dielectric constants. A composite containing 30% PZT and 70% silicone elastomer has a \bar{g}_{33}

($=\bar{d}_{33}/\bar{K}_{33}\epsilon_0$) coefficient of about 200×10^{-3} Vm/N compared to 25×10^{-3} for the solid ceramic. For hydrostatic conditions, $\bar{g}_h(=\bar{d}_h/\bar{K}_{33}\epsilon_0)$ is about 100×10^{-3} for many of the silicone rubber composites, while that of solid PZT is only 3×10^{-3} . Epoxy composites have somewhat smaller voltage coefficients than those made with silicone elastomer. The hydrostatic figure of merit ($d_h g_h$) for hydrophone applications is

PIEZOELECTRIC 3-3 COMPOSITES

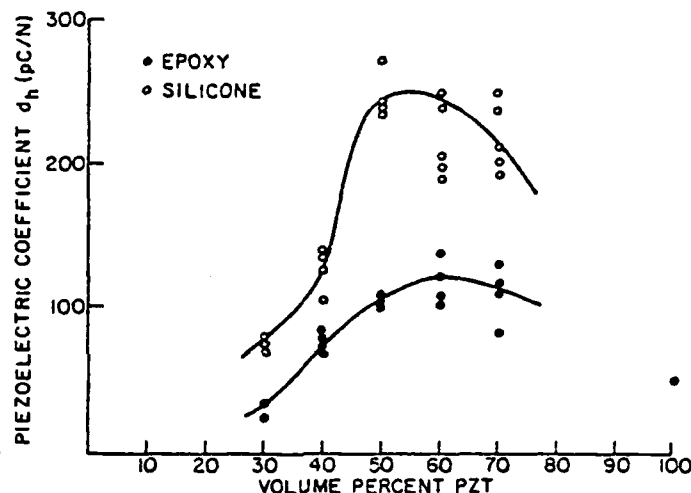


FIGURE 5 Hydrostatic piezoelectric coefficient \bar{d}_h for PZT-polymer composites.

largest for PZT-silicone rubber composites containing 50% PZT. For these samples \bar{d}_h exceeds 2×10^{-11} C/Vm/N, more than a hundred times larger than solid PZT ceramics.

The results compare favorably with measurements on similar materials. Using the same technique described in this paper, Shrout¹ previously prepared a number of PZT-polymer composites containing 30 volume percent PZT. The PZT-silicone rubber samples had dielectric constants between 40 and 200, \bar{d}_{33} values in the range $80-240 \times 10^{-12}$ C/N, and \bar{g}_A values of $50-70 \times 10^{-3}$ Vm/N. Piezoelectric coefficients for PZT-epoxy composites were somewhat smaller: \bar{d}_{33} $60-110 \times 10^{-12}$ and \bar{g}_A about 40×10^{-3} . Porous interconnected PZT-silicone rubber samples prepared by Nagata and co-workers⁴ gave $\bar{g}_{33} = 130 \times 10^{-3}$ Vm/N. These composites contained 48 volume % PZT. The ladder-type composites reported by Miyashita and co-workers⁵ gave slightly lower values of 90×10^{-3} for \bar{g}_{33} .

THEORETICAL MODEL

The physical properties of 3-3 composites can be described with the cubic array illustrated in Figure 6. The model consists of intersecting rectangular columns of PZT arranged in three perpendicular directions and embedded in a polymer matrix. For simplicity, it is assumed that one set of columns is parallel to the poling direction (X_3).

and that this set of columns are fully poled, while those in the perpendicular directions along X_1 and X_2 are unpoled.

Berlincourt⁷ used a similar model to explain the piezoelectric properties of PZT sponge, a porous ceramic made by Clevite Corporation about twenty years ago. The sponge was 3-3 structure made from a slurry of PZT, water, and soapsuds, but it was difficult to back-fill, and therefore composites were not prepared.

In one "unit cell" of the cubic array, there are four kinds of PZT blocks: (i) rectangular blocks parallel to X_1 , (ii) rectangular blocks parallel to X_2 , (iii) rectangular blocks parallel to X_3 , and (iv) cubic blocks at the intersections. The cubic lattice contains equal number of the four types. If the

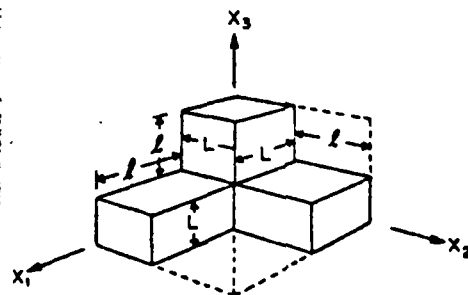


FIGURE 6 The repeat unit of a cubic skeleton used to model the dielectric and piezoelectric properties of 3-3 composites.

length of the rectangular blocks is l , and the width L , then the volume of the rectangular blocks is L^2l and that of the cubic blocks L^3 . In one unit cell of the cubic array, the volume of PZT is $L^3 + 3L^2l$, and the volume fraction PZT is

$$v = \frac{L^3 + 3L^2l}{(L + l)^3} \quad (1)$$

The remainder of the volume is filled with polymer.

Dielectric constants

The dielectric constant of interest is \bar{K}_{33} since the electrode surfaces are perpendicular to X_3 . In the notation used here, \bar{K}_{33} is the dielectric constant of the composite, ${}^1\bar{K}_{33}$ is the dielectric constant of PZT, and ${}^2\bar{K}_{33}$ is that of the polymer. Since ${}^1\bar{K}_{33} \gg {}^2\bar{K}_{33}$, the dielectric properties of PZT tend to dominate the calculations. The rectangular blocks parallel to X_3 , together with the cubic blocks, contribute most to \bar{K}_{33} . The blocks parallel to X_1 and X_2 are connected in series with polymer and therefore contribute relatively little.

For a unit cube ($L + l = 1$), the dielectric constant is approximately

$$\bar{K}_{33} \approx {}^1\bar{K}_{33} L^2 \quad (2)$$

where L is the width of the rectangular blocks (Figure 6), expressed in cell fractions. This assumes that the permittivity of PZT (${}^1K \sim 1800$) is far larger than that of the polymer (${}^2K \sim 10$). Using the relationship between L , l , and v given in Eq. (1), the dielectric constant of the composite can be written as a function of the volume fraction PZT (v). This is plotted in Figure 7. The measured dielectric constants are lower than the predicted values. This may be due to deficiencies in the theoretical model, but the cracks caused by poling (see Figure 2a) undoubtedly contribute to the discrepancy. Since the cracks are oriented perpendicular to the poling direction, the material is essentially divided up into capacitive elements with air and PZT connected in series. Under these conditions, the permittivity drops rapidly with only a slight amount of fracture. Silicone rubber provides less mechanical support for the ceramic than does epoxy. This may explain why more cracking was observed in the silicone rubber com-

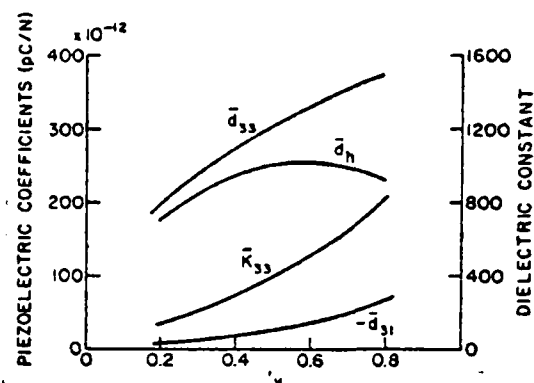


FIGURE 7 Piezoelectric and dielectric coefficients calculated from the cubic array model.

posites, and why they have lower dielectric constants.

The dielectric constant of a 3-3 composite decreases rapidly with increasing polymer content. For simple parallel connection, a linear relation between the dielectric constant and the volume fraction PZT is expected. For a cubic lattice model, the decrease is faster than linear, which is advantageous for the piezoelectric voltage coefficient. The reason for the rapid decrease is that much of the PZT is in series with polymer.

Piezoelectric coefficients

The longitudinal coefficient \bar{d}_{33} relates the polarization component P_3 to stress component σ_3 . For a composite, the magnitude of \bar{d}_{33} depends strongly on what fraction of the stress is borne by the piezoelectric element. Ideally, the stiff piezoelectric ceramic bears all the stress and the polymer none. For a perfect parallel connection

$$\bar{d}_{33} = \frac{{}^1v {}^1d_{33} {}^2s_{33} + {}^2v {}^2d_{33} {}^1s_{33}}{{}^1v {}^2s_{33} + {}^2v {}^1s_{33}} \quad (3)$$

where 1v and 2v are the respective volume fractions of PZT and polymer. Longitudinal compliances are denoted by ${}^1s_{33}$ and ${}^2s_{33}$, and the piezoelectric effect of the polymer is assumed to be zero ${}^2d_{33} = 0$.

Composites with 3-3 connectivity are partially in parallel and partially in series, and therefore Eq. (3) will not be accurate. Referring to Figure 6, the portion of PZT in parallel with the polymer

PIEZOELECTRIC 3-3 COMPOSITES

matrix consists of the cubic blocks together with the rectangular columns parallel to X_1 . This part of the PZT skeleton is assumed to be fully poled, and therefore piezoelectrically active. The rectangular blocks parallel to X_1 and X_2 are in series with polymer, and since they are unpoled, contribute nothing to the piezoelectric effect. Thus much of the PZT (approximately two-thirds for small fractions) is inactive, and the composite behaves as if it contains a much smaller volume fraction PZT. The formula for d_{31} can be rewritten as

$$\bar{d}_{31} = \frac{{}^1v^* {}^1d_{31} {}^2s_{33}^*}{{}^1v^* {}^2s_{33}^* + {}^2v^* {}^1s_{33}} \quad (4)$$

where ${}^1v^*$ is the volume fraction of active PZT and ${}^2v^*$ is the volume fraction of polymer loaded with inactive PZT. ${}^2s_{33}^*$ is the modified compliance of the polymer. The volume fraction of active PZT is

$${}^1v^* = \frac{L^3 + L^2l}{(L + l)^3} \quad (5)$$

where L and l are the dimensions referred to Figure 6. The loaded polymer volume fraction ${}^2v^* = 1 - {}^1v^*$. Elastic compliance coefficient ${}^2s_{33}^*$ is less than ${}^2s_{33}$, but is substantially larger than ${}^1s_{33}$, the compliance of pure PZT. In Figure 7, the value of \bar{d}_{31} is plotted as a function of 1v , the total volume fraction of PZT, assuming a value of 0.1 for ${}^1s_{33}/{}^2s_{33}$. If this ratio is very much smaller, \bar{d}_{31} is independent of 1v , reverting to the ideal parallel connection model.

Piezoelectric coefficient \bar{d}_{31} is more straightforward. Two parts of the PZT network are piezoelectric, the rectangular columns parallel to X_2 and the cubic blocks at the intersecting columns. Since stress component σ_1 is carried by the lateral rectangular columns, the stress is transmitted to the cubic blocks but not to the vertical columns.

Therefore only the cubic blocks contribute to \bar{d}_{31} :

$$\bar{d}_{31} = L^3 {}^1d_{31} / (L + l)^3.$$

In Figure 7, \bar{d}_{31} is plotted as a function of total volume fraction PZT. When 1v is large, the composite consists mainly of cubic intersections, and \bar{d}_{31} is large. When 1v is very small, the intersection cubes nearly disappear, and so does \bar{d}_{31} . The rapid decrease of \bar{d}_{31} with 1v is a strong contributing factor to the hydrostatic sensitivity.

The hydrostatic piezoelectric coefficient \bar{d}_h is obtained from $\bar{d}_{33} + 2\bar{d}_{31}$ and is plotted as a function of 1v in Figure 7. Note that \bar{d}_h goes through a broad maximum near the 50% composition, similar to the experimental values (Figure 5). In general the model gives good agreement with the experimental results.

ACKNOWLEDGEMENTS

We wish to thank our colleagues at the Materials Research Laboratory for their advice and encouragement. This work was supported by the Office of Naval Research through Contract No. N00014-78-C-0291.

REFERENCES

1. R. E. Newham, D. P. Skinner and L. E. Cross, *Mat. Res. Bull.*, 13, 525 (1978).
2. D. P. Skinner, R. E. Newham and L. E. Cross, *Mat. Res. Bull.*, 13, 599 (1978).
3. T. R. Shrout, W. A. Schulze and J. V. Biggers, *Mat. Res. Bull.*, 14, 1553 (1979).
4. K. Nagata, H. Igarashi, K. Okazaki and R. C. Bradt, *Jap. J. Appl. Phys.*, 19, L37 (1980).
5. M. Miyashita, K. Takano and T. Toda, *Ferroelectrics*, 28, 397 (1980).
6. R. E. Newham, D. P. Skinner, K. A. Klicker, A. S. Bhalla, B. Hardiman and T. R. Gururaja, *Ferroelectrics*, 27, 49-55 (1980).
7. D. Bertincourt, "Properties of Sponge Ceramic," Clevite Corporation Internal Report, December 1960.

APPENDIX 7

Ferroelectric Composites for Hydrophones

FERROELECTRIC COMPOSITES FOR HYDROPHONES

S.Y. Lynn, R.E. Newham, K.A. Klicker, K. Rittenmyer, A. Safari and W.A. Schulze
Materials Research Laboratory, The Pennsylvania State University, University Park,
PA 16802, USA

Abstract—Considerations of the influence of crystal symmetry, macrosymmetry, and inter-phase connectivity have been used to explore possible macrostructures of interest as piezoelectric composites. Based on these design considerations, polymer-ceramic composites have been fabricated with 3-3 phase connectivity by the replication of natural template structures such as coral, or by a simplified fabrication technique of mixing volatilizable plastic spheres and PZT powders. 1-3 or 2-3 composites were made by perforated method. Polymer-Ceramic composites with 3-1 phase connectivity were made by embedding PZT rods or PZT spheres in various polymers. A modified connectivity model with 3-1-0 phase connectivity was introduced to improve the Poisson contraction problem found in 3-1 composites. In 3-1-0 composites voids were introduced into the polymer matrix to form a third phase which is isolated. All types of composites have been studied and it is shown that they have slightly lower permittivity, greatly improved d_h and produce a much lighter material that can be adjusted to neutral buoyancy.

CONNECTIVITY

Connectivity is the key feature in designing the microstructure of PZT-polymer composites. Each phase in a composite may be self-connected in zero, one, two, or three dimensions. Using an orthogonal axis system, for diphasic composites, there are ten connectivities designated as 0-0, 1-0, 2-0, 3-0, 1-1, 2-1, 3-1, 2-2, 3-2, and 3-3. A 2-1 connectivity pattern, for example, has one phase self-connected in two dimensional layers, the other self-connected in one-dimensional chains or fibers. The connectivity patterns are not geometrically unique. In the case of a 2-1 pattern the fibers of the second phase might be perpendicular to the layers of the first phase or might be parallel to the layers.

PIEZOELECTRIC COMPOSITES WITH 3-3 CONNECTIVITY

There is considerable practical interest in developing low-density, compliant, flexible piezoelectric transducers. A low-density piezoelectric would have better acoustic coupling to water and have more easily adjusted buoyancy than the high-density PZT ceramics now used for hydrophones. A compliant material would have

Table 1 Hydrostatic Mode Materials

	density (gm/cm^3)	d_{33} ($\times 10^{-12}$ C/V)	ϵ_{33}	d_h ($\times 10^{-3}$ m/V)	$d_h d_{33}$ ($\times 10^{-15}$ C/V)
PZT	7.9	65.9	1500	-	180
REPLANTING 3-3 Composite	1.1	35.8	50	140	2800
EPOXY/PZT 3-1 Composite	1.37	39.7	97	69	6100
PZT/POLYURETHANE 3-1-0 Composite	0.39	176.2	83	239	42,100
SP/PZT/SPHERES 3-1-0 Composite	1.3	80	78	117	9360
RENEW/PZT/SPHERES 3-1-0 Composite	1.1	82.8	84	85	5338
RENEW/PZT/FOAM 3-1-0 Composite	0.9	132.4	73	206	27,100
1-3 EPOXY-PZT COMPOSITE	1.2	230	760	34	7800
2-3 EPOXY-PZT COMPOSITE	1.2	322	320	113	36,300

*Spore Low Viscosity Embedding media, Ernest F. Fullum, Inc., Schenectady, NY.
**E. B. Plastics, Lansing, MI 48909.

better resistance to mechanical shock than a conventional ceramic transducer and a large compliance would also suggest high damping, which is desirable in a passive device. The development of a piezoelectric material which exhibits this combination of properties may be carried out in basically two different ways: one is to look for a single phase material, the other is to design a composite material. One typical example of the former material is the development of PVF₂ (polyvinylidene fluoride). The latter will be discussed here.

PIEZOELECTRIC COMPOSITES WITH 3-3 CONNECTIVITY

3-3 PZT-polymer composites were investigated by Skinner et al². In a 3-3 material, both phases are continuously connected in all 3 dimensions. The 3-3 composite was fabricated with a replamine process using a coral template, and a high purity silicone rubber was chosen as the second phase. An extremely flexible piezoelectric composite was obtained by crushing the ceramic phase (PZT). The permittivity of this crushed 3-3 replamine composite was greatly reduced (to about 40), while the average longitudinal piezoelectric coefficient \bar{d}_{33} only reduced moderately (about 100 pC N^{-1}). Hence the average longitudinal piezoelectric voltage coefficient, $\bar{g}_{33} (= \bar{d}_{33} / \bar{\epsilon}_{33})$ of these flexible composites is approximately $300 \times 10^{-3} \text{ V m N}^{-1}$, which is fifteen times better than a homogeneous PZT transducer. Table 1 lists some of the properties measured. Because of the time-consuming procedure of the replamine process, an alternative fabrication process of the 3-3 composite was proposed by Shrout^{3,4}. This simplified fabrication technique involves the mixing of volatilizable plastic phase and PZT powders. SEM micrographs revealed that these composites have microstructure and properties similar to the replamine samples (Table 1). The principal advantage of this method is that it is readily adapted to mass production.

PIEZOELECTRIC COMPOSITES WITH 1-3 or 2-3 CONNECTIVITY

Perforated Polymer-PZT composites with 1-3 and 2-3 connectivity were studied by Safari⁵. These materials are similar to the 3-3 composites with the important difference in that they have solid planes of PZT perpendicular to the poling direction. This assumes that the electrode is rigid and most of the stress in the plane perpendicular to the polarization is applied to the active ceramic. The rigid electrode also stiffens the composite laterally and greatly reduces the d_{31} coupling to d_h .

The composites produced by drilling channels in conventionally prepared prepolarized ceramic. 1-3 has channels running along one axis while 2-3 also has orthogonal channels. The material is then filled and embedded in epoxy.

As with other composite forms the \bar{K}_{33} is reduced and \bar{d}_{33} remains high, yielding a much increased g_h and $d_h g_h$ product. Specific experimental parameters are listed for comparison on Table 1.

PIEZOELECTRIC COMPOSITES WITH 3-1 CONNECTIVITY

3-1 connectivity composite in which polymer phase is self-connected three dimensionally and the piezoelectric ceramic is self-connected one dimensionally was developed by Klicker⁶. In a 3-1 composite, PZT rods were embedded in a continuous polymer matrix. Under the idealized situation in which the polymer phase is far more compliant than PZT, the stress that falls on the polymer will transfer to the PZT rods. The stress amplification on the PZT phase along with the reduced permittivity will thus enhance the piezoelectric voltage coefficient. To provide a better understanding of piezoelectric composites, the following factors have been varied: volume fraction PZT, rod diameter, and sample thickness. Figure 1 shows the \bar{d}_{33} as function of volume percent PZT. For PZT volume percentages down to 40% the \bar{d}_{33} are comparable to the value of d_{33} for solid PZT. Below 40% PZT, the \bar{d}_{33} values of all the composites

FERROELECTRIC COMPOSITES FOR HYDROPHONES

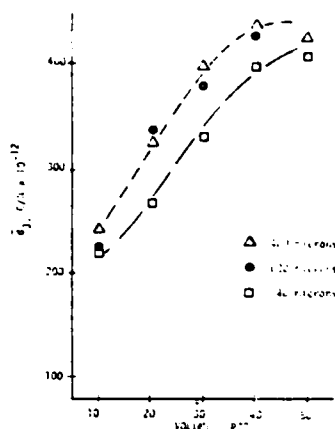


Fig.1 \bar{d}_{33} vs volume % PZT

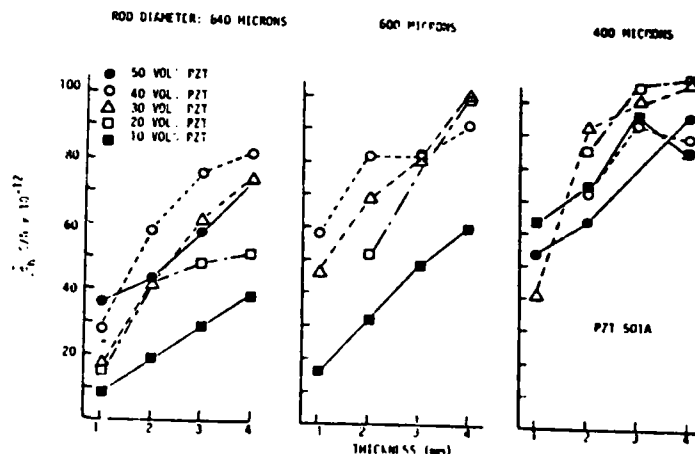


Fig.2 \bar{d}_h as function of volume % PZT, rod diameter and composite thickness.

decrease but it is significant that the \bar{d}_{33} of all the 10% composites is still greater than half the value for pure PZT. In Fig.2, \bar{d}_h is plotted as a function of composite thickness, rod diameter, and volume percent PZT. The composites, regardless of composite thickness, rod diameter, or volume percent PZT have a \bar{d}_h greater than that for solid PZT. The calculation of average relative permittivity, \bar{K}_{33} , uses parallel elements and the value of \bar{K}_{33} varies linearly with the volume fractions of the two phase present. Since the permittivity of polymer phase is extremely low (~ 7) compared to PZT (>1200), the value of \bar{K}_{33} may be approximated as $K_{PZT} \times \text{vol \% PZT}$. The experimental values of \bar{K}_{33} of composites agree with calculated levels (Fig.3). Since \bar{g}_h equals \bar{d}_h divided by $\bar{K}_{33} \cdot \epsilon_0$ constant or slightly decreasing values of \bar{d}_h with decrease

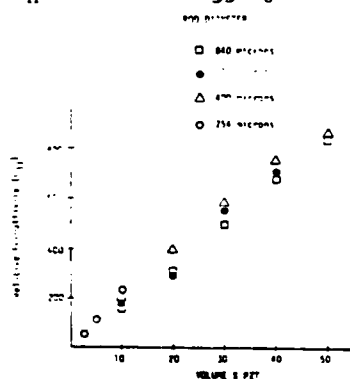


Fig.3 Relative permittivity as a function of volume % PZT.

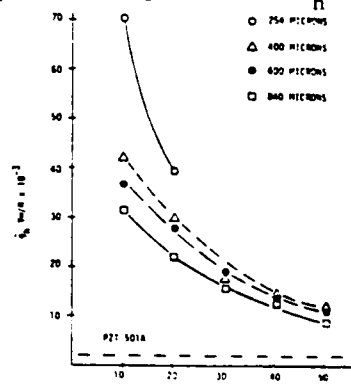


Fig.4 \bar{g}_h as a function of volume % PZT.

ing volume percent PZT result in increases in the value of \bar{g}_h . Fig.4 reveals this relationship. Piezoelectric coefficients of 3-1 composite are shown in Table 1. Composites were developed with a \bar{d}_h about 2.5 times that of solid PZT and a \bar{g}_h at least 20 times greater.

PIEZOELECTRIC COMPOSITES WITH 3-1-0 CONNECTIVITY

The magnitude of the $\bar{d}_h \cdot \bar{g}_h$ product of a 3-1 composite with PZT rods in polymer matrix is large, but is far less than the theoretical value. Part of the reason is that the poisson ratio of the polymer used is fairly high thus an internal stress exists which opposes the applied stress, and the stress amplification of a 3-1 connectivity model is greatly reduced. One way to reduce the poisson ratio of a polymer is to introduce porosity into it.⁶ The fabrication of 3-1 composites with porous polyurethane was developed by Klicker.⁶ Introduction of porosity into the polyurethane matrix has a dramatic effect on \bar{d}_h . Composites made with 4 volume % PZT rods 240 μ m in diameter in a foamed polyurethane with 45% porosity had a $\bar{d}_h \bar{g}_h$ product close to $100,000 \times 10^{-15} \text{ m}^2/\text{N}$, which is more than an order of magnitude greater than the $\bar{d}_h \bar{g}_h$ product of composites with a non-porous epoxy matrix (Table 1). But this porous polyurethane composite is very pressure dependent above 200psi. Other types of 3-1-0 composites were studied by Lynn⁷. Porosity was introduced into different types of polymer matrix either by adding a foaming agent or by mixing commercial hollow glass spheres with the polymer. Using a foamed REN epoxy, composites with 4 volume % of 280 μ m diameter rods showed a three-fold increase in \bar{d}_h above the unfoamed REN epoxy. When hollow glass spheres of an average diameter of 80 μ m and 2 μ m wall thickness were mixed in REN and Spurr's epoxy \bar{d}_h increased about 2 times greater than the plain epoxy composites (Table 1). For all the composites with glass spheres, no pressure dependence were found, while in foamed REN epoxy composite the pressure dependence still exists.

SUMMARY

Composite piezoelectric elements form an interesting family of materials which highlight the major advantages composite structures afford in improving coupled properties in solids for transduction applications. By careful consideration of the crystal symmetry, macrosymmetry, and possible modes of phase interconnection (connectivity) which can be realised by modern processing technologies, it is possible to design new composite transducers with property combinations tailored for specific device requirements.

We believe that the composite materials offer a new versatility in property combinations, and it will be most interesting to observe how this is taken up and exploited in subsequent generations of piezoelectric devices.

REFERENCES

1. R. E. Newnham, D. P. Skinner, and L. E. Cross, Mat. Res. Bull. 13 525 (1978).
2. D. P. Skinner, R. E. Newnham, and L. E. Cross, Mat. Res. Bull. 13 599 (1978).
3. T. R. Shrout, W. A. Schulze, and J. V. Biggers, Mat. Res. Bull. 14 1553 (1979).
4. K. Rittenmyer, T. R. Shrout, and R. E. Newnham, "Piezoelectric 3-3 Composites" (Submitting).
5. A. Safari, A. Halliyal, L. J. Bowen, R. E. Newnham, Ferroelectric (Submitting).
6. K. A. Klicker, Ph.D. Thesis, The Pennsylvania University, 1980.
7. S. Y. Lynn, M.S. Thesis, The Pennsylvania University, 1981.

APPENDIX 8

Piezoelectric SbSI:Polymer Composites

PIEZOELECTRIC SbSI:POLYMER COMPOSITES

A. S. BHALLA, R. E. NEWNHAM, T. R. SHROUT and L. E. CROSS

Materials Research Laboratory, The Pennsylvania State University, University Park, PA 16802, USA

(Received February 11, 1981)

Following the principle of connectivity in two phase systems, composites of SbSI and Spurr's epoxy in 1:3 and 3:3 modes were prepared. Piezoelectric strain coefficients d_{33} and d_h , and dielectric constant K were measured over a temperature range encompassing the transition temperature.

Interactions between the polymer and SbSI cause a shift in the dielectric peak to higher temperatures. The hydrostatic voltage coefficient $g_h \approx 110 \times 10^{-1} \text{ m}^2/\text{C}$ and hydrophone sensitivity $d_h \cdot g_h \approx 10^{-10} \text{ m}^2/\text{N}$ are substantially higher than those of SbSI single crystals and most other piezoelectrics.

INTRODUCTION

Antimony sulphur iodide (SbSI) is the most important member of a family of ferroelectric semiconductors¹⁻² with formula $A^V B^{VI} X^{VII}$. In the ferroelectric phase below 20°C it belongs to the orthorhombic point group symmetry $mm2$ and has very large piezoelectric strain coefficient d_{33} and d_h along the polar c -axis³ ($d_{33} = 4000 \times 10^{-12} \text{ C/N}$ at T_c). The transition is accompanied by an exceedingly large permittivity ($K \approx 6 \times 10^4$ at T_c), substantially reducing the voltage coefficient $g_{33} = d_{33}/K_{33}$. If the dielectric constant K_{33} of SbSI can be reduced then the material becomes an attractive candidate for piezoelectric detectors and high efficiency electromechanical transducers.

Based on certain interphase connectivity concepts in a two phase system, PZT:polymer composites have been investigated in the past for hydrophone applications.⁴⁻⁶ Very large reductions in the dielectric constant and enhancement in the hydrophone figures of merit g_h and $d_h \cdot g_h$ were reported. In this paper we describe composites of SbSI:polymer prepared in the 1:3, 3:1 and 3:3 connectivity patterns.[†]

SbSI exhibits a very large structural anisotropy along the polar c -axis. In various attempts of crystal growth⁷ of SbSI a needle like morphology of

the crystals has predominated with the length of the needles being parallel to the piezoelectric c -axis. The cross-section of the needles can be controlled by adjusting the growth parameters, making SbSI suitable for 1:3 composites. This paper reports the dielectric and piezoelectric properties of composites fabricated from SbSI and polymers and their possible application as hydrophone elements.

EXPERIMENTAL

SbSI:polymer samples were prepared in 1:3 and (1:3)(3:3) connectivity patterns with the single crystal needles of SbSI as a starting material. SbSI polycrystalline boules in the form of a bundle of slender needles oriented parallel to the c -direction were grown from the melt using the Bridgman method. The composite samples were prepared in two different ways.

In the first two specimens as grown boules were vacuum filled with Spurr's epoxy[‡] and cured at 80°C. The composite boules thus prepared were heated to 200°C under 7000 psi argon gas atmosphere. The procedure increased the density of the samples by eliminating the voids in the composite. The connectivity in these samples is a mixture of the 1:3 and 3:3 pattern (Figure 1). Sample No. 1 contained 55 vol.% and No. 2 65 vol.% SbSI.

[†] 1:3 connectivity means that the active piezoelectric component SbSI is self-connected in only one direction in a three dimensionally connected matrix of a second phase (e.g. epoxy). The other symbols can be explained in a similar fashion.

[‡] Spurr's epoxy, Polysciences Inc., Warrington, PA.



FIGURE 1 Section of a SbSI:Spurrs composite prepared from as grown SbSI boule brighter areas are SbSI crystals ($\times 200$).

A third sample was prepared by separating the needles apart, aligning them parallel to their length and then filling under vacuum with the Spurrs epoxy and followed by curing at 80°C for 8 hours. These samples were engineered in a 1:3 connectivity pattern (Sample No. 3, 50 vol.% SbSI).

Sections 2–3 mm thick were cut normal to the *c*-axis and then polished and electroded. Finally the samples were shaped in the form of circular disks for the electrical measurements. The fraction of SbSI in the samples was determined from density measurements on the composites.

The piezoelectric strain coefficients d_{33} and d_h and dielectric constant K_{33} were measured as a function of temperature over a range encompassing the phase transition temperature. The piezoelectric voltage coefficients g_{33} and g_h and the hydrophone figure of merit $d_h \cdot g_h$ were computed from the measured d_{33} , d_h and K_{33} values. d_{33} coefficients were measured from 0°C to 50°C using the Berlincourt d_{33} meter† in a temperature controlled chamber. Measurements were also made by a resonance technique and the d_{33} , d_{31} and coupling coefficient k , were calculated. The dielectric constants were measured with an automated capacitance bridge.‡ d_h was measured by a pseudostatic DC method. Samples were placed in the hydro-

static pressure vessel and kept at the desired temperature during measurements. Using an oil medium hydrostatic pressure was applied at a rate of 3.5 MPa/sec and the generated charge measured. In all measurements the samples were poled with a DC field of 1–2 KV/cm while being cooled through the phase transition to about 0°C . At 0°C the poling field was removed gradually in order to minimize the possibility of back switching caused by the space charge built up during the poling procedure. All the data were collected in the dark and during the heating cycles. Typical heating rates were $2^\circ\text{C}/\text{min}$ for the d_{33} and K_{33} runs and $< 0.5^\circ\text{C}/\text{min}$ for the hydrostatic d_h measurements.

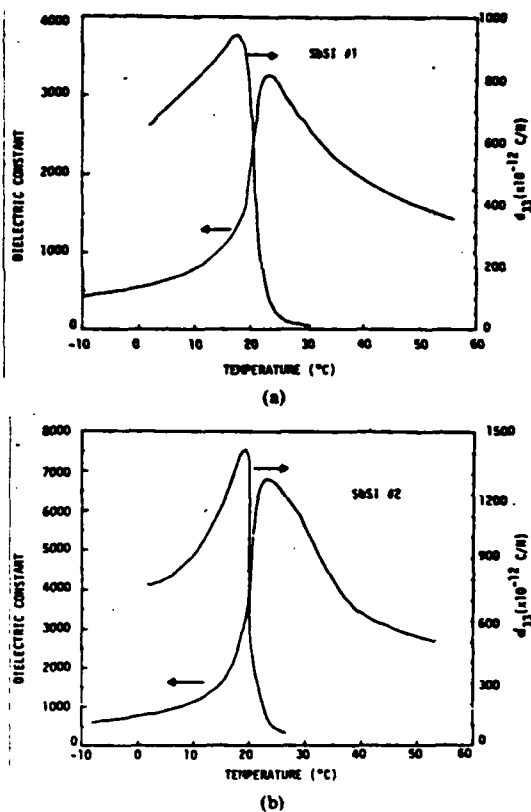


FIGURE 2 Dielectric constants and piezoelectric coefficients of composite samples as a function of temperature (a) sample #1, 55 vol.% SbSI and (b) sample #2, 65 vol.% SbSI. Dielectric $K(T)$ maxima in both samples peak around 23°C where as piezoelectric $d_{33}(T)$ maxima occur at 19°C .

† Model 333 Channel Products, Chagrin Falls, Ohio.

‡ HP Automated Capacitance Bridge Model 4270, Japan.

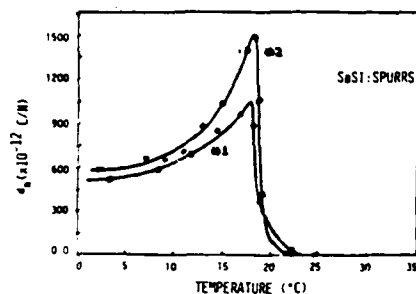


FIGURE 3 Hydrostatic piezoelectric strain coefficients d_{31} and d_{33} measured as a function of temperature (sample #1 & #2).

RESULTS AND DISCUSSION

Figure 2 shows the piezoelectric d_{33} coefficients (measured by the Berlincourt meter) and dielectric constants of composite samples No. 1 and 2 plotted as a function of temperature. The d_{33} values reach a maximum at $T_c \approx 19^\circ\text{C}$ for both samples with the dielectric constant peaks at slightly higher temperatures. Resonance studies showed a large coupling constant k_t and a very poor lateral coupling in these samples. It was estimated that the d_{31} in composite SbSI samples was very small ($\approx 10 \times 10^{-12} \text{ C/N}$) compared to the d_{33} coefficients. Figure 3 shows the hydrostatic piezoelectric strain coefficients plotted as a function of temperature for the same samples. The d_{31} coefficients are approximately equal to the d_{33} values. In SbSI crystals $d_{33} \gg d_{32} > d_{31}$ and d_{31} & d_{32} are of opposite sign and thus only small differences in d_{33} and d_{31} are expected for the composites. This is borne

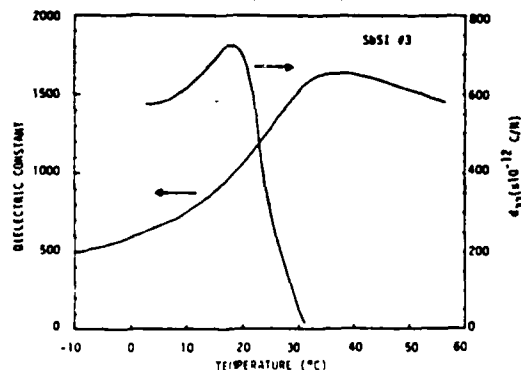


FIGURE 4 Dielectric constants and piezoelectric strain coefficients d_{31} of a 1:3 SbSI:Spurrs composite as a function of temperature (sample #3). $K(T)$ maximizes around 35°C .

out in samples #1 and 2 where d_{31} and d_{33} appear to be uncoupled due to the modified stress behavior within the SbSI:polymer composites. Similar effects have been observed in PZT:polymer composites where d_{31} values as large as seven times those of solid PZT have been reported.⁶

The behavior of the dielectric constant with temperature is shown in Figure 2. The transition temperature as determined from the dielectric measurements was about 23°C , some 4°C higher than the piezoelectric peak. When the method of composite preparation is modified as in the case of sample No. 3, the stress behavior is apparently altered, the piezoelectric and dielectric maxima were found to differ by 14°C (Figure 4). This behavior is not well understood but could be reproduced in several SbSI:polymer composites. The Curie temperature of SbSI (as determined from K vs T measurements) increases with tensile stress along the polar direction.⁸ SbSI needles in the polymer matrix are under tensile stress because of differences in the thermal expansion coefficients of SbSI and the polymer and this may be responsible for the change in T_c . Since various parts of the SbSI needles in the composites experience different stresses and hence go through the phase transition at slightly different temperatures, the characteristic sharp dielectric maximum at T_c of a stress free single crystal is broadened and shifted to higher temperatures. Moreover the dielectric properties are not very sensitive to the state of poling but are controlled mainly by the mechanical boundary conditions. In contrast the pyroelectric and piezoelectric properties are influenced by both the temperature and the domain configuration. Pyroelectricity and piezoelectricity are absent until the sample is poled and this requires that all segments of an SbSI needle be in the ferroelectric state below T_c . If some segments are above T_c and some below, the needle cannot be poled. On the other hand, the dielectric constant is not affected in the same way. The dielectric constant of SbSI is high both above and below T_c . Therefore its maximum occurs near the average T_c of the various SbSI segments while that of the piezoelectric and pyroelectric coefficients occurs near the lowest T_c . Hence the peak in the dielectric constant is displaced toward higher temperature relative to the piezoelectric maximum. This distribution of Curie temperatures in composites also explains the broadness of the $K(T)$ and $d(T)$ curves.

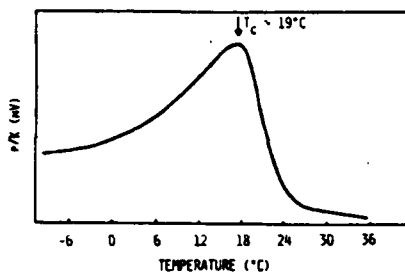


FIGURE 5 Pyroelectric voltage response at various temperatures as measured on SbSI:Spurrs composites in the Chynoweth experiment.

Since the values of d_{33} and K_{33} were collected separately in independent experiments, corroborating evidence was sought. Simultaneous pyroelectric (p) and dielectric measurements substantiated the above measurements and gave the direct evidence for the separation of the dielectric peak from those associated with the pyroelectric or piezoelectric effects. The pyroelectric coefficient was determined by the Byre Roundy method,⁹ maximized at 19°C, as in the piezoelectric measurements of samples No. 1 and 2. Based on thermodynamic arguments, the ferroelectric Curie constant C , the spontaneous polarization P_s , the dielectric constant K_{33} and pyroelectric coefficient p are related by the expression

$$\frac{p}{K_{33}} = \frac{P_s}{C} \quad (1)$$

Equation (1) suggests that the ratio p/K_{33} approaches zero near T_c . Figure 5 shows the pyroelectric voltage response plotted as function of temperature in the Chynoweth experiment.¹⁰ The maximum at T_c in the response curve demon-

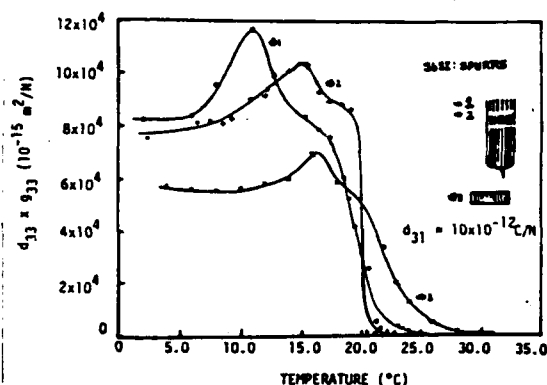


FIGURE 6 Measured values of $d_{33} \times g_{33}$ as a function of temperature for sample #1, 2 and 3.

strated the fact that K and p were not following the same temperature dependence that $K(T)$ and $p(T)$ have maxima at different temperatures.

This particular study made the SbSI: polymer composites very attractive candidate material for the hydrophone elements. For the most efficient hydrophone element material it is desirable to maximize

$$\text{Sensitivity} = \left(\frac{\text{Max. charge}}{\text{area}} \right) \left(\frac{\text{Max. voltage}}{\text{thickness}} \right) \quad (2)$$

or in other words the figure of merit for hydrophone sensitivity is represented by $d_h g_h$ or d_h^2/K . The measured values of $d_h g_h \approx d_{33} \cdot g_{33}$ are plotted in Figure 6 as a function of temperature. Because of the shift in the dielectric peak to the higher

TABLE I

Hydrostatic piezoelectric coefficients d_h , g_h and $d_h \cdot g_h$ measured for SbSI:Spurrs composites and various piezoelectric hydrophone materials.

Material	$d_h \sim d_{33} (10^{-12} \text{C/N})$		$g_h (\times 10^{-3} \text{m}^2/\text{C})$	$d_h \times g_h (\times 10^{-15} \frac{\text{m}^2}{\text{N}})$
Sample #1 (55 vol.% SbSI)	950(19°C)	720(5°C)	112(5°C)	$8 \times 10^4 - 10^5 (0-15^\circ\text{C})$
Sample #2 (65 vol.% SbSI)	1500(19°C)	810(5°C)	98(5°C)	$8 \times 10^4 - 10^5 (0-15^\circ\text{C})$
Sample #3 (50 vol.% SbSI)	750(19°C)	590(5°C)	100(5°C)	$6 - 7 \times 10^4 (0-15^\circ\text{C})$
SbSI Single Crystals	800(10°C)		8(10°C)	$7 \times 10^3 (10^\circ\text{C})$
PVF ₂	11(25°C)		104(25°C)	$1 \times 10^3 (25^\circ\text{C})$
PZT-501	50(25°C)		4(25°C)	$2 \times 10^2 (25^\circ\text{C})$
PbNb ₂ O ₆	67(25°C)		30(25°C)	$2 \times 10^3 (25^\circ\text{C})$

PIEZOELECTRIC SbSI-POLYMER COMPOSITES

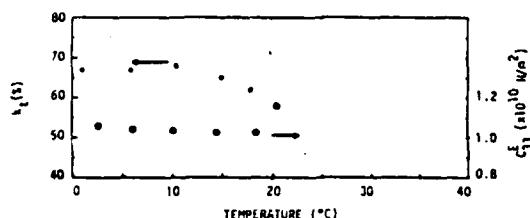


FIGURE 7 Mechanical coupling constant and the C_{33} of a SbSI:Spurrs composite sample #1 as a function of temperature.

temperature side, the $d_h \cdot g_h$ and g_h values for SbSI composites are enhanced. The $d_h \cdot g_h$ parameters are compared with other potential hydrophone materials in Table I. Mechanically, the composite SbSI elements are stronger than solid SbSI and showed high coupling constant k_t over temperatures up to T_c with relatively little temperature dependence of these coefficients (Figure 7).

The low transition temperature of SbSI limits its applicability in electro-acoustic devices. Attempts have been made to raise the T_c of SbSI by doping with oxygen and alloying it with Sb_2S_3 or the other members of the SbSI family.^{11,12} Sb_2S_3 :SbSI and SbSI: Sb_2O_3 compositions enhanced the T_c (up to 35°C) but the piezoelectric properties were substantially reduced. By proper doping of SbSI, T_c can be raised without substantial sacrifice in the piezoelectric properties and an even wider effective working temperature range. Sizeable improvements in g_h and $d_h \cdot g_h$ can be achieved by fabricating SbSI-polymer composites. Work in this direction is in progress and will be reported elsewhere.

SUMMARY

1. SbSI:polymer SPURRS composites with (1:3) and (1:3)(3:3) connectivity patterns were made by vacuum filling as grown SbSI boules and by aligning bundles of SbSI needles parallel to polar axis and embedding in epoxy.

2. Piezoelectric coefficients $d_{31} \approx 10 \times 10^{-12}$ C/N and $d_{33} \approx d_h \approx 1500 \times 10^{-12}$ C/N were observed.

3. In the composite the effect of d_{31} was substantially reduced. The dependence of dielectric and piezoelectric response on temperature in composite was modified compared to the pure SbSI crystals. The dielectric and piezoelectric maximas in the temperature behavior were separated by 4–14°C depending on the method of preparation of the composites.

4. Figures of merit for the hydrophone sensitivity $d_h g_h \approx 10^3 \times 10^{-15}$ m²/N were achieved in the composites.

5. High coupling constant $k_t \approx 70\%$ was observed in SbSI composites.

ACKNOWLEDGEMENT

This work was sponsored by the Office of the Naval Research under contract No. N00014-78-C-00291.

REFERENCES

1. E. Fatuzzo, G. Harbeke, W. J. Merz, R. Nitsche, H. Roetschi and W. Ruppel, *Phys. Rev.*, **127**, 2036 (1962).
2. R. Nitsche and W. J. Merz, *J. Phys. Chem. Solids*, **13**, 154 (1960).
3. D. Berlincourt, H. Jaffe, W. J. Merz and R. Nitsche, *Appl. Phys. Lett.*, **4**, 61 (1964).
4. R. E. Newnham, D. P. Skinner and L. E. Cross, *Mat. Res. Bull.*, **13**, 525 (1978).
5. D. P. Skinner, R. E. Newnham and L. E. Cross, *Mat. Res. Bull.*, **13**, 599 (1978).
6. R. E. Newnham, L. J. Bowen, K. A. Klicker and L. E. Cross, *Mats. in Engg.*, **11**, 93 (1980).
7. A. S. Bhalla, K. E. Spear and L. E. Cross, *Mat. Res. Bull.*, **14**, 423 (1979).
8. M. D. Volnyanskii, A. Yu Kudzin and A. N. Sukhanskii, *Sov. Phys.—Crystallography*, **17**, 364 (1972).
9. R. L. Byer and C. B. Roundy, *Ferroelectrics*, **3**, 333 (1972).
10. A. G. Chynoweth, *Phys. Rev.*, **102**, 705 (1956).
11. L. M. Belyaev, V. A. Lydkhovitskaya and I. M. Silverstrova, *Izv. Akad. Nauk. SSSR. Neorg. Mater.*, **6**, 429 (1970).
12. R. Nitsche, H. Roetschi and P. Wild, *Appl. Phys. Lett.*, **4**, 210 (1964).

APPENDIX 9

Piezoelectric and Elastic Properties of Barium
Germanium Titanate and Lithium Borosilicate Glass Ceramics

PIEZOELECTRIC AND ELASTIC PROPERTIES OF BARIUM GERMANIUM TITANATE AND LITHIUM BOROSILICATE GLASS-CERAMICS

A. Halliyal, A.S. Bhalla, R.E. Newnham, and L.E. Cross

Materials Research Laboratory
The Pennsylvania State University
University Park, PA 16802

Abstract

Piezoelectric barium germanium titanate and lithium borosilicate glass-ceramics were prepared by crystallizing the glasses in a temperature gradient. The piezoelectric constants, electromechanical coupling factors and elastic constants of the glass-ceramics were measured by the resonance method. Some of the glass-ceramics exhibit high electromechanical coupling factors and low temperature coefficient of resonance making them of interest as temperature compensated resonators.

Introduction

Several nonferroelectric polar glass-ceramics have been studied from the point of view of their application in piezoelectric devices and pyroelectric detectors¹⁻⁵. It has been shown that it is possible to prepare glass-ceramics with good crystallographic and polar orientation by crystallizing the glasses in a temperature gradient resulting in glass ceramics with reasonably good piezoelectric properties. Detailed studies of the piezoelectric properties of barium germanium titanate³ and lithium borosilicate⁴ glass ceramics showed that the piezoelectric properties of these glass-ceramics are comparable to those of commonly used piezoelectric materials. Some glass ceramics in the $\text{Li}_2\text{O-SiO}_2\text{-B}_2\text{O}_3$ system showed high electromechanical coupling coefficients and low temperature coefficient of resonance (TCR)⁴. It has been suggested that because of their good electromechanical properties and a high degree of crystallographic orientation near the glass-ceramic surfaces, lithium borosilicate glass-ceramics might find an application in SAW devices⁴.

Glass ceramic piezoelectrics can be easily fabricated in large sizes and their properties can be optimized by adjusting the glass composition and processing parameters.

In the present paper we report elastic and piezoelectric measurements on fresnoite ($\text{Ba}_2\text{Si}_2\text{TiO}_8$) glass ceramics and a few compositions in the $\text{Li}_2\text{O-SiO}_2\text{-B}_2\text{O}_3$ system. Piezoelectric, elastic and electromechanical coefficients of glass ceramics of composition $\text{Ba}_2\text{Ge}_2\text{TiO}_8$ (BGT), $\text{Ba}_2\text{Ge}_2\text{TiO}_8\text{-Ba}_2\text{Si}_2\text{TiO}_8$ solid solution (BGST) with excess silica, and $\text{LiO}_2\text{-(2-x)SiO}_2\text{-xB}_2\text{O}_3$ glass-ceramics here investigated by resonance methods. The measured values are compared with the reported properties of $\text{Ba}_2\text{Ge}_2\text{TiO}_8$ and $\text{Ba}_2\text{Si}_2\text{TiO}_8$ single crystals.

Experimental Procedure

The procedure followed for preparing glass-ceramics with oriented crystallites is essentially the same as that reported in earlier studies^{2,3}. The glass samples were prepared by mixing reagent grade chemicals in the desired molar ratio and melting in a platinum crucible, using a globar furnace. The glass samples were crystallized in a temperature gradient by placing polished glass disks on a microscope hot stage⁶. Details concerning the heating cycles employed during crystallization of the glasses can be found in references 1-3. The crystalline phases in the glass-ceramic samples were identified from x-ray powder diffraction patterns.

Piezoelectric constant d_{33} parallel to the crystallization direction was measured using a d_{33} -meter^{**}. For resonance studies, samples were prepared in the form of circular disks 8 mm in diameter and 0.3 to 0.6 mm in thickness. Gold electrodes were sputtered on the polished surfaces. Resonance behavior in the thickness mode and planar mode were investigated using a spectrum analyzer[†]. The resonance frequency constants, electromechanical coupling factors and mechanical quality factor Q were determined by measuring the resonance and anti resonance frequencies. From these values, some of the elastic and piezoelectric coefficients were calculated. The temperature coefficient of resonance (TCR) was evaluated by measuring the resonance frequency as a function of temperature at intervals of 5° in the temperature range -20 to 100°C.

Results and Discussion

The crystalline phases identified from the x-ray powder diffraction patterns are listed in Table I, along with the densities and dielectric constants. All the crystalline phases belong to polar point groups, and hence the piezoelectric properties of the glass-ceramic are not diluted by inactive phases. The densities and dielectric constants of BGT and BGST glass-ceramics are in close agreement with those of $\text{Ba}_2\text{Ge}_2\text{TiO}_8$ and $\text{Ba}_2\text{Si}_2\text{TiO}_8$ single crystals.

*E. Leitz, Inc., Rochleigh, NJ, Model No. 493.

**Channel Products, Chesterland, OH, Model CPDT 330C

†Hewlett-Packard, Loveland, CO, Model 3585A.

Table 1.
Physical Properties of Glass-Ceramics

Composition	Crystalline* Phases	Dielectric constant ϵ_{33}/ϵ_0	ρ gm/cm ³
2BaO-2GeO ₂ -TiO ₂ (BGT)	B ₂ TG ₂	15	4.8
2BaO-2SiO ₂ -GeO ₂ -TiO ₂ (BGST)	B ₂ TG ₂ + B ₂ TS ₂ (solid solution)	10.3	4.3
Li ₂ O-1.8SiO ₂ -0.2B ₂ O ₃	LS ₂ + LB ₂ + LS	9	2.3
Li ₂ O-1.33SiO ₂ -0.66B ₂ O ₃	LS ₂ + LB ₂ + LS	8	2.3
Ba ₂ Ge ₂ TiO ₈ (Single crystal)	-----	13	4.84
Ba ₂ Si ₂ TiO ₈ (single crystal)	-----	11	4.45

*Abbreviation for Phases: B₂TG₂ = Ba₂Ge₂TiO₈, B₂TS₂ = Ba₂Si₂TiO₈, LS₂ = Li₂O-2SiO₂, LB₂ = Li₂O-2B₂O₃, LS = Li₂O-SiO₂.

As mentioned earlier, the glass-ceramics prepared by crystallizing the glasses in a temperature gradient show a high degree of crystallographic orientation parallel to the temperature gradient. Needle-like crystallites grow from the hot face deep into the sample along the direction of the temperature gradient. The c-axes of the crystallites show preferred orientation but the a or b do not. The alignment of the polar c-axes is responsible for the pyroelectric and piezoelectric properties of the glass ceramics. The properties of the glass ceramics are isotropic in the plane perpendicular to the c-axes of the crystallites.

A ferroelectric ceramic material prepared by conventional sintering methods is non-piezoelectric even though the individual crystals may be strongly piezoelectric. To convert the ceramic into a piezoelectric, it is necessary to pole the ceramic with an external electric field⁶.

Thus the symmetry of a poled ceramic body is ∞m and for piezoelectric and elastic phenomena this is equivalent to hexagonal symmetry $6 mm$. Since the polar glass-ceramics with oriented crystallites and the poled ceramics both have only one polar direction, the symmetries are the same (∞m). The independent, non-zero elastic, piezoelectric and dielectric constants for this symmetry are s_{11} , s_{12} , s_{13} , s_{33} , s_{55} , d_{31} , d_{33} , d_{15} ; ϵ_{11} and ϵ_{33} . Additional non zero coefficients are related to these by symmetry relations.

The values of piezoelectric d coefficients, the elastic constants and the electromechanical coupling coefficients of the glass-ceramics are given in Table 2. The values of piezoelectric d coefficients and elastic coefficients of BGT and BGST glass-ceramics are comparable to the values of Ba₂Ge₂TiO₈ and Ba₂Si₂TiO₈ single crystals, from which we conclude that there are no substantial differences in the elastic behavior of the glass and crystalline phases in the glass-ceramics.

The electromechanical coupling coefficients k_t and k_p of BGT glass-ceramics are lower than the corresponding values of Ba₂Ge₂TiO₈ single crystal³, but those of BGST glass-ceramics are slightly

higher. The planar coupling k_p of Li₂O-1.8SiO₂-0.2B₂O₃ glass ceramic⁴ is higher than LiTaO₃ and other commonly used piezoelectric materials. The mechanical quality factors Q are surprisingly high for the glass-ceramics (300-1000).

A typical resonance spectrum observed in glass-ceramic samples is shown in Figure 1, and a plot of relative resonance frequency Δf_R as a function of temperature is shown in Figure 2, where

$$\Delta f_R = \frac{f_T - f_{RT}}{f_{RT}}$$

Here, f_T is the resonance frequency at temperature T and f_{RT} is the resonance frequency at room temperature. The temperature coefficients of resonance (TCR), calculated from the slopes of Δf_R vs T plots are listed in Table 2.

The TCR values of BGT and BGST glass-ceramics are larger than those of either Ba₂Ge₂TiO₈ and Ba₂Si₂TiO₈ single crystals. For lithium borosilicate glass ceramics the TCR values are comparable to the values of commonly used piezoelectric single crystals⁴. TCR of Li₂O-1.33SiO₂-0.66B₂O₃ glass-ceramic is 30 ppm/°C in the temperature range 20-60°C (Fig. 2), the useful operating range for most piezoelectric devices.

The strong dependence of the electromechanical coupling coefficients and TCR on the composition of the parent glass suggests that further improvements in the properties are possible by suitably modifying the composition. In addition, the amount and orientation of the different crystalline phases can be controlled by employing suitable heat treatment cycles providing another controlling factor to tailor the properties of glass-ceramics.

Summary

The piezoelectric coefficients and elastic constants of several piezoelectric glass-ceramics were measured by resonance methods. It is possible to fabricate large inexpensive glass-ceramic piezoelectric devices with substantial electromechanical coupling factors and low TCR. The

Table 2.
Piezoelectric and Elastic Constants

Property	Ba ₂ Ge ₂ TiO ₈ Glass-Ceramic	BCST Glass-Ceramic	Ba ₂ Ge ₂ TiO ₈ Single Crystal	Ba ₂ Si ₂ TiO ₈ Single Crystal	Li ₂ O-1.85SiO ₂ - 0.2B ₂ O ₃	Li ₂ O-1.33SiO ₂ - 0.66B ₂ O ₃
$d_{33} \times 10^{-12} \text{C/N}$	6	6	8	3.8	6	3
$d_{31} \times 10^{-12} \text{C/N}$	1.2	2.1	2.0	2.7	2.4	1.5
$s_{11} \times 10^{-12} \text{m}^2/\text{N}$	9.2	9.0	8.8	7.6	9.5	11
$s_{12} \times 10^{-12} \text{m}^2/\text{N}$	-1.9	-2.3	-1.9	-1.6	-2.4	-2.8
$s_{66} \times 10^{-12} \text{m}^2/\text{N}$	22	22	21	17	24	27
$c_{33} \times 10^{12} \text{N/m}^2$	0.13	0.12	0.09	0.08	---	---
N_t (mt. Hz)	2500	2600	2150	---	---	---
N_p (mt. Hz)	3100	3500	2900	---	4500	4200
k_t	0.075	0.15	0.10	---	---	---
k_p	0.045	0.12	0.10	---	0.14	0.09
k_{31}	0.04	0.07	0.06	0.10	0.09	0.05
Q	700	300	---	650	1000	400
TCR ppm/°C (0-100°C) z-cut	95	>100	48	51	60	30 (20-60°C)

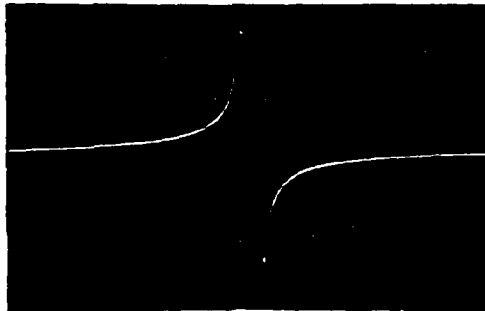


Figure 1. Resonance spectrum for Li₂O-1.85SiO₂-0.2B₂O₃ (horizontal scale = 6.8 kHz vertical = 5 dB).

piezoelectric properties of the glass-ceramics are comparable to those of single crystals, and can be optimized by proper choice of composition and heat treatment. The glass-ceramic piezoelectric materials may be useful in temperature compensated bulk resonators, in SAW devices and in flexural mode resonators.

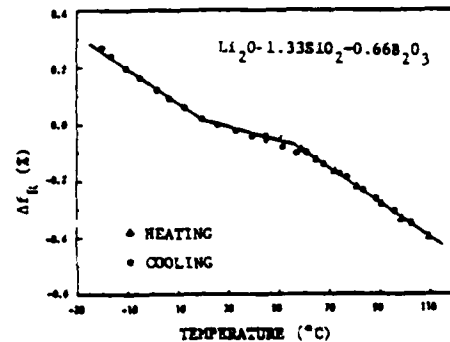


Figure 2. Relative resonance frequency as a function of temperature for Li₂O-1.33SiO₂-0.66B₂O₃.

Acknowledgment

This work was sponsored by the U.S. Army Research Office (DAAG29-80-C-0008).

References

1. G.J. Gardopée, R.E. Newnham, A.S. Bhalla, Ferroelectrics 33, 155 (1981).
2. A. Halliyal, A.S. Bhalla, R.E. Newnham, L.E. Cross, J. Mater. Sci. 16, 1023 (1981).
3. A. Halliyal, A.S. Bhalla, R.E. Newnham, L.E. Cross, and T.R. Gururaja, J. Mater. Sci. (accepted).
4. A. Halliyal, A.S. Bhalla, R.E. Newnham, L.E. Cross, J. Appl. Phys. (accepted).
5. A. Halliyal, A.S. Bhalla, R.E. Newnham, L.E. Cross, Ferroelectrics (1981) (accepted).
6. B. Jaffe, W.R. Cook, Jr., and H. Jaffe, Piezoelectric Ceramics, Academic Press, London and NY (1971).

APPENDIX 10

Densification in PZT

DENSIFICATION IN PZT

S. VENKATARAMANI, J.V. BIGGERS

Materials Research Laboratory, The Pennsylvania State University, University Park, PA 16802, USA

The reaction sequence of PZT formation from the mixture of $\text{PbO-ZrO}_2\text{-TiO}_2$ has been extensively studied¹⁻³. However, there have been no studies on the morphological changes occurring during the calcination process. The dependence of the characteristics and properties of the ceramic on the calcining conditions though has been well noted⁴⁻⁵, no systematic explanations have been given for the reasons of such dependencies.

Inhomogeneous sintering has been observed in PZT tapes and disks⁶ and was attributed to packing characteristics and chemical inhomogeneities. Earlier efforts to reactively sinter PZT ceramics from uncalcined oxide mixtures were in vain due to the "anomalous" expansion of the compacts during the sintering process⁷.

The purpose of this study was to investigate the dilatometric behavior of the compacts during calcining and its influence of sintering and properties of PZT ceramics.

EXPERIMENTAL

The PZT 60/40 ($\text{PbZr}_{0.6}\text{Ti}_{0.4}\text{O}_3$) composition was prepared from the reagent grade oxides via the usual processing steps—ball milling and drying. Four different calcinations were carried out with varying temperature/time conditions to produce different phase assemblages: (i) uncalcined (as mixed); (ii) calcines at 600° for 3 hours; (iii) calcined at 700°C/3 hours and (iv) calcined at 800° for 6 hours. Calcining was done by placing the ZrO_2 Saggers containing the PZT mix into an electric muffle furnace preheated to the required temperature for the specified period of time.

The calcined powders were characterized for (i) surface area by a BET technique; (ii) particle size and shape distribution by CESEMI and (iii) qualitative and quantitative phase analysis by x-ray diffraction. For details of the analyses see Table I. Sintered alumina rods covered with platinum foil with a LVDT attachment were used for the dilatometric studies. The samples were heated at a constant rate of 200°C/hr from room temperature to 1300°C and cooled back at the same rate.

Isothermal studies were carried out by introducing the crucibles containing the PZT samples and the PbO source pellets into a muffle furnace maintained at specific temperatures (1000, 1100, 1200 and 1300°C) and quenching after a stipulated period of soak (1 min-12 hrs). Sintering studies were also done on all samples at constant rate of heating (200°C/hr) up to 1300°C.

Studies on reactive sintering were done on (PZT 60/40, PZT 401, PZT 501) compositions calcined to 840°C, the temperature at which the expansion maximum was noted. Dilatometric and isothermal studies (at 700, 800, 900, 1000 and 1150°C) were done with pellets as mentioned earlier. Dense pellets (>97% theoretical) were obtained by sintering at 1150°C for 1/2 hour. The physical, microstructural and electromechanical characteristics of these were compared with standard samples of PZT 60/40 obtained by sintering at 1300°C for half-hr; pellets made from completely calcined single phase PZT calcines.

TABLE 1. PZT 60/40 calcines-characterization data.

Nomenclature	Calcining Conditions	Phase
MO UNC	Uncalcined	PbO ZrO ₂ TiO ₂
MO 600/3	600°C/3 hr	PbO PbTiO ₃ ZrO ₂ PbO _{ss} ^a
MO 700/3	700°C/3 hr	PbO PbO _{ss} PbTiO ₃ 'PZT' ^b ZrO ₂
MO CAL	800°C/6 hr	PZT

^aA tetragonal PbO solid solution containing PbTiO₃ phase.

^bA PZT phase of varying Zr/Ti ratios.

and (ii) the formation of PbO_{ss} containing some PbTiO₃ dissolved into a tetragonal PbO

Geometric densities of fired samples were obtained from weight and dimension measurements. Microstructural analysis was done on polished and fractured surfaces. The dielectric and electromechanical properties were obtained 24 hrs after poling which was accomplished by applying a 25-30 kV/cm DC field at ~120°C for 5 min across the silver electroded samples in an oil bath. The dielectric constant, k , and the loss factor, $\tan\delta$ were obtained using a Hewlett-Packard automatic capacitance bridge. The piezoelectric coefficient, d_{33} , was measured in a Berlincourt d_{33} meter. Resonance techniques described in IRE Standards (1961) were used to obtain the coupling coefficient, k_p , and the quality factor Q .

RESULTS AND CONCLUSIONS

Figure 1 is the dilatometric behavior of the compacts from the various calcines as a function of temperature. The two distinct regions of expansion in the uncalcined sample correspond to the two different stages of reaction as was seen from the x-ray analysis.

(i) The formation of PbTiO₃ around 450-600°C

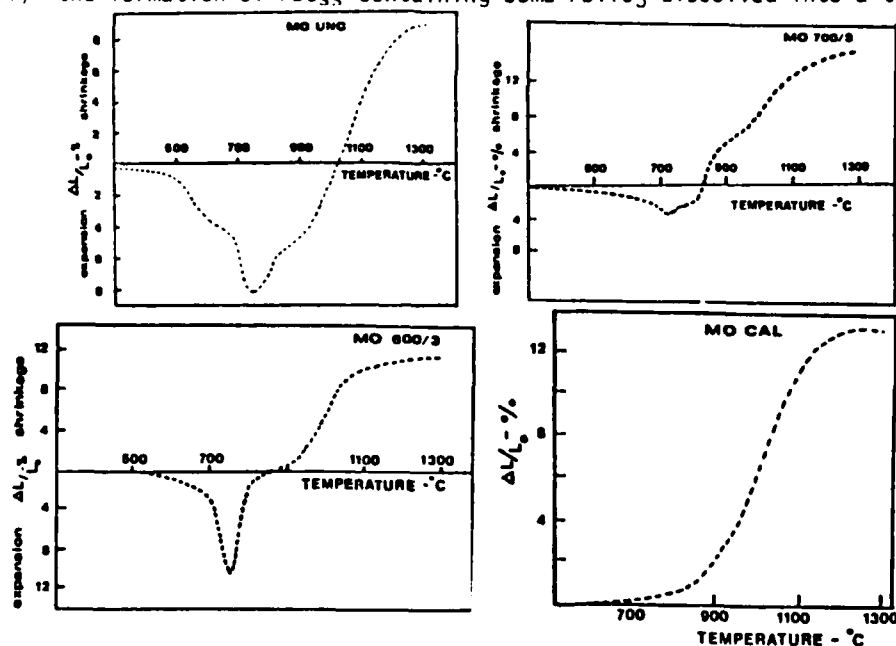


FIGURE 1. Dilatometric behavior of PZT during calcining.

DENSIFICATION IN PZT

and (PZT) compounds of varying Zr/Ti ratios. The final stages of the stoichiometric PZT formation is accompanied by a rapid shrinkage above 800°C up to 900°C above which densification starts to occur. The SEM micrographs of the fractured surfaces of compacts quenched at various temperatures during calcining also showed interesting changes in the microstructure as a function of temperature. Dense platey regions richer in PbO and TiO₂ were noted around 700-750°C from the selected area x-ray energy emission analyses of these regions. These are possibly the reaction products PbTiO₃ and PbO_{ss}. The absence of the specific expansion regions—region 1 around 600°C in MO 600/3 samples and region 1 and most of region 2 in MO 700/3 samples which had the corresponding phase distribution of these materials (Table 1) also prove the relationship between the expansions and the reaction sequences. The expansion is due to (i) the topological nature of the reactions—diffusion of PbO into TiO₂ particles and the formation of PbTiO₃ on the TiO₂ skeletal regions and (ii) the differences in the molar volumes of the product PbTiO₃ (38 ml) and TiO₂ (20.8 ml). Further reactions involving ZrO₂ also occur in a similar manner at the P/Z and P/T and P/PT/Z interfaces, causing expansion of the compact. The rapid shrinkage during the final stages of PZT formation is due to particle coarsening, higher product densities and phase transformations.

INHOMOGENEOUS DENSIFICATIONS

The results of the isothermal sintering at 1100°C studies on the pellets from the different calcines are shown in Figure 2. At all the sintering temperatures the uncalcined and partially calcined specimens initially expand as PZT formation occurred, resulting in a porous ceramic. On further heating, sintering occurs only within the ceramic regions leaving the large pores unclosed. The values slopes of the log-log plots of the density change vs time curves ($n \approx 0.3$) indicate that sintering occurs through a diffusion process. Higher temperature and/or periods of soak are required for the occurrence large scale of diffusion processes to close the pores. The green density vs fired density characteristics (Fig. 3) showing the linear dependence indicate the inhomogeneous densification phenomenon occurring in these samples. Similar observations have been made earlier⁶ and were attributed to the same phenomenon. The inhomogeneous densification is attributed to the volume changes during calcining and the chemical heterogeneities and reaction sintering in the ceramic regions of the expanded compacts.

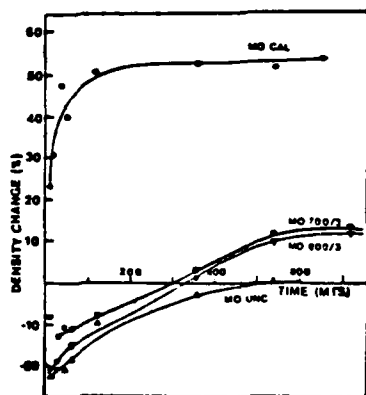


FIGURE 2. Isothermal sintering studies at 1100°C.

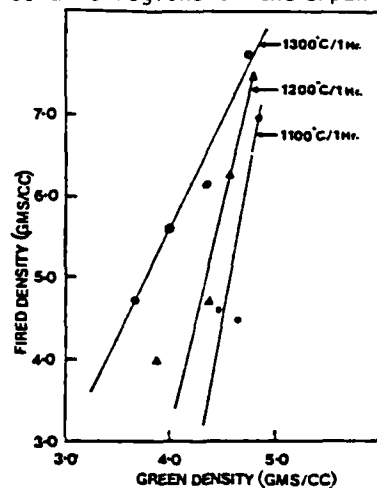


FIGURE 3. Green density vs fired density characteristics.

The percent density change and percent shrinkage as a function of sintering temperature is shown in Fig. 4. It is obvious that the reactive sintered sample undergoes enhanced densification up to $\sim 900^\circ\text{C}$ (15% change in density and 5% linear shrinkage). The x-ray analysis of quenched samples at intermediate temperatures showed the decrease of PbO , PT and ZrO_2 contents and an increase in the PZT content and sharpening of the PZT peaks. The lower value of the activation energy (68 kJ/mole) calculated from the slope of the log shrinkage vs $1000/T$ plots also indicates the enhanced densification. The near zero slope above 1150°C also confirms that densification is complete around that region. The microstructural analyses and isothermal sintering data showed no evidences of fine particle sintering such as rapid particle coarsening and densification within the initial few seconds. Hence, the enhanced densification is possibly in part due to the chemical reactions and phase transitions occurring at the final stages of PZT formation in the partially calcined starting material. Table 2 illustrates the properties of reactive sintered samples in comparison with corresponding standard samples of the same composition. The effect of the finer grain structure as evidenced from the micrographs were obvious in the values of the various electromechanical properties esp dielectric constant, d_{33} and k_p .

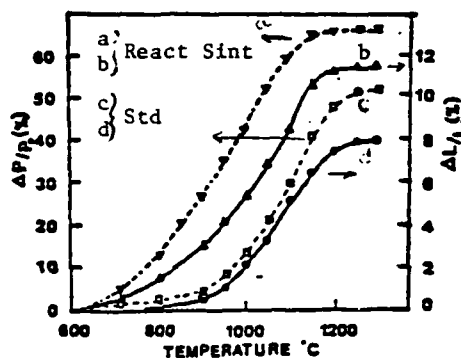


FIGURE 4. Dilatometric and density change characteristics

REFERENCES

1. Y. Matsuo, H. Sasaki, *J. Amer. Ceram. Soc.* 48, 289 (1965).
2. W.M. Speri, D. Eng. Thesis, Rutgers University (1969).
3. D.L. Hankey, Ph.D. Thesis, The Pennsylvania State University (1980).
4. D.A. Buckner, P.D. Wilcox, *Technical Report*, U.S. Atomic Energy Commission (1971).
5. A.H. Webster, T.B. Weston, V.M. McNamara, *J. Canad. Ceram. Soc.* 35, 61 (1966).
6. L.J. Bowen, T.R. ShROUT, S. Venkataramani, J.V. Biggers, *Annual Report*, Office of Naval Research (1980).
7. K. Okazaki, *J. Ceram. Assoc. Japan* 13, 17 (1965).

TABLE 2. Reactive Sintering: Electromechanical Properties

Comp.	Calcining and Sintering Conditions	Density (g/cc)		K			Tan δ			d_{33} (pCm ⁻¹)	k_p	Q
		Green	Fired	1kHz	10kHz	100kHz	1kHz	10kHz	100kHz			
PZT	CAL: 840 SINT: 1150/1/2	5.05	7.84	450	440	435	.04	.025	.021	100/125	0.35	240
PZT	CAL: 850/5 SINT: 1150/1/2	4.96	7.45	390	380	386	.008	.009	.010	130/130	0.41	330
401	CAL: 840 SINT: 1150/1/2	4.30	7.70	990	978	970	.015	.013	.013	140/235	0.41	220
401	CAL: 850/5 SINT: 1200/1/2	4.95	7.45	1060	1050	1112	.015	.008	.010	290/310	0.60	215
501	CAL: 840 SINT: 1150/1/2	4.94	6.73	897	896	913	.026	.023	.027	340/345	0.44	75
501	CAL: 850/5 SINT: 1200/1/2	4.93	7.30	1345	1315	1370	.028	.023	.036	340/345	0.59	85

APPENDIX 11

Calorimetric and Phenomenological Studies of the $\text{PbZrO}_3\text{:PbTiO}_3$ System

CALORIMETRIC AND PHENOMENOLOGICAL STUDIES OF THE $\text{PbZrO}_3\text{:PbTiO}_3$ SYSTEM

A. AMIN,^{*} L.E. CROSS AND R.E. NEWNHAM

Materials Research Laboratory, The Pennsylvania State University, University Park, PA 16802.

Abstract—The perovskite structure solid solutions between antiferroelectric PbZrO_3 and ferroelectric PbTiO_3 embrace a number of technologically important piezoelectric compositions grouped near the morphotropic phase boundary (composition close to Zr:Ti ratio 1:1). Heats of transition $Q(\text{J/m}^3)$ and ferroelectric transition temperature $T_c(\text{K})$ for a series of carefully prepared (chemically co-precipitated) composition in the $\text{Pb}(\text{Zr}_x\text{Ti}_{1-x})\text{O}_3$ solid solution system in the range $0.0 < x < 0.6$ were measured using a Perkin Elmer DSC2 thermal analyser under computer control. The composition dependence of the transition entropy $S(\text{J/m}^3/\text{deg})$ and the Curie Weiss constant were deduced from a combination of calorimetric and phenomenological data. The anomalous behaviour of the heat of transition for compositions near the morphotropic boundary is discussed on the basis of an extended phenomenological theory for the $\text{PbZrO}_3\text{:PbTiO}_3$ system⁽¹⁾.

INTRODUCTION

Earlier measurements of the thermal parameters associated with the ferroelectric: paraelectric phase change in the $\text{PbZrO}_3\text{:PbTiO}_3$ solid solutions⁽²⁾ suggest that the thermal changes become anomalously small for compositions close to the morphotropic phase boundary, which occurs near the 1:1 Zr:Ti composition. In this earlier study however, samples were prepared by calcining and sintering the mixed oxide powders, and it is now well known that this preparation method can lead to compositional inhomogeneity particularly near the middle of the solid solution phase field.

To check the earlier data, and to compare with the predictions of a recently extended thermodynamic phenomenology⁽¹⁾, it appeared desirable to check the earlier work by using rather carefully chemically co-precipitated homogeneous compositions with the best available thermal analysis equipment.

SAMPLE PREPARATION AND CHARACTERIZATION

Seven samples in the solid solution system $\text{Pb}(\text{Zr}_x\text{Ti}_{1-x})\text{O}_3$, $0.0 < x < 0.6$ were prepared by a chemical coprecipitation technique. The starting materials [spectroscopic grade lead oxide, zirconium tetra-n-butoxide (ZBT) and titanium tetra-n-butoxide (TBT)] were weighed according to the desired stoichiometry and blended with isopropyl alcohol in a mixer for 3 minutes while deionized water was slowly added. The white precipitated slurry was pan dried, then ball milled with ZrO_2 balls and distilled water for 8 hours. The product was again pan dried and calcined at 600°C for 6 hours, followed by regrinding and recalcination at 800°C for 3 hours. X-ray powder patterns taken with CuK_α radiation showed sharp diffraction peaks up to high angles. There

were no phases present other than (P4mm) for compositions with $0.0 \leq x \leq 0.50$, and (R3m) for compositions with $0.50 \leq x \leq 0.60$.

CALORIMETRIC MEASUREMENTS

Heats of transition ($Q(J/M^3)$) and transition temperatures $T_C(K)$ were measured for each composition using the Perkin-Elmer DSC2 thermal analyzer under full computer control. The instrument was calibrated using indium as a standard. The heat of fusion of indium being taken as 6.79 cal/gm was reproducible within $\pm 2\%$. The proper correction factor was then applied to all measured Q values. The measurements were performed on 4 samples of each composition. The estimated errors were $\pm 3\%$ and $\pm 0.5\%$ for the Q and T_C values respectively. Detailed description of the automatic data collection, reduction, and integration method are given in the Perkin-Elmer DSC2 reference manual. Numerical values of $Q(J/M^3)$ and $T_C(K)$ as function of composition are given in Figure 1.

PHENOMENOLOGICAL THEORY

In the Landau-Ginzburg-Devonshire approach developed in (1), the energy function takes the form.

$$\Delta G_1 = \frac{(T-\theta)}{2\epsilon_0 C} p^2 + \text{temperature independent higher order terms.} \quad (1)$$

where ΔG_1 is the Elastic Gibbs Free Energy

P the dielectric polarization of the single domain

T the temperature

θ the Curie Weiss temperature

ϵ_0 the permittivity of free space (8.854×10^{-12} F/m)

C the Curie Weiss Constant.

The partial derivative of ΔG_1 at constant stress gives the negative of the entropy change, i.e.

$$-\Delta S = \frac{p_s^2}{2\epsilon_0 C} \quad (2)$$

The heat flow $Q = \Delta ST$, is for temperatures close to the Curie point T_C given by ΔST_C , so that the entropy change ΔS is

$$-\Delta S = \frac{Q}{T_C} = \frac{p_s^2}{2\epsilon_0 C} \quad (3)$$

Thus taking the magnitude of P_s obtained previously in reference (1) it is possible to derive the magnitude of the Curie constant T_C for each composition in the sequence. These data are plotted in Figure 2.

DISCUSSION

The data for Q presented in Figure 1 are in excellent qualitative agreement with the earlier data of Yves Setiveau et al.(2). The very low values of heat of transition for compositions close to morphotropy are confirmed and it is evident that the low values were not due to compositional heterogeneity. In the earlier thermodynamic formulation it was assumed in the absence of reliable dielectric data, that the Curie constant C had a constant value of 3.0×10^5 . The rather strong variation with

CALORIMETRIC AND PHENOMENOLOGICAL STUDIES OF THE $\text{PbZrO}_3\text{:PbTiO}_3$ SYSTEM

composition suggested by the data in Figure 2 will in fact bring the model permittivities and d constants much closer to those of the measured multidomain poled polycrystal and suggest that extrinsic domain contributions are not as important as was expected. Clearly some confirmation of these indirect deductions would be highly desirable, and point up the importance of improved high frequency dielectric measurement on well characterized homogeneous sample to verify directly the proposed trend.

REFERENCES

- (1) A. Amin, B. Badger, H.A. McKinstry, and L.E. Cross, An Elastic Gibbs Free Energy for the $\text{PbZrO}_3\text{:PbTiO}_3$ Solid Solution System. J. Appl. Phys. In press.
- (2) Yves Setiveau, Michel Troccaz, Lucieu Eyraud and Marc Richard. C.R. Acad. Sci., Paris, Serie B T266, 1968.

*Present address: Texas Instruments, Adv. Development Laboratory, 34 Forest St., Attleboro, MA 02703.

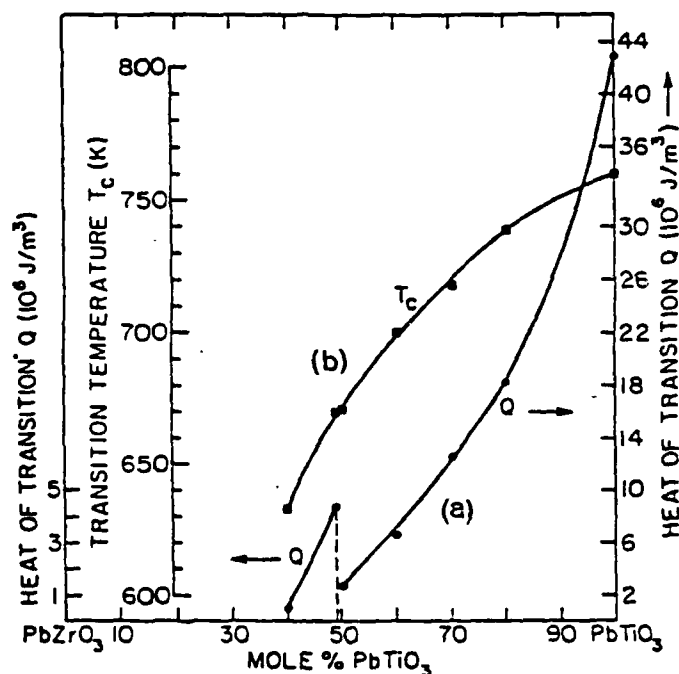


Figure 1. Curie temperatures and heats of transition for $\text{PbTiO}_3\text{:PbZrO}_3$ solid solutions.
 (a) Heats of transition
 (b) Transition temperatures

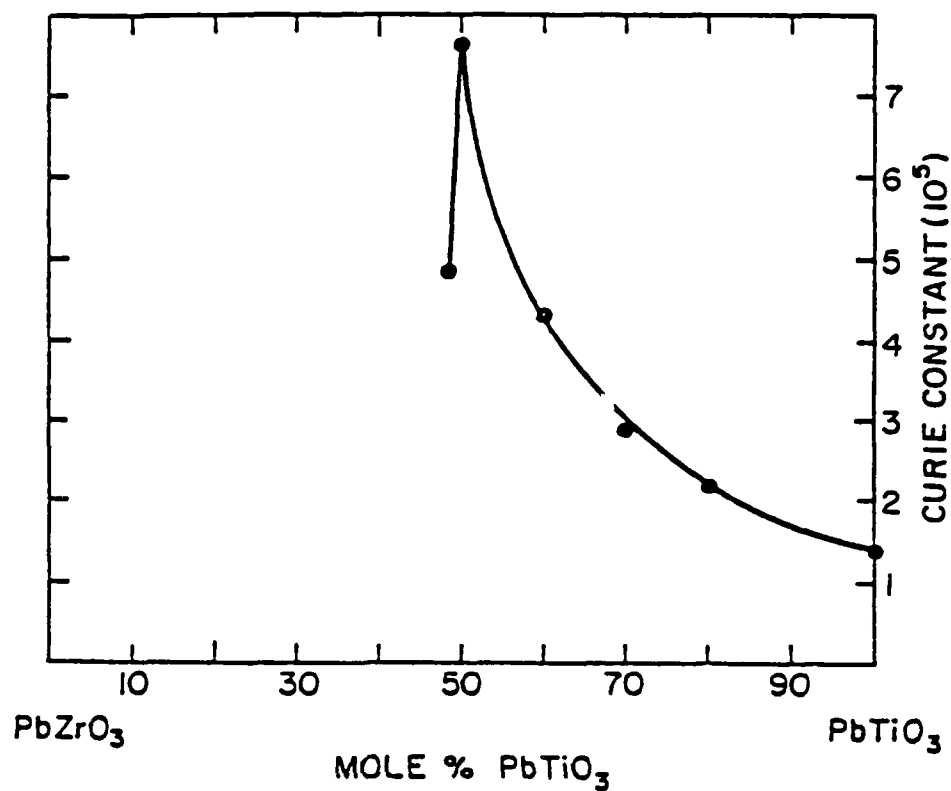


Figure 2. Curie Weiss constants for PbTiO_3 : PbZrO_3 solid solutions.

ACKNOWLEDGMENT

This work was supported by the Office of Naval Research under Contract No. N00014-78-C-0291. The preparation of PZT samples was carried through by Dr. S. Venkataramani.

AD-A114 497

PENNSYLVANIA STATE UNIV UNIVERSITY PARK MATERIALS RE--ETC F/6 20/3
TARGETED BASIC STUDIES OF FERROELECTRIC AND FERROELASTIC MATERIALS--ETC(U)
NOV 81 L E CROSS, R E NEWNHAM, G R BARSCH N00014-78-C-0291

UNCLASSIFIED

NL

2 OF 2

AD-A114 497



END
DATE
FILMED
6 82
DTIC

APPENDIX 12

Phenomenological and Structural Study of a Low-Temperature Phase Transition in the PbZrO_3 - PbTiO_3 System

Phenomenological and Structural Study of a Low-Temperature Phase Transition in the PbZrO_3 - PbTiO_3 System

A. AMIN, R. E. NEWNHAM, AND L. E. CROSS

*Materials Research Laboratory, The Pennsylvania State University,
University Park, Pennsylvania 16802*

AND D. E. COX

*Physics Department, Brookhaven National Laboratory, Upton, New York
11973*

Received January 14, 1980; in revised form October 2, 1980

The Landau-Ginsburg-Devonshire phenomenological theory has been applied to the PbZrO_3 - PbTiO_3 crystalline solid solution system to explore the behavior of the rhombohedral-tetragonal morphotropic phase boundary in the region below room temperature. The theory suggests that morphotropy is preserved, i.e., that the phase boundary occurs at nearly the same composition right down to 0 K. The rhombohedral ($R3m$)-rhombohedral ($R3c$) phase transition was investigated for a composition $\text{PbZr}_{0.6}\text{Ti}_{0.4}\text{O}_3$ using neutron diffraction. Structures in both phases were refined by the Rietveld profile fitting technique. The transition behavior in this composition was indicative of a diffuse-type phase transition, with a transition temperature somewhere between 250 and 300 K. The diffuse nature of this transition is perhaps due to short-range ordering of Zr and Ti. However, powder neutron diffraction is not ideal for determining critical behavior; therefore, it is difficult to make a quantitative conclusion in this respect. Values of the spontaneous polarization were obtained from the (Zr/Ti) shifts, and compared to those deduced from phenomenological theory.

Introduction

The perovskite solid solution between antiferroelectric PbZrO_3 and ferroelectric PbTiO_3 (PZT) contains a number of extremely important compositions used in the electronics industry (1). Many piezoelectric devices are made from poled PZT ceramics with compositions near the morphotropic phase boundary (MPB), the rhombohedral-tetragonal phase transition boundary (Fig. 1), where electromechanical coupling coefficients are unusually high.

In this work we report the results of applying the Landau-Ginsburg-Devon-

shire theory to PZT compositions near the morphotropic phase boundary at 248, 98, and 8 K, and a neutron diffraction investigation of the structure of one such composition, $\text{PbZr}_{0.6}\text{Ti}_{0.4}\text{O}_3$ at 295 and 9 K.

From an X-ray and neutron diffraction study of $\text{PbZr}_{0.58}\text{Ti}_{0.42}\text{O}_3$ and $\text{PbZr}_{0.9}\text{Ti}_{0.1}\text{O}_3$ at room temperature, Michel *et al.* (10) concluded that the space groups were $R3m$ and $R3c$ respectively, the latter involving doubling of the unit cell edges. In a recent neutron diffraction investigation Glazer *et al.* (11) have confirmed the existence of a transition from $R3c$ to $R3m$ symmetry in $\text{PbZr}_{0.9}\text{Ti}_{0.1}\text{O}_3$ with increasing temperature

PHASE TRANSITION IN PbZrO_3 - PbTiO_3

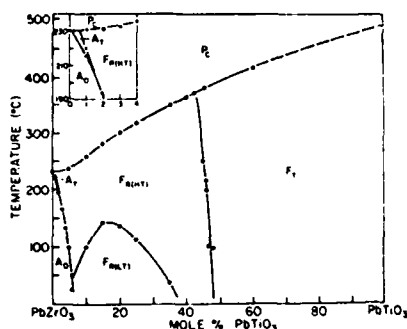


FIG. 1. PbZrO_3 - PbTiO_3 phase diagram (after Jaffe *et al.* (1)).

between 60 and 100°C and have determined the cation displacements as a function of temperature between 25 and 250°C.

Based on the phase diagram in Fig. 1, there should be a rhombohedral-rhombohedral phase transition below room temperature near the morphotropic boundary. The low-temperature rhombohedral cell is twice the size of the high-temperature cell. Mechanical Q measurements by Kruger (9) seem to indicate such a transition. This is not, however, a reliable method of establishing phase boundaries.

To verify the existence of the transition

we have done neutron diffraction experiments on $\text{PbZr}_{0.6}\text{Ti}_{0.4}\text{O}_3$ at two different temperatures (295 and 9 K). The structures were refined by the Rietveld method (2). Pyroelectric discharge experiments were carried out to explore the material response in the low-temperature region.

Landau-Ginsburg-Devonshire Phenomenology

For many ferroelectric crystals it has proved useful to correlate the dielectric, piezoelectric, elastic, and thermal properties of the paraelectric and ferroelectric phases by a thermodynamic free-energy theory. The Landau-Ginsburg-Devonshire (LGD) formalism gives an excellent description of these properties. A summary of past results can be found in the books on ferroelectricity by Jona and Shirane (3), Fatuzzo and Merz (4), and Lines and Glass (5).

Consider the free-energy function for a simple proper ferroelectric derived from a prototypic phase of symmetry $Pm\bar{3}m$. For Brillouin zone center modes, the free energy may be written as a power series in dielectric polarization P (6, 7) as follows:

$$\begin{aligned} \Delta G = & A(P_1^2 + P_2^2 + P_3^2) + B(P_1^4 + P_2^4 + P_3^4) + C(P_1^2 P_2^2 + P_2^2 P_3^2 + P_3^2 P_1^2) \\ & + D(P_1^6 + P_2^6 + P_3^6) + E(P_1^4 P_2^2 + P_2^4 P_1^2 + P_1^4 P_3^2 + P_3^4 P_1^2 + P_2^4 P_3^2 + P_3^4 P_2^2) \\ & + FP_1^2 P_2^2 P_3^2 - \frac{1}{2} S_{11}^p(X_1^2 + X_2^2 + X_3^2) - S_{12}^p(X_1 X_2 + X_2 X_3 + X_3 X_1) \\ & - \frac{1}{2} S_{44}^p(X_1^2 + X_2^2 + X_3^2) - Q_{11}(X_1 P_1^2 + X_2 P_2^2 + X_3 P_3^2) \\ & - Q_{12}(X_1(P_2^2 + P_3^2) + X_2(P_1^2 + P_3^2) + X_3(P_1^2 + P_2^2)) \\ & - Q_{44}(X_1 P_2 P_3 + X_2 P_1 P_3 + X_3 P_1 P_2), \end{aligned} \quad (1)$$

where A , B , C , D , E , and F are related to the dielectric stiffness and higher-order stiffness coefficients, S_{11}^p , S_{12}^p , and S_{44}^p are the elastic compliances measured at constant polarization, and Q_{11} , Q_{12} , Q_{44} are the cubic electrostriction constants in polariza-

tion notation. The expression is complete up to all six power terms in polarization, but contains only first-order terms in electrostrictive and elastic behavior.

Adjustable parameters in the free-energy function which fit the observed PbZrO_3 -

PbTiO_3 phase diagram and the observed physical properties (dielectric, piezoelectric, and coupling coefficients) have been determined (8). Numerical values of ΔG for the tetragonal modification ($P4mm$) are plotted as a function of composition in Fig. 2 for three different temperatures (248, 98, and 8 K). The results are also given for the rhombohedral ($R3m$) and orthorhombic ($Bmm2$) cells. The rhombohedral-tetragonal degeneracy at the morphotropic phase boundary is temperature independent, as suggested by Fig. 1. The theory suggests that morphotropy is preserved: i.e., that the phase boundary between the tetragonal and rhombohedral phase fields occurs at nearly the same composition right down to 0 K.

Sample Preparation

The $\text{PbZr}_{0.6}\text{Ti}_{0.4}\text{O}_3$ sample used for the neutron diffraction powder pattern and the pyroelectric discharge experiments was prepared by a chemical coprecipitation method. The starting materials [spectroscopic-grade lead oxide, zirconium tetra-*n*-butoxide (ZBT) and titanium tetra-*n*-butoxide (TBT)] were weighed and blended with isopropyl alcohol in a mixer for 3 min while deionized water was slowly added. The white precipitated slurry was pan dried, then ball milled with ZrO_2 balls and distilled water for 8 hr. The product was again pan dried and calcined at 600°C for 6 hr, followed by regrinding and recalcination at 800°C for 3 hr. X-Ray powder patterns taken with $\text{CuK}\alpha$ radiation showed sharp diffraction peaks up to high angles. There were no phases present other than rhombohedral ($R3m$) PZT.

Neutron Diffraction Studies

Data Collection

Neutron data from a $\text{PbZr}_{0.6}\text{Ti}_{0.4}\text{O}_3$ pellet

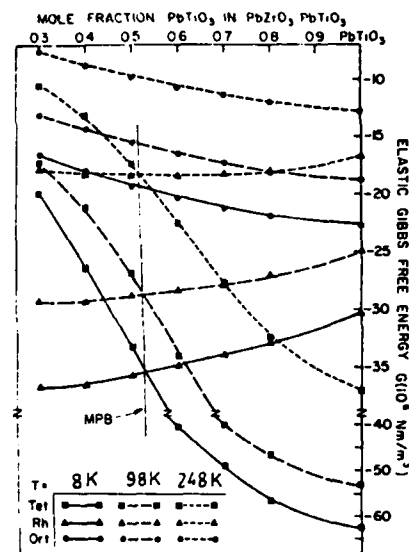


FIG. 2. Elastic Gibbs free energy as a function of composition across the single-cell region of the PZT phase diagram for three temperatures below room temperature.

were collected at the Brookhaven high-flux beam reactor at $T = 295$ and 9 K. Pyrolytic graphite in the (002) and (004) reflection positions were used as monochromator and analyzer, respectively. The neutron wavelength was 1.429 Å for the 9 K patterns and 1.650 Å for the 295 K pattern. Higher-order components were removed with a pyrolytic graphite filter. Data were collected at 0.05° intervals over each peak within a 2θ range 40–125° for the 295 and 9 K scans.

The 295 K data showed only reflections characteristics of the $R3m$ symmetry ($a \sim 4$ Å), but at 9 K a number of extra reflections were observed. The extra reflections observed at 9 K could be identified as the 311, 313, 511, 531, 531, . . . , and others with h, k , and l all odd indexed on a doubled cell ($a \sim 8$ Å).

Structural Model and Data Reduction

Based on previous studies (10, 11), the

rhombohedral-rhombohedral transition was expected to stem from the tilt system $a^- a^- a^-$ [Glazer (12)] or $\phi \phi \phi$ [Aleksandrov (13)]. In the Glazer notation, the system of "rigid octahedra" tilts is represented by the symbol $a^i b^j c^k$ where a , b , and c represent rotations about the three pseudocubic axes. The superscripts i , j , and k denote the sense of rotations of adjacent corner-linked octahedra, such that + means the same sense, - means opposite sense, and 0 means no rotation. Therefore, the tilt system $a^- a^- a^-$ means three equal rotations of the Zr/TiO_6 octahedra about the pseudocubic axes $\langle 100 \rangle$, with neighboring octahedra rotating in opposite senses. The tilt system $a^- a^- a^-$ produces $R3c$ (nonpolar) symmetry for the lower-temperature phase (9 K). However, since this transition is expected to be similar to those reported previously for other PZT compositions (10, 11), the structure was refined in space group ($R3c$). The polarity results from cation displacements along the rhombohedral $[111]$ direction.

The $\text{PbZr}_{0.6}\text{Ti}_{0.4}\text{O}_3$ structures were refined by means of the profile-fitting technique (2, 14). The following scattering lengths were used: 0.94, 0.71, -0.34, and 0.58×10^{-12} cm for Pb, Zr, Ti, and O, respectively. The refined parameters included a scale factor, three half-width parameters defining the Gaussian line shapes, a counter-zero error, isotropic temperature factors, atomic coordinates, and unit cell parameters.

In the rhombohedral phases we chose to use the double pseudocubic cell ($a \sim 8 \text{ \AA}$). The fractional atomic coordinates of the $R3c$ phase are then given by (21).

	x	y	z
Pb	$\frac{1}{4} + s$	$\frac{1}{4} + s$	$\frac{1}{4} + s$
Zr/Ti	t	t	t
O	$-e + d$	$\frac{1}{4} - 2d$	$e + d$

s and t represent the fractional cation displacements along the three-fold axis,

measured with respect to an origin lying midway between opposite faces of an oxygen octahedron. The parameter d is a measure of the octahedron distortion, which makes the upper and lower faces different. The e parameter indicates the rotation of an octahedron about the triad axis, with an angle of tilt ω , given by $\tan \omega = 4(3)^{1/2}e$.

In the $R3m$ phase there are no tilts, and e is equal to zero. The pseudocubic cell is not doubled in this phase, but to facilitate comparison of the two phases we also used a doubled cell to describe $R3m$. This was accomplished for $R3m$ by using the same symmetry operators used for $R3c$ and adding the constraint $x = y$ for the prototype oxygen atom, in addition to $x + y + z = \frac{1}{4}$.

Table I summarizes the refined parameters in each phase. The numbers between brackets represent the standard deviation in the least significant digit. Figure 3 shows calculated and observed intensity profiles for the two phases. The fit between observed and calculated profiles is quite good. The metal-oxygen bond lengths determined by neutron diffraction together with the sum of ionic radii "IR" of Shannon and Prewitt (15), are listed in Table II.

In addition, a limited amount of data was collected as a function of temperature with 2.46 \AA neutrons. The evolution of the strongest superlattice reflection, pseudocubic (311), is illustrated in Fig. 4, and the integrated intensities normalized with respect to the fundamental (220) reflection are shown in Fig. 5. From this it can be inferred that the transition is unusually broad, and starts somewhat between 250 and 300 K. The analogous transformation in $\text{PbZr}_{0.6}\text{Ti}_{0.4}\text{O}_3$ is similarly rather poorly defined (16, 17).

Close inspection of the data taken at 295 K with 1.65 \AA neutrons reveals a quite distinct modulation to the background scattering, as can be seen in Fig. 6 (lower

TABLE I
REFINED PARAMETER FOR $\text{PbZr}_{0.8}\text{Ti}_{0.2}\text{O}_3$

Temperature (K)	9	295
Shape parameters		
Phase	F_R (LT)	F_R (HT)
Space group	$R3c$ (C_{3v}^2)	$R3m$ (C_{3v}^1)
a_h (Å)	5.7597 (5)	5.7550 (4)
c_h (Å)	14.2510 (12)	14.2138 (11)
$2a$ (Å)	8.1730 (6)	8.1618 (4)
α (°)	89.614 (3)	89.676 (3)
Distortion parameters		
s	0.0343 (3)	0.0310 (4)
t	0.0114 (5)	0.0108 (7)
d	-0.0028 (1)	-0.0023 (1)
e	0.0105 (2)	—
ω (°)	4.2 (1)	—
Thermal parameters		
B (Pb)	0.57 (5)	1.9 (1)
B (Zr, Ti)	1.50 (2)	1.10 (17)
B (O)	1.24 (8)	1.57 (7)
Statistical parameters		
Number of parameters (P)	14	13
Number of observations (N)	802	934
Number of reflections	75	44
R_1 (%) ^a	1.68	4.85
R_2 (%) ^b	10.37	11.08
R_3 (%) ^c	11.70	14.28
R_{exp} (%) ^d	9.55	6.34

^a $R_1 = 100 \sum [I_{\text{obs}} - (1/c)I_{\text{calc}}] / \sum I_{\text{obs}}$.

^b $R_2 = 100 \sum [y_{\text{obs}} - (1/c)y_{\text{calc}}] / \sum y_{\text{obs}}$.

^c $R_3 = 100 \{ \sum w[y_{\text{obs}} - (1/c)y_{\text{calc}}]^2 / \sum w[y_{\text{obs}}]^2 \}^{1/2}$.

^d R_{exp} (the expected R factor) = $100\{(N - P + C) / \sum w[y_{\text{obs}}]^2\}^{1/2}$.

Note. I_{obs} , I_{calc} = observed and calculated integrated intensity of each reflection. y_{obs} , y_{calc} = observed and calculated profile data. w = weight allotted to each data point.

pattern). This type of modulation most likely arises from static displacements in preferred directions, since random displacements would simply lead to a monotonically increasing background, as is characteristic of thermal diffuse scattering. Calculations show that a simple model involving relaxation of about 0.1 Å of the six oxygen atoms in a TiO_6 octahedron towards

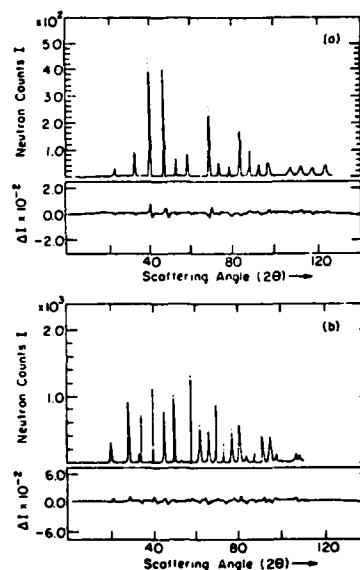


FIG. 3. Observed (dots) and calculated (full line) neutron intensity profile for the two phases of $\text{PbZr}_{0.8}\text{Ti}_{0.2}\text{O}_3$. The lower trace in each case is the difference between observed and calculated profiles. (a) F_R (HT) at 295 K; (b) F_R (LT) at 9 K.

the small Ti atom is qualitatively consistent with the general shape of the curve. However, the 221 K data from the temperature-dependence experiments which were obtained with much better counting statistics, show some structure in the Q range 0.9–0.3

TABLE II
METAL–OXYGEN BOND LENGTHS

Bond type ^a	Bond length (Å)		Sum of "IR"
	T = 295 K	T = 9 K	
Zr–Ti–O ₁	1.995	2.005	2.07
Zr–Ti–O ₂	2.098	2.101	
Pb–O ₁	2.912	3.041	2.89
Pb–O ₂	2.515	2.481	

^a O₁ and O₂ represent the oxygen atoms in the upper and lower faces respectively of an octahedron viewed along [111].

PHASE TRANSITION IN $\text{PbZr}_{0.6}\text{Ti}_{0.4}\text{O}_3$

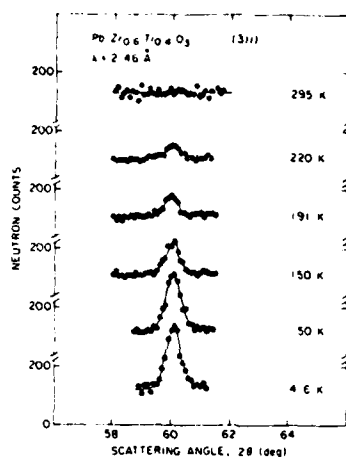


FIG. 4. Evolution of the pseudocubic (311) peak as a function of temperature. Data have been scaled for direct composition with the 4.6 K data, except for the 295 K results, which were obtained under slightly different conditions.

\AA^{-1} , indicative of additional correlations (Fig. 6, inset). These may reflect short-range order which is a precursor of the tetragonal phase, or perhaps a tendency towards ordering of Zr and Ti.

Pyroelectric Discharge Experiment

The Chynoweth (18) technique used to

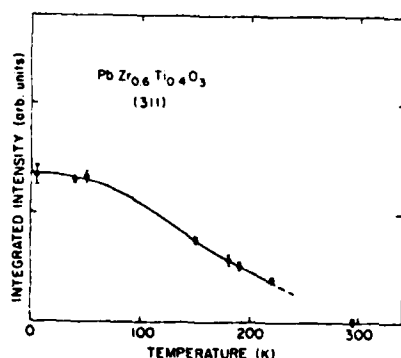


FIG. 5. Temperature dependence of the integrated intensity of the pseudocubic (311) reflection.

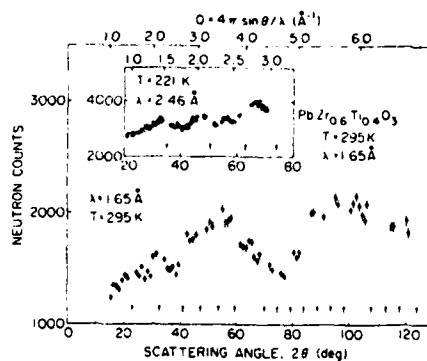


FIG. 6. Diffuse neutron scattering from $\text{PbZr}_{0.6}\text{Ti}_{0.4}\text{O}_3$. Lower diagram shows data taken at 295 K with 1.65 Å neutrons. Inset shows data taken with better counting statistics at 221 K with 2.46 Å neutrons. Gaps in data correspond to Bragg peaks. Arrows indicate peak positions derived from a primitive pseudocubic perovskite cell with $a = 4.08 \text{ \AA}$.

explore the material pyroelectric response in the low-temperature region is shown in Fig. 7. The sample (a ceramic disk 2.8 mm

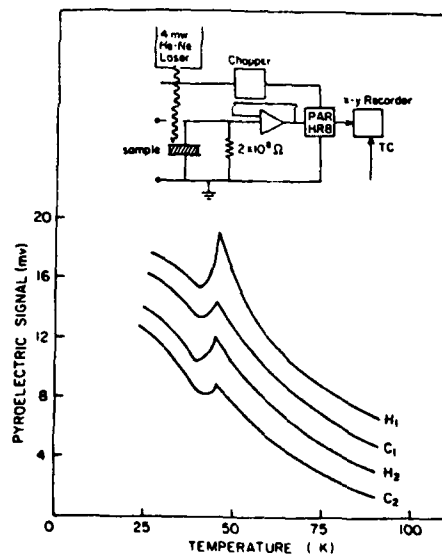


FIG. 7. Experimental arrangement and the pyroelectric signal as a function of temperature. The four curves represent successive heating and cooling cycles.

in diameter and 0.11 mm thick) was electroded with evaporated silver and mounted on a glass substrate. Using an electric field of 20 kV/cm, the ceramic was poled at room temperature. Carbon black was coated on the upper silver electrode to absorb light. The sample was then mounted in a recessed copper holder and cooled with liquid helium in an Air Products LT-3-110 cold finger. A buffer FET preamplifier positioned within the cold finger was used to minimize loading capacitance on the sample, thereby maintaining reasonable signal levels. The sample was irradiated by a chopped defocused 4-mW He-Ne laser and the pyroelectric signal detected with a lock-in amplifier (PAR-HR8). The level of pyroelectric signal (mV) as a function of temperature for two heating/cooling cycles (H_1 , C_1) and (H_2 , C_2) is shown in Fig. 7. The heating/cooling rates were about 4–5 K/min.

The observed peak in the pyroelectric signal around 50 K is not due to a ferroelectric–ferroelectric phase transition. It is probably due to (i) a relaxation effect in the sample as evidenced by the gradual decay of the 311 intensity in this temperature region; (ii) release of energy stored in a form of secondary cell activity involving oxygen vacancies which act as charge carriers and interact with the metal electrodes (22, 23). The laser beam chopper frequency is stable to $\pm 0.1\%$ in the frequency range 5–4000 Hz, therefore we exclude the non-uniform heating or cooling effect "false-pyroelectricity" (24) as a possible cause of the observed signal.

Correlation of the Spontaneous Polarization and Atomic Displacements

Based on a survey of 10 different ferroelectrics, Abrahams *et al.* (19) found that the spontaneous polarization P_s along the polar axis is linearly related to the homopolar atom shift δz (Å) by the relation

TABLE III
Zr/Ti ATOM SHIFTS AND SPONTANEOUS POLARIZATION

T (K)	Zr/Ti Shifts δz (Å)	P_s [111] from Eq. (2) (C/m ² ·Å)	P_s [111] from (LGD) Eq. (1) (C/m ² ·Å)
295	0.154 (9)	0.39 (3)	0.34
9	0.162 (7)	0.41 (2)	0.39 ^a

^a Taking into account the zone center mode only.

$$P_s = K \delta z, \quad (2)$$

where $K = 2.58$ (9) C/m²·Å.

A slightly different value of $K = 2.51$ (7) was found to hold for the PbZrO₃–PbTiO₃ system (20). Table III shows a comparison between P_s [111] as calculated from Eq. (2) using the experimentally determined Zr/Ti shifts, and the P_s [111] values obtained from the (LGD) phenomenology. The agreement between the phenomenological P_s values and the values determined from Eq. (2) is quite good.

Summary and Conclusions

A rhombohedral ($R3m$)–rhombohedral ($R3c$) phase transition was found to occur in PbZr_{0.6}Ti_{0.4}O₃. The structures above and below the phase transition temperature were refined by the neutron profile fitting method (2, 14). The transition behavior in this composition shows more interesting features. It can be seen from Fig. 4 that the temperature dependence of the 311 intensity is rather unusual in that it does not approach the temperature axis very sharply to give a well-defined transition. The transition is unusually broad and starts between 250 and 300 K. The diffuse nature of this transition is perhaps due to short-range ordering of Zr and Ti. However, it is always difficult to separate Bragg- and diffuse-scattering components from powder data, therefore, it is premature to make any quantitative conclusions in this respect.

PHASE TRANSITION IN PbZrO_3 - PbTiO_3

The Landau-Ginsburg-Devonshire (LGD) phenomenological results showed no anomalies of morphotropy compositions below room temperature. The spontaneous polarization values P_s as determined from the phenomenological theory are in surprisingly good agreement with the values calculated from the Zr/Ti shifts using Abrahams, Kurtz, and Jamieson's relation.

Acknowledgments

Ahmed Amin wishes to thank the Brookhaven National Laboratory for the kind hospitality during his stay there. This work was supported by the Office of Naval Research, Contract N00014-78-C-0291, and Division of Basic Energy Sciences, U.S. Department of Energy, under Contract EY-76-C-02-0016.

References

1. B. JAFFE, W. R. COOK, AND H. JAFFE, "Piezoelectric Ceramics," Academic Press, London/New York (1971).
2. H. M. RIETVELD, *J. Appl. Crystallogr.* **2**, 65 (1969).
3. F. JONA AND G. SHIRANE, "Ferroelectric Crystals," Pergamon, Oxford (1962).
4. E. FATUZZO AND W. J. MERZ, "Ferroelectricity," New York (1967).
5. E. M. LINES AND A. M. GLASS, "Principles and Applications of Ferroelectrics and Related Materials," Oxford Univ. Press (Clarendon), London/New York (1977).
6. A. F. DEVONSHIRE, *Philos. Mag.* **40**, 1040 (1949).
7. V. GINSBURG, *J. Exp. Theor. Phys. USSR* **15**, 739 (1945).
8. A. AMIN, B. BADGER, JR., H. MCKINSIRY, AND L. E. CROSS, *J. Appl. Phys.*, in press.
9. H. A. KRUGER, "Final Technical Report," Clevite Corporation, Cleveland (1971).
10. C. MICHEL, J. M. MOREAU, G. D. ACHENBACH, R. GERSON, AND W. J. JAMES, *Solid State Commun.* **1**, 865 (1969).
11. A. M. GLAZER, S. A. MABUD, AND R. CLARKE, *Acta Crystallogr. Sect. B* **34**, 1060 (1978).
12. A. M. GLAZER, *Acta Crystallogr. Sect. B* **28**, 3384 (1972).
13. K. S. ALEKSANDROV, *Ferroelectrics* **14**, 801 (1976).
14. A. W. HEWAT, *J. Phys. C* **6**, 2559 (1973).
15. R. D. SHANNON AND C. T. PREWITT, *Acta Crystallogr. Sect. B* **25**, 925 (1969).
16. R. CLARKE AND A. M. GLAZER, *J. Phys. C* **7**, 2147 (1974).
17. D. BAÜRLE AND A. PINCUK, *Solid State Commun.* **19**, 1169 (1976).
18. A. G. CHYNOWETH, *J. Appl. Phys.* **27**, 78 (1956).
19. S. C. ABRAHAMS, S. K. KURTZ, AND P. B. JAMIESON, *Phys. Rev.* **172**, 551 (1968).
20. A. AMIN, R. E. NEWMHAM, AND L. E. CROSS, to be published.
21. H. D. MEGAW AND C. N. W. DARLINGTON, *Acta Crystallogr. Sect. A* **31**, 161 (1975).
22. J. D. HURD, A. W. SIMPSON, AND R. H. TREDGOLD, *Proc. Phys. Soc.* **73**, 448 (1959).
23. J. W. NORTHRIP, *Bull. Amer. Phys. Soc.* **4**, 424 (1959); *J. Appl. Phys.* **31**, 2293 (1960).
24. W. G. Cady, "Piezoelectricity," McGraw-Hill, New York (1946).

APPENDIX 13

Studies of Ferroelectric Surfaces Using
Ion Beam and Chemical Etching Techniques

STUDIES OF FERROELECTRIC SURFACES USING ION BEAM AND CHEMICAL ETCHING TECHNIQUES

L.L. TONGSON, A.S. BHALLA and L.E. CROSS *

Materials Research Laboratory, The Pennsylvania State University, University Park, PA 16802, USA

Abstract—The chemical nature of the intrinsic surface layer in BaTiO₃ single crystals and the positive and negative surfaces of Gd₂(MoO₄)₃ have been determined using the specular reflection of low energy inert gas ions. Potassium and fluorine were detected impurities in Remeika-grown BaTiO₃ crystals. The positive and negative surface of gadolinium molybdate crystals were chemically identical. However, significant effects of the orientation of the electric polarization vector on the scattering of incident He-4 ions were observed. The ion-beam irradiated areas showed a passivation effect towards chemical etchants.

INTRODUCTION

Several experimental studies¹ have provided indirect evidence of a "modified" layer at the surfaces of ferroelectric materials. Such layers can exert significant influence on the coercive field, switching time, permittivity, etc., in very thin specimens. Generally, two types of models have been proposed: (1) a physical model of space charge layers due to surface ionic vacancies, and (2) a chemical model in which the thin layer is part of the crystal² and may be chemically different from the bulk.^{3,4} In gadolinium molybdate (GMO), the apparent influence of the electric fields associated with the emergent spontaneous polarization on the chemical reactivity of the surface has been utilized to reveal the domain structure.⁵ That is, when dipped in a dilute hydrofluoric acid, coherent and firmly adhering films of gadolinium fluoride are produced on the surface.⁶ The thickness of the film differs for domains of opposite polarity, so that the underlying domain structure is revealed in reflected white light by clear interference colors.

The elastic scattering of low energy inert gas ions has been utilized to determine the chemical nature of (1) "as-grown" BaTiO₃ surfaces, and (2) polar surfaces of GMO single crystals.

EXPERIMENTAL PROCEDURE

The multi-domain, unpoled, BaTiO₃ single crystals were grown by the Remeika method in a potassium fluoride flux. The surfaces were examined in the "as-grown" condition, i.e., without etching or polishing to determine the intrinsic layer.

The GMO samples were cut from a single crystal boule with the major faces perpendicular to the ferroelectric [001] axis. After polishing with 1/4 μ m alumina powder, the plates were poled by applying a shear stress along a *b* axis. Essentially single domain surfaces were utilized; the polarity was determined using a Berlincourt d33 meter.

In ion surface scattering (ISS), a beam of low energy (<2 kV) inert gas ions impinges the sample surface and the energies of ions elastically scattered by surface

atoms in a known direction are measured. The struck atoms are identified according to mass by applying conservation of momentum and energy.

The ISS data were obtained at typical probe ion current densities of about 20-25 $\mu\text{A}/\text{cm}^2$ using a 1mm-FWHM-diam 1500 eV He^+ ion beam. The scattering angle was 90° . For studying oppositely poled surfaces of GMO, the spectra were recorded under identical experimental conditions, i.e. constant ion beam and charge neutralization currents. Shifts in position of the scattered ion peaks as a function of surface potential were studied by biasing a metallic target at +21.6, 0, and -21.6 volts with respect to ground.

RESULTS AND DISCUSSION

BaTiO₃ crystals. Fig. 1 shows the ISS data obtained from the "as-grown" BaTiO₃ crystal. The predominant impurities were potassium and fluorine. The plot shows that the Ba peak grows as the potassium peak decreases. When K was no longer detectable, the Ba signal assumed a stable value. Similar opposite variations were observed in the oxygen and fluorine signals. These results were consistent with the suggestion that potassium and fluorine form substitutional impurities in Ba and O sites, respectively.⁷ Since Ba, Ti and oxygen were detected initially, these impurities were not uniformly distributed on the surface.

GMO crystals. The composition of the outer surface of a polished GMO crystal is revealed in a series of scans shown in Fig. 2. One interesting feature is the variation of the Mo signal relative to the Gd peak. The initial spectra of Fig. 2a indicated a predominantly Mo rich layer. After 40 min of ion bombardment, Fig. 2c, the Mo peak was lower than the Gd signal. No changes from the spectra shown in Fig. 2c were observed even under prolonged ion bombardment.

Spectral features revealed by Fig. 2a were independent of surface preparation techniques: (1) mechanically polished (MP), (2) MP and annealed in air for 20 h at 120°C,

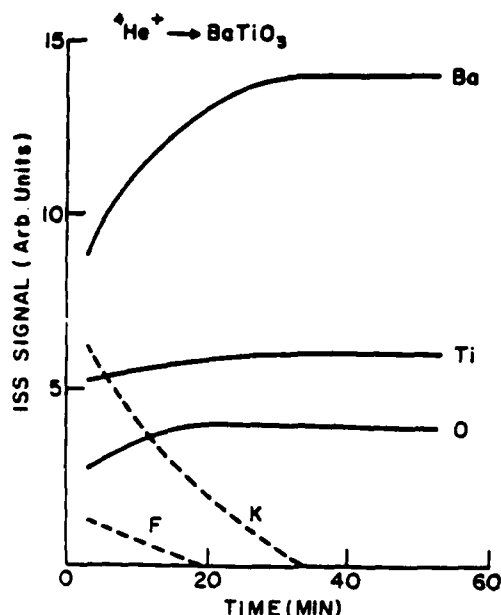


FIG. 1. ISS signal vs. sputtering time for the intrinsic layer in Remeika grown BaTiO₃ crystals.

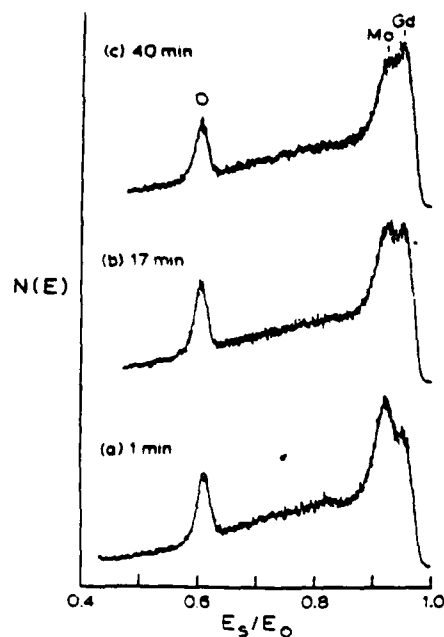


FIG. 2. The spectrum of $^4\text{He}^+$ ions scattered from a GMO crystal at (a) 1 min, (b) 17 min and (c) 40 min of ion bombardment.

STUDIES OF FERROELECTRIC SURFACES USING ION BEAM AND CHEMICAL ETCHING ...

and (3) MP and chemically etched in HNO_3 acid. Variations of the Gd and Mo signals with ion bombardment time were the same for "positive" and "negative" surfaces.

Fig. 3 shows the effects of changing the surface potential on the position of the scattered ion peak, for 1500 eV Ne-20 ions incident on cobalt. Biasing the target above (below) ground shifts the scattered ion peak towards higher (lower) energy ratios. The additional peaks at $E_s/E_0 < 0.100$ correspond to target atoms which are ejected or sputtered as ions. The sputtered ion peaks start at 0,0 and ≈ 12 V above ground when the target is biased at -21.6, 0.00 and +21.6 V relative to ground, respectively. That is, at positive bias, the beginning of the sputtered peaks is shifted towards higher energies.

Fig. 4 shows the spectrum of sputtered and scattered ions for He-4 incident on (a) the domain with the positive end of the dipole on the surface, and (b) the negative domain of GdO. In Fig. 4a, the position of the oxygen and gadolinium peaks are displaced from their normal values of 0.600 and 0.950 in 90° ISS. No shifts in position of the corresponding peaks for the negative domain were detected. Subtle differences in the energy distribution and intensity of sputtered ions from these two types of domains were noted. A reduction in intensity accompanied by a broader distribution in energy was obtained in Fig. 4a.

The displacement of ion scattering peaks from positions predicted by binary scattering was discussed by Helbig et al.⁸ They showed that displacement to higher energies due to charging in insulating samples is caused by the repelling field which changes both the scattering angle and the impact energy of the incident ion during the collision. The data in Fig. 4a do not show a shift in the appearance threshold of the sputtered peak. Hence, the displacement of the scattered peaks cannot be due to positive charge build-up on the surface.

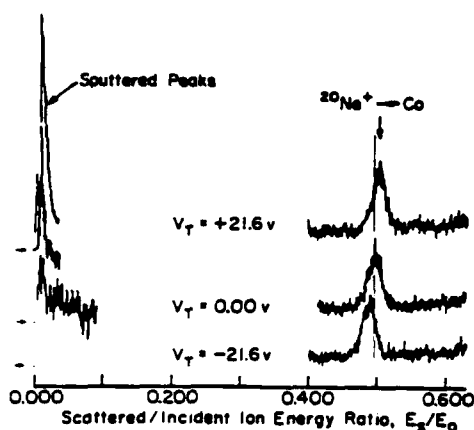


FIG. 3. Sputtered and scattered ion spectra for 1500 eV Ne-20 ions incident to cobalt for target bias of -21.6, 0.00 and +21.6 v relative to ground.

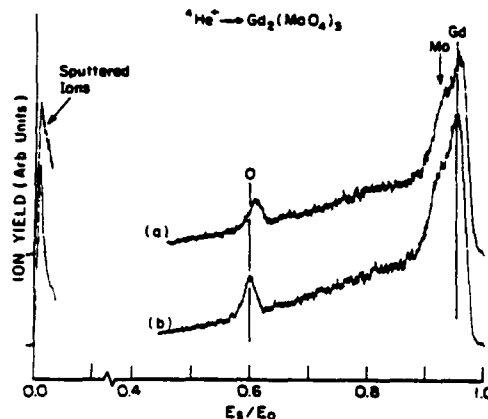


FIG. 4. Scattered and sputtered ion spectra for 1500 eV 4He^+ incident on (a) the domain with the positive end of the dipole on the surface, and (b) the negative domain of GdO crystals.

Passivation of GdO surfaces. We observed that irradiating the GdO surfaces with He, Ne or Ar ions caused marked changes in the chemical reactivity of the bombarded region.⁹ These areas exhibited passivation against chemical attack by dilute HF. Figure 5 shows this effect in which only the grid-covered portion of the crystal was decorated with GdF_3 .

In order to confirm the vast reduction in chemical reactivity of the ion bombarded surface, the ISS spectra of passivated and unpassivated areas were compared. The fluorine signal in the passivated region was less than 5% of its value from the decorated portion.

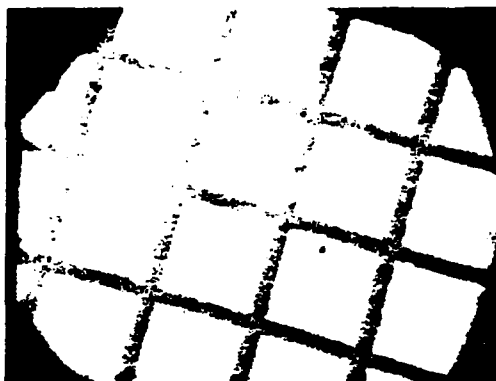


FIG. 5. Passivated and unpassivated areas revealed by decoration of ion beam irradiated c surface of GMO crystal.

In addition to this small fluorine signal, the ISS spectra from the bombarded surface were similar to Fig. 2c.

Amorphising a very thin surface layer to the extent of reducing its chemical reactivity and implantation of inert gas ions have been proposed⁹ to explain the observed passivation. The phenomenon may be of considerable interest in device applications of GMO.

REFERENCES

1. M.E. Lines and A.M. Glass, Principles and Applications of Ferroelectrics and Related Materials (Clarendon Press, Oxford, 1977), p. 117.
2. M.E. Drougard and R. Landauer, J. Appl. Phys., 30, 1663 (1959).
3. F.C. Lissalde and J.C. Peuzin, Ferroelectrics, 4, 159 (1972).
4. Yu. Ya. Tomashpolskii, E.N. Lubnin and M.A. Sevost'yanov, Sov. Phys. Crystallogr., 22, 330 (1977).
5. A.S. Bhalla and L.E. Cross, J. Mater. Sci., 12, 2346 (1977).
6. A.S. Bhalla, L.L. Tongson, I.S.T. Tsong and L.E. Cross, Thin Solid Films, 53, 55 (1978).
7. H. Arend, P. Coufova and J. Novak, J. Amer. Cer. Soc., 50, 22 (1967).
8. H.F. Helbig, P.J. Adelman, A.C. Miller and A.W. Czanderna, Nucl. Instrum. and Methods, 149, 581 (1978).
9. A. Bhalla, L.E. Cross and L. Tongson, Phys. Stat. Sol. (a), 45, K1 (1978).

*Also affiliated with the Department of Electrical Engineering.

APPENDIX 14

Interactions Between Orthogonal Domain Walls in Gadolinium Molybdate

INTERACTIONS BETWEEN ORTHOGONAL DOMAIN WALLS IN GADOLINIUM MOLYBDATE

A.S. BHALLA AND L.E. CROSS

Materials Research Laboratory, The Pennsylvania State University, University Park, PA 16802

Abstract—Detailed investigation of orthogonal domains in (001) sections of single crystal ferroelectric ferroelastic gadolinium molybdate ($\text{Gd}_2(\text{MoO}_4)_3$, GMO) have been undertaken using a high resolution decoration technique. Both the cusplike features and the bowing of the planar walls in the extended strain fields are observed. Thickness of the 180 degree walls as revealed by the decoration technique is estimated to be less than 1μ .

INTRODUCTION

The interactions between domain walls in ferroelastic:ferroelectrics are of fundamental interest and also of practical importance in the development of controlled domain geometries for certain device applications¹. Orthogonal walls occur quite frequently in ferroelastic crystals and often involve large associated strain fields. The problem of wedge shaped domains and of the shape of wedge terminations near orthogonal plane walls has been treated recently by Indenbom and Chamrov². This analysis suggests the existence of a cusp at the tip of a wedge which approaches an orthogonal wall.

In the present paper detailed investigation of orthogonal domains in (001) sections of single crystal ferroelectric:ferroelastic gadolinium molybdate ($\text{Gd}_2(\text{MoO}_4)_3$, GMO) have been undertaken using chemical etching techniques.

EXPERIMENTAL RESULTS AND DISCUSSION

HCl, HNO_3 and HF acids attack (001) surfaces of GMO single crystals but each one in slightly different way. Hydrochloric acid (10%) reveals domain walls, dislocations and the phase boundaries in negative domains only. Dilute HNO_3 (5-10%) reveals dislocation sites, domain walls and phase boundaries in both positive and negative domains. A 1-2% water solution of hydrofluoric acid reveals the domain walls only but the etching rates are different for positive and negative domains. Based on these studies, a simple technique has been developed to study the domain structure of GMO. Under suitable conditions the reaction in weak hydrofluoric (1%) acid can produce uniform, coherent and firmly adhering films of GdF_3 . Since on the (001) crystal faces the reaction rates differ for positive and negative emergent domains and domain walls area the film thickness is different over domains of different sign and the domain wall. The large differences of optical refractive index between GdF_3 and $\text{Gd}_2(\text{MoO}_4)_3$ causes film of suitable thickness to exhibit strong interference colors in reflected white light which clearly reveal the underlying domain structure³ and the domain wall. The technique has a very high resolution ($\sim 1 \mu$) and is utilized in the present studies to

examine the domain geometries as influenced by the dislocation features associated with the domain walls, domain tips and at the junction of the orthogonal domains.

On the basis of dislocation theory domain walls can be represented as an array of edge dislocations continuously distributed along the direction of the wall. In GMO the domain walls run along $[110]$ and $[1\bar{1}0]$ in the c -plane. The planar antiparallel domains adjacent to these walls are in twin relationship with each other. In a non-planar or wedge shaped domain the domain tip can be considered as the assemblage of dislocations⁴ with a resultant burger vector $\beta = 2\omega e_{xy}$, where ω is the domain width and e_{xy} is the spontaneous shear strain. Figure 1(a) shows the dislocation etch pit at the tip of the wedge domain and the different types of pits revealed in positive and negative domains Fig. 1(b). Such features could be revealed by the chemical action of dil. HNO_3 on the "decorated" (001) surfaces of GMO.

The interactions between the various types of domain walls in GMO on the basis of dislocation theory is shown in Figure 2. In the case of a right angle wall two possible mismatched $2e_{xy}$ or $-2e_{xy}$ between the lattices at the domain wall occurs. A strain field is created to accommodate the mismatch of the lattices of two domains. Two orthogonal families of domain have the large strain fields associated at the junction which can be represented by the resultant edge dislocation (Figures 2 and 3). Such dislocation strain or stress fields result in the bowing of the planar walls and cusp-like features at the junction². Some of these features have been studied on thin sections of GMO in transmission electron microscopy⁵ but other studies on the bulk samples have not shown clearly these characteristics due to the lack of desired resolution. In our studies we were able to reveal the dislocation strain fields at the junction and the bowing of the walls in the extended strain fields by decoration technique (Figure 4). Even though the stable configuration at the junction is reached, a substantial amount of strain energy due to lattice misfit is preserved in the area as shown by the decoration colors in the region. A subsequent etching of the crystal with 5% HNO_3 revealed the presence of these strain fields as indicated by the dislocation etch pits at the junction of the wedge shaped domain approaching the orthogonal wall.

180 degree domain wall thickness in a ferroelastic-ferroelectric GMO crystal are estimated by various authors (Table 1) to be of several hundred lattice spacings in contrast to ferroelectric BaTiO_3 where these thicknesses are only a few lattice spacings⁶. Kittel⁷ has predicted theoretically the thicker ferroelastic walls and estimated the 180 degree wall thickness in GMO $\sim 0.4\mu$ and 90° domain walls in $\text{BaTiO}_3 \sim 0.1\mu$ thick. These estimates are in close agreement with the experimentally observed values between 0.8μ and 3μ in GMO for the 180 degree walls⁸ and 0.4μ in BaTiO_3 ⁹.

The decoration technique has resolution better than 1μ and domain tips of $\sim 1\mu$ observed in the present studies suggested the domain wall thickness $< 1\mu$. The various reported values of the domain wall thickness in the bulk crystals are much larger than the 100 \AA value reported by electron microscopic observations on 2000 \AA thick crystals. The discrepancy may be due to the surface tension forces which become prominently more effective in controlling the elastic fields and deviation of the domain walls from their proper planes in a very thin crystal.

ACKNOWLEDGEMENT

This work was sponsored by the U.S. Office of Naval Research, Contract No. N00014-78-C-0291.

INTERACTIONS BETWEEN ORTHOGONAL DOMAIN WALLS IN GADOLINIUM MOLYBDATE

Table 1. Domain wall thickness in ferroelectric-ferroelastic GdMO single crystal as estimated by various techniques.

Author	wall thickness (μ)	c-plate thickness (mm)	Technique
Kittel ⁷	0.4	--	Theoretical modeling
Shepherd et al. ⁸	0.8	0.76	Raman Scattering
	3 μ	0.76	Polarizing microscope with highly convergent beam
Suzuki ¹⁰	1.3	0.76	Fraunhofer diffraction
Yamamoto et al. ¹¹	0.01	2 x 10 ⁻⁴	Electron microscope
Present studies	<1 μ	0.5 - 1	"Decoration"

REFERENCES

1. U.S. Patent 3,799,648 (1974).
2. V.L. Indenbom and V.A. Chumov, Sov. Phys. Crystallogr. **25**, 123 (1980).
3. The vivid interference colors are shown in A.S. Bhalla and L.E. Cross, J. Mater. Sci. **12**, 2346 (1977).
4. J. Bornarel and J. Lajzerowicz, Ferroelectrics **4**, 177 (1972).
5. N. Yamamoto, K. Yagi and G. Honjo, Phys. Stat. Sol. (a) **41**, 523 (1977); **42**, 257 (1977).
6. T. Malis and H. Gleiter, J. Appl. Phys. **47**, 5195 (1976).
7. C. Kittel, Sol. State Commun. **10**, 119 (1972).
8. I.W. Shepherd and J.R. Barkley, Sol. State Commun. **10**, 123 (1972).
9. E.A. Little, Phys. Rev. **98**, 978 (1955).
10. K. Suzuki, Sol. State Commun. **11**, 937 (1972).
11. N. Yamamoto, K. Yagi and G. Honjo, Phil. Mag. **30**, 1161 (1974).

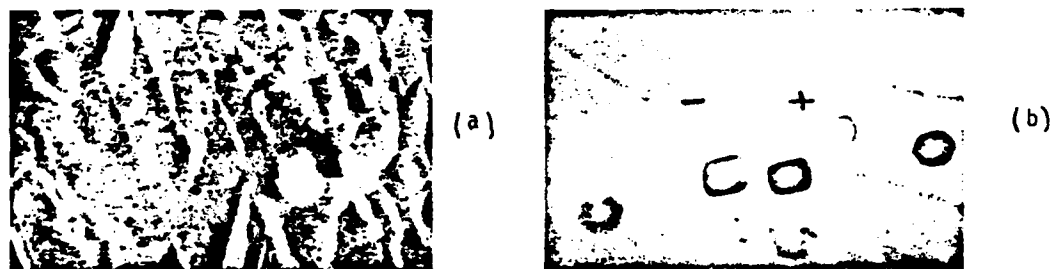


Figure 1. (a) dislocation etch pit at the tip (A) of the wedge domain ($\times 600$) and (b) dislocation etch pits in positive and negative domains as revealed by etching of (001) surfaces of GdMO with 5% HNO_3 water solution ($\times 200$).

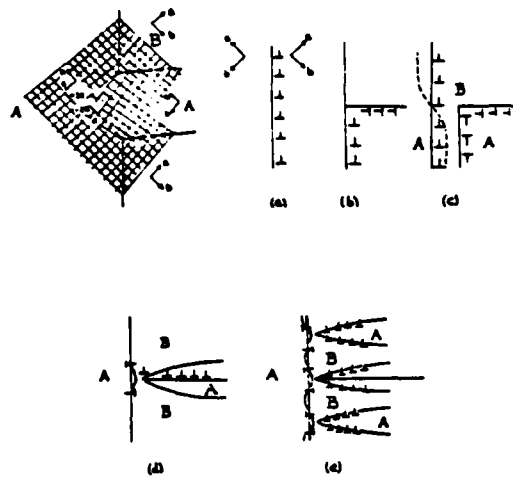


Figure 2. Lattice mismatch at the junction of orthogonal domain walls. Dislocation representations of (a) domain wall (b) right angle domain wall (c) interaction between the planar and right angle domain wall (d) and (e) twin wedge model at the intersection of the orthogonal walls.



Figure 3. Dislocation etch pits (A) at the junction of the orthogonal domains, (001) surface, (x200).

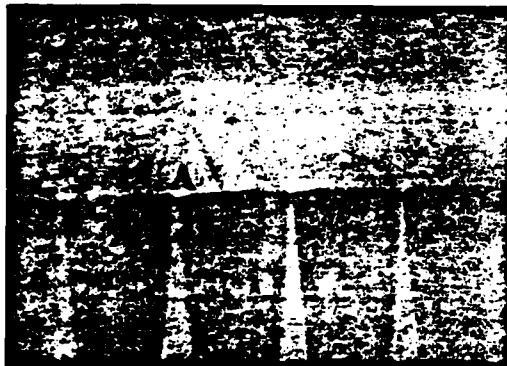


Figure 4. Bowing of the planar wall and the cusplike features at the junction of the orthogonal domains as revealed by the decoration technique. 'A' Residual stress fields (x1200).

APPENDIX 15

Unusual Ferroelastic Behavior in
Ferroelectric Lead Bismuth Niobate ($\text{PbBi}_2\text{Nb}_2\text{O}_9$)

UNUSUAL FERROELASTIC BEHAVIOR IN FERROELECTRIC LEAD
BISMUTH NIOBATE ($\text{PbBi}_2\text{Nb}_2\text{O}_9$)

O. DELAPORTE, G.R. BARSCH, L.E. CROSS
Materials Research Laboratory, The Pennsylvania State
University, University Park, PA 16802, USA

E. RYBA
Department of Materials Science, The Pennsylvania State
University, University Park, PA 16802, USA

Abstract X-ray and optical measurements are used to show that the spontaneous strain ($b/a-1$) and optical birefringence Δn_{ab} in single crystals of ferroelectric $\text{PbBi}_2\text{Nb}_2\text{O}_9$ are a function of the state of electrical poling, going to a zero in the unpoled state. In poled crystals all spontaneous strain is lost at a temperature $\sim 200^\circ\text{C}$ below the dielectric Curie temperature in a manner reminiscent of the behavior of the perovskite relaxor ferroelectrics which have diffuse phase transitions.

Lead bismuth niobate ($\text{PbBi}_2\text{Nb}_2\text{O}_9$) is one member of a large family of ferroelectric bismuth oxide layer structure compounds.¹⁻³ In PBN, the bismuth oxide $\text{Bi}_2\text{O}_7^{2+}$ layers are separated by two perovskite-like $\text{PbNb}_2\text{O}_7^{2-}$ sheets.⁴ The structure has been reported to be orthorhombic C_{2v}^{18} ($Fmm2$)⁵ and it is expected to have 4 domain states in which the polar axis lies along 110 , $\bar{1}10$, $1\bar{1}0$, or $\bar{1}\bar{1}0$ in the plane normal to the prototypic 4-fold axis. The prototypic group is centric so that 180° domain states will be strain identical (ferroelectric) whilst 90° domains will exhibit ferroelastic behavior. Earlier spontaneous strain measurements by Ismailzade⁵ on powder samples show an unusual slow tailing off of the spontaneous strain at temperatures well below the dielectric Curie point, with a gradual disappearance of the last vestiges of strain very close to T_c .

Single crystal boules of PBN for this study were grown by Dr. M. Brun by Czochralski pulling⁶ and exhibited large $5 \times 5 \times 5$ mm volumes which appear optically twin free.

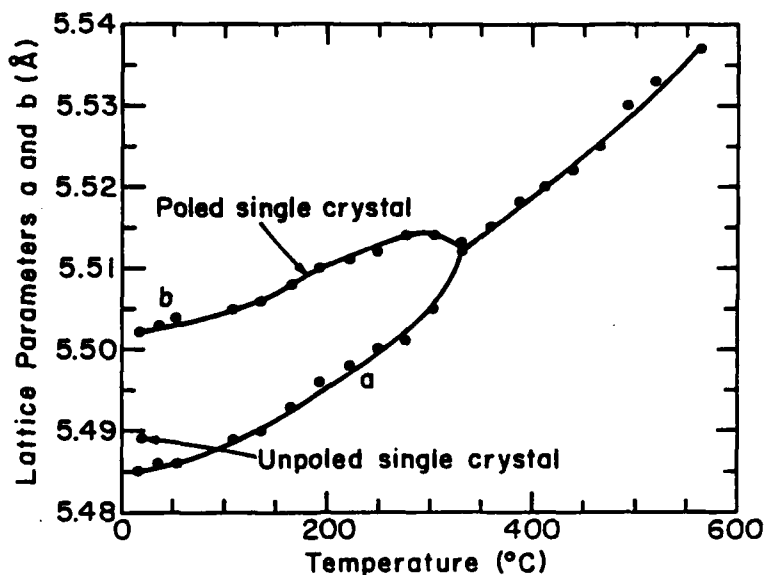


FIGURE 1. Lattice parameters a and b versus temperature for single crystal lead bismuth niobate (PBN).

X-ray measurements taken on annealed unpoled single crystals using a Picker 4-circle goniometer show no measurable difference in b- and a-axial lengths (datum point in Fig. 1). Also, c sections of the annealed crystal examined in polarized light show no birefringence ($\Delta n_{ab} \approx 0$). On poling under DC field of 10 kV/cm, however, the crystals exhibit clearly different b- and a-axial dimensions ($b/a \neq 1$), Fig. 1, but the distinction is lost at a temperature of 325°C, more than 200°C below the dielectric Curie Maximum. In polarized light, the poled sample also shows a clear birefringence $\Delta n_{ab} = 0.0035$ measured in white light using a Berek type compensator.

Dielectric measurements on 'a' axis plates show an obvious Curie maximum in ϵ_{11} near 555°C (Fig. 2) and Curie Weiss behavior ($C = 1.4 \times 10^5 \text{ } ^\circ\text{K}$) above T_c . In the lower temperature domain below T_c , a shoulder sometimes appears in the curve on first heating (Fig. 2) which appears to have a dispersive character.

On the poled 'a' plate after 27 kV/cm for 20 minutes, a d_{11} of 24×10^{-12} C/N was measured using a Berlincourt d_{33} meter.

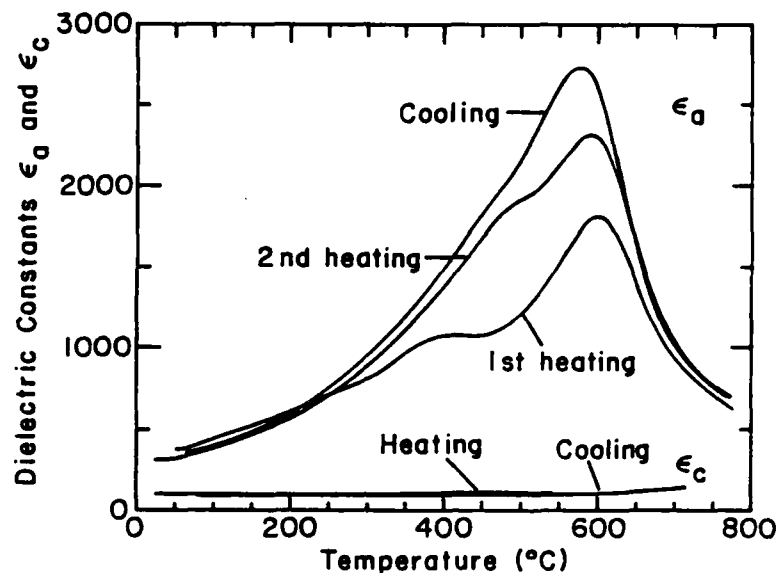


FIGURE 2. Weak field dielectric constants ϵ_a and ϵ_c versus temperature for single crystal lead bismuth niobate (PBN) measured at a frequency of 10 kHz.

It is interesting to note the similarity in the behavior of PBN to that of single crystals in the perovskite family which exhibit diffuse phase transitions, e.g., $\text{Pb}(\text{Mg}_{1/3}\text{Nb}_{2/3})\text{O}_3$. In these materials again there is the absence of any measurable spontaneous strain in the unpoled crystals⁷, zero birefringence⁸ and similar poling behavior, with Δn going to zero at a temperature much below the dielectric Curie point maximum.⁸

For PBN, it is suggested that a micro-domain structure with dimensions less than the wavelength of light may also be responsible for cancelling the birefringence. The interesting new feature in our measurements is the clear evidence that spontaneous strain is also effectively eliminated. We are tempted to believe that the low spontaneous strain of the poled crystal $b/a \approx 1.003$ may permit the normally strain-forbidden (001) domain walls to occur. Thus closely knit overlapping orthogonal domains may eliminate Δn and clamp out the strain b/a .

It is difficult to ascertain from present data whether the absence of $b/a \neq 1$ above 325°C in the poled crystal is due to instability of the micro-domain structure, as in $\text{Pb}(\text{Mg}_{1/3}\text{Nb}_{2/3})\text{O}_3$, or is associated with a second phase change. Clearly, from the piezoelectric datum, the phase below 325°C in the poled crystal is ferroelectric, in the species $4/\text{mmm}$ (2) $\text{D}_4 \text{Fmm}2$. Additional measurements are now being undertaken to better characterize the intermediate temperature region.

REFERENCES

1. B. Aurivillius, Ark. Kemi, 1, 463 (1949).
2. E.C. Subbarao, J. Phys. Chem. Solids, 23, 665 (1962).
3. K.H. Hellwege, Landolt-Börnstein, Group III, Volume 16, Ferroelectrics and Related Substances, Subvolume a, Section 9 (Springer, NY, 1979), pp. 230-243.
4. R.E. Newnham, R.W. Wolfe, J.F. Dorrian, Mat. Res. Bull., 6, 1029 (1971).
5. I.G. Ismailzade, Izv. Akad. Nauk SSSR Ser. Fiz., 24, 1198 (1960); Bull. Acad. Sci. USSR, Phys. Ser., 24, 1201 (1960).
6. G.R. Barsch, K.E. Spear, Air Force Report #RADC-TR-79-4; M. Brun, K.E. Spear, to be published.
7. G.A. Smolenskii, V.A. Isupov, A.I. Agranovskaya, N.N. Krainik, Fiz. Tverd. Tela, 2, 2982 (1960); Sov. Phys. Solid State, 2, 2584 (1961).
8. V.A. Bokov, I.E. Myl'nikova, Fiz. Tverd. Tela, 3, 841 (1961); Sov. Phys. Solid State, 3, 613 (1961).

APPENDIX 16

Shape-Memory Effect in PLZT Ferroelectric Ceramics

Shape-Memory Effect in PLZT Ferroelectric Ceramics

T. KIMURA, R. E. NEWNHAM and L. E. CROSS

*Materials Research Laboratory, The Pennsylvania State University,
University Park, Pennsylvania 16802, U.S.A.*

(Received April 30, 1981)

The shape-memory effect in PLZT (Lead Lanthanum Zirconate Titanate) ceramics with composition $x/65/35$ ($4.0 \leq x \leq 8.0$) has been investigated using bending experiments and temperature cycling. Relationships between load and the degree of bending, together with their temperature dependence, have been determined, and characteristic temperatures associated with the onset and disappearance of the pseudo-plastic shape change are compared with the observed dielectric anomalies. Effects of mechanical stress and electric field on the shape-memory temperatures and the magnitude of strain have also been investigated. It is concluded that domain alignment and the temperature-dependence of spontaneous strain are important factors governing the shape-memory effect in ferroelectrics. Preferred-orientation effects have been confirmed by X-ray diffraction analysis.

1 INTRODUCTION

The recovery of a plastically deformed material to its original shape by heating is called the shape-memory effect. This effect has been extensively studied in metallic alloys and is generally associated with martensitic phase transformations (Warlimont, 1976; Delaey, Krishnan, Tas, and Warlimont, 1974). Phase transformations in ferroelectric materials are not martensitic, but Schmidt and Boczek (1978) observed apparently similar effects in PLZT ceramics. Details of the phenomena occurring in PLZT are not clear.

Applications for PLZT ceramics include a number of different optical devices (Haertling and Land, 1971; Maldonado and Meitzler, 1970, 1971; Maldonado and Anderson, 1971). The materials of interest are conventionally referred to in the $x/y/z$ notation, where x gives the atomic percentage of La and y/z is the Zr to Ti ratio. Attention has generally been concentrated

on materials of composition $x/65/35$. Those with $x > 4.5$ exhibit an interesting phenomenon called *penferroelectricity* (Meitzler and O'Bryan, 1973), *quasi-ferroelectricity* (Carl and Geisen, 1973) or $\beta \rightarrow \alpha$ phase transformation (Keve and Annis, 1973). PLZT specimens with $x = 8.0$ show relaxor behavior with a diffuse phase transition.

This paper describes the shape-memory effect in PLZT ceramics with La concentrations between 4.0 and 8.0 at. %. Because of their simplicity, bending experiments were used to investigate the shape change. The effects of stress and La content on the magnitude of bending strain, and on the memory effect were determined. The characteristic temperatures associated with the shape-memory effect were compared with the dielectric anomalies, and it was concluded that ferroelectric domains are the main cause of the shape-memory effect in ferroelectric ceramics.

2 EXPERIMENTAL

Five hot-pressed PLZT ceramic wafers with compositions $x/65/35$ ($x = 4.0, 6.5, 7.0, 7.5$ and 8.0) were obtained from Dr. William Harrison at Honeywell Inc. The wafers were cut and polished into rectangular bars of width 2 mm, thickness 0.35 mm and length 15 mm, and then annealed at 600°C for 15 h.

Bending experiments were used to measure the shape change. The specimen was positioned on two knife-edge supports separated by 12 mm, and surrounded by a small brass box. A heater placed under the box could raise the temperature up to 270°C , as measured by a thermocouple positioned near the sample. One end of a glass rod was placed at the center of the sample and the other end attached to a dilatometer probe. Movement of the probe was measured with a differential transformer. To apply load to the sample, lead weights were placed on a shelf attached to the glass rod.

The sample was heated to a selected temperature above the Curie temperature, and the load was then applied. The sample was then cooled to room temperature under constant load. At room temperature the load was removed (except for the 8.6 g weight of the measurement probe) and the sample was then reheated. During the reheating cycle, the glass rod and dilatometer probe maintained contact with the sample to measure the amount of bending.

Stress and strain were calculated assuming a circular arc. Since both stress and strain are functions of position throughout the cross-section of the bar, the calculated values are for the maximum stress and strain present on the outside surface of the bar.

Dielectric properties were measured at frequencies of 1, 10, 100 and 1000 kHz. The major face of the bar was electroded by Au-evaporation and poled with a DC field of 15 kV/cm at room temperature. Dielectric constant and

SHAPE-MEMORY EFFECT IN PLZT

loss factor were measured by a capacitance bridge at a constant heating rate of $2^\circ/\text{mm}$.

The samples with $x = 4.0$ and 7.0% La (width 2 mm, thickness 1 mm and length 12 mm) were squeezed at 400 kg/cm^2 (equivalent to the bending load of 86 g) at 310°C and 800°C , respectively, and cooled to room temperature. Sample faces, perpendicular and parallel to the stress direction, were examined by X-ray diffraction using Ni-filtered $\text{CuK}\alpha$ radiation and compared with a diffraction pattern recorded before squeezing.

3 STRESS-STRAIN-TEMPERATURE RELATIONSHIPS

Figure 1 shows the typical behavior of the bending strain with temperature under several different loads. Application of a load at high temperature bent the sample bar elastically, and the bending returned to zero upon removal of the load. The magnitude of elastic bending agreed with the value calculated using the reported values of s_{11} (Schmidt and Boczek, 1978; O'Bryan, 1973). On cooling under load, the magnitude of bending did

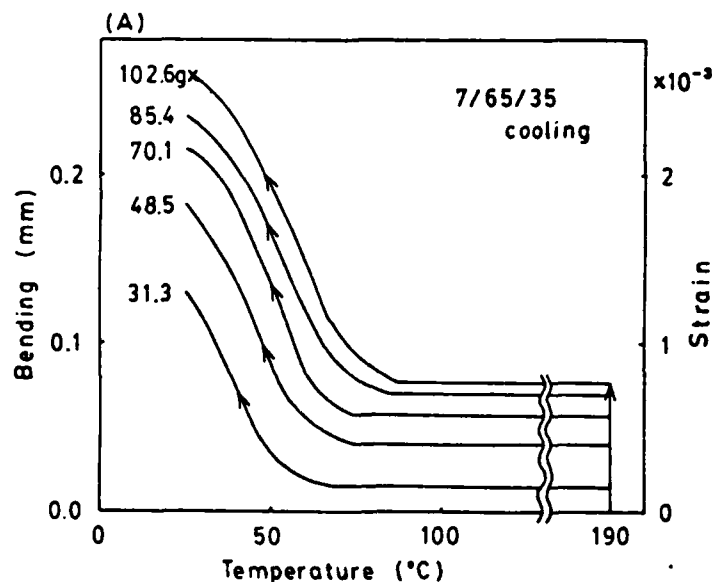


FIGURE 1(A) Bending behavior of a 7.0/65/3.5 ceramic as a function of temperature during cooling under several fixed loads. A load of 102.6 g caused fracture of the sample during cooling as indicated by X.

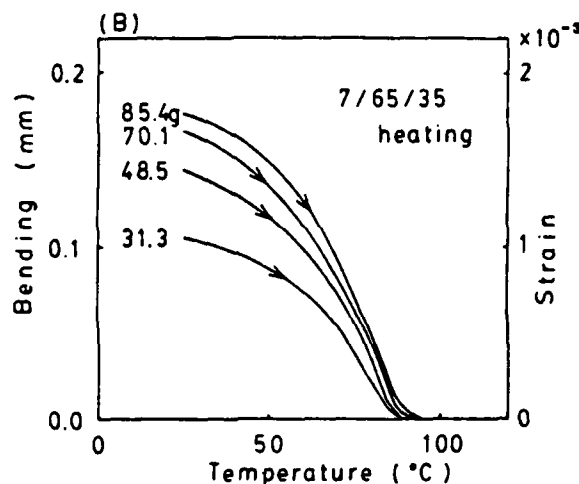


FIGURE 1(B) Bending behavior of a 70/65/35 ceramic during heating without load. The weights used to produce deformation during the preceding cooling cycle are given beside each curve.

not change appreciably down to a certain temperature T_s , at which bending began to increase rapidly, and continued increasing to room temperature. When the weight was removed at room temperature, there was a slight reduction in the amount of bending. The reduction in bending agreed with the value calculated from the s_{11} coefficient, indicating that this part of the strain was elastic. Reheating without load decreased the plastic portion of bending until it became zero at temperature T_f . The original shape was completely recovered by heating.

The elastic part of the bending increased linearly with the increase in load, but the plastic contribution tended to saturate. The amount of load also affected the characteristic temperature T_s . The initial deformation temperature T_s shifted to higher values under larger loads, but the shape-recovery temperature T_f did not depend noticeably on the size of load applied during cooling. Further increase in the load caused fracture of the sample during cooling, as indicated in Figure 1(A).

4 EFFECT OF La CONTENT ON THE STRAIN-TEMPERATURE RELATION

Figure 2 shows the effect of La content on the strain-temperature relation under various loads. Data showing maximum bending for each composition were selected; further increases in load caused fracture of the samples.

SHAPE-MEMORY EFFECT IN PLZT

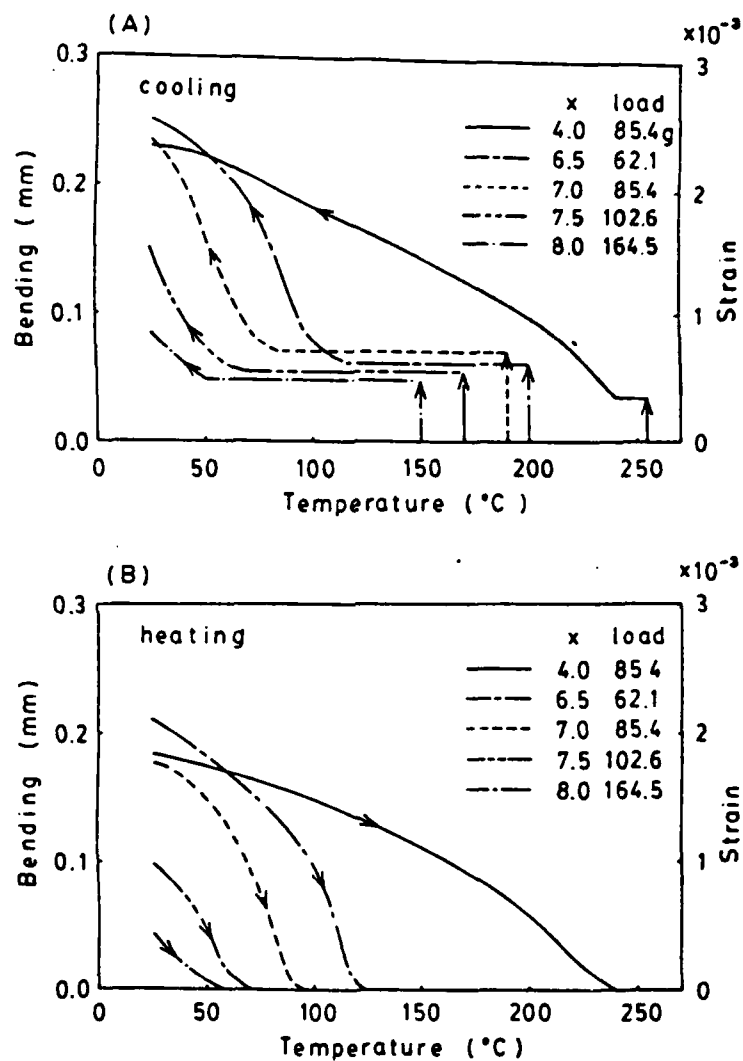


FIGURE 2 Effects of La content on the temperature-dependence of bending during (A) cooling under constant load and (B) heating without load.

Figure 3 shows the relations between temperatures T_s and T_f and the amount of load, as well as the load which caused fracture.

As judged from the amount of bending and dependence of T_s on load, the shape-memory behavior of the sample with $x = 4.0$ was different from that in the composition range $6.5 \leq x \leq 8.0$. For samples with $6.5 \leq x \leq 8.0$, those of higher La content showed less bending at room temperature as well as lower deformation temperatures T_s and restoration temperatures T_f . Larger loads were required to produce an equivalent bending in samples with high La content. The deformation temperature T_s was significantly lower than T_f . Furthermore, T_s increased appreciably with increasing load but T_f did not depend strongly on load. For the sample with $x = 4.0$, the characteristic temperatures T_s and T_f were the highest within the composition range examined, but the magnitude of bending at room temperature was about the same as the other samples. Furthermore, T_s and T_f were equal for the 4% sample and did not depend on the load applied.

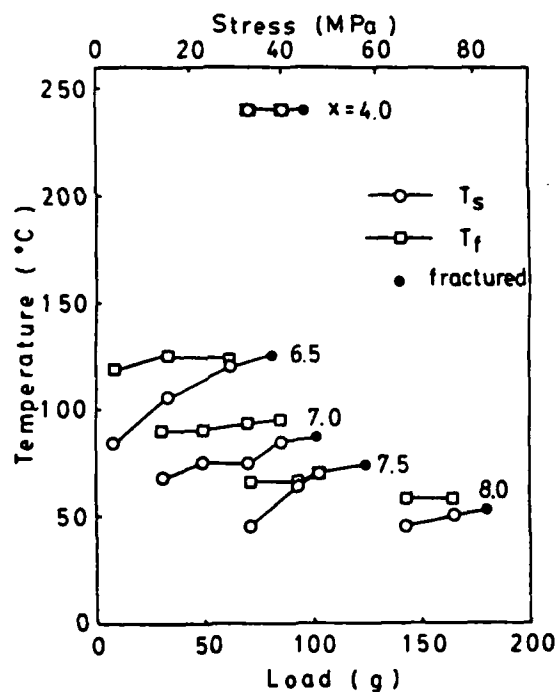


FIGURE 3 Relationships between characteristic temperatures T_s and T_f and the amount of load.

SHAPE-MEMORY EFFECT IN PLZT

Another difference in the $x = 4.0$ sample was the behavior of bending during temperature-cycling under no load. After the samples were cooled under constant load, they were reheated to a certain temperature below T_f and then recooled without load. The bending increased as the temperature was lowered. For the $x = 4.0$ sample, the relation between bending and temperature was the same as that observed originally when cooled under stress, when the sample was reheated up to 10°C below T_f . Reheating above T_f and cooling without load caused no bending. In samples with $6.5 \leq x \leq 8.0$, the amount of bending observed during recoiling was smaller than that of the initial cooling under load, and room-temperature bending was dependent on the temperature at which recoiling was begun. For example in the case of the $x = 7.0$ sample deformed at 85.4 g ($T_f = 96^\circ\text{C}$), recoiling from 56°C reduced the room-temperature bending to 70% of the original value, and from 74°C the amount was 400%.

5 RELATION BETWEEN DIELECTRIC AND MECHANICAL PROPERTIES

The dielectric constant of poled samples with $6.5 \leq x \leq 8.0$ showed relaxor behavior in which the temperature of the dielectric maximum T_c depended on the measuring frequency. Furthermore there was a pre-maximum peak

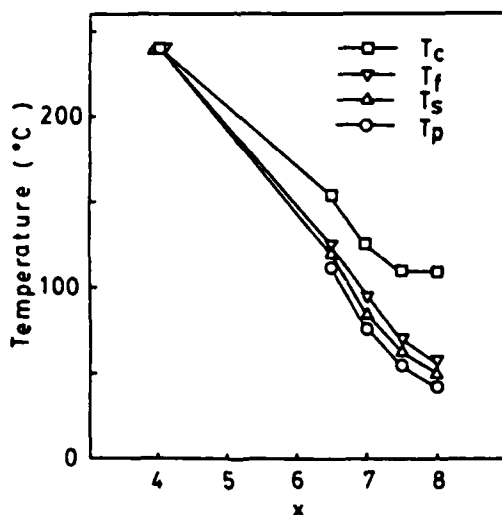


FIGURE 4 Curie temperature T_c , pre-maximum temperature T_p , deformation temperature T_s , and restoration temperature T_f as a function of La content x .

associated with the disappearance of ferroelectric domains. The temperature of the pre-maximum peak T_p did not depend strongly on measuring frequency. In the case of $x = 4.0$, there was no pre-maximum peak and T_c did not depend on measuring frequency.

Figure 4 shows the relationship between La content and the characteristic temperatures T_c , T_p , T_s and T_f . The values of T_s and T_f were collected from the data shown in Fig. 2, and the T_c values correspond to those measured at 1 kHz. The T_s and T_f temperatures of the sample with $x = 4.0$ coincide with T_c , but those of the sample with $6.5 \leq x \leq 8.0$ lay between T_c and T_p . The dependence of T_s and T_f on La content more closely resembles that of T_p rather than T_c .

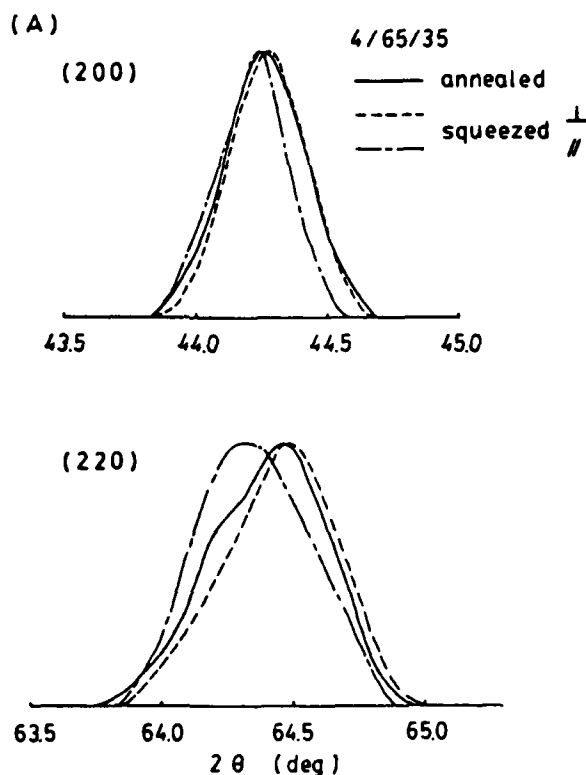


FIGURE 5 X-ray diffraction profiles of annealed (—) and compressed PLZT (---) face perpendicular, and (—) face parallel to stress direction) for (A) $x = 4.0$.

SHAPE-MEMORY EFFECT IN PLZT

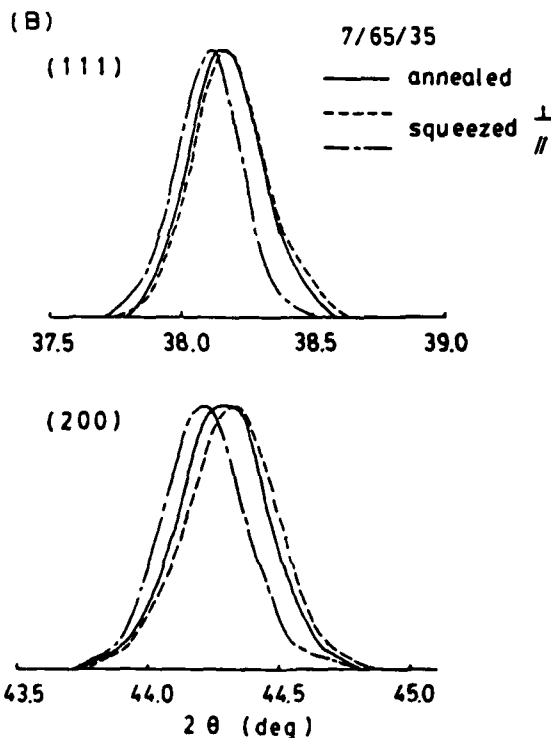


FIGURE 5 (contd.) for (B) $x = 7.0$.

6 X-RAY MEASUREMENT

Seven strong diffraction lines (110, 111, 200, 210, 211, 220 and 310) of annealed and compressed samples were examined. Figure 5 shows a few peak profiles and Table 1 lists the diffraction angles. The unit cell of the annealed samples was either rhombohedral ($x = 4.0$) with $a = 4.094$ Å and $\alpha = 89.76^\circ$, or cubic ($x = 7.0$) with $a = 4.086$ Å, in good agreement with the reported structures and cell size (Keve and Bye, 1975; O'Bryan and Meitzler, 1972).

Peaks from the compressed samples shifted to higher values for faces cut perpendicular to the stress direction, and to lower angles for faces parallel to the stress. As expected for compression, the d -spacings of the faces oriented perpendicular to the stress direction were smaller than those of the faces

cut parallel to the stress. Peaks from the faces perpendicular to the stress were similar to those of the annealed sample.

Quantitative determination of phases present in the compressed samples was difficult because good high-angle diffraction data were not available. Because the largest differences in d -spacings between mutually perpendicular faces were between (220) and (200) for the $x = 4.0$ sample and between (200) and (111) for the $x = 7.0$ specimen, the structures were judged to be rhombohedral ($x = 7.0$).

7 DISCUSSION

For compositions with $x \leq 4.0$, the samples behave like normal ferroelectrics, but for those in the range $8 \geq x \geq 6.5$, domains are not observed on cooling through T_c , nor do they disappear at T_c on heating. Ordered domains in a poled ceramic disappear at T_p in this composition range. The close relationship between the shape-memory temperatures T_s and T_f , and T_c and T_p suggests that the domain process plays an important role in the shape-memory effect. Mechanical stress orders the domains at T_c ($x = 4.0$) or at T_p ($6.5 \leq x \leq 8.0$) during cooling, which results in a large pseudo-plastic strain at room temperature. Heating eliminates the domains and restores the original shape.

X-ray diffraction measurements on the compressed samples (Figure 5 and Table I) gave the largest d -spacings from sample faces oriented parallel

TABLE I
Diffraction angles of annealed and compressed PLZT x 65/35 with
 $x = 4.0$ and 7.0

hkl	Angle of peak maximum, 2θ ($^\circ$)					
	$x = 4.0$			$x = 7.0$		
	Annealed	Compressed \perp	Compressed \parallel	Annealed	Compressed \perp	Compressed \parallel
110	30.91	30.92	30.89	30.94	30.96	30.90
111	38.13	38.14	38.10	38.15	38.16	38.11
200	44.26	44.28	44.24	44.28	44.33	44.22
210	49.79	49.80	49.72	49.84	49.86	49.78
211	55.00	55.01	54.90	55.01	55.05	54.93
220	64.46	64.48	64.30	64.47	64.51	64.39
310	73.14	73.18	73.07	73.16	73.24	73.07

\perp Faces perpendicular to stress.

\parallel Faces parallel to stress.

SHAPE-MEMORY EFFECT IN PLZT

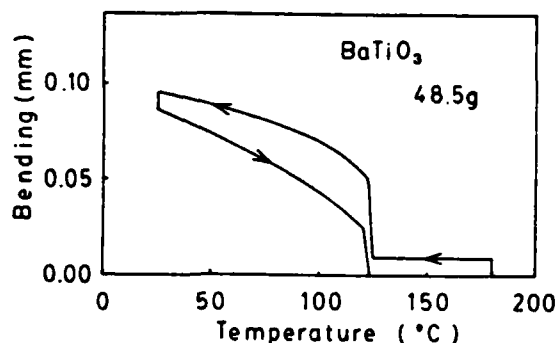
to the stress direction. This means that the polar directions are preferentially aligned perpendicular to the compressional stress.

For samples with La content $6.5 \leq x \leq 8.0$, the deformation temperature T_d depends on load, but the restoration temperature T_r does not (Figure 3). Electrically, the discontinuity temperature in polarization shifts to higher values when the dc bias field increases (Keve and Annis, 1973). This abrupt change in polarization with temperature is associated with the domain phenomena occurring at T_p . This effect is analogous to the shift in T_d and T_r under mechanical stress. Since no mechanical stress was applied during heating, however, the restoration temperature T_r was not influenced by the stress applied during cooling. Apparently, mechanical stress has similar effects to an electric field in aligning domains. The anisotropic thermal expansion coefficients (O'Bryan and Meitzler, 1972) observed in hot-pressed PLZT ($x = 8.0$) further supports this view. Radial stresses developed during cooling in the hot-pressing procedure cause domain alignment below the Curie temperature. Thermal expansion coefficients parallel to the direction of the compressional stress are higher than in annealed material, while negative coefficients are observed in the direction of tensile stresses.

These facts show that the polar direction can be easily aligned by stress when the sample is cooled through the temperature at which the domains form. Tensile stress aligns the polar direction parallel to the stress direction, and compressive stress favors domains in the perpendicular direction.

The relationship between bending and temperature shown in Figures 1 and 2 differs from the results reported by Schmidt and Boczek (1978), especially with regard to the shape of the cooling curve and the magnitude of bending. They observed a large bending at high temperature, and an elastic compliance about 300 times larger than the value determined by resonance measurement. This discrepancy might be attributed to the method of supporting the sample. Schmidt and Boczek used a cantilever method, in which one end of the sample was fixed, but this results in a rather complicated stress state. In our experiment, the samples were freely held by two supports. Under these circumstances, the stress state at a supporting position is not as complicated. Since stress levels strongly affect the shape-memory effect, the discrepancy in the results may be attributable to the experimental method.

Schmidt and Boczek (1978) postulated, on the basis of their data, that the relaxor or diffuse phase transformation was essential to obtain the shape-memory effect in ferroelectrics. The PLZT sample with $x = 4.0$, however, is not a relaxor. The fact that this sample shows a shape-memory effect indicates that the relaxor behaviour is not an essential property. To confirm this idea, BaTiO₃ ceramic bar with the same shape and size as the PLZT samples was examined. Figure 6 shows the bending-temperature relation. Upon cooling from 180°C under constant stress, bending increased

FIGURE 6 Temperature-dependence of bending of BaTiO₃.

abruptly between 125° and 122°C and more slowly below 122°C. When the sample was reheated after removing the load at room temperature, bending decreased gradually up to 121°C and then fell sharply to zero between 121° and 123°C. This abrupt change in shape near the Curie temperature (126°C) coincides with the discontinuity in the lattice parameters, and indicates that domain formation and disappearance are likely causes of the shape-memory effect in ferroelectrics.

The maximum room-temperature strain obtained in these experiments was 2.1×10^{-3} in the sample with $x = 6.5$. The stress field is complicated in the bending test and it is difficult to understand which of the stresses, tension or compression, govern the strain. However, the observed strain can be compared with electrically-induced strain. In the sample with $x = 7.0$, the strains parallel and perpendicular to the electric field at room temperature are 2.1×10^{-3} and 0.5×10^{-3} , respectively (Smith, 1973). In our experiment the plastic part of the strain at room temperature in such a sample was 1.8×10^{-3} (Figure 1), which is comparable to the strain parallel to the electric field. Table II lists the values calculated from the data in Table I. The strains were calculated by comparing the d -spacings between compressed and annealed samples. In both samples, the strains observed in the faces parallel to the stress direction were larger than those in perpendicular faces. In the compressed samples, the polar axes are nearly perpendicular to the stress direction as discussed previously. The large strains observed parallel to the stress direction coincide with the large strains measured parallel to the electric field.

Large strains under tensile stress have been observed in samples with $x = 1.3$ and 6.0 (Meitzler and O'Bryan, 1971). At room temperature, the maximum strain in the $x = 6.0$ sample was 2.5×10^{-3} , which is almost the same strain observed in the present experiments. A structural phase change

SHAPE-MEMORY EFFECT IN PLZT

TABLE II
Differences of d -spacing between annealed
and compressed samples

hkl	$\frac{d \text{ compressed} - d \text{ annealed}}{d \text{ annealed}} \times 10^3$			
	$x = 4.0$		$x = 8.0$	
	\perp	\parallel	\perp	\parallel
110	-0.3	0.7	-0.7	1.4
111	-0.2	0.8	-0.3	1.0
200	-0.4	0.4	-1.1	1.3
210	-0.2	1.3	-0.4	1.1
211	-0.2	1.7	-0.7	1.3
220	-0.3	2.2	-0.6	1.1
310	-0.5	0.9	-0.9	1.1

accompanied by a high degree of preferred orientation parallel to the direction of the applied tensile force is the cause of the large strains.

Figure 7 shows the temperature-dependence of the plastic part of the strain plotted with reduced temperature T/T_s and T/T_f . In the case of cooling under stress, the relationship between strain and the reduced temperature can be expressed by a single curve, except for the $x = 4.0$ sample. For the heating cycle, the relations for $x = 6.5$ and 7.0 coincide but others do not; all lie under the curve for $x = 6.5$ and 7.0 . The behavior of the $x = 4.0$ ceramic might be attributed to differences in crystal structure. The structures of the compressed samples were rhombohedral ($x = 4.0$) and tetragonal or of mixed phases ($x = 7.0$). The single curve relating strain and the reduced temperature shown in Figure 7(A) would imply that the crystal structures of $6.5 \leq x \leq 8.0$ are the same. In perovskites, the strain associated with a tetragonal distortion is generally larger than that of a rhombohedral distortion. Inversion of the magnitude of strain between $x = 4.0$ and 6.5 might result from such a difference in crystal structure.

Disagreement of the relation between strain and reduced temperature in the heating cycle for samples with $6.5 \leq x \leq 8.0$ might be attributed to the temperature at which the load was removed. To confirm this conjecture, two additional experiments were undertaken. In the first experiment, the weight was removed at various temperatures during the cooling. Figure 8 shows the result for $x = 7.0$. When unloaded at high temperatures (but below T_f), the reduction in bending was larger than that observed at room temperature.

In the second experiment, the sample was loaded at room temperature and then heated. Room-temperature bending was almost the same as that observed when the cooled sample was unloaded at room temperature (Figure 1). Bending increased during heating up to a certain temperature, and then

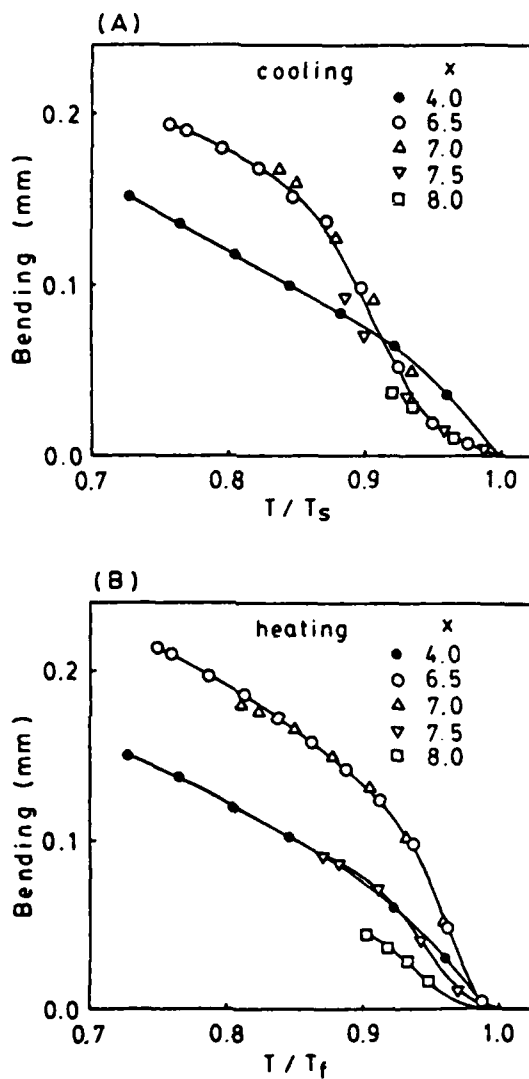


FIGURE 7 Relations between bending and reduced temperatures (A) T/T_s during cooling under constant load and (B) T/T_f during heating without load.

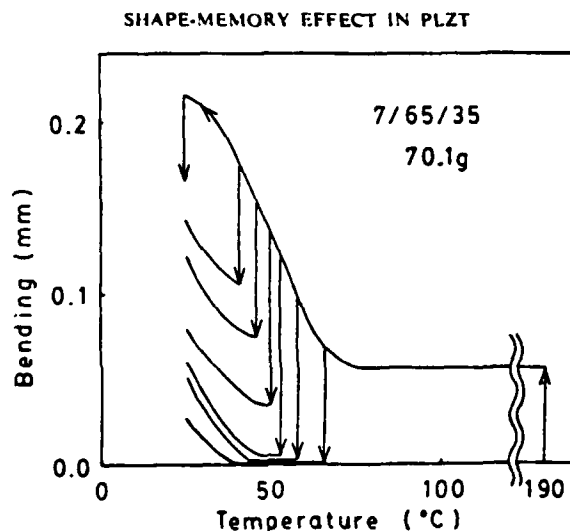


FIGURE 8 Reduction of bending by removal of the load at different temperatures in the sample 7/65/35.

decreased at higher temperatures, as shown in Figure 9. This result indicates that below T_p the stresses caused a phase transformation to a distorted structure with an aligned polar direction. The magnitude of the bending up to the temperature at which bending became a maximum is indicative of the ease of domain wall motion, i.e., the mechanical coercivity decreases with increasing temperature. Decrease in the bending at still higher temperature results from a reduction of the spontaneous strain.

Based on these two additional experiments, the following explanation appears feasible. The presence of mechanical stress forces domain alignment, so that a single curve expresses the relationship between strain and reduced temperature in the cooling cycle, as shown in Figure 7(A). Removal of the stress at room temperature releases the external constraint, and the internal stresses developed during cooling under stress tend to stabilize the structure. Since the difference between T_p and room temperature are large for $x = 6.5$ and 7.0 , the domain walls cannot move, and the only reduction in bending during unloading is elastic in nature. For $x = 7.5$ and 8.0 , on the other hand, T_p is low and some of the domains reorient to a more stable configuration during stress removal at room temperature. In other words, the mechanical relaxation time at room temperature decreases with increasing La content (Esaklul, Gerberich and Koepke, 1980). The reduction of bending accompanying unloading at room temperature has both elastic and domain

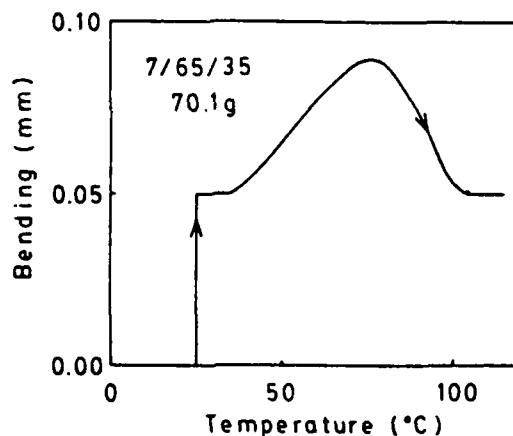


FIGURE 9 Temperature-dependence of bending during heating under constant load of 70.1 g.

contributions for $x = 7.5$ and 8.0 , resulting in the different curves in Figure 7(B).

The anomalous behavior caused by temperature cycling without load can also be explained by this idea. For $x = 7.0$, heating to high temperatures just below T_f causes domain re-orientation, resulting in smaller strains when recooled to room temperature. But several cycles between room temperature and 10°C below T_f did not lead to appreciable domain re-orientation.

8 CONCLUSION

The strains associated with the shape-memory effect in ferroelectric ceramics can be explained as follows. Above T_c the crystallites are cubic, and domains form when the sample is cooled through the transition temperature under stress. Mechanical stress causes partial alignment of the polarization directions (but not the absolute sense). The degree of alignment is determined by the magnitude of the stress, as in the case of electrical poling. In the perovskite structures, the polar axis is longer than the other axes. Polar axes tend to align parallel to a tensile stress. Domains with polarization vectors perpendicular to the stress direction are favored for compressional stresses. The alignment in a ceramic is not complete, however, because of random grain orientation and because of internal stresses between neighboring grains. After the domain pattern is formed, further cooling has little

SHAPE-MEMORY EFFECT IN PLZT

effect on the domain walls. But cooling increases the spontaneous strain of the distorted unit cell, and therefore the total strain increases as the temperature is decreased.

When the lattice parameters change discontinuously at the ferroelectric transition temperature, an abrupt change in shape takes place, as in the case of BaTiO_3 . When the lattice parameters change continuously, a gradual shape-change temperature-change is observed, as in the case of PLZT.

When stress is removed at room temperature, the total strain is reduced by an amount equivalent to the elastic contribution. If domain walls can move at room temperature, further reduction in total strain occurs by domain re-orientation as in the case of PLZT samples with $7.5 \leq x \leq 8.0$.

Upon heating without load, the decrease in spontaneous strain causes a gradual reduction in total strain. Domain re-orientation near the transition temperature contributes a further decrease in strain. Finally the spontaneous strain disappears at T_f , and the total strain goes to zero. In other words the shape-memory effect in ferroelectrics is caused by domain alignment together with the temperature-dependence of spontaneous strain.

Acknowledgements

This work was sponsored by the U.S. Army Research Office (DAAG29-80-C-0008). We also wish to thank Dr. William Harrison for supplying the samples, and Mr. James Laughner for his assistance with the experiments.

References

- Carl, K. and K. Geisen (1973). Dielectric and optical properties of a quasi-ferroelectric PLZT ceramic. *Proc. IEEE*, **61**, 967.
- Delacy, L., R. V. Krishnan, H. Tas and H. Warlimont (1974). Thermoelasticity, pseudoelectricity and the memory effects associated with martensitic transformations, *J. Mater. Sci.*, **9**, 1521, 1536, 1545.
- Esakul, K. A., W. W. Gerberich and B. G. Koepke (1980). Stress relaxation in PZT. *J. Amer. Ceram. Soc.*, **63**, 25.
- Haertling, G. H. and C. E. Land (1971). Hot-pressed (Pb, La) (Zr, Ti) O_3 ferroelectric ceramics for electrooptic applications. *J. Amer. Ceram. Soc.*, **54**, 1.
- Keve, E. T. and A. D. Annis (1973). Studies of phase transformations and properties of some PLZT ceramics. *Ferroelectrics*, **5**, 77.
- Keve, E. T. and K. L. Byc (1975). Phase identification and domain structure in PLZT ceramics. *J. Appl. Phys.*, **46**, 810.
- Maldonado, J. R. and L. K. Anderson (1971). Strain-biased ferroelectric-photoconductor image storage, and display devices operated in a reflection mode. *IEEE Trans. Electron Devices*, **18**, 774.
- Maldonado, J. R. and A. H. Meitzler (1970). Ferroelectric ceramic light gates operated in a voltage-controlled mode. *IEEE Trans. Electron Devices*, **17**, 148.
- Maldonado, J. R. and A. H. Meitzler (1971). Strain-biased ferroelectric-photoconductor image storage and display devices. *Proc. IEEE*, **59**, 368.
- Meitzler, A. H. and H. M. O'Bryan, Jr., (1971). Ferroelastic behavior of PLZT ceramics when subjected to large tensile strains. *App. Phys. Letters*, **19**, 106.

T. KIMURA, R. E. NEWNHAM AND L. E. CROSS

- Meitzler, A. H. and H. M. O'Bryan, Jr. (1973). Polymorphism and penferroelectricity in PLZT ceramics. *Proc. IEEE*, **61**, 959.
- O'Bryan, Jr., H. M. and A. H. Meitzler (1972). Enhanced ordering of ferroelectric domains in PLZT ceramics. *Bull. Amer. Ceram. Soc.*, **51**, 459.
- O'Bryan, Jr., H. M. (1973). Phase relations in (Pb, La) $Zr_{0.85}Ti_{0.35}O_3$. *J. Amer. Ceram. Soc.*, **56**, 385.
- Schmidt, G. and I. Boczek (1978). Pseudoelasticity and shape memory of PLZT ceramic. *Phys. Stat. Sol. (a)* **50**, K109.
- Schulze, W. A., J. V. Biggers and L. E. Cross (1978). Aging of dielectric dispersion in PLZT relaxor ceramics. *J. Amer. Ceram. Soc.*, **61**, 46.
- Smith, W. D. (1973). Electrically-controlled secondary phase in PLZT ceramics. In L. E. Cross (Ed), *Phase Transitions*, Pergamon Press, New York, pp. 71.
- Warlimont, H. (1976). Shape-memory effects. *Mater. Sci. Engineering*, **25**, 139.

APPENDIX 17

Lithium Niobate Bicrystal

LITHIUM NIOBATE BICRYSTAL

YAO XI and L.E. CROSS*

Materials Research Laboratory, The Pennsylvania State University, University Park, PA 16802, USA

Abstract—In studies directed towards improving the basic understanding of the influence of grain boundaries upon the properties of electroceramic materials, studies are being made of artificial planar boundaries created in single domain ferroelectric lithium niobate crystals by thermally bonding carefully polished (001) surfaces. Bonding of "clean" surfaces is accomplished under a uniaxial compressive stress of 10^6 N/M² at between 1050 and 1100°C in a time of order 16 to 24 hours. Optical and SEM characterization of the boundary plane is given. New domain features of bicrystal are discussed. In encounter bicrystal, domain shifting through the boundary and domain splitting are observed. Dielectric data for bicrystal are presented.

INTRODUCTION

In this study, the influence of planar diffusion bonded boundaries upon the properties of lithium niobate bicrystals are explored. A major advantage of the niobate over other ferroelectric mixed oxides is that good thermal compression bonding can be achieved at temperatures below the Curie point (T_c), the original single domain configuration preserved and the influence of head to head (H-H), tail to tail (T-T) and head to tail (H-T) configurations of the polar axis examined.

The eventual objective of the study is to derive from the detailed measurements on precisely oriented planar boundaries some of the characteristics of grain boundaries in polycrystal ceramic ferroelectrics.

PREPARATION OF LiNbO₃ CRYSTAL

Single domain lithium niobate crystal are cut along (001) surface and then carefully ground and polished. The average roughness of the surface is about $1 \cdot 10^{-6}$ M. The flatness is about $2 \cdot 10^{-6}$ M/CM measured by stylus gauge. The single crystal wafers with equal or unequal thickness are stacked with different polarity and different mutual twist angle about the rhombohedral c-axis and then wrapped with platinum foil. Bonding of bicrystal is accomplished under a uniaxial compressive stress of 10^6 N/M² at between 1050°C and 1100°C in a time of order 16 to 24 hours. Higher pressures cause cracking of the crystal during bonding. Several kinds of LiNbO₃ bicrystal are obtained. They can be divided into two main groups, the linked type with head to tail connection and the encounter type with head to head or tail to tail connection of P_s.

BONDING CONDITION OF LiNbO₃ BICRYSTAL

Good bonding is obtained by the hot pressing technique as described above. The bicrystal is transparent and strong. The fracture surface of bicrystal reveals that

cracking always passes straight across the boundary, without obvious interruption.

However, the bonded surface viewed through the bicrystal surface appears rough and "ceramic-like" after hot pressing as shown in Fig. 1. Small voids still remain in the boundary as shown in Fig. 2. Residual stress also quite likely exists in the boundary, which mainly comes from nonuniform strain during hot pressing.

The SEM picture of an etched boundary reveals that a lot of etch pyramids exist on both sides of the boundary with their apices connected as shown in Fig. 3. The connection of the apices suggests that the bonding starts from many separate bonding centers and then spreads outwards to form the complete boundary.

DOMAIN CONFIGURATION

The domain structure after bonding is explored by etching with a mixture of $\text{HF}:\text{HNO}_3 = 1:2$ for 30 minutes at its boiling temperature, 110°C . For the linked type bicrystals, the original single domain states are completely preserved.

In encounter type bicrystals, though the major parts preserve the original configuration, thin lamellar domains parallel to the bonded surface often appear.

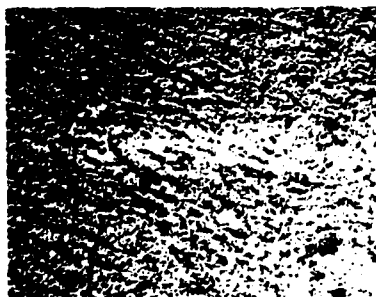


FIGURE 1. Boundary Surface of Bicrystal (X100).

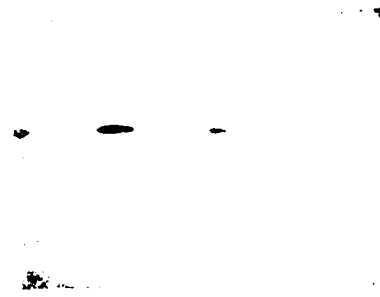


FIGURE 2. Voids Along Bicrystal Boundary (X1000).



FIGURE 3. Etching Pyramids Along Bicrystal Boundary.

It appears from the residual orthogonal domains which sometimes appear that the entering domain moves through the bonding surface but leaves some small residual dead-like regions of the original polarity in its passage (Fig. 4). The reason for the domain shifting and splitting is probably associated with internal fields established under the external short circuit during parts of the heating and cooling cycle during bonding.

ELECTRICAL AND ELECTROMECHANICAL MEASUREMENTS

The dielectric permittivity of both single and bicrystal of the dimensions $1 \times 1 \times 0.5 \text{ mm}^3$ is completely featureless over the range 10 to 1 MHz and no significant difference is evident. Loss spectra in the bicrystal

LITHIUM NIOBATE CRYSTAL

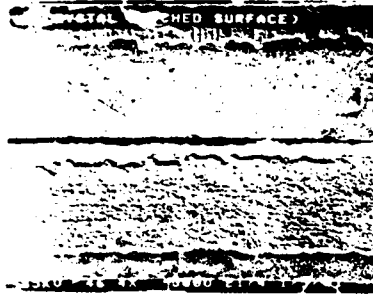


FIGURE 4. Encountering Domain Moves Through the Bonding Surface.

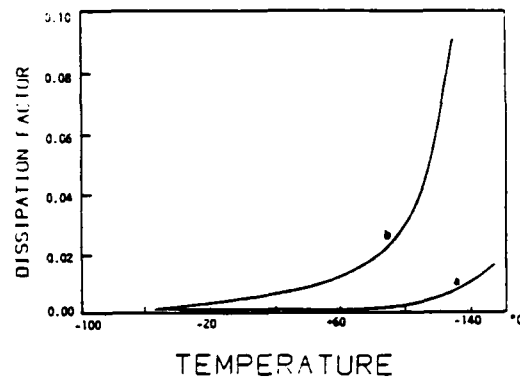


FIGURE 5. Dissipation Factor of (a) Single Crystal and (b) Bicrystal (1 kHz).

appear more dominated by conductivity, with strong rise at lower frequency and higher temperature; however, the activation energy for conduction calculated from $\log R$ vs $1/T$ (Fig. 6) is 0.53 eV—the same value as in the single crystal—suggesting that the lattice discontinuity at the boundary is a prolific source of additional charge carriers.

The permittivity and dissipation factor spectra of bicrystal in the range of 10^3 – 10^5 Hz are dominated by piezoelectric thickness resonances. A series of dissipation peaks from fundamental and overtone resonance appear in the loss spectrum. No apparent relaxations due to the lattice discontinuity of bicrystal boundary can be found. Only in the case of one H-H' twisted encounter bonded crystal was a dissipation peak observed near room temperature at 1 kHz (Fig. 7).

The piezoelectric coefficient d_{33} of lithium bicrystal is measured by Berlincourt d_{33} meter. The d_{33} of linked bicrystal is the same as single crystal. The d_{33} of encounter bicrystal with equal wafer thickness is negligible as expected due to the compensation of antipolarized crystal wafers. The d_{33} of encounter bicrystal with unequal wafer thickness is lower than single crystal. Its value depends on the ratio of wafer thickness. Furthermore, the d_{33} always exhibits unsymmetrical behavior when measured on opposite directions. This is because of the incomplete compensation and the splitting of the domain configuration.

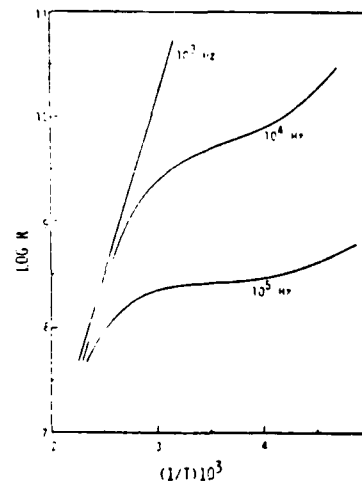
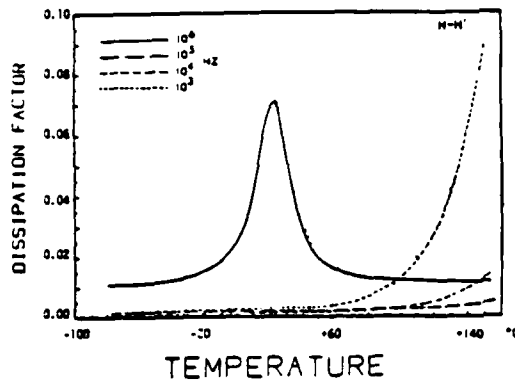


FIGURE 6. ($\log R - 1/T$) of Bicrystal.

SUMMARY

Clean and strong LiNbO_3 bicrystal can be obtained by hot pressing technique. The original domain configuration of bicrystal can be largely preserved through the bonding process. In encounter type bicrystal the domain always shifts across the bicrystal boundary. Bicrystal boundary is a source of charge carriers which causes the high dielectric loss at high temperature and low frequency. No important dielectric relaxation has been found in the frequency and temperature region investigated.



ACKNOWLEDGMENT

This work was supported by the Office of Naval Research, Contract No. N00014-78-C-0227.

FIGURE 7. Dissipation Peak in Encounter Bicrystal.

REFERENCES

1. N. Ohnishi and T. Lizuha, J. Appl. Phys. 46, 4699 (1975).

*Also affiliated with Department of Electrical Engineering.

APPENDIX 18

Primary and Secondary Pyroelectricity

phys. stat. sol. (a) 58, K19 (1980)

Subject classification: 14.4 and 14.4.1; 22.4; 22.4.1; 22.4.2; 22.8; 22.8.1

Materials Research Laboratory, The Pennsylvania State University, University Park¹⁾

Primary and Secondary Pyroelectricity

By

A.S. BHALLA and R.E. NEWNHAM

The pyroelectric coefficient (p) of a material under constant stress and electric field is defined by the expression

$$p = \left(\frac{\partial P_s}{\partial T} \right)_{E, \sigma} \quad (1)$$

where P_s is the spontaneous polarization, T the temperature, E the electric field, and σ the elastic stress /1, 2/. Thermodynamic analysis of the pyroelectric effect yields the expression

$$p_i^\sigma = p_i^\epsilon + d_{ijk}^T c_{jklm}^T E \alpha_{lm}^\sigma \quad (2)$$

where p_i^σ is the total pyroelectric effect measured at constant stress, and p_i^ϵ , the pyroelectric effect at constant strain ϵ , is called the primary effect. The second term of (2) is the contribution caused by thermal deformation of the crystal and is known as the secondary pyroelectric effect. d , c , and α are the piezoelectric, elastic stiffness, and the thermal expansion coefficients of the crystal, respectively. (A third contribution to the pyroelectric effect, known as the tertiary pyroelectric effect /3/, arises from inhomogeneous temperature distributions within the sample. Since the origin of the tertiary effect depends on experimental conditions, it is not included in the present study.)

In ferroelectric pyroelectrics the primary effect is large and negative because the spontaneous polarization diminishes with increasing temperature. The secondary effect is considerably smaller and may have either sign depending on the values of the constants. Thus the experimentally observed pyroelectric coefficients are dominated by the primary effect and are negative

1) University Park, PA 16802, USA.

Table 1

Primary, secondary, and the observed pyroelectric effect in various pyroelectric materials.
Room-temperature values

materials	point group symmetry	observed total effect ($\mu\text{C}/\text{m}^2\text{ K}$)	calculated secondary effect ($\mu\text{C}/\text{m}^2\text{ K}$)	primary effect ($\mu\text{C}/\text{m}^2\text{ K}$)	references
A) ferroelectrics					
a) ceramics					
$\text{Pb}(\text{Zr}_{0.52}\text{Ti}_{0.48})\text{O}_3:1\text{ wt}\%\text{Nb}_2\text{O}_5$	∞mm	- 50	+60	-110.0	/6/
BaTiO_3	∞mm	-190.0	+80.0	-270.0	/5/
$\text{Pb}(\text{Zr}_{0.95}\text{Ti}_{0.05})\text{O}_3:1\text{ wt}\%\text{Nb}_2\text{O}_5$	∞mm	-268.0	+37.7	-305.7	/7/
b) single crystal					
$\text{Sr}_{0.5}\text{Ba}_{0.5}\text{Nb}_2\text{O}_6$	4mm	-550	-21.0	-529.0	/9/
TGS	2	-270	+60.0	-330.0	/11, 12/*)
LiTaO_3	3m	-176	+ 2.00	-178	/4, 12/
LiNbO_3	3m	- 83.0	+12.9	- 95.9	/4, 14, 13/
$\text{Pb}_5\text{Ge}_3\text{O}_{11}$	3	- 95.0	+15.5	-110.5	/4, 15, 16/
$\text{Ba}_2\text{NaNb}_5\text{O}_{15}$ **)	2mm	-100.0	+41.8	-141.8	/17, 18, 19/
NaNO_2	2mm	-140.0	- 5.0	-135.0	/20, 4, 21/

*) Average value of the wide range of reported values between 200 to 350 $\mu\text{C}/\text{m}^2\text{ K}$.

**) Maximum value of p measured on the sample.

Table 1 - Continued

materials	point group symmetry	observed total effect ($\mu\text{C}/\text{m}^2\text{K}$)	calculated secondary effect ($\mu\text{C}/\text{m}^2\text{K}$)	primary effect ($\mu\text{C}/\text{m}^2\text{K}$)	references
<u>E) non-ferroelectric</u>					
$\text{Li}_2\text{SO}_4 \cdot \text{H}_2\text{O}$	2	+86.3	+ 26.1	+60.2	/8/
tourmaline	3m	+ 4.0	+ 3.2	+ 0.8	/1/
bone	∞	$+25 \times 10^{-4}$	$+117 \times 10^{-4}$	-92.0×10^{-4}	/22/
$\text{Ba}_2\text{Si}_2\text{TiO}_8$	4mm	+10	+22, +16	-12.0, -6.0	/23/
Li_2GeO_3	2mm	-27	- 12.8	-14.2	/24/
$\text{Ba}(\text{NO}_2)_2 \cdot \text{H}_2\text{O}$		-25.3	- 3.3	-22.0	/25/
<u>C) semiconductors</u>					
CdS	6mm	-4.0	-1.0	-3.0	/26/
CdSe	6mm	-3.5	-0.56	-2.94	/25/
ZnO	6mm	-9.4	-2.5	-6.9	/27, 28/
ZnS ^{***})	6mm	0.43	+0.34		/4, 29/
BeO	6mm	-3.40	-0.008	-3.39	/4, 29/

***) No reported sign for p_i^σ ; no information about polytypic nature of the sample.

in ferroelectric crystals. In non-ferroelectric pyroelectric crystals there is no simple way to predict the sign and the magnitude of these coefficients. In practice the total pyroelectric effect can be measured and the secondary effect calculated from the constants d, α , and c . But in only a few materials /4/ have the primary and secondary pyroelectric components been evaluated: BaTiO_3 /5/, PZT /6, 7/, $\text{Li}_2\text{SO}_4 \cdot \text{H}_2\text{O}$ /8/, and $\text{Sr}_{0.5}\text{Ba}_{0.5}\text{Nb}_2\text{O}_6$ /9/.

For a number of applications, such as infrared detectors and vidicons, it is desirable to know the magnitude and sign of the contributions to the total pyroelectric effect. During our studies of diphasic pyroelectric composites /10/, we surveyed various families of pyroelectric materials and separated the primary and the secondary effects. The results are listed in Table 1. The secondary contributions for various crystal symmetry groups were calculated from the following equations:

$$p_{\text{sec}} = d_{21}(c_{11}\alpha_1 + c_{12}\alpha_2 + c_{13}\alpha_3 + c_{15}\alpha_5) + \\ + d_{22}(c_{12}\alpha_1 + c_{22}\alpha_2 + c_{23}\alpha_3 + c_{25}\alpha_5) + \quad \text{point group 2,} \\ + d_{23}(c_{13}\alpha_1 + c_{23}\alpha_2 + c_{33}\alpha_3 + c_{35}\alpha_5) + \quad \text{b polar axis;} \\ + d_{25}(c_{15}\alpha_1 + c_{25}\alpha_2 + c_{35}\alpha_3 + c_{55}\alpha_5) ,$$

$$p_{\text{sec}} = d_{31}(c_{11}\alpha_1 + c_{12}\alpha_2 + c_{13}\alpha_3) + \quad \text{point group mm2,} \\ + d_{32}(c_{12}\alpha_1 + c_{22}\alpha_2 + c_{23}\alpha_3) + \quad \text{c polar axis;} \\ + d_{33}(c_{13}\alpha_1 + c_{23}\alpha_2 + c_{33}\alpha_3) ,$$

$$p_{\text{sec}} = 2d_{31}(c_{11}\alpha_1 + c_{12}\alpha_1 + c_{13}\alpha_3) + \quad \text{point groups} \\ + d_{33}(2c_{13}\alpha_1 + c_{33}\alpha_3) , \quad \text{3.3m, 4.4mm, 6.6mm,} \\ \text{c polar axis.}$$

Point group ∞mm of the poled ceramic samples leads to equations equivalent in form to the hexagonal crystal system. The ∞ axis is parallel to the poling direction and is denoted as x_3 .

The values of the constants are taken from the recent literature or from the Landolt-Börnstein Tables, as noted in Table 1. It is evident from the data that in ferroelectric ceramics and single crystals, both the primary and total pyroelectric effects are large and negative. Secondary coefficients in ferroelectric single crystals are comparatively small and positive with the exception of SBN and NaNO_2 where the secondary pyroelectric effect is small and negative, enhancing the primary pyroelectric effect. In TGS, $\text{Ba}_2\text{NaNb}_2\text{O}_5$, and the ceramics PZT and BaTiO_3 , the secondary effect is more substantial.

Compared to ferroelectrics, tourmaline and other non-ferroelectric polar materials show rather small pyroelectric effects. In these materials, the total and the secondary coefficients carry the same sign, and in most cases they are positive. The secondary effect arising from piezoelectricity and thermal expansion makes a large contribution to the total pyroelectric effect. In tourmaline for instance, 80% of the pyroelectric signal is of secondary origin. Fresnoite, $\text{Ba}_2\text{TiSi}_2\text{O}_8$, is another mineral in which pyroelectricity is dominated by the secondary effect. In semiconductor pyroelectrics with the wurtzite structure, the effect is very small, with all coefficients having the same sign.

It is clear from the table that both the primary and secondary effects are important, and that certain trends emerge regarding the magnitude and sign of the coefficients. All pyroelectric materials do not follow the same pattern, but members of the same family share common features: In ferroelectrics all the observed coefficients are negative and dominated by the primary effect, in contrast to non-ferroelectric pyroelectrics where secondary effects are more substantial.

This work was sponsored by the Office of Naval Research through contract N00014-78-C-0291 and Advanced Research Project Agency through contract MDA 903-78-C-0306.

References

- /1/ J. F. NYE, *Physical Properties of Crystals*, Oxford University Press, London 1957 (p. 189).
- /2/ R. E. NEWNHAM, *Structure - Property Relations*, Springer-Verlag, New York 1975.
- /3/ L. B. SCHEIN, P. J. CRESSMAN, and L. E. CROSS, *Ferroelectrics* 22, 945 (1979).

- /4/ Landolt-Börnstein, New Series, Ferro- and Antiferroelectric Materials, Vol. III/3, 1973, Vol. III/5, 1975; Numerical Data and Functional Relationships in Science and Technology, Vol. 11, 1978, Ed. H. HELLWEGE.
- /5/ T. A. PERLS, T. J. DIESEL, and W. I. BOBROV, J. appl. Phys. 29, 1297 (1958).
- /6/ W. R. COOK, Jr., D. A. BERLINCOURT, and F. J. SCHOLZ, J. appl. Phys. 34, 1392 (1963).
- /7/ L. Z. KENNEDY and J. L. WENTZ, J. appl. Phys. 35, 1767 (1964).
- /8/ S. B. LANG, Phys. Rev. B 4, 3603 (1971).
- /9/ S. T. LIU and L. E. CROSS, phys. stat. sol. (a) 41, K83 (1977).
- /10/ R. E. NEWNHAM, D. P. SKINNER, K. A. KLICKER, A. S. BHALLA, B. HARDIMAN, and T. R. GURURAJA, to be published in Ferroelectrics.
- /11/ S. HAUSSÜHL and J. ALBERS, Ferroelectrics 15, 73 (1977).
- /12/ T. IKEDA, Y. TANAKA, and H. TOYODA, Japan. J. appl. Phys. 1, 13 (1962).
R. L. BYER and C. R. ROUNDY, Ferroelectrics 3, 333 (1972).
- /13/ A. M. GLASS and M. E. LINES, Phys. Rev. B 13, 180 (1976).
- /14/ A. W. WARNER, M. ONOE, and G. A. COQUIN, J. Acoust. Soc. Amer. 42, 1223 (1967).
- /15/ T. YAMADA, H. IWASAKI, and N. NIZEKI, J. appl. Phys. 43, 772 (1972).
- /16/ G. R. JONES, N. SHAW, and A. W. VERE, Electronics Letters 8, 345 (1972).
- /17/ A. W. WARNER, G. A. COQUIN, and J. L. FINK, J. appl. Phys. 40, 4353 (1969).
- /18/ S. SINGH, S. A. DRACER, and J. G. GEUSIC, Phys. Rev. B 2, 2709 (1970).
- /19/ R. B. RICE and H. FAY, J. appl. Phys. 40, 909 (1969).
- /20/ S. HOSHINO and I. SHIBUYA, J. Phys. Soc. Japan 16, 1254 (1961).
- /21/ B. G. F. TAYLOR and H. A. H. BOOT, Contemp. Phys. 14, 55 (1973).
- /22/ S. B. LANG, Nature 224, 798 (1969).
- /23/ S. HAUSSÜHL, J. Crystal Growth 40, 200 (1977).
M. KIMURA, Japan. J. appl. Phys. 48, 2850 (1977).
- /24/ D. S. ROBERTSON, I. M. YOUNG, F. W. AINGER, C. O' HARA, and A. M. GLAZER, J. Phys. D 12, 611 (1979).
- /25/ V. V. GLADKII and I. S. ZHELUDEV, Soviet Phys. - Cryst. 12, 788 (1968).
- /26/ D. BERLINCOURT, H. JAFFE, and L. R. SHIOZAWA, Phys. Rev. 129, 1009 (1963).
- /27/ T. B. BATEMAN, J. appl. Phys. 33, 3309 (1962).
- /28/ G. HEILAND and H. IBACH, Solid State Commun. 4, 353 (1966).
- /29/ Thermophysical Properties of Matter, IPRC Data Service, Vol. 13, Thermal Expansion - Non-Metallic Solids.

(Received November 28, 1979)

APPENDIX 19

Pyroelectricity in SbSI

PYROELECTRICITY IN SbSI

A. S. BHALLA, R. E. NEWNHAM and L. E. CROSS

*Materials Research Laboratory, The Pennsylvania State University,
University Park, Pennsylvania 16802*

and

J. P. DOUGHERTY⁺ and W. A. SMITH

Philips Laboratories, Briarcliff Manor, NY 10510

(Received July 30, 1980)

Large pyroelectric coefficient ($1.2 \times 10^4 \mu\text{C}/\text{m}^2\text{C}$ at $T - T_c \approx 2^\circ\text{C}$) in single crystals of SbSI were measured over a temperature range encompassing the ferroelectric phase transition. Simultaneous measurement of the pyroelectric and dielectric constants were made and the pyroelectric figure of merit p/K was evaluated at various temperatures.

INTRODUCTION

Antimony sulfur iodide (SbSI) is the most important member of a family^{1,2} of ferroelectric semiconductors with formula $A^{\text{VI}}B^{\text{VI}}X^{\text{VII}}$. It has a displacive first order ferroelectric transition near 20°C . The Curie temperature T_c depends on the growth method and chemical stoichiometry of the crystal.^{3,4} In the ferroelectric phase, SbSI belongs to point group $\text{mm}2$ in the orthorhombic system and exhibits a very large structural anisotropy along the polar c -axis.^{5,6} The transition is accompanied by an exceedingly high permittivity at T_c . Crystals grow as bundles of fine needles parallel to the c -axis making it rather difficult to obtain good electrical measurements on these crystals because of their small cross-sectional area and the uncertainty of the single-crystal nature of the sample. So far, no reliable measurements of the pyroelectric coefficient and its temperature dependence have been reported in the literature. In this paper we describe the simultaneous measurement of the pyroelectric and dielectric constants on SbSI crystals using a modified Byer-Roundy method.⁷ This technique eliminates uncertainties in temperature by measuring p and K simultane-

ously. The pyroelectric figure of merit p/K is evaluated over a temperature range encompassing the ferroelectric phase transition.

MEASUREMENT TECHNIQUE

Measurement of the pyroelectric coefficient p and the dielectric permittivity K was carried out using an automated measurement technique.⁷ In this system, the pyroelectric coefficient is determined by measuring the DC discharging (or charging) current (i) from a sample of known electrode area (A) subjected to a controlled rate of change of temperature (dT/dt). The pyroelectric coefficient p is given by

$$p = \frac{i/A}{dT/dt} \quad (1)$$

It is important to compare the measured pyroelectric coefficient for both heating and cooling over a number of temperature cycles because there are several possible sources of current arising from the release of trapped or injected charge and from conduction currents under bias. Comparing heating and cooling curves after different modes of poling and under different cycling conditions provides a way of eliminating some of these extraneous effects.

⁺ Present address: Gulton Industries, 212 Durham Avenue, Metuchen, NJ 08840.

Simultaneous pyroelectric and dielectric measurements are made by dividing the circuit into high and low frequency parts. The low frequency (essentially DC) side of the circuit is used to apply the DC bias and measure the capacitance at 1 MHz through the high frequency branch of the circuit. The two halves are electrically isolated from each other. Automated control is accomplished with a Hewlett-Packard 3052A Automated Data Acquisition System. The pyroelectric measurement system is based on a HP9825A minicomputer with instrument control and data transfer provided by the HPIB interface bus (IEEE 488 Standard). Data are stored on magnetic tape cartridges and plotted on a digital plotter. The computer controls the temperature (heating rate) and bias applied to the sample. The overall system speed is 3 to 4 complete measurement cycles per second with data stored only when any one of the measured quantities exceeds a preset percentage of absolute change.

The sample temperature is determined with the well-calibrated platinum resistance thermometer. Time is determined using an HP98035A interface clock. From the time and temperature measurements, dT/dt is calculated. In our arrangement, the pyroelectric coefficient can be studied in the temperature range between -30 and 200°C .

EXPERIMENTAL

Crystals of SbSI were grown from an SbI₃ flux using the Bridgman method and a vapor transport technique.^{9,10} A few good quality single crystals with well-defined morphology were selected. Crystals were examined with a polarizing microscope for optical quality and foreign inclusions. Chemical homogeneity was evaluated by electron microprobe analysis in a scanning electron microscope. Vapor-grown crystals were slightly off stoichiometry with a slight excess of sulfur together with oxygen impurities. Cross-sectional areas of the crystals were measured by optical microscopy. Two ends of the crystals were electroded with Ag-paste, and gold wires 5 mil in diameter were attached to the ends. Crystals were suspended from the gold wire electrodes in a special specimen holder and then positioned in a silicone oil bath. The SbSI samples were kept dark to avoid the possibility of photocurrents. Samples were poled with DC fields of 500 V/cm to 1 KV/cm while being cooled from 45°C to about 10°C . At 10°C

the poling field was removed gradually in order to minimize the possibility of back switching caused by the space charge built up under DC field. Samples were held at that temperature up to several hours before collecting the pyroelectric data in the heating cycles. Typical heating rates were $1^\circ\text{C}/\text{min}$ to $4^\circ\text{C}/\text{min}$ in various runs.

RESULTS AND DISCUSSION

Figure 1 shows the temperature dependence of the dielectric constant of vapor-grown SbSI measured at 1 MHz with and without extra bias. An electric field of -800 V/cm was applied while heating the crystal in Run No. 1 and during the cooling cycle in Run No. 2. In Run No. 3 the sample was heated at $2^\circ\text{C}/\text{min}$ from 5°C to 40°C under zero field. Simultaneous measurements of the sample capacitance and the pyroelectric output current were made. The sample was then cooled through the phase transition under a positive field of 800 V/cm. Dielectric and pyroelectric data were again collected in Run No. 5 while heating the sample.

Figure 2 shows the current density measured during cycles No. 3 and 5. The change in sign of the current density with the reversal of the poling field indicates clearly that the origin of the current is the pyroelectric effect in SbSI. The pyroelectric coefficients calculated from Eq. 1 are plotted in Figure 3 for various temperatures. The pyroelectric coefficients are unusually large, even at temperatures well removed from the transition (Figure 4). In the vapor-grown crystals, typical values of the pyroelectric coefficients were 1.2×10^4

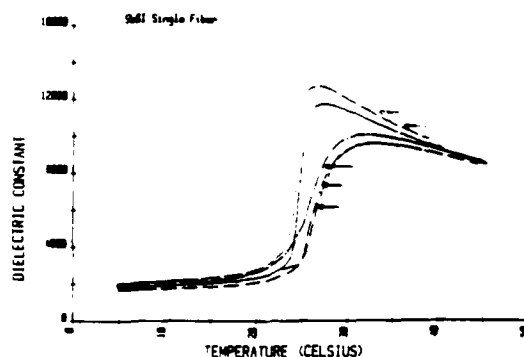


FIGURE 1 Temperature dependence of the dielectric constant of vapor grown SbSI at 1 MHz. (1) and (2) with bias-800 V/cm. (3) no bias. (4) bias -800 V/cm. and (5) no bias

PYROELECTRICITY IN SbSI

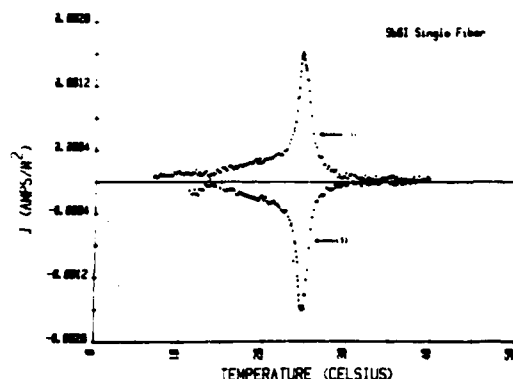


FIGURE 2 Pyroelectric current density with the reversal of the poling field.

$\mu\text{C}/\text{m}^2\text{K}$ at $(T-T_c) = 2^\circ$ and $6 \times 10^4 \mu\text{C}/\text{m}^2\text{K}$ at the peak respectively. The spontaneous polarization (P_s) $23 \mu\text{C}/\text{cm}^2$ (Figure 5) calculated from the integration of pyroelectric current agrees well with the value of $25 \mu\text{C}/\text{cm}^2$ reported in the literature.

Both the dielectric and the pyroelectric data show a sharp transition around 24.7°C , slightly higher than the value reported for flux-grown crystals. Apparently the vapor-grown crystals contain oxygen impurities and excess sulfur which result in a small increase in the transition temperature. The pyroelectric properties are relatively unaffected by the small amount of impurities, as evident from the pyroelectric data gathered on flux-grown crystals.

The pyroelectric figure of merit (p/K) for SbSI was computed from the pyroelectric coefficient p

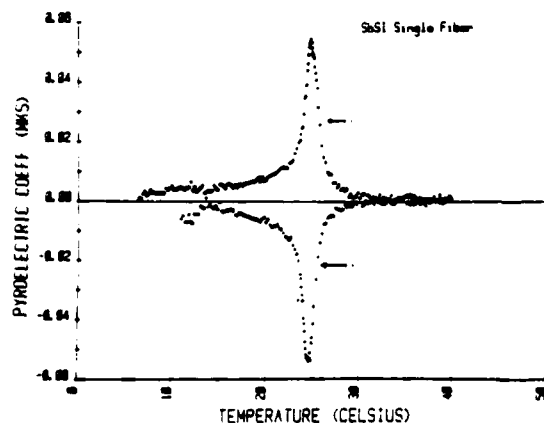


FIGURE 3 Pyroelectric coefficient of vapor grown SbSI crystal.

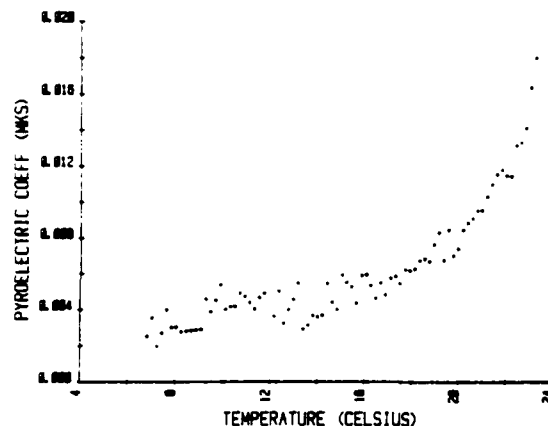


FIGURE 4 p vs T for the vapor grown SbSI single crystal fiber below the ferroelectric transition ($T_c \sim 24.7^\circ\text{C}$).

and the dielectric constant K measured at various temperatures, and is plotted in Figure 6. From 5°C to about 20°C , p/K is 2×10^{-6} (MKS) but rises sharply to 10^{-5} at the transition, comparable to the TGS (1.1×10^{-5} MKS).

According to Devonshire's phenomenological theory of ferroelectricity, for a crystal in the stress-free state thermodynamic potential $A(P)$ can be expressed as

$$A(P) = A_0(T) + \frac{\beta}{2}(T-T_0)P^2 + \frac{rP^4}{4} + \frac{\delta P^6}{6} + \dots \quad (2)$$

where P is the electric polarization and β , r , and δ are temperature-independent coefficients. Using

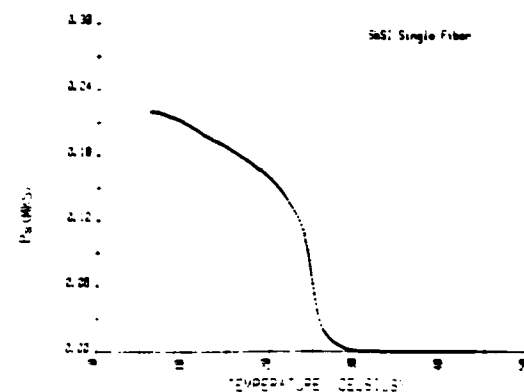


FIGURE 5 P_s vs T as calculated from the pyroelectric data.

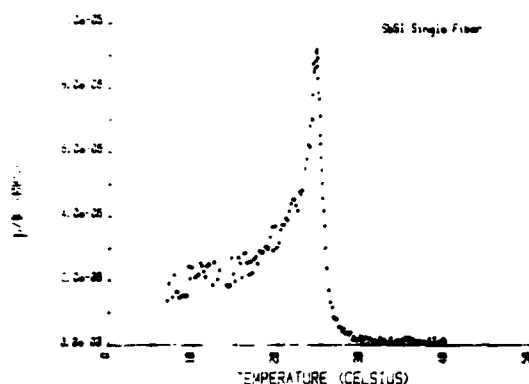


FIGURE 6 p/K as computed from the measured pyroelectric coefficient and the dielectric constant at various temperatures encompassing the phase transition.

only the second order terms, Liu and Zook¹¹ derived a relation

$$\frac{p}{K} = \frac{P_s}{C} \quad (3)$$

where C is the Curie constant and assumed to be temperature independent. Eq. (3) indicates that the figure of merit p/K should follow the slope of P_s vs T curve. The validity of this relation was tested on SBN using the Chynoweth method, and on TGS and DTGFB using an automated Byer-Roundy technique.¹² The experimental values and the theoretical predictions are in agreement over a temperature range 20°C below the transition in TGS and DTGFB.

It is clear from Figures 5 and 6 that $p/K(T)$ does not follow the temperature dependence of P_s . The discrepancy might be real, or it could arise from errors in the measured values of p and K . The spontaneous polarization P_s computed from the integration of p is in good agreement with the value obtained from the E - D curve supporting the validity of the pyroelectric coefficient measurements. This suggests the possibility of discrepancies in the dielectric constant. In the present set-up the dielectric constants at 1 MHz are not measured under steady-state conditions, and thus do not give the isothermal values needed to establish the validity of relation (3). The measured values are closer to the adiabatic dielectric permittivity. This suggests a correction to the measured permittivity based on the following relation.¹³

$$K_T = K_S + \frac{p^2 T}{\epsilon_0 c_p} \quad (4)$$

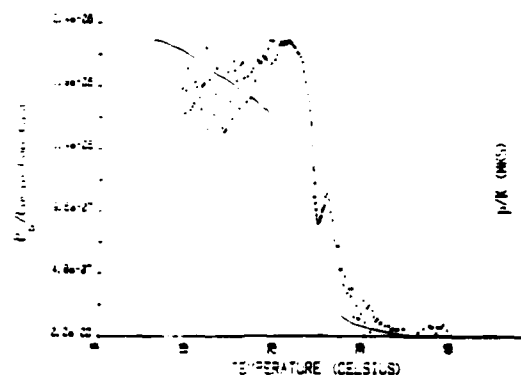


FIGURE 7 Plots of P_s/C and p/K vs temperature, after applying the isothermal correction to the dielectric constant.

where K_T and K_S are the isothermal and adiabatic dielectric constants, and c_p is the volume specific heat of SbSI. Isothermal dielectric constants were calculated at various temperatures. A sharp dielectric anomaly representing the first order transition appears at 24.7°C. Revised plots of (p/K_T) vs T and (P_s/C) vs T are shown in Figure 7. Both functions show a sharp decrease near the Curie temperature, but some anomalies in p/K_T remain. Further study of the higher order terms in the Devonshire theory and of the temperature dependence of the property coefficients is needed.

The highest value of the figure of merit (p/K_T) is about 2.4×10^{-6} measured 5° below T_c .

ACKNOWLEDGEMENT

We wish to thank our colleagues at the Materials Research Laboratory for their advice and assistance. This work was sponsored by the Defense Advanced Research Projects Agency (Contract No. DARPA Project No. P-15124-MS).

REFERENCES

1. E. Fatuzzo, G. Harbeke, W. J. Merz, R. Nitsche, H. Roetchi and W. Ruppel, *Phys. Rev.*, **127**, 2036 (1962).
2. R. Nitsche and W. J. Merz, *J. Phys. Chem. Solids*, **13**, 154 (1960).
3. L. M. Belyaev, V. A. Lyakhovitskaya and I. M. Sil'vestrova, *Izv. Akad. Nauk SSSR. Neorgan. Mat.*, **6**, 429 (1970).
4. S. S. Boksha, V. A. Lyakhovitskaya, I. M. Sil'vestrova and N. A. Tikhomirova, *Izv. Akad. Nauk SSSR. Neorgan. Mat.*, **6**, 1951 (1970).
5. E. Dönges, *Z. Anorg. Allgem. Chem.*, **263**, 112 (1950).
6. A. Kikuchi, Y. Oka and E. Sawaguchi, *J. Phys. Soc. Japan*, **23**, 337 (1967).

PYROELECTRICITY IN SbSI

7. J. P. Dougherty and R. J. Seymour, *Rev. Sci. Instr.*, **51**, 229 (1980).
8. R. L. Byer and C. B. Roundy, *Ferroelectrics*, **3**, 333 (1972).
9. A. S. Bhalla, K. E. Spear and L. E. Cross, *Mat. Res. Bull.*, **14**, 423 (1979).
10. K. Nassau, J. W. Shiever and M. Kowalchik, *J. Cryst. Growth*, **7**, 237 (1970).
11. S. T. Liu and J. D. Zook, *Ferroelectrics*, **7**, 171 (1974).
12. R. J. Seymour, J. P. Dougherty and A. Shaulov, *Ferroelectrics*, **29**, 163 (1980).
13. M. E. Lines and A. M. Glass, *Principles and Applications of Ferroelectrics and Related Materials*, Clarendon Press, Oxford, 1977, p. 129.

APPENDIX 20

$\text{Ba}_2\text{TiGe}_2\text{O}_8$ and $\text{Ba}_2\text{TiSi}_2\text{O}_8$ Pyroelectric Glass-Ceramics

Ba₂TiGe₂O₈ and Ba₂TiSi₂O₈ pyroelectric glass-ceramics

A. HALLIYAL, A. S. BHALLA, R. E. NEWNHAM, L. E. CROSS
*Materials Research Laboratory, The Pennsylvania State University, University Park,
Pennsylvania 16802, USA*

Pyroelectric glass-ceramics of composition Ba₂TiGe₂O₈ and Ba₂TiSi₂O₈ were prepared by crystallizing the glasses in a temperature gradient. High pyroelectric responses up to 50% of the single-crystal values were observed because of the high degree of orientation of the crystallites in the glass-ceramic samples. The piezoelectric and dielectric properties of the glasses and the glass-ceramics are also consistent with the properties of the single crystals.

1. Introduction

Pyroelectric lithium disilicate glass-ceramics have recently been prepared by growing highly orientated surface layers of lithium disilicate crystals by crystallizing the glasses of stoichiometric glass compositions Li₂O · 2SiO₂ in a temperature gradient [1]. This technique provides a method of fabricating large and inexpensive pyroelectric devices. However, one difficulty encountered in working with the lithium disilicate pyroelectric glass-ceramic was that thin targets (of thickness, $d < 200 \mu\text{m}$) cut perpendicular to the growth direction (the polar c -axis of Li₂Si₂O₅) were extremely fragile and could not be prepared routinely.

In this study pyroelectric glass-ceramics of barium titanium silicate (BTS: Ba₂TiSi₂O₈ or fersnoite) and barium titanium germanate (BTG: Ba₂TiGe₂O₈) are described, the physical properties of which are superior to Li₂Si₂O₅. Thin sections of these glass-ceramics, less than 100 μm in thickness, can easily be prepared since they are mechanically much stronger. Glass-ceramics of BTG and BTS were prepared by crystallizing glasses of stoichiometric compositions of BTG and a silica-rich composition (64SiO₂–36BaTiO₃) of BTS in a thermal gradient. The dielectric and pyroelectric properties were measured and compared with the properties of single crystals.

In the single-crystal form fersnoite belongs to

the crystallographic point group 4mm and is pyroelectric [2]. Ba₂TiGe₂O₈ is reported to be a ferroelastic [3, 4] below 810°C and belongs to the orthorhombic polar point group mm2. In the paraelastic phase above the transition temperature, T_c , BTG also belongs to the tetragonal point group 4mm.

Glass-ceramics in the BaTiO₃–SiO₂ system have been previously investigated. Herczog [5] studied the crystallization of BaTiO₃ in a silicate glass matrix. Dielectric and electro-optic measurements on transparent glass-ceramics containing ferroelectric BaTiO₃ in a glass matrix have also been reported [6]. However, the primary interest in these materials has been concerned with the dielectric and electro-optic properties of the glass-ceramics, and in the ferroelectric nature of BaTiO₃ crystallites surrounded by a glass matrix. In these studies no efforts have been made to develop glass-ceramics containing orientated crystallites. The present study describes the preparation and characterization of glass-ceramics containing orientated crystallites of the pyroelectric (but non-ferroelectric) BTS and BTG phases.

2. Experimental details

Glasses of composition 64SiO₂ · 36BaO · 36TiO₂ were prepared by mixing reagent-grade silicic acid*, barium carbonate[†] and titanic oxide[‡].

*J. T. Baker Chemical Co., Phillipsburg, NJ, USA.

[†]Fisher Scientific Co., Phillipsburg, NJ, USA.

[‡]Fagle – Picher Industries, Inc., Quapaw, Oklahoma, USA.

followed by melting in a global furnace. Fresnoite has a high melting point (1400°C) and thus, it was difficult to obtain bubble-free glasses of the stoichiometric composition. To avoid this problem, a composition was selected which lies near the eutectic point on the silica-rich side of the BaTiO₃-SiO₂ binary phase diagram [7]. This composition lies well within the range of glass formation in the BaTiO₃-SiO₂ system.

In the case of BTG, reagent-grade barium carbonate, germanium oxide* and titanic oxide were mixed and melted in the furnace. In both cases, the melts were maintained at 1375°C for 24 hours for fining and homogenization. Transparent samples were obtained by pouring the melt into a graphite mould. The samples which crystallized during pouring of the melt were remelted and poured again into the graphite mould in order to ensure transparent glass samples. All the glass samples were annealed at 600°C for 12 hours and then cut and polished in the form of thick disks in preparation for the crystallization studies. To determine the crystallization temperatures of the glass compositions, differential thermal analysis (DTA) measurements were performed on the glass samples. Exothermic peaks were observed at 860°C in the case of BTS and at 800°C in the case of BTG, as shown in Fig. 1.

Crystallization was carried out in a temperature gradient by placing the polished glass samples, in the form of thick disks, on a microscope hot stage.† The temperature gradient near the hottest temperature zone was perpendicular to the surface of the sample and it was estimated to be about 100°C mm⁻¹. Typical heating cycles used for glass crystallization are shown in Fig. 2. The heating cycle consisted of an initial rapid rise in temperature to minimize volume nucleation, followed by a slow increase in temperature at a rate of about 3°C min⁻¹. After reaching the maximum crystallization temperature (1100°C for BTS and 1000°C for BTG), the samples were held at this temperature for 24 hours. The temperature was then decreased rapidly to room temperature. The thicknesses of the crystallized portions of the glasses ranged from 1 to 2 mm, depending on the heating cycle.

The degree of preferred orientation of the

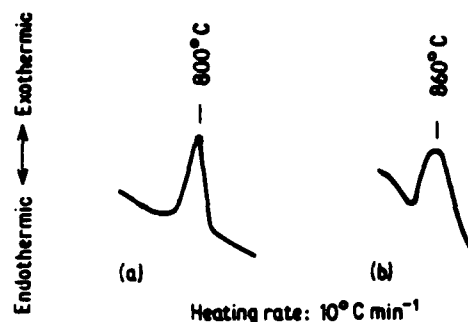


Figure 1 DTA heating curves of (a) BTG and (b) BTS glasses.

glass-ceramic was evaluated from X-ray diffractometer patterns. X-ray diffraction (XRD) patterns were recorded on surfaces normal to the direction of the temperature gradient (Fig. 3). The XRD patterns were compared with the standard powder diffraction patterns to determine the relative degree of orientation. The dielectric constants of glass and glass-ceramic disks were measured with a capacitance bridge. The piezoelectric behaviour parallel to the crystallization direction was studied using a d_{33} -meter.‡ The samples were thinned down to about 200 µm in thickness and the pyroelectric response was measured by the dynamic Chynoweth technique [8] at a modulating frequency of 4 Hz. The pyroelectric signals on glass-ceramics were compared with the responses from single crystals of the BTG and BTS. The densities of BTG, BTS glasses and glass-ceramic samples were determined by a mercury porosimeter§ and compared with the densities of single crystals.

3. Results and discussion

Table I summarizes the data for the glass and glass-ceramic samples. Single-crystal values are also listed for comparison.

X-ray powder diffraction patterns of the crystallized samples showed that the principal crystallized phases were fresnoite in the BTS glass-ceramics and Ba₂Ge₂TiO₈ in the BTG glass-ceramic samples. A few low-intensity peaks of an unidentified phase were observed in the powder diffraction patterns of both compositions. The samples showed highly orientated crystal growth

* Eagle-Picher Industries, Inc., Quapaw, Oklahoma, USA.

† Model No. 493, manufactured by E. Leitz, Inc., Rockleigh, NJ, USA.

‡ Model CPDT 3300, manufactured by Channel Products, Chesterland, OH, USA.

§ Model JS-7146, manufactured by American Instrument Co., Silver Spring, MD, USA.

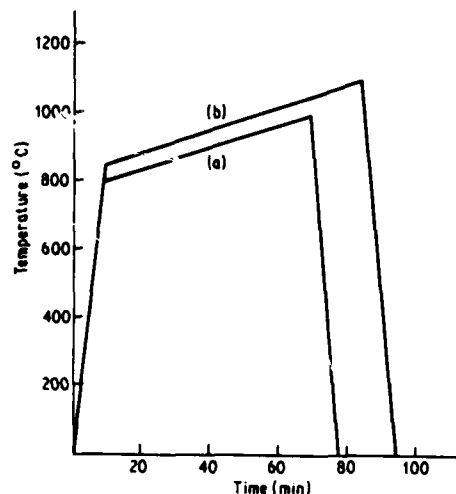


Figure 2 Heating cycles used for crystallizing (a) BTG and (b) BTS glasses.

in a direction parallel to the temperature gradient, with the polar c -axis perpendicular to the hot surface of the sample. As shown in Fig. 4, the 002 reflection was the strongest in the X-ray patterns of the crystallized surfaces. The ratio of the intensity of the 002 peak to that of the 211 peak was taken as a measure of the relative degree of orientation. The intensity ratios are given in Table I. Comparison of the intensity ratios in the glass-ceramic samples with the intensity ratios of a standard powder pattern, showed a high degree of orientation of the crystallites in the glass-ceramics. An even higher degree of orientation was obtained in the samples with good surface finish.

The degree of preferred orientation in crystallized samples of BTS and BTG was similar to that observed previously [1] in $\text{Li}_2\text{Si}_2\text{O}_5$. It was observed that the degree of orientation of the crystallites in the isothermally crystallized glass-ceramics was poor compared to the samples crystallized in a temperature gradient. In addition, detailed studies of the microstructure of the crystallized samples showed that the thickness of the well-orientated region was larger in the case of samples crystallized in a temperature gradient, indicating that thermal gradient crystallization is preferable for obtaining well orientated glass-ceramics.

The main reason for the orientation of the crystallites is surface-nucleated crystallization which takes place in both the isothermal and temperature-gradient crystallization. A higher degree of electrical and crystallographic orientation is obtained in the temperature-gradient crystallization method due to the absence of volume nucleation; however, in the case of isothermal crystallization, the orientation of the crystallites is limited to a layer only a few micrometers thick due to the simultaneous occurrence of volume nucleation. Atkinson and McMillan [9] attempted to produce a $\text{Li}_2\text{Si}_2\text{O}_5$ glass-ceramic with an aligned microstructure by a hot-extrusion method. They were partially successful in obtaining glass-ceramic samples with the disilicate crystal crystallographically-aligned parallel to the extrusion axis. However, the degree of orientation of the crystallites was less than that obtained in glass-ceramic samples prepared by crystallizing the glasses in a temperature gradient [1].

The density of BTG glass was about the same as

TABLE I Summary of data for glass and glass-ceramic samples

Sample	X-ray intensities, $I(002)/I(211)$	Dielectric constant, ϵ^*	Dissipation factor*	Density (g cm^{-3})	d_{11} ($\times 10^{12} \text{ C N}^{-1}$)	Pyroelectric response
BTG glass	—	17	0.003	4.74	—	50% to 60% of single- crystal value
BTG glass-ceramic	85	15.0	0.002	4.56	5 to 7	
$\text{Ba}_2\text{Ge}_2\text{TiO}_8$ single crystal	0.2 (standard powder pattern)	$\epsilon_{11} = 20$ $\epsilon_{22} = 20$ $\epsilon_{33} = 13$	0.003	4.84	8	
BTS glass	—	15	0.002	4.01	—	50% to 60% of single- crystal value
BTS glass-ceramic	15	12.5	0.002	3.90	2 to 3	
$\text{Ba}_2\text{Si}_2\text{TiO}_8$ single crystal	0.2 (standard powder pattern)	$\epsilon_{11} = \epsilon_{22} = 15$ $\epsilon_{33} = 11$	0.003	4.45	3.8	

*Measurements were made at 1 MHz for the glass and glass-ceramic and at 1 kHz for single crystals.

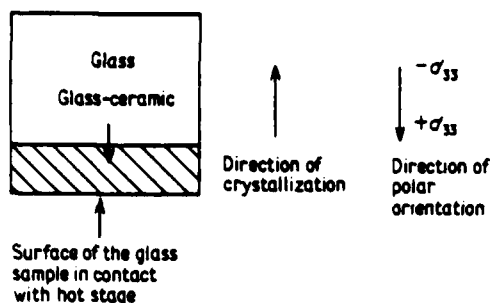


Figure 3 The direction of polar orientation in glass-ceramic samples.

the single-crystal form (Table I), while that of BTS glass was slightly lower than the density of fersnoite single crystals because of the excess silica used in the BTS composition. Only a small decrease in density occurred on crystallization of the glass phases, indicating a low concentration of voids in the glass-ceramic samples. Samples as thin as $100\mu\text{m}$ could be prepared without difficulty because of the absence of pores and cracks.

The dielectric constants of BTS and BTG glasses measured at 1 MHz are very close to the mean dielectric constant, $(\epsilon_{11} + \epsilon_{22} + \epsilon_{33})/3$, of the corresponding crystalline phases. On crystal-

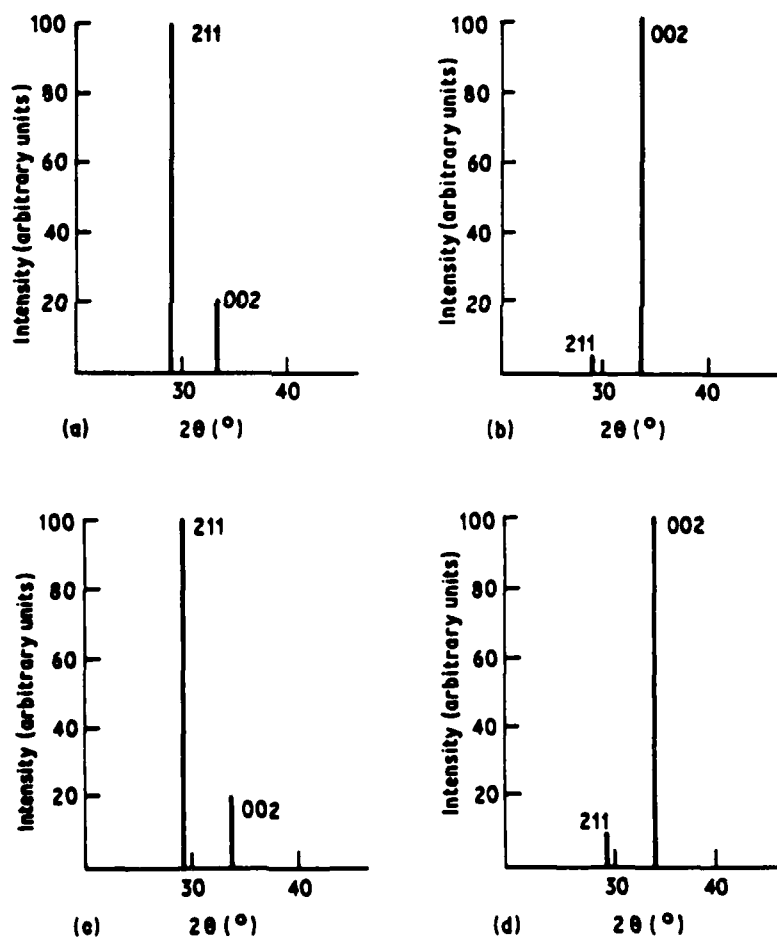


Figure 4 X-ray diffraction patterns of (a) BaTiO_3 standard powder diffraction pattern, (b) BTG glass-ceramic, (c) $\text{Ba}_2\text{TiSi}_2\text{O}_{10}$ standard powder diffraction pattern, and (d) BTS glass-ceramic.

lization, the dielectric constants of the glass-ceramic samples show a slight decrease; the dielectric constant measured in the crystallization direction is closer to the ϵ_3 -values of the single crystals. This is consistent with the fact that the c -axis is the preferred orientation direction in the glass-ceramic, as indicated by X-ray diffraction analysis.

The loss tangent factors of the glass-ceramics were similar to those measured on single crystals.

Piezoelectric coefficients, d_{33} , measured in the crystallization direction in glass-ceramics were comparable to the single-crystal d_{33} coefficient values reported [2-4] for BTS and BTG. Opposite faces of the sample gave opposite signs for the piezoelectric constant. The large magnitude of d_{33} -values and its sign reversal suggest that the crystallites in the glass-ceramics are not only orientated along the c -axis in the crystallization direction, but that most of the crystallites have the same polarity as well. The fact that the d_{33} -values remained constant over the entire surface of the glass-ceramic testifies to the uniformity and the homogeneity of the samples.

As in the previous study of lithium disilicate [1], it was observed that the temperature gradient dictated both the electrical and crystallographic alignment. In all samples the polar orientation was antiparallel to the direction in which crystallization proceeds into the glass, with the positive end of the dipole pointing toward the high-temperature end of the sample, as depicted in Fig. 3. There may be several causes for the polar alignment of the crystallites. One possible cause is the existence of high local electric fields resulting from surface pyroelectric charges [10]. These local electric fields might dictate the orientation of the dipoles as crystallization proceeds into the glass. A second possible cause is the nature of the surface chemistry. It is known that low charge cations such as Li^+ or Ba^{2+} migrate to the surface upon heating [11]. This higher surface concentration of cations could influence the nature of both the crystallization and polar orientation. It is possible that as the crystallization proceeds into the bulk of the glass, starting from a cation-rich surface, the positive end of the dipole moments in the crystallites will be directed toward the hot surface.

The pyroelectric response on the glass ceramics was studied by the dynamic Chynoweth method. Pyroelectric voltage responses of between 50 and 60% of the single-crystal values were obtained

reproducibly with the glass-ceramic samples. The sign of the pyroelectric coefficient is negative for BTG single crystals and positive for BTS. A similar difference in sign was observed with glass-ceramics. For a simple pyroelectric detector, the figure of merit is given by p/ϵ , where p is the pyroelectric coefficient and ϵ is the dielectric permittivity. The pyroelectric coefficients of single crystals of $\text{Ba}_2\text{TiGe}_2\text{O}_8$ and $\text{Ba}_2\text{TiSi}_2\text{O}_8$ are 3 and $10 \mu\text{C m}^{-2} \text{ } ^\circ\text{C}^{-1}$, respectively [12]. Since the dielectric constants of the glass-ceramics are comparable with those of single crystals, it can be concluded that the pyroelectric coefficients of the glass-ceramics are of the same order of magnitude as those of the single crystals. Specimens of 100 to 500 μm in thickness were studied during pyroelectric tests. Samples of large surface area and less than 100 μm in thickness were mechanically strong and gave reproducible results, suggesting their use as pyroelectric detectors.

4. Conclusions

Glass-ceramics of composition $\text{Ba}_2\text{TiGe}_2\text{O}_8$ and $\text{Ba}_2\text{TiSi}_2\text{O}_8$ were prepared by crystallizing the glasses in a temperature gradient. The glass-ceramics show preferred orientation, with the polar c -axis parallel to the temperature gradient. Pyroelectric responses up to 50% of the single-crystal values were observed on these glass-ceramic samples. Measurement of the density, dielectric constant, and piezoelectric constant gave results comparable to the reported single-crystal properties.

Acknowledgement

We wish to thank our colleagues at the Materials Research Laboratory for their advice and assistance. This work was sponsored by the U.S. Army Office of Research and Development (Contract Grant No. DAAG29-78-0033) and by Defense Advanced Research Projects Agency (Contract DARPA Project No. P-15124-MS).

References

1. G. J. GARDOPEE, R. E. NEWNHAM, A. G. HALLIYAL and A. S. BHALLA, *Appl. Phys. Lett.* **36** (1980) 817.
2. M. KIMURA, Y. FUGINO and T. KAWAMURA, *ibid.* **29** (1976) 227.
3. M. KIMURA, K. DOI, S. NANAMATSU and T. KAWAMURA, *ibid.* **23** (1973) 531.
4. M. KIMURA, K. UTSUMI and S. NANAMATSU, *ibid.* **47** (1976) 2249.

5. A. HERCZOG, *J. Amer. Ceram. Soc.* 47 (1964) 107.
6. N. F. BORRELLI and M. M. LAYTON, *J. Non-Cryst. Sol.* 6 (1971) 197.
7. D. E. RASE and R. ROY, *J. Amer. Ceram. Soc.* 38 (1955) 393.
8. A. G. CHYNOWETH, *J. Appl. Phys.* 27 (1956) 78.
9. D. I. H. ATKINSON and P. W. McMILLAN, *J. Mater. Sci.* 12 (1977) 443.
10. P. E. BLOOMFIELD, I. LEFKOWITZ and A. D. ARONOFF, *Phys. Rev. B* 4 (1971) 974.
11. G. E. RINDONE, in *Proceedings of the Symposium on Nucleation and Crystallization in Glasses and Melts*, edited by M. K. Roser, G. Smith and H. Insley (American Ceramic Society, Columbus, Ohio, 1962) pp. 63-69.
12. A. S. BHALLA, unpublished work.

Received 4 July and accepted 22 September 1980.

ANHARMONIC PERTURBATION CALCULATION OF ELECTROSTRICTION FOR SrTiO_3
B.N.N. Achar and G.R. Barsch

Abstract

The hydrostatic electrostriction coefficient of SrTiO_3 has been calculated as a function of temperature on the basis of anharmonic perturbation theory. The same anharmonic shell model as used for the calculation of the electrostriction coefficients of the static crystal is employed. The anharmonic contributions from the Coulomb interactions are found to be comparable to those from the short-range interactions, and their inclusion leads to better agreement with experimental data than calculations based on the model of Bruce and Cowley.

PHENOMENOLOGICAL THEORY OF THE TEMPERATURE VARIATION OF ELECTROSTRICTION
OF FERROELECTRICS IN THE PARAELECTRIC PHASE

G.R. Barsch, B.N.N. Achar and L.E. Cross

Abstract

A properly constructed static Landau-Devonshire free energy function implies the validity of the Curie-Weiss law for a homogeneously strained crystal up to first order in the strain and has been used to deduce phenomenological expressions for the temperature dependence of the first order electrostriction coefficients of ferroelectric crystals in the paraelectric phase. If the prototype phase has cubic symmetry, the coefficients $Q_{rs,ij}$ depend linearly on temperature. Moreover, if the ferroelectric transition is of second order the electrostriction coefficients pertaining to shear deformations vanish at the Curie temperature T_C . These theoretical results are in agreement with the experimental data available for perovskite oxides.

DIFFUSE FERROELECTRIC PHASE TRANSITION AND CATION ORDER IN THE SOLID
SOLUTION SYSTEM $\text{Pb}(\text{Sc}_{1/2}\text{Nb}_{1/2})\text{O}_3:\text{Pb}(\text{Sc}_{1/2}\text{Ta}_{1/2})\text{O}_3$

Chen Zhili, N. Setter, L.E. Cross

Abstract

Earlier studies have shown that in $\text{Pb}(\text{Sc}_{1/2}\text{Ta}_{1/2})\text{O}_3$ PST and $\text{Pb}(\text{Sc}_{1/2}\text{Nb}_{1/2})\text{O}_3$ which are simple cubic perovskites, the degree of ordering of the different B site cations in the ABO_3 structure can be controlled thermally. Quenched disordered crystals and ceramics show diffuse dispersive dielectric properties, while well annealed ordered materials exhibit "normal" sharp first order transitions. In this work the solid solutions between PST and PSN are shown to permit control of both the centroid and the span of the diffuse Curie range. Since the depolarization curve can be modified by both compositions and cation ordering, interesting pyroelectric effects are possible.

ELECTROSTRICTIVE EFFECTS IN POTASSIUM TANTALATE NIOBATE

K. Uchino, S. Nomura, L.E. Cross, and R.E. Newnham

Abstract

Electrostrictive effects in the potassium tantalate niobate solid solution ($\text{K}(\text{Ta}_{0.55}\text{Nb}_{0.45})\text{O}_3$) have been investigated. The electrostrictive coefficients were determined by a strain gauge technique and by the measurement of hydrostatic pressure dependence of dielectric constant near the Curie temperature. The Q values obtained are $Q_{11} = 9.5 \times 10^{-2}$, $Q_{12} = -3.6 \times 10^{-2}$ and $Q_h = 2.3 \times 10^{-2} \text{ m}^4\text{C}^{-2}$, which are almost the same as those of end-members, KTaO_3 and KNbO_3 . The "constant QC rule" is maintained in this solid solution.

TRANSVERSE HONEYCOMB COMPOSITE TRANSDUCERS

A. Safari, A. Halliyal, R.E. Newnham and I.M. Lachman

Abstract

Composites with 3-1 connectivity were fabricated by impregnating an extruded, sintered honeycomb configuration of PZT with epoxy. The composites had lower density ($\sim 300 \text{ Kg/m}^3$) and lower dielectric constant (≈ 400) than that of solid PZT. The maximum piezoelectric \bar{d}_{33} coefficient of the composites was 350 pC/N, and the maximum hydrostatic \bar{d}_h 220 pC/N. \bar{g}_h and $\bar{d}_h \bar{g}_h$ of the composites were an order of magnitude higher than that of solid PZT. Considering the symmetry and phase connectivity of the individual phases in the composite, an explanation is given for the improved piezoelectric properties of the composites.

FLEXIBLE COMPOSITE TRANSDUCERS

A. Safari, A. Halliyal, L.J. Bowen and R.E. Newnham

Abstract

Flexible piezoelectric composites made from PZT spheres and polymers with 1-3 connectivity were fabricated using several types of polymers. The dielectric constant of the composites were 300 to 400 and the piezoelectric voltage coefficients g_{33} were 45 to 55 $\times 10^{-3} \text{ V}\cdot\text{m/N}$. The high-frequency properties of the composites were measured in both the thickness and radial mode of resonance. The frequency constants and the coupling coefficients of the composites for the thickness mode of resonance are comparable with the corresponding values for PZT. Possible applications of the composites are indicated.

HIGH FREQUENCY APPLICATIONS OF PZT/POLYMER COMPOSITE MATERIALS

T.R. Gururaja, W.A. Schulze, T.R. Shrout, A. Safari, L. Webster, L.E. Cross

Abstract

PZT/polymer composite hydrophone materials for four connectivity patterns have been evaluated for high frequency applications such as ultrasonic medical diagnosis and nondestructive testing. The amplitude and bandwidth of the pulse echo test are used as the principal figure of merit. Transducers made with the PZT rods cast in an epoxy matrix have pulse echo sensitivity comparable to unmatched commercial transducers.

STUDY OF THE PIEZOELECTRIC PROPERTIES OF $\text{Ba}_2\text{Ge}_2\text{TiO}_8$
GLASS-CERAMIC AND SINGLE CRYSTALS

A. Halliyal, A.S. Bhalla, R.E. Newnham, L.E. Cross and T.R. Gururaja

Abstract

Glass-ceramics of composition $\text{Ba}_2\text{Ge}_2\text{TiO}_8$ with oriented crystallites were prepared by crystallizing the glasses in a temperature gradient. The degree of preferred orientation of the crystallites as a function of depth was studied. Piezoelectric resonance properties of both the glass-ceramics and the single crystals were studied. The piezoelectric d_{33} coefficient, the frequency constants and the electromechanical coupling coefficients of the glass-ceramic were comparable to the single-crystal values.

PIEZOELECTRIC PROPERTIES OF LITHIUM BOROSILICATE GLASS CERAMICS

A. Halliyal, A.S. Bhalla, R.E. Newnham and L.E. Cross

Abstract

Glass ceramics in the system $\text{Li}_2\text{O}-\text{SiO}_2-\text{B}_2\text{O}_3$, with oriented crystallites were prepared by crystallizing the glasses in a temperature gradient. Piezoelectric and electromechanical properties of the glass ceramics are reported. Some of the compositions exhibit low temperature coefficient of resonance, comparable to LiTiO_3 single crystals. Advantages of fabricating glass-ceramic piezoelectric resonators are described and the possibility of using them in surface acoustic wave (SAW) devices is suggested.

FABRICATION AND ELECTRICAL PROPERTIES OF GRAIN ORIENTED $\text{Bi}_4\text{Ti}_3\text{O}_{12}$ CERAMICS

S. Swartz, W.A. Schulze and J.V. Biggers

Abstract

A fabrication process has been developed by which $\text{Bi}_4\text{Ti}_3\text{O}_{12}$ can be made in ceramic form with high densities (92% theoretical) and substantial grain orientations (>95%). The process consists of molten salt synthesis of platelets of $\text{Bi}_4\text{Ti}_3\text{O}_{12}$, tape casting, and conventional sintering. Electrical measurements have verified the high degree of grain orientation obtained in these ceramics. Permittivities in the a-b oriented direction (along the plane of the tape) and the c oriented direction (perpendicular to the plane of the tape) at 100 KHz are 153 ± 5 and 118 ± 5 , respectively. Conductivities at 1 KHz and 500°C in the a-b and c oriented directions are 6.3×10^{-2} and $4.2 \times 10^{-3} (\text{ohm-m})^{-1}$, respectively. The c oriented direction was poled to a d_{33} of 5×10^{-12} C/N with the application of a DC field. The a-b oriented direction was poled to a d_{33} of 10×10^{-12} C/N with the application of a pulsed field on cooling through the transition.

ORDERING IN $\text{Pb}(\text{Mg}_{1/3}\text{Nb}_{2/3})\text{O}_3$ - $\text{Pb}(\text{Mg}_{1/2}\text{W}_{1/2})\text{O}_3$ SOLID SOLUTIONS

A. Amin, R.E. Newnham, L.E. Cross, S. Nomura and D.E. Cox

Abstract

Compositional ordering was found to occur in the ferroelectric $(1-x)$ $\text{Pb}(\text{Mg}_{1/3}\text{Nb}_{2/3})\text{O}_3$ antiferroelectric x $\text{Pb}(\text{Mg}_{1/2}\text{W}_{1/2})\text{O}_3$ solid solution system. X-ray diffraction and neutron profile fitting structure refinement were used to refine one such composition with $x = 0.9$. The paraelectric structure of compositions with $x < 0.2$ is that of the disordered perovskite (space group $\text{Pm}3\text{m}$), whereas for $0.2 \leq x < 1.0$ the structure is that of ordered perovskite (space group $\text{Fm}3\text{m}$). The oxygen octahedra in the ordered state are regular but no longer equivalent.

LOW ENERGY INERT GAS ION SCATTERING FROM GdF_3 , Gd_2O_3 AND $\text{Gd}_2(\text{MoO}_4)_3$ SURFACES: 1. INELASTIC EFFECTS

L.L. Tongson, A.S. Bhalla and B.E. Knox

Abstract

Inelastic effects in the scattering of Ar-40, Ne-20 and He-4 ions from GdF_3 and Gd_2O_3 have been studied. Such effects give rise to the low energy 'tail' of the elastic peaks in ion surface scattering (ISS). Experimental data show that the extent of 'tailing' increases from Ar-40 to He-4. For each probe ion type, the background is significantly greater in GdF_3 than in Gd_2O_3 . The significance of (1) surface structure, (2) the surface polarization model and ion surface scattering, and (3) electronic effects on this low energy background will be shown by discussing the present data as well as supplementary results on He-4 ion scattering from selected oxides and polar surfaces of $\text{Gd}_2(\text{MoO}_4)_3$.

#75

INVESTIGATION OF BaTiO_3 and $\text{Gd}_2(\text{MoO}_4)_3$ CRYSTAL SURFACES BY
COMPLEMENTARY AES AND ISS TECHNIQUES

L.L. Tongson, A.S. Bhalla, L.E. Cross and B.E. Knox

Abstract

The chemical nature of the intrinsic surface layer in BaTiO_3 single crystals and the positive and negative surfaces of gadolinium molybdate have been determined using AES and ISS. Potassium and fluorine were detected in BaTiO_3 crystals grown by the Remeika method. The ratio of the AES 417 eV to 411 eV peaks of Ti in BaTiO_3 was stable under ion and electron beam irradiation. ISS showed that the positive and negative surface of gadolinium molybdate crystals were chemically identical, with both types exhibiting similar variations in the Gd and Mo signals with ion bombardment time. However, marked differences in the spectra of sputtered and scattered ions from each type were observed.

#76

DIRECT METHOD OF MEASURING ION BEAM IRRADIATED AREAS

A.S. Bhalla and L. Tongson

#77

LUMINESCENCE OF Tb^{3+} AND Eu^{3+} ACTIVATED FERROELECTRIC-FERROELASTIC
GADOLINIUM MOLYBDATE

B.K. Chandrasekhar, A.S. Bhalla and William B. White

#82

PRIMARY AND SECONDARY PYROELECTRICITY IN PROPER AND IMPROPER FERROELECTRICS
A.S. Bhalla and L.E. Cross

Abstract

Primary and secondary components of the total pyroelectricity have been separated for a number of proper and improper ferroelectrics, polar nonferroelectrics, and II-VI semiconductor family materials. The relation $1/k^{3/4} \approx 3 \times 10^{-9}$ C/cm²°K holds for TGS, doped TGS, and the solid solution series of the TGS family.

PYROELECTRIC PZT-POLYMER COMPOSITES

A.S. Bhalla, R.E. Newnham, L.E. Cross and W.A. Schulze

Abstract

PZT-Spurrs composites fabricated by the replamine technique improves the pyroelectric figure of merit p/ϵ by a factor of 7 over that of solid PZT. The temperature dependence of the pyroelectric response exhibits an interesting compensation point where the primary and secondary effects cancel out. At room temperature the hard plastic mechanically clamps the PZT, but at higher temperatures the plastic softens. PZT-soft polymer composites showed no enhancement of the pyroelectric figure of merit. Major changes in the pyroelectric response were noted when the sample thickness was comparable to the scale of the composite heterogeneity.

POLAR GLASS CERAMICS

A. Halliwal, A.S. Bhalla, R.E. Newnham and L.E. Cross

Abstract

Pyroelectric-piezoelectric glass ceramics of polar materials like $\text{Li}_2\text{Si}_2\text{O}_5$, $\text{Ba}_2\text{TiGe}_2\text{O}_8$, $\text{Ba}_2\text{TiSi}_2\text{O}_8$, and various compositions in the systems $\text{Li}_2\text{O}-\text{B}_2\text{O}_3$, $\text{Li}_2\text{O}-\text{SiO}_2-\text{ZnO}$, $\text{Li}_2\text{O}-\text{SiO}_2-\text{B}_2\text{O}_3$ have been prepared by oriented recrystallization of the glasses under a strong temperature gradient, providing a simple inexpensive process for preparing piezoelectric and pyroelectric materials. High pyroelectric responses were observed in these glass-ceramics. Values of piezoelectric d_{33} coefficients, frequency constants, electromechanical coupling coefficients and dielectric properties of glass-ceramics were in close agreement with the values of respective single crystals.

PYROELECTRIC $\text{Li}_2\text{Si}_2\text{O}_5$ GLASS-CERAMICS

G.J. Gardopee, R.E. Newnham and A.S. Bhalla

Abstract

Highly oriented surface layers of lithium disilicate crystals were grown by crystallizing glasses of the composition $\text{Li}_2\text{O}:\text{SiO}_2$. The thickness of the oriented layer was a function of the thermal treatment. The crystallites in these layers were oriented with their c-axes perpendicular to the sample surface. These layers were found to be pyroelectric as determined by the Chynoweth technique. The pyroelectric responses of the glass-ceramics crystallized in a thermal gradient were approximately four times larger than that of a tourmaline crystal of similar dimensions.

PYROELECTRIC GLASS-CERAMICS

G.J. Gardopee, R.E. Newnham, A.G. Halliyal and A.S. Bhalla

Abstract

Highly oriented surface layers of lithium disilicate crystals were grown by crystallizing glasses of composition $\text{Li}_2\text{Si}_2\text{O}_5$ in a temperature gradient. The polar c axes of the crystallites were oriented parallel to the temperature gradient and perpendicular to the sample surface. The pyroelectric response of the glass-ceramic crystallized in a thermal gradient was approximately four times larger than that of a tourmaline crystal of similar dimensions. The time dependence of the pyroelectric signal obeys the thin-film equivalent circuit model developed by Chynoweth.

#90

FERROIC CRYSTALS, CERAMICS, AND COMPOSITES

R.E. Newnham and L.E. Cross

Abstract

Movable twins or domains are the characteristic feature of ferroic crystals. Four topics of current interest are reviewed in this paper: secondary ferroics (ferrobielasticity in quartz), diffuse phase transitions (relaxor ferroelectric lead magnesium niobate), composite ferroics (PZT-polymer piezoelectric devices), and improper ferroics (magnetoferroelectricity in Cr_2BeO_4).

#91

FERROIC CRYSTALS

R.E. Newnham

#92

CRYSTALLOGRAPHY AT PENN STATE

R.E. Newnham

BASIC DISTRIBUTION LIST

Technical and Summary Reports

November 1979

<u>Organization</u>	<u>Copies</u>	<u>Organization</u>	<u>Copies</u>
Defense Documentation Center Cameron Station Alexandria, VA 22314	12	Naval Air Propulsion Test Center Trenton, NJ 08628 ATTN: Library	1
Office of Naval Research Department of the Navy 800 M. Quincy Street Arlington, VA 22217 ATTN: Code 471	1	Naval Construction Battalion Civil Engineering Laboratory Port Hueneme, CA 93043 ATTN: Materials Division	1
Code 470	1	Naval Electronics Laboratory San Diego, CA 92152 ATTN: Electron Materials Sciences Division	1
Commanding Officer Office of Naval Research Branch Office Building 114, Section D 666 Summer Street Boston, MA 02210	1	Naval Missile Center Materials Consultant Code 3312-1 Point Mugu, CA 92041	1
Commanding Officer Office of Naval Research Branch Office 536 South Clark Street Chicago, IL 60605	1	Commanding Officer Naval Surface Weapons Center White Oak Laboratory Silver Spring, MD 20910 ATTN: Library	1
Office of Naval Research San Francisco Area Office One Hallidie Plaza Suite 601 San Francisco, CA 94102	1	Commander David W. Taylor Naval Ship Research and Development Center Bethesda, MD 20084	1
Naval Research Laboratory Washington, DC 20375 ATTN: Codes 6000	1	Naval Oceans Systems Center San Diego, CA 92132 ATTN: Library	1
6100	1	Naval Underwater System Center Newport, RI 02840 ATTN: Library	1
6300	1	Naval Postgraduate School Monterey, CA 93940 ATTN: Mechanical Engineering Department	1
2627	1	Naval Weapons Center China Lake, CA 93555 ATTN: Library	1
Naval Air Development Center Code 606 Warminster, PA 18974 ATTN: Mr. F. S. Williams	1		

BASIC DISTRIBUTION LIST (cont'd)

<u>Organization</u>	<u>Copies</u>	<u>Organization</u>	<u>Copies</u>
Naval Air Systems Command Washington, DC 20360 ATTN: Codes 52031 52032	1 1	NASA Lewis Research Center 21000 Brookpark Road Cleveland, OH 44135 ATTN: Library	1
Naval Sea System Command Washington, DC 20362 ATTN: Code 05R	1	National Bureau of Standards Washington, DC 20234 ATTN: Metals Science and Standards Division	1
Naval Facilities Engineering Command Alexandria, VA 22331 ATTN: Code 03	1	Ceramics Glass and Solid State Science Division Fracture and Deformation Division	1 1
Scientific Advisor Commandant of the Marine Corps Washington, DC 20380 ATTN: Code AX	1	Director Applied Physics Laboratory University of Washington 1013 Northeast Fortieth Street Seattle, WA 98105	1
Army Research Office P. O. Box 12211 Triangle Park, NC 27709 ATTN: Metallurgy & Ceramics Program	1	Defense Metals and Ceramics Information Center Battelle Memorial Institute 505 King Avenue Columbus, OH 43201	1
Army Materials and Mechanics Research Center Watertown, MA 02172 ATTN: Research Programs Office		Metals and Ceramics Division Oak Ridge National Laboratory P. O. Box X Oak Ridge, TN 37380	1
Air Force Office of Scientific Research/NE Building 410 Bolling Air Force Base Washington, DC 20332 ATTN: Chemical Science Directorate Electronics & Materials Sciences Directorate	1 1	Los Alamos Scientific Laboratory P. O. Box 1663 Los Alamos, NM 87544 ATTN: Report Librarian	1
Air Force Materials Laboratory Wright-Patterson AFB Dayton, OH 45433	1	Argonne National Laboratory Metallurgy Division P. O. Box 229 Lemont, IL 60439	1
Library Building 50, Room 134 Lawrence Radiation Laboratory Berkeley, CA	1	Brookhaven National Laboratory Technical Information Division Upton, Long Island New York 11973 ATTN: Research Library	1
NASA Headquarters Washington, DC 20546 ATTN: Code RRM	1	Office of Naval Research Branch Office 1030 East Green Street Pasadena, CA 91106	1

SUPPLEMENTARY DISTRIBUTION LIST A
Electronic, Magnetic, and Optical Ceramics

032
June 1980

Advanced Research Projects Agency
Materials Science Director
1400 Wilson Boulevard
Arlington, VA 22209

Dr. Don Berlincourt
Channel Products
16722 Park Circle Drive W.
Chagrin Falls, OH 44022

Dr. J. V. Biggers
Pennsylvania State University
Materials Research Laboratory
University Park, PA 16802

Mr. George Boyer
Sensor Systems Program
Office of Naval Research
Code 222
Arlington, VA 22217

Professor R. Bradt
Ceramics Section
Materials Sciences Department
The Pennsylvania State University
University Park, PA 16802

Dr. Dean Buckner
Piezo Products Division
Gulton Industries
P. O. Box 4300
Fullerton, CA 92634

Dr. Robert Callahan
Channel Industries
839 Ward Drive
Box 3680
Santa Barbara, CA 93105

Professor L. E. Cross
The Pennsylvania State University
Materials Research Laboratory
University Park, PA 16802

Mr. N. Coda
Vice President for Engineering
Erie Technological Products
West College Avenue
State College, PA 16802

Dr. Gene Haertling
Motorola Corporation
3434 Vassar, NE
Albuquerque, NM 87107

Dr. W. B. Harrison
Honeywell Ceramics Center
1885 Douglas Drive
Golden Valley, MN 55422

Dr. C. M. Stickley, V. P.
The BDM Corporation
7915 Jones Branch Drive
McLean, VA 22102

Dr. L. L. Hench
Department of Metallurgy
University of Florida
Gainesville, FL 32603

Dr. B. F. Rider
Rockwell International
400 Collins Road NE
Cedar Rapids, IA 52406

Dr. F. Robert Hill
Marine Resources
755 Highway 17 & 92
Fern Park, FL 32730

Dr. Bernard Jaffe
232 Forbes Road
Bedford, OH 44146

Dr. B. G. Koepke
Honeywell, Inc.
Corporate Research Center
10701 Lyndale Avenue South
Bloomington, MN 55420

Dr. R. Lapetina
Edo Western Corporation
2645 South 300 West
Salt Lake City, UT 84115

Mr. C. LeBlanc
Naval Underwater Systems Center
TD 121
Newport, RI 02840

Dr. N. Perrone
Code 474
Office of Naval Research
800 N. Quincy Street
Arlington, VA 22217

Dr. Frank Recny
General Electric Company
Court Street
Plant Building C
Box 1122
Syracuse, NY 13201

Dr. J. H. Rosolowski
General Electric Company
Research and Development Center
P. O. Box 8
Schenectady, NY 02301

Dr. P. L. Smith
Naval Research Laboratory
Code 6361
Washington, DC 20375

Dr. R. W. Timme
Naval Research Laboratory
Code 8275
Underwater Sound Reference Division
P. O. Box 8337
Orlando, FL 32806

Dr. Charles C. Walker
Naval Sea Systems Command
National Center #3
2531 Jefferson Davis Highway
Arlington, VA 20390

Dr. Paul D. Wilcox
Sandia Laboratories
Division 2521
Albuquerque, NM 87115

The State University of New York
at Alfred
Material Sciences Division
Alfred, NY

Dr. R. Rice
Naval Research Laboratory
Code 6360
Washington, DC 20375

Professor R. Roy
The Pennsylvania State University
Materials Research Laboratory
University Park, PA 16802

Dr. N. Tallan
AFML Wright-Patterson AFB
Dayton, OH 45433

Dr. H. E. Bennett
Naval Weapons Center
Code 3818
China Lake, CA 93555

Dr. Michael Bell
Inorganic Materials Division
National Bureau of Standards
Washington, DC 20234

Dr. R. Bratton
Westinghouse Research Laboratory
Pittsburgh, PA 15235

Dr. Joe Dougherty, Dir. Engr.
Gulton Industries
212 Durham Avenue
Metuchen, NJ 08840

Dr. James Pappis
Raytheon Co., Research Division
28 Seyon Street
Waltham, MA 02154

Dr. Perry A. Miles
Raytheon Co., Research Division
28 Seyon Street
Waltham, MA 02154

Dr. P. E. D. Morgan
Rockwell Science Center
1049 Camino Dos Rios
P. O. Box 1085
Thousand Oaks, CA 91360

Dr. G. Ewell
MS6-D163
Hughes Aircraft Company
Centinela & Teale Streets
Culver City, CA 90230

Dr. David C. Hill
Member Technical Staff
Texas Instruments, Inc.
Attleboro, MA 02703

Dr. S. K. Kurtz, V. P.
Clairol, Inc.
2 Blachley Road
Stamford, CT 06902

Dr. Herb Moss
RCA Laboratories
Princeton, NJ 08540

Dr. R. E. Newnham
Materials Research Laboratory
The Pennsylvania State University
University Park, PA 16802

Dr. Charles S. Sahagian, Chief
EM Technology Branch, SSS Division
HQ Rome Air Dev. Center (AFSC)
Deputy for Electronic Technology
Hanscom AFB, MA 01731

Dr. J. Smith
GTE Sylvania
100 Endicott Street
Danvers, MA 01923

Dr. Wallace A. Smith
North American Philips Laboratories
345 Scarborough Road
Briarcliff Manor, NY 10510

Mr. Raymond E. Sparks
Technology Library R220
Delco Electronics Division/GMC
P. O. Box 1104
Kokomo, IN 46901

Dr. Manfred Kahn
Senior Scientist, Prod. Dev.
AVX Ceramics, P. O. Box 867
Myrtle Beach, SC 29577

Mr. G. Goodman, Manager
Corporation of Applied Research Group
Globe-Union Inc.
5757 North Green Bay Avenue
Milwaukee, WI 53201

Dr. George W. Taylor
Princeton Resources, Inc.
P. O. Box 211
Princeton, NJ 08540

Mr. John J. Thiermann
Physics International
2700 Merced Street
San Leandro, CA 94577

Dr. D. Carson
Code 7122
Naval Ocean Systems Center
San Diego, CA 92152

Dr. C. Hicks
Code 631
Naval Ocean Systems Center
San Diego, CA 92152

Dr. R. Smith
Code 7122
Naval Ocean Systems Center
San Diego, CA 92152

Professor R. Buchanan
Department of Ceramic Engineering
University of Illinois
Urbana, Illinois 61801

Professor B. A. Auld
Stanford University
W. W. Hansen Laboratories of Physics
Stanford, CA 94306

Dr. S. Musikant
General Electric Co.
3188 Chestnut Street
Philadelphia, PA 19101

Dr. A. Gentile
Hughes Research Laboratories
3011 Malibu Canyon Road
Malibu, CA 90265

Dr. J. Harrington
Hughes Research Laboratories
3011 Malibu Canyon Road
Malibu, CA 90265

Professor G. Kino
Stanford University
Stanford, CA 94305

Dr. A. E. Clark
Naval Surface Weapons Center
White Oak Laboratory
Silver Spring, MD 20910

Dr. Gordon Martin
2627 Burgener
San Diego CA 92110

Eric Udd
McDonnell Douglas Astronautics
5301 Bolsa Ave
Huntington Beach CA 92647

Director
Applied Research Lab
The Pennsylvania State Univ.
University Park, PA 16802

Army Research Office
Box CM, Duke Station
Attn: Met. & Ceram. Div.
Durham, NC 27706

National Bur. Standards
Inorganic Mats. Division
Washington DC 20234

National Bur. Standards
Metallurgy Division
Washington DC 20234

Naval Air Systems Comm.
Code 320
Washington DC 20360

Pacific Missile Test Center
Materials Consultant
Code 4121
Pt. Mugu, CA 93042

Naval Research Lab
Code 6400
Washington DC 20390

Naval Sea System Command
Code 035
Washington DC 20362

Naval Ship Engr. Center
Code 6101, CTR BG #2
3700 East-West Highway
Prince Georges Plaza
Hyattsville, MD 20782

Office of Naval Research
Department of the Navy
Code 102
Arlington, VA 22217

Dr. G. Bansal
Battelle Laboratories
505 King Avenue
Columbus, OH 43201

Dr. George Benthien
Naval Ocean Systems Center
Code 212
San Diego, CA 92152

Mr. N. Coda, VP Engr.
Erie Technol. Products
Res. and Dev.
Erie, PA 16512

Dr. G. Denman, Code LPJ
AFML, Wright-Patterson AFB
Dayton, OH 45433

Sheldon Detwiler, Disp. Mgr.
Adv. Technol. Laboratories
13208 Northrup Way, PO Box 6639
Bellevue, WA 98007

Dr. W.G.D. Frederick
AFML, Wright-Patterson AFB
Dayton, OH 45433

Dr. P. Giellisse
University of Rhode Island
Kingston, RI 02881

Mr. G. Hayes
Naval Weapons Center
China Lake, CA 93555

Dr. R.N. Katz
Army Materials and Mechanics
Research Center
Watertown, MA 02171

Dr. P.L. Lall
Office of Naval Research
666 Summer Street
Boston, MA 02210

Dr. P. Land
AFML, Wright-Patterson AFB
Dayton, OH 45433

Dr. F.F. Lange
Rockwell International
PO Box 1085
1049 Camino Dos Rios
Thousand Oaks, CA 91360

Dr. Eugene A. Larson, Pres.
Blue River Laboratories
PO Box 442
Lewistown, PA 17044

Mr. K. Letson
Redstone Arsenal
Huntsville, AL 35809

Dr. N. Macmillan
Materials Research Laboratory
The Pennsylvania State Univ.
University Park, PA 16802

Mr. F. Markarian
Naval Weapons Center
China Lake, CA 93555

Mr. K.D. McHenry
Yoneywell Corp. Tech. Center
10701 Lyndale Avenue South
Bloomington, MN 55420

Dr. R.R. Neurgaonkar
Rockwell International Science Center
1049 Camino Dos Rios
PO Box 1085
Thousand Oaks, CA 91360

Norton Company - Library
Industrial Ceramics Division
Worcester, MA 01606

James W. Pell
Manager of Development
Rohe Scientific Corporation
2722 S. Fairview Street
Santa Ana, CA 92704

Dr. R.C. Pohanka
Room 619, Ballston Tower
800 N. Quincy Street
Arlington, VA 22217

Dr. R.A. Queeney
126 Hammond Building
The Pennsylvania State Univ.
University Park, PA 16802

J.J. Rasmussen, Manager
Applied Research Division
Montana Energy and MHD R&D
PO Box 3809
Butte, Montana 59701

Dr. R. Ruh
AFML, Wright-Patterson AFB
Dayton, OH 45433

James Runt
313 Steidle Bldg
The Pennsylvania State Univ.
University Park, PA 16802

Mr. G. Schmitt
AFML, Wright-Patterson AFB
Dayton, OH 45433

Dr. T. Sentementes
GTE Sylvania
100 Endicott Street
Danvers, MA 01923

State University of New York
College of Ceramics
Alfred University
Attn: Library
Alfred, NY 14802

Dr. R.E. Tressler
Ceramic Science Section
226 Steidle Building
The Pennsylvania State Univ.
University Park, PA 16802

Eric Udd
McDonnell Douglas Astron.
5301 Bolsa Avenue
Huntington Beach, CA 92647

Dr. T. Vasilos
AVCO R & Adv. Dev. Division
201 Lowell Street
Wilmington, MA 01887

Mr. J.D. Walton
Engineering Experiment Station
Georgia Institute of Technology
Atlanta, GA 30332

Mr. L.B. Weckesser
Applied Physics Laboratory
Johns Hopkins Road
Laurel, MD 20810

END

DATE
FILMED

6-82

DTIC